MATERIAL-TO-SYSTEM ANALYSIS OF LITHIUM – SULFUR AND LITHIUM – OXYGEN BATTERIES

by

Ayşegül Kılıç

B.S., Chemical Engineering, Boğaziçi University, 2016

M.S., Chemical Engineering, Boğaziçi University, 2019

Submitted to the Institute for Graduate Studies in
Science and Engineering in partial fulfillment of
the requirements for the degree of
Doctor of Philosophy

Graduate Program in Chemical Engineering

Boğaziçi University

2024

to my daughter and my large family

ACKNOWLEDGEMENTS

I would like to express my sincere gratitude to my thesis advisor, Assoc. Prof. Damla Eroglu. Every time I needed help, she was always there for me; to support, to encourage and to motivate me in every aspect of my life. Her positive attitude, enthusiasm towards science, and discipline showed me how to be a good researcher. I feel fortunate to have her as my thesis advisor and would like to have life-long bonds with her.

I would like to thank Prof. Ramazan Yıldırım for his contribution to my thesis, my personal development in data science and his student-friendly attitude. I also thank to my thesis committee members. Assoc. Prof. Uğur Ünal always gave valuable comments on my progress reports and opened his research facilities to support our work. I also thank Assoc. Prof. Oktay Demircan for his support as well and for showing a positive attitude towards us knowing that we can always consult him and use his lab devices as well. Finally, I acknowledge Prof. Erdem Günay for his time, evaluation of my thesis, and valuable comments on it.

I would like to extend my sincere thanks to my friends Ayça Fırtın and Kağan Yüksel for their valuable friendships, teamwork, and every support they made during my PhD degree. I also thank all the Eroglu lab members, we were a great team together. I also thank my old friends, Gülşah Gül, Özlem Özbek, Feyza Kevser Öner, Elif Esvap, Müge Kasım, and all the graduate students and members of our department.

Words cannot express my gratitude to my daughter, Deren Zümra, and my husband, Fikret Kılıç, for being in my life and making life more meaningful. Heartful thanks to my parents, Nezahat and İdris Karakuş, my four engineer siblings Tuğba, Cemal, Melike, and Cemil, and my lovely niece Zeynep Erva. I also appreciate the support from my mother-in-law Fazilet Kılıç.

The support of TUBITAK 1001 (Project No: 221M542) and BAP (Project No: 19384) is greatly acknowledged.

ABSTRACT

MATERIAL-TO-SYSTEM ANALYSIS OF LITHIUM – SULFUR AND LITHIUM – OXYGEN BATTERIES

Developing beyond lithium-ion batteries (LIBs) is critical for fulfilling the high energy demand of future vehicles. In this respect, lithium-sulfur (Li-S) and lithium-oxygen (Li-O_2) batteries were studied here to understand the effect of cell design and materials on the battery performance. The studies of Li-S batteries involve three main methods: experimental characterization, system-level performance modeling, and machine learning (ML). Instead, only ML models were developed for Li-O_2 batteries. First, association rule mining (ARM) was utilized to understand the cell and materials design effects on Li-S battery performance using the data collected from the literature. For Li-S batteries, the encapsulation material type was the most important feature, and system-level performances were highly improved with ionic liquid (IL) electrolytes. Next, polysulfide (PS) solubility in ILs and IL properties were determined for 36260 ILs using the COnductor-like Screening Model for Realistic Solvents (COSMO-RS) calculations. 6 ILs were experimentally tested to determine the solubility ranges of ILs for high-performance Li-S cells. Afterward, extreme gradient boosting (XGBoost) and ARM were utilized to predict and identify promising ILs and their features. Imidazolium cations with either borates or bis_imide anion group were the most promising IL pairs. Encapsulation cathodes were also studied. UiO66/Graphene nanoplatelet (GNP) composites increased the rate performances of Li-S cells where 50 wt.% UiO66 loading was the optimum for balancing electron transfer and PS chemisorption. Vanadium and Cobalt-doped ketjen black cathodes increased the system-level performances of Li-S batteries. ARM was also used for Li-O_2 battery literature data; metallic cathode ingredients LaFe oxides, Ni oxides, and electrolyte solvents significantly impact battery performance. Last, gas solubilities of nearly 30,000 ILs were calculated using COSMO-RS, and random forest (RF) was used to build predictive models. Anion descriptors were more determinative of the gas solubilities.

ÖZET

LİTYUM-SÜLFÜR VE LİTYUM-OKSİJEN BATARYALARININ MALZEMEDEN SİSTEME ANALİZİ

Lityum-iyon bataryalarından (LIB) daha iyi kapasite gösterecek batarya gelişimi, yüksek enerji talep eden gelecekteki araçlar için oldukça önemlidir. Bu bağlamda, bu çalışmada tasarım parametreleri ve malzeme etkisinin lityum-sülfür (Li-S) ve lityum-oksijen ($Li-O_2$) batarya performansı üzerine etkileri incelenmiştir. Li-S bataryaları üç metotla incelenmiştir: elektrokimyasal karakterizasyon, sistem-düzeyi performans modellemesi ve son olarak makine öğrenmesi. $Li-O_2$ bataryaları içinse sadece makine öğrenmesi metotları kullanılmıştır. İlk olarak, hücre ve materyal tasarımlarının Li-S batarya performansının üzerine etkileri literatür verileri ile, birliktelik kuralları analizi (ARM) kullanılarak açıklanmıştır. Li-S bataryaları için emprenye malzeme tipi en önemli faktördür ve sistem-düzeyi performans, iyonik sıvı (IL) elektrolitler ile birlikte önemli derecede arttırılmışıtr. Bir sonraki kısımda, Li-S bataryaları için elektrolit geliştirme amacıyla 36260 IL için IL'lerin polisülfit (PS) çözünürlükleri COSMO-RS hesaplamalarıyla belirlenmiştir. 6 iyonik sıvı için elektrokimyasal testler yapılmış olup yüksek performanslı Li-S bataryaları için gereken vizkosite ve çözünürlük limitleri belirlenmiştir. İmidazol katyonları ile borat veya bis_imid grupları en çok umud vaad eden IL çiftidir. Emprenye katot malzemeler de çalışılmıştır. Elektron iletkenliği ve kimyasal adsorpsiyonu dengelenmiş, yarı yarıya kütlece oran gösteren UiO66/Grafen nanoplatelet (GNP) kompozit Li-S hücrelerinin hız performansını arttırmıştır. Vanadyum ve kobalt katkılı ketjen siyahı katotlar, düşük elektrolit-sülfür (E/S) oranı ve yüksek sülfür yoğunluğunda sistem-düzeyi performansı arttırmıştır. ARM, $Li-O_2$ batarya literatüründe de kullanılmış ve LaFe ve Ni oksitlerler birlikte, elektrolit çözücüsünün performansı ciddi bir şekilde etkilediği görülmüştür. Son olarak, 30,000 IL için gaz çözünürlükleri COSMO-RS kullanılarak hesaplanmış ve rassal orman (RF) ile öngörücü modelleler kurulmuştur. Anyon tanımlayıcıların gaz çözünürlükleri üstünde daha etkili olduğu görülmüştür.

TABLE OF CONTENTS

LIST OF FIGURES

LIST OF TABLES

LIST OF SYMBOLS

a	Cathode electrochemically active area, cm^2/cm^3
$A_{cathode}$	Cathode area, cm^2
A_{cell}	Cell area, cm^2
ASI	Area-specific impedance, $\Omega\ cm^2$
ASI_{cc-}	Negative current collector ASI, $\Omega\ cm^2$
ASI_{cc+}	Positive current collector ASI, $\Omega\ cm^2$
ASI_{cell}	Total ASI of the cell, $\Omega\ cm^2$
ASI_{ne}	Negative electrode ASI, $\Omega\ cm^2$
ASI_p	ASI of the cell at rated power, $\Omega\ cm^2$
ASI_{pe}	Positive electrode ASI, $\Omega\ cm^2$
ASI_{sep}	Separator ASI, $\Omega\ cm^2$
C	Cell capacity, Ah
c_{pe}	Positive electrode capacity mAh/cm^3
E	Battery pack energy, kWh
F	Faraday's constant, C/mol
I	Current density, A/cm^2
I_e	Average current density, A/cm^2
$i_{o,ne}$	Negative electrode exchange current density, A/cm^2
$i_{o,pe}$	Positive electrode exchange current density, A/cm^2
I_p	Current density at rated power, A/cm^2
L_{pe}	Positive electrode thickness, cm
$L_{pe,max}$	Maximum cathode thickness, cm
L_{sep}	Separator thickness, cm
N_{cell}	Number of cells in a pack
P	Battery pack power, kW
R	Gas constant, J/(mol.K)
T	Temperature, K
U_{batt}	Average open-circuit battery voltage, V
$U_{ocv,p}$	Open-circuit cell voltage, V

V_{cell}	Cell voltage, V
V_e	Voltage at rated energy, V
V_p	Voltage at rated power, V
w_s	Sulfur weight fraction in the cathode
α	Transfer coefficient
β	$ape,cF/RT$
δ	$\beta\|I\|L_{pe}(1/\kappa_{eff}+1/\sigma_{eff})$
ϵ	$\beta\|I \mid Lpe /\kappa_{eff}$
ε	Electrolyte volume fraction in the cathode
ε_b	Binder volume fraction in the cathode
ε_c	Carbon volume fraction in the cathode
ε_{dis}	Discharged volume fraction in the cathode, mAh/cm^3
ε_s	S volume fraction in the cathode
η_{cc-}	Negative current collector overpotential, V
η_{cc+}	Positive current collector overpotential, V
η_{cell}	Total overpotential of the cell, V
η_{ne}	Negative electrode overpotential, V
η_{pe}	Positive electrode overpotential, V
η_{sep}	Separator overpotential, V
θ	First integration constant for Tafel polarization
κ	Positive electrode ionic conductivity, S/cm
κ_{eff}	Positive electrode effective ionic conductivity, S/cm
κ_{sep}	Separator ionic conductivity, S/cm
$\kappa_{sep,eff}$	Separator effective ionic conductivity, S/cm
ν	$(l^2pe\ (\alpha_{pe,a}+\alpha_{pe,c})ai_{0,pe}\ F/RT\ (1/\kappa_{eff}+1/\sigma_{eff}))^{1/2}$
ρ_c	Carbon density, g/cm^3
σ	Positive electrode electronic condutivity, S/cm
σ_{eff}	Positive electrode effective electronic conductivity, S/cm
ψ	Second integration constant for Tafel polarization

LIST OF ACRONYMS/ABBREVIATIONS

1-D	One-Dimensional
3-D	Three-Dimensional
ACN	Acetonitrile
AI	Artificial Intelligence
ANN	Artificial Neural Networks
ARM	Association Rule Mining
ASI	Area Specific Impedence
AUC	Area Under the Receiver Operating Characteristic Curve
BatPaC	Battery Performance and Cost
BET	Brunauer-Emmett-Teller
BETA	Bis(pentafluoroethanesulfonyl)amide
BF4	Tetrafluoroborate
BMIM	1-butyl-3-methyl-imidazolium
BTC	1,3,5-benzenetricarboxylic acid
C-rate	Current Rate
C/S	Carbon-to-Sulfur
C4dmim	1-butyl-2,3-dimethylimidazolium
C4mpyr	1-butyl-1-methylpyrrolidinium
CGCNN	Crystal Graph Convolutional Neural Networks
CMC	Carboxymethyl Cellulose
CMK-3	Mesoporous Carbon
CNF	Carbon Nanofiber
CNN	Convolutional Neural Networks
CNT	Carbon Nanotube
COSMO-RS	COnductor-like Screening Model for Realistic Solvents
CV	Cycling Voltammetry
DEC	Diethyl Carbonate
DEGDME	Diethylene Glycol Dimethyl Ether
DEME	N,N-diethyl-N-methyl-N-(2-methoxyethyl)ammonium

DFT	Density Functional Theory
DMA	Dimethylacetamide
DMC	Dimethyl Carbonate
DMDS	Dimethyl Disulfide
DME	1,2-dimethoxyethane
DMSO	Dimethylsulfoxide
DNN	Deep Neural Network
DoD	Depth of Discharge
DOL	1,3-Dioxolane
DT	Decision Tree
E/S	Electrolyte-to-Sulfur
EC	Ethylene Carbonate
EGDME	Ethylene Glycol Dimethyl Ether
EMC	Ethyl−Methyl Carbonate
EMIM	1-ethyl-3-methylimidazolium
ERT	Extreme Regression Trees
ETFE	Ethyl-1,1,2,2-tetrafluoroethylether
FSI	Bis(fluorosufonyl)imide
FTIR	Fourier Transform Infrared Spectroscopy
G3	Triglyme
G4	Tetraglyme
GBT	Gradient Boosting Trees
GNP	Graphene Nanoplatelet
GO	Graphene Oxide
GPR	Gaussian Process Regressor
HCS	Hollow Carbon Sphere
HFE	1,1,2,2-tetrafluoroethyl 2,2,3,3-tetrafluoropropyl ether
HKUST	Hong Kong University of Science and Technology
IL	Ionic liquid
IP	Imidazolium-Based Ionic Polymer
K-ion	Potassium-Ion
kNN	k-Nearest Neighbors
KRR	Kernel Ridge Regression

LA	Polymer n-Lauryl Acrylate
LASSO	Least Absolute Shrinkage And Selection Operator
LATP	$Li_{(1 + x + y)}Al_xTi_{(2-x)}Si_yP_{(3-y)}O_{12}$
LHCE	Localized High-Concentration Electrolyte
Li-O_2	Lithium-Oxygen
Li-S	Lithium-Sulfur
Li(G3)	Li(triglyme)
$Li(G_3)_1TFSI$	Li(triglyme)[bis(trifluoromethanesulfonyl)amide]
Li(G4)	Li(tetraglyme)
LIB	Li-Ion Battery
LiFSI	Lithium Bis(fluorosulfonyl)imide
LiODFB	Lithium Difluoro(oxalate)borate
LiPAA	Lithium Polyacrylate
LiTDI	Lithium Trifluoromethyl-4,5-Dicyanoimidazole
LiTf	Lithium Trifluoromethanesulfonate ($LiCF_3SO_3$)
LiTFSI	Lithium Bis(trifluoromethanesulfonyl)amide
LogR	Logistic Regression
LR	Linear Regression
MAE	Mean Absolute Error
MD	Molecular Dynamics
ML	Machine Learning
MLP	Multilayer Perceptron
MLR	Multiple Linear Regression
MOF	Metal Organic Framework
MS	Molecular Solvent
MWCNT	Multiwalled Carbon Nanotube
Na-ion	Sodium-Ion
NB	Naive Bayes
NMC	Nickel-Manganese-Cobalt
NMP	N-methyl-2-pyrolidone
NN	Neural Network
NP	Not Provided
OCV	Open Cell Voltage

OER	Oxygen Evolution Reaction
OMC	Ordered Mesoporous Carbon
ORR	Oxygen Reduction Reaction
OTE	1,1,2,2-tetrafluoroethyl Ether
P13	N-methyl-n-propylpyrrolidinium
P14	N-butyl-n-methylpyrrolidinium
P1A3	N-Methyl-n-Allylpyrrolidinium
P2225	Triethylpentylphosphonium
PAA	Polyacrylic Acid
PANI	Polyaniline
PC	Propylene Carbonate
PDADMA-T	Polydiallyldimethylammonium Having Quaternary Ammonium Cation and bis(Trifluoromethane)Sulfonimide
PDC	Peak Discharge Capacity
PDDA	Poly(diallyl dimethylammonium) Chloride
PEDOT	Poly(3,4-ethylenedioxythiophene)
PEG	Polyethylene Glycol
PEGDME	Poly(Ethylene Glycol) Dimethyl Ether
PEO	Poly(ethylene oxide)
PMIM	1-methyl-3-propylimidazolium
PP13	N-methyl-n-propylpiperidinium
PP14	1-butyl-1-methylpiperidinium
PS	Polysulfide
PSM	Polysulfide Shuttle Mechanisms
PSS	Polystyrene Sulfonate
PTFE	Polytetrafluoroethylene
PVA	Polyvinyl Alcohol
PVC	Polyvinylchloride
PVDF	Polyvinylidene Fluoride
PVP	Polyvinylpyrrolidone
Pyr1,2O1	N-methoxyethyl-n-methylpyrrolidinium
Ref.	Reference
RF	Random Forest

rGO	Reduced Graphene Oxide
RMSE	Root Mean Squared Error
RR	Ridge Regression
RTIL	Room Temperature Ionic Liquid
SBR	Styrene-Butadiene Rubber
SEI	Solid Electrolyte Interface
SEM	Scanning electron microscopy
SIL	Solvate Ionic Liquid
SOH	State Of Health
SSE	Solid-State Electrolytes
SVM	Support Vector Machines
TBMA	Tributylmethylammonium
TEGDME	Tetraethylene Glycol Dimethyl Ether
TES	Triethylsulfonium
TFSI	Bis(trifluoromethanesulfonyl)imide
TFTFE	1,1,2,2-Tetrafluoroethyl 2,2,2-trifluoroethyl ether
TGA	Thermal Gravimetric Analysis
TL	Transfer Learning
TMS	Tetramethylene Sulfone
TMU	N,n,n’,n’-tetramethylurea
Tri-EGDME	Triethylene Glycol Dimethyl Ether
TTE	1,1,2,2-tetrafluoroethyl- 2,2,3,3-tetrafluoropropyl ether
U0	Standard Potential
UG	UiO66+Graphene Nanoplatelet Composite
UGS	UiO66+Graphene Nanoplatelet+S Composite
WOS	Web Of Science
XGBoost	Extreme Gradient Boosting
XRD	X-ray Diffraction Spectroscopy

1. INTRODUCTION

Fossil fuels are the most widely used energy sources in today's activities. The use of fossil fuels has led to environmental problems and global warming [1,2]. In addition to the environmental concerns, the limiting reserves of fossil fuels will not meet the growing world energy demand. Hence, many researchers are working to develop high-efficiency renewable energy systems that contain energy harvesting and storing units. Wind and solar energy are commonly used renewable systems that convert natural energy to electricity. Since these energy sources are intermittent and the energy demand is dependent on the consumer's needs, energy should be stored to be released when the production does not meet the demand.

Accounting for 28 % of the world's total energy consumption, transportation is one of the major sectors in which the utilization of renewable energy is critical to abandoning fossil fuels. In this respect, many automobile producers have started to launch the production of hybrid and electric vehicles to reach the countries' efforts to diminish carbon dioxide (CO_2) emissions. Currently, LIBs are widely used as energy storage systems in electric vehicles. However, these batteries are expensive. In addition, with energy densities of 150-300 Wh/kg, these batteries have limiting capacities to increase the ranges of the vehicles [3]. In this respect, beyond lithium-ion batteries have drawn attention due to their high theoretical capacities. Among them, Li-S batteries have gained significant importance in recent years due to their high theoretical capacity [4]. Li-S batteries are highly promising since they have the potential to attain much higher gravimetric and volumetric energy densities than LIBs in the future [5,6]. In addition to Li-S, Li-O_2 batteries also gained significant attention as they offer the highest theoretical specific capacity [7,8].

Although Li-S batteries are very promising to replace the LIBs, there are several problems that should be solved to enable commercialization. This requires the optimization of the critical parameters both at the materials and system levels using experimental and modeling methods as complementary techniques to design high-performing Li-S battery systems. In this respect, in this thesis, system-level modeling and experimental characterization, in addition to ML techniques, were used together to conduct a material-to-

system analysis of the Li-S batteries for determining the effect of critical design parameters and material properties on the cell- and system-level performances of the Li-S batteries.

On the other hand, the high theoretical capacities of Li-O_2 batteries have not been achieved yet, mainly due to issues related to the oxygen cathode. The open-to-gas environment, sluggish reaction kinetics, side reactions, and instability of the electrolytes are the main problems of Li-O_2 batteries, resulting in poor battery performances [9]. These problems are even more severe than the issues of Li-S cells, as the experimental studies on the Li-O_2 cells are more limited. To overcome these problems, several materials and cell design parameters were studied in this thesis using ML analysis.

1.1. Li-S Batteries

The basic scheme of a Li-S cell can be seen in Figure 1.1. As seen in the figure, a Li-S battery contains an anode, a separator, a cathode, and a liquid electrolyte like conventional batteries. In Li-S batteries, metallic Li anode is used as the anode, whereas the cathode consists of a conductive matrix, binder, and sulfur as the active material. Most high-capacity battery systems have Li metal as the anode due to its very high theoretical specific capacity of 3860 mAh/g Li and low molecular weight of 6.94 g/mol. In addition, it has the highest standard oxidation potential of 3.04 V, which leads to a high battery power [10]. Moreover, sulfur is one of the most abundant, non-toxic, and inexpensive elements in nature, and it has a specific capacity of 1675 mAh/g [6], [11,12]. Hence, it is proposed to be a good cathode candidate for inexpensive, high-capacity batteries [6], [12].

3860 mAh/g and 1675 mAh/g are the specific capacities of Li and S, respectively. In addition, the theoretical gravimetric energy density of a Li-S battery is 2600 Wh/kg, which is almost 6 times higher than LIBs [13]. During discharge, lithium metal is oxidized, and sulfur is reduced simultaneously in the anode and the cathode, respectively. Oxidized Li ions transport through the electrolyte from the anode to the cathode to react with the reduced sulfur. The overall reaction of Li-S batteries producing 2.2 V (vs. Li/ Li^+) is given as

$$16Li^+ + 8S + 16e^- \rightarrow 8Li_2S. \quad (1.1)$$

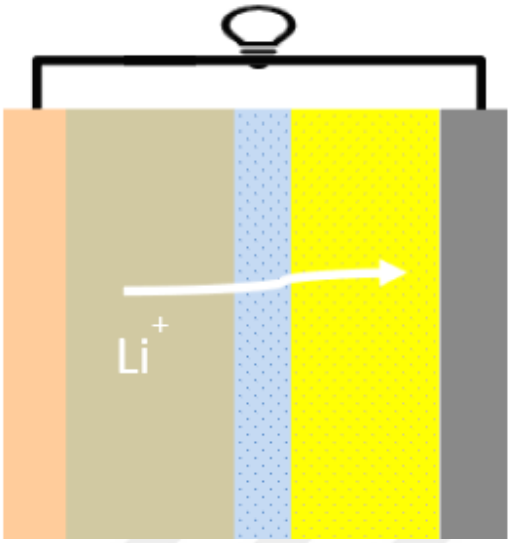

Figure 1.1. The basic schematic diagram of a Li-S cell.

A typical discharge profile of a Li-S cell is shown in Figure 1.2**,** where there are two plateaus, around 2.4 V and 2.1 V, named the high and low voltage discharge plateaus [14]. Multi-step reactions are taking place in the cathode during discharge. Although the exact reactions are not identified yet, several attempts have been made to define the highly complex multi-step reactions taking place during discharge [15–18]. One of the proposed reaction scheme depending on the discharge regions are shown in Figure 1.2, and it is defined as

$$Li \rightarrow Li^+ + e^-, \tag{1.2}$$

$$^1/_2\ S_8 + e^- \rightarrow {}^1/_2\ S_8^{2-}, \tag{1.3}$$

$$2Li^+ + S_8^{2-} \rightarrow Li_2S_8, \tag{1.4}$$

$$Li_2S_8 + 2Li \rightarrow Li_2S_{8-n} + Li_2S_n, \tag{1.5}$$

$$2Li_2S_n + (2n-4)Li \rightarrow nLi_2S_2, \tag{1.6}$$

$$Li_2S_n + (2n-2)Li \rightarrow nLi_2S, \tag{1.7}$$

$$Li_2S_2 + 2Li \rightarrow Li_2S. \tag{1.8}$$

The equations corresponding the regions are as follows: Equation (1.2) to Equation (1.4) for Region 1, Equation (1.5) for Region 2, Equation (1.6) to Equation (1.7) for Region 3 and Equation (1.8) for Region 4 [19]**.** In general, high-chain PS are formed in the high discharge plateau, and they are further reduced to short-chain PSs later in the low discharge plateau with the final discharge product Li_2S. A sudden voltage drop is obtained due to the insulating nature of this discharge product, which results in very slow reaction kinetics [19]**.**

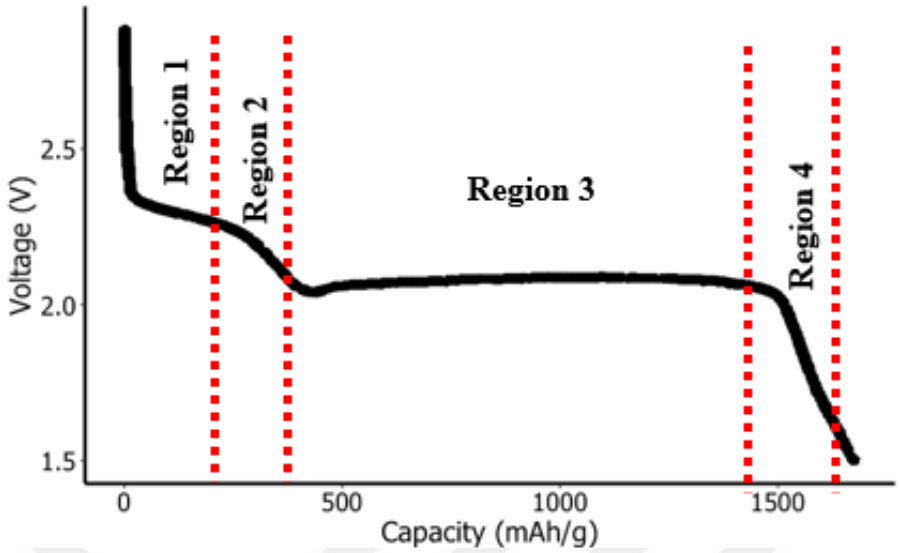

Figure 1.2. Cell voltage versus capacity graph of a typical Li-S cell.

Although the theoretical capacity of Li-S batteries is high, there are several problems that limit the usable capacity and cycle life. The complex working mechanisms of sulfur cathodes are the main reasons for these problems [20]. These challenges can be listed as follows:

- The insulating nature of both sulfur and Li_2S results in low sulfur utilization and requirements of having conductive materials in the cathode. This increases the dead mass of the cells, which does not contribute to the cell performance. Hence, specially designed conductive materials with high surface areas and porosities should be utilized in the sulfur cathodes. There are lots of studies in the literature trying to find the best structures to load more active material into lower amounts of conductive networks to increase the energy density of both cells and battery systems [21]. The type and properties of the conductive material used in these encapsulated sulfur cathodes play a critical role in battery performance.
- As aforementioned, there are various PSs (Li_2S_x, $2 \leq x \leq 8$) formed as intermediate products during discharge. The high-order PSs should be converted to the low-order PSs and eventually to solid Li_2S during discharge. Solid Li_2S should be oxidized back to solid sulfur during charge to have reversible usable capacity. However, PSs are highly soluble in conventional electrolytes and can shuttle between the cathode and the anode during cycling. This PS shuttle mechanism leads to anode deterioration,

active material loss, and low Coulombic efficiency [22,23]. There are various strategies to prevent the shuttle mechanism, such as designing coated separators, three-dimensional (3-D) conductive networks, and new electrolyte solvents [24].

- There are various products present in the complete discharge and charge states of a Li-S cell. During discharge, solid elemental sulfur with 2.07 g/cm^3 density is converted to Li_2S with 1.66 g/cm^3 density. Due to the density difference, a volume change of up to 76 % can be observed. This may lead to unstable cathode structures and early cathode decomposition [25]. In this respect, the type and structure of the conductive materials are also very important to have stable cathodes [26,27].
- Although Li metal is a desired anode material due to its low standard potential, its high reactivity causes early cell failure and safety problems. Li metal can react with the electrolyte, separator, and other cell components. That high reactivity may result in both Li metal and electrolyte depletion in the cells. To build safer batteries that offer long-term stability, the design of new electrolyte materials, additives, or protective layers has been investigated in the literature [28,29].

Although Li-S batteries are very promising in terms of their high theoretical specific capacity, due to the aforementioned problems, practical system- and cell-level energy densities are not comparable with the LIBs yet. To enable the commercialization of Li-S batteries, research should be focused on material research, electrode architecture, and cell engineering. Hence, materials and cell design parameters such as sulfur content, sulfur loading, electrode thickness, electrolyte type, electrolyte-to-sulfur ratio, encapsulation conductive material type, and battery system design should all be considered together [30].

The electrolyte is one of the important components of batteries, where ion transfer between the anode and the cathode takes place in all electrochemical systems. The electrolyte should be inert to the other cell components. It should also be stable over the working voltage window. Due to the complex electrochemical reactions taking place in Li-S cells, electrolytes of Li-S cells should have additional properties. One of the most important characteristics is the solubility of the PSs in these electrolytes, as very high solubilities lead to an increase in the PSM and result in low cell efficiencies [31]. The most common electrolyte used in Li-S cells is 1,3-dioxalane (DOL):1,2-dimethoxyethane (DME)

(1:1 vol.%) solvents containing lithium bis(trifluoromethane)sulfonimide (LiTFSI) and lithium nitrate ($LiNO_3$) salts [24]. Ionic liquids have been shown to be promising electrolytes by preventing the PS shuttle mechanism and increasing working voltage window.

The system- and cell-level performance of Li-S batteries are heavily dependent on the cathode. One of the main hurdles of the sulfur cathode is the insulating nature of sulfur and the discharge product Li_2S [32]. That leads to a requirement for conductive materials in addition to sulfur, which results in an increase in the dead weight of the cells. In order to minimize the dead weight, great research effort has been made to obtain materials with a large specific surface area. In addition, depending on the conductive materials type, a binder may also be required in the cathode to increase structural stability [33]. Hence, an efficient cathode design is crucial for Li-S batteries.

The parameters that will be investigated in this thesis are related to the positive electrodes and electrolytes of Li-S batteries. Encapsulation material type and sulfur loading, which are determined to be critical cathode parameters, will be investigated to develop cathodes that have high sulfur loadings together with high sulfur utilization, which are crucial to attain high cell- and system-level specific energies. This is only possible if sulfur is contained in a highly porous and interconnected encapsulation network that allows high electronic conductivity. Electrolyte-to-sulfur (E/S) ratio and IL type will also be investigated as the electrolyte parameters to improve both the capacities and efficiencies of Li-S cells.

1.2. Lithium-Oxygen Batteries

Li-air batteries may have the potential to surpass LIBs as they have the highest theoretical specific capacity among the beyond LIBs. Based on the discharge product Li_2O_2, the specific energy is around 3500 Wh/kg, offering the highest energy among the metal-air batteries. Similar to Li-S cells, Li-O_2 batteries have a pure metallic lithium anode, a porous separator, an electrolyte, and a porous cathode. One difference is that the cathode active material is gaseous, as seen in Figure 1.3. Pure lithium metal is typically used as the anode of lithium-air batteries because it is the lightest metal but yet has the highest oxidation potential of 3.040 V, providing 3860 mAh/g specific capacity [10]. The high reactivity of

the lithium metal is always a problem in lithium-based batteries. However, lithium metal becomes more problematic in these batteries due to the gaseous reactants, which may further deteriorate lithium metal. To protect the anode, the separator should be selected carefully, blocking the transfer of gases. Currently, due to their low costs and high durability, polyolefins are used widely as separators in lithium-air cells [34].

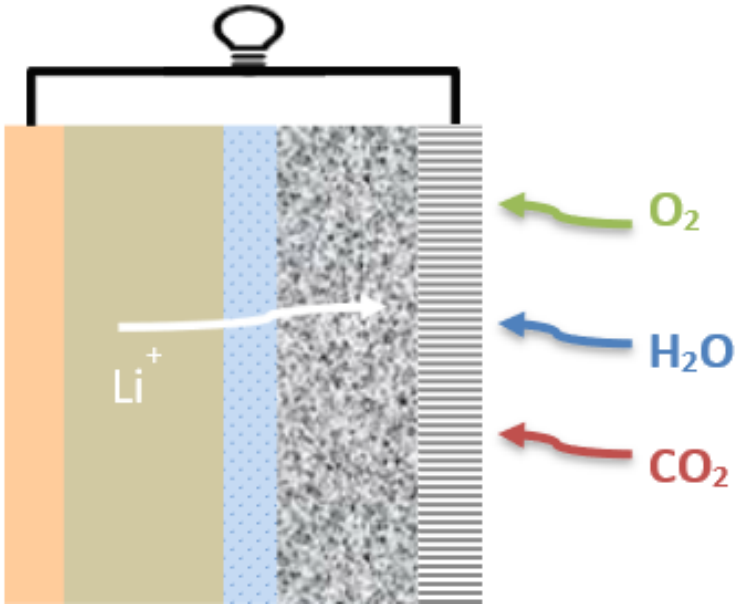

Figure 1.3. The basic schematic diagram of a Li-air cell.

Generally, liquid electrolytes are used in batteries; solid electrolytes are less common in the literature. In addition to the standard liquid electrolyte properties, such as chemical and mechanical durability with low vapor pressure, gas solubilities are also major concerns. Only dissolved gases can participate in the electrochemical reactions. Hence, it is very critical to favor high oxygen solubilities with a restriction on the solubilities of the other gases. According to the literature, non-aqueous electrolytes containing lithium salts are the typical electrolyte systems of Li-O_2 batteries [35–37].

Oxygen reduction reactions (ORRs) take place in the cathodes of Li-O_2 batteries, where Li^+ ions coming from the anode side, electrons supplied through the outer circuit and dissolved oxygen meet on the surface of a solid network. To enhance the reaction kinetics, fast electron transfer is very critical. Thus, the cathode network should have high porosity with high electronic conductivity. Additional catalyst materials like metals are commonly

preferred to further increase the kinetics [38]. Typically, a binder is also added to increase the structural integrity of the cathodes. Carbon paper may also be utilized as an additional gas diffusion layer for the homogeneous distribution of oxygen to improve cell performance [39,40]. ORRs are

$$O_2 + Li^+ + e^- \longrightarrow LiO_2, \quad (1.9)$$

$$2LiO_2 \longrightarrow Li_2O_2 + O_2, \quad (1.10)$$

and/or

$$LiO_2 + Li^+ + e^- \longrightarrow Li_2O_2, \quad (1.11)$$

oxygen evolution reaction (OER) is

$$Li_2O_2 \longrightarrow O_2 + 2Li^+ + 2e^-, \quad (1.12)$$

where the overall reaction is

$$2Li + O_2 \leftrightarrows Li_2O_2, \quad (1.13)$$

with U^0 is 2.96 V vs. Li/Li^+. The reactions of the lithium-oxygen batteries are shown in Equation (1.9) to Equation (1.13) [41]. As seen from the equations, Li_2O_2 is the end discharge product of Li-O_2 batteries.

For a smooth operation of Li-O_2 batteries the reactions presented in Equation 1.13 should be reversible. In other words, once the Li_2O_2 is deposited on the cathode matrix, it shoud be easily turned to oxygen and also lithium should be protected. However, this is generally prevented by several side reactions taking place inside a Li-O_2 cells. One of the main reasons of the side reactions is the impurities like atmospheric gases including nitrogen (N_2), carbon dioxide (CO_2) and water (H_2O). Both N_2 and H_2O gases can react with lithium anode, leading to loss of lithium material. Meanwhile, CO_2 tends to react with Li_2O_2 to form Li_2CO_3, which is more stable and prevent the reversible conversion of Li_2O_2 to oxygen gas [42]. The possible side reactions are

$$4Li + O_2 + 2CO_2 \rightarrow 2Li_2CO_3, \quad (1.14)$$

$$Li_2O + CO_2 \rightarrow Li_2CO_3, \quad (1.15)$$

$$2Li_2O_2 + 2CO_2 \rightarrow 2Li_2CO_3 + O_2, \quad (1.16)$$

$$2LiOH + CO_2 \rightarrow Li_2CO_3 + H_2O, \quad (1.17)$$

$$2Li + 2H_2O \rightarrow 2LiOH + H_2, \quad (1.18)$$

$$LiOH + H_2O \rightarrow LiOH.H_2O, \quad (1.19)$$

$$Li_2O_2 + H_2O \rightarrow LiOH + H_2O_2, \quad (1.20)$$

$$4Li + O_2 + 2H_2O \rightarrow 4LiOH, \quad (1.21)$$

$$2Li_2O_2 + 2H_2O \rightarrow 4LiOH + O_2, \quad (1.22)$$

$$Li_2O_2 + H_2O \rightarrow LiOOH + LiOH, \quad (1.23)$$

$$LiOH + H_2O_2 \rightarrow LiOOH + H_2O, \quad (1.24)$$

$$6Li + N_2 \rightarrow 2Li_3N, \quad (1.25)$$

$$Li_3N + 3H_2O \rightarrow 3LiOH + NH_3. \quad (1.26)$$

1.3. Scope of the Current Work

The aim of this thesis is to increase the performance of beyond LIBs, specifically, Li-S and Li-O_2 batteries, by conducting a detailed material-to-system analysis. At first, studies on Li-S batteries were performed. The effect of important design parameters, which are sulfur loading, electrolyte-to-sulfur (E/S) ratio, and electrolyte and encapsulation material types, on the cell- and system-level performances of Li-S batteries were investigated. In order to achieve this goal, experimental (electrochemical characterization) and theoretical (ML and system-level performance modeling) methods were used as complementary techniques to connect the material properties to the cell- and system-level performances of the Li-S batteries. In this respect, the findings of this thesis contribute highly to both the Li-S battery literature and the industry.

There are many works reported in the literature focusing on reaching the theoretical capacities (1675 mAh/g) and increasing the cycle lives of Li-S batteries. Although these performance metrics are very important, the final performance indicators are the system-level energy density and specific energy of the Li-S battery. However, there are very limited studies investigating the system-level performance. Hence, by using encapsulated cathodes and promising electrolyte materials and taking cell design parameters into account, the main aim of this research is to design a Li-S cell with high specific capacity and cycle life together with high specific energy and energy density. While doing this, ML techniques were also used to identify the promising materials and hidden correlations in the literature, where more than 8000 articles have already been published. From this perspective, this is a highly novel investigation of the effect of encapsulated cathode properties, electrolyte types, and cell design parameters on Li-S battery performance using three different techniques.

The second main topic of this thesis is Li-O_2 batteries, as they possess much higher theoretical capacities. However, their development is much more problematic as they contain an active material in the gas phase, where gas is distributed over an electronically conductive matrix. The design of the positive electrode is important for smooth oxygen redox reactions, in other words, to diminish the mass and kinetic resistances. Meanwhile, the electrolyte must be suitable for oxygen dissolution, it should be stable, and it should have low vapor pressure. Unfortunately, the experimentation of these batteries is much harder. In this respect, all the information on the experimental works that have been done already should be utilized. In addition, computational methods should be used for fast screening of various materials that are suitable for Li-O_2 batteries. Hence, ML methods were used for analyzing the important materials and cell design factors for the development of high-performance Li-O_2 batteries in this thesis. Moreover, high-throughput screening of ionic liquids as the electrolytes of Li-O_2 batteries was presented.

This thesis consists of chapters listed as Introduction, Literature Survey, Results and Discussion, and Conclusions and Recommendations. Chapter 2 presents detailed summaries of the literature for both Li-S and Li-O_2 batteries and ML studies in battery science, modified from our review paper published recently in the Journal of Energy Storage [9]. In Chapter 3, the methods and materials utilized in the thesis were explained in detail. In the scope of this thesis, the Results and Discussion part was divided into two; studies on Li-S and Li-O_2 batteries were given in Part 1 and Part 2 of Chapter 4, respectively. Part 1 of Chapter 4 contains 5 sub-sections. In the first sub-section, the effect of materials and design parameters on Li-S battery performance was analyzed by means of ML by using the literature data, and it was published in the Chemical Engineering Journal in 2020 [43]. Section 2 contains a similar ML analysis, but this time, the dataset contains experimental data on Li-S cells containing IL electrolytes only; this study was published in the International Journal of Energy Research in 2022 [44]. Section 3 reports the screening of IL electrolytes based on the viscosities and PS solubilities for Li-S batteries. In addition, ML models were developed to enable the prediction of these properties for any IL and to find potential ILs for Li-S batteries. The manuscript detailing these results is in preparation. In Section 4 and Section 5, the effect of different encapsulation materials on the Li-S battery performance was

investigated. In Section 4, the impact of composite cathodes made of MOF/Graphene nanoplatelets on Li-S cell performance was experimentally tested. The manuscript presenting the results in this section is published in Energy Technology journal [45]. Finally, the effect of vanadium and cobalt-doped ketjen black cathodes and the design parameters on the Li-S cell- and system-level performances were presented in Section 4.1.5. Part of this chapter has already been published in the ACS Applied Energy Materials in 2023 [46], and the second part is published in ChemElectroChem [47]. In Part 2 (section 4.2), ML studies on the Li-O_2 batteries were done. In Section 4.2.1, the literature data were collected to analyze the common trends and to reveal hidden correlations to find favorable materials and cell design for high capacities; this study was published in the Journal of The Electrochemical Society in 2021 [48]. Finally, the gas solubilities of the ILs were screened, and ML models were proposed for identifying promising IL electrolytes for Li-O_2 batteries. A manuscript on these results is currently in preparation.

2. LITERATURE SURVEY

2.1. Li-S Batteries

2.1.1. Effect of Sulfur Loading

Schneider et al. have developed binder-free and free-standing N-doped cathodes with thicknesses lower than 200 μm. To prepare high sulfur loaded cathodes, a facile hard-templating method was used in this study. The 3-D structure of carbon developed in this study has 1.78 cm^3/g total pore volume and 80 m^2/g surface area. The porous structure enabled efficient contact between sulfur and the conductive network, even with small amounts. The cathodes having sulfur loadings in the ranges of 2.5 and 8.5 mg/cm^2 at 10 μL/mg E/S ratio and C/20 current rate (C-rate) were investigated. The cycling results showed that the sulfur utilization decreases linearly with sulfur loading. According to the specific capacity results, sulfur utilization was 70 % and 20 % for sulfur loadings of 2.5 and 8.5 mg/cm^2, respectively. On the other hand, similar areal capacities were obtained for all of the sulfur loadings [49].

Doan et al. investigated the sulfur loading effect using sulfur-pyrolyzed polyacrylonitrile composite cathodes doped with $Mg_{0.6}Ni_{0.4}O$ nanoparticles. Sulfur loadings were investigated from 0.55 mg/cm^2 to 5.9 mg/cm^2. Cycling results at 0.2 C showed that good capacity retention is obtained in 70 cycles with sulfur loadings lower than 3.1 mg/cm^2. However, rapid capacity decrease was observed after 50 cycles for higher loadings (>3.1 mg/cm^2). This was attributed to the removal of thick cathodes from Al foil current collectors and more PS formation at high sulfur loadings. Higher PS formation in the same electrolyte volume triggers the PS shuttle mechanism that leads to low Coulombic efficiency and capacity fading [50].

Sulfur loading was defined as the areal capacity in the work reported by Sun et al. Galvanostatic cycling tests were performed using loadings between 0.5 to 7.5 mAh/cm^2. Low sulfur utilization was observed with sulfur loadings higher than 3.0 mAh/cm^2. It was observed that the conversion of soluble Li_2S_4 to insoluble discharge product Li_2S/Li_2S_2 was

not efficiently taking place at the low voltage plateau around 2.1 V. This conversion was recovered after several activation cycles for up to 4.5 mAh/cm^2 loading, whereas no recovery is observed with 7 mAh/cm^2 even after 100 cycles [51].

The problems and the solution strategies regarding the use of high sulfur loadings in the Li-S battery were reviewed in a recent work by Hu et al.. To sum up, it was emphasized that high sulfur loading is needed to scale up lab-scale research and enable industrialization. To have high sulfur loadings, thicker cathodes should be prepared, which results in new problems in the cathode, electrolyte, and anode. Structural deformations and reduced diffusion distance are the main problems of having thick cathodes. On the other hand, the PS shuttle mechanism is triggered with high sulfur loadings, and more Li dendrites are formed on the anode side. The most efficient method to solve these problems proposed by the authors is utilizing highly porous encapsulation cathodes and optimizing the amount of electrolytes compatible with the lithium anodes [52]. This paper also shows the importance of the three other parameters: effect of encapsulation, E/S ratio, and types and amount of ionic liquids as electrolytes, and emphasizes the need for a mechanistic study, which should take all the parameters into account.

2.1.2. Effect of Encapsulation Material

In a review done by Zhang et al., it is stated that the development of encapsulation materials is very important to develop cathode hosts to mitigate the problems of Li-S batteries. The cathode hosts, encapsulation materials, in other words, should be electronically conductive, have a high surface area, high structural stability, and finally, have PS chemisorption on the surface. So far, various hosts, more specifically carbon-based materials like graphene and its derivatives, carbon nanotubes (CNT), and metal compounds, have been developed. Metal-organic frameworks (MOFs) have already been utilized in energy research due to their high porosities (>0.5 cm^3/g) and surface areas (>3000 m^2/g). Although there is some research in the literature, the utilization of MOF materials as sulfur hosts is limited due to low electrical conductivity. Hence, the MOF composites and MOF-derived materials are more common in the sulfur cathodes to increase sulfur utilization [53]. Liu et al. used the composite of UiO-66 and carbon nanotubes in the sulfur cathodes to increase the cycling ability of Li-S batteries. UiO-66/CNT composite with covalently

bonded sulfur leads to a physical connection of sulfur with its host that prevents sulfur delocalization and leads to sulfur stabilization. It also fixes PSs at their original state and reduces the shuttle effect. Hence, the composites of UiO-66/CNT covalently bonded with sulfur showed good cycling stability even at high current rates. With covalently bonded sulfur, 80.2% capacity retention was obtained at 2C and ended up at 416 mAh/g after 900 cycles [54].

Another composite was done by Wang et al., where sulfur was integrated with two carbon sources. One of the carbon sources is the MOF-derived, N-doped, and CoP nanoparticles having carbon nanoarrays. First, Co-MOF was infiltrated on carbon cloth, and it was carbonized and phosphorized simultaneously. Afterward, sulfur was added to the composite by the standard melt-diffusion method. This self-standing composite showed around 1400 mAh/g initial discharge capacity and decreased to 900 mAh/g after a few cycles at 2C. After 600 cycles, the cells preserved most of their capacity and ended up with an 800 mAh/g specific capacity [55].

In another study developed by Wang et al., HKUST-1 MOF was used as the cathode host for trapping sulfur and reducing sulfur loss due to excess dissolution. This MOF contains Cu^{+2} open sites that lead to better sulfur confinement. Two sets were prepared: one where sulfur and MOF were mechanically mixed (HKUST-1/S) and one where they were heated at 428 K for 24 h in an argon atmosphere (HKUST-1⊃S). The synthesized HKUST-1 has 1500 m^2/g surface area, which is reduced to 97 m^2 for HKUST-1⊃S. The cathodes have approximately 40 wt.% sulfur with around 0.5 mg/cm^2 loadings, and the standard LiTFSI and $LiNO_3$ containing DOL:DME electrolyte were used. Both samples exhibited initial discharge capacities of around 1500 mAh/g, which decreased to 500 mAh/g and 350 mAh/g for HKUST-1⊃S and HKUST-1/S after 170 cycles at 0.1C [56].

Zheng et al. developed a Ni-based MOF named Ni_6(benzene-1,3,5-tribenzoate)$_4$(4,4'-bipyridyl) that is proposed to have sulfur immobilization capability. The bare surface area of this composite was calculated as 5243 m^2/g, which is enormous, with a blend of macropores (~2.8 nm) and micropores (~1.4 nm). 60 wt.% sulfur was loaded to these pores of Ni-MOF by a simple melt-diffusion strategy. It was stated that the PSs were trapped inside the pores physically, and Ni^{2+} centers interact with the PS base that adheres PSs to the

cathode surface. The specific capacities were determined at 0.1C with a 1.5 V-3.0 V voltage window of 689 mAh/g. Although high capacity retention was observed, the initial discharge capacity is lower than that of the carbon/sulfur composite. The addition of transition oxides and the alterations in the organic ligand chain was proposed [57].

Heteroatom doping into carbon materials has also been a widely followed strategy in the literature. The advantages of heteroatom doping are basically active site generation and an increase in electronic conductivities. Hence, heteroatom doping leads to increased cycling and rate performances [58]. Huang et al. used nitrogen and phosphorus-doped carbon having various pore sizes obtained from free-drying and carbonization of egg shells, which were used as the cathode hosts in Li-S batteries. The initial discharge capacity of this material was 1635 mAh/g for 0.57 mg/cm^2 loaded cathodes at 0.1C, which ended up 762 mAh/g after 100 cycles at 0.1 A/g current rate [59]. Wu et al. also used sulfur encapsulated with N, O-codoped carbon with trimodal pores as the main cathode host. Afterward, this composite was mixed with acetylene black and polyvinylidene fluoride (PVDF) at a 7:2:1 wt.% ratio, respectively. This cathode exhibited good cycling stability even at 1C, with only 0.057 % capacity decay per cycle for 800 cycles.

Yuan et al. investigated the performance of self-standing CNT paper in sulfur cathodes. Using a facile bottom-up method, cathodes with sulfur loadings higher than 6.3 mg/cm^2 were fabricated. Both short- and long-range CNTs were employed to provide a framework for sulfur deposition, long-range conductive network, and intercrossed binder, respectively. Cycling results of 150 cycles showed 995 mAh/g initial capacity, implying 60% sulfur utilization with 0.20 % capacity decay per cycle with only one layer. The capacity and sulfur loading were tripled by stacking three layers in the cathodes [60].

There are many works in the literature investigating various types of encapsulation materials. Many studies utilized graphene oxides together with materials such as metal-organic frameworks, anthraquinone, amylopectin, and polypyrrole [61–64]. On the other hand, there are other materials, such as porous carbons and CNT, that were investigated as encapsulation materials**.** These materials were used mainly to suppress the PS shuttle mechanism, increase the electronic conductivity, load a high amount of active material, and

provide a stable network that can stand large volume changes during discharge and charge [43].

2.1.3. Effect of E/S Ratio

According to the techno-economic model proposed by Eroglu et al., the system-level specific energy and energy density of a Li-S battery are highly dependent on the amount of electrolyte used in these batteries. It was stated that although excess electrolyte is preferred to increase sulfur utilization and prevent electrolyte depletion and PSM, having too much electrolyte devastates the specific energy. The pack-level specific energies were found as 100 Wh/kg and 400 Wh/kg for batteries having 10 mL/g and 1 mL/g E/S ratios, respectively [65]. Urbonaite and Novak found the optimum E/S ratio as 22 mL/g among E/S=13 mL/g and E/S=43 mL/g for the standard cathodes prepared by mixing 60:30:10 wt.% sulfur, carbon black and PEO, respectively. In these cells, E/S=43 mL/g showed the poorest cycling performance. This work suggests that electrolyte parameters, such as the amount and the additive and salt types, are more effective on the cell performance rather than the electrode properties [21].

Chu et al. investigated the effect of having a high donor-number salt anion on the performance of Li-S batteries having lean electrolyte conditions. It was stated that having too much electrolyte decreases the energy density of the cells. On the other hand, decreasing electrolyte amount causes limited PS solubility, hence sluggish reaction kinetics, low sulfur utilization, and unconstraint Li_2S deposition and accumulation. These were supposed to be the main reasons for the increase in cell resistance and early cell failure in lean electrolyte conditions. According to the study, the PS solubility should be high in cells operating with a limited amount of electrolyte. The high solubility of PSs in the DOL:DME electrolyte having 0.4 M LiTFSI and 0.6 M $LiNO_3$, high NO^-_3 salt anion, enhanced the cell capacity for E/S=5 mL/g. It was found that the cells have capacities around 1200 mAh/g at 0.1C and prolonged that capacity even after 100 cycles [43].

Chung and Manthiram (2018) investigated the effect of the E/S ratio on the discharge capacity using graphene/cotton-carbon cathodes. The cells having 30 mg/cm^2 sulfur loading and 60 wt.% sulfur content at E/S ratios of 10, 8, 6, and 5 mL/g were investigated in this

study. The cells were cycled at both 0.1C and 0.2C. The electrochemical performance decreased at 0.2C due to low sulfur utilization at low E/S ratios. According to the study, the E/S ratio should be higher than 7 to prevent the adverse effects of lean electrolyte conditions. On the other hand, for cathodes having cotton-carbon only, the optimum E/S ratio was found to be 10 mL/g to have high sulfur utilization. Lower E/S ratios resulted in unstable cycling performances due to wetting problems of the high porosity cathodes. Hence, E/S ratios should be determined by considering the cathode parameters [66]. On the other hand, the cycle stability and sulfur utilization of the cells having different amounts of electrolyte, in other words, the E/S ratio, at a constant sulfur loading, were studied by Brückner et al. Vertically-aligned carbon nanotubes were used as the cathode in this study. It was found that high E/S ratios result in high capacities and cycle lives. On the other hand, the E/S ratio should be restricted to 4 mL/g to provide high energy density batteries [67].

2.1.4. Effect of Ionic Liquid Type

There are many types of ionic liquids that were investigated as electrolytes in Li-S batteries in the literature, some of them are listed in Table 2.1. Yuan et al. performed one of the early studies utilizing room-temperature ionic liquids (RTILs) as electrolytes in Li-S batteries. Cyclic voltammetry (CV) results showed that the working potential of N-methyl-N-butyl-piperidinium bis(trifluoromethanesulfonyl)iminde ([PP14]-[TFSI]) was around 5.2 V to -0.15 V (vs. Li/Li^+). Hence, it is stable for both lithium anodes and sulfur cathodes. Due to the low PS solubility in the IL, the PS shuttle mechanism was inhibited. The initial discharge capacity was almost doubled from 600 mAh/g to 1055 mAh/g when RTIL was used rather than using ethylene carbonate:dimethyl carbonate (EC:DMC) electrolyte with 1.0 M $LiPF_6$. However, the cycling performance was limited [68].

Zhang et al. used solvate ionic liquids in cathodes having porous carbon:sulfur composites having polyvinyl alcohol (PVA) as a binder with 0.5 mg/cm^2 sulfur loading and 60 wt.% sulfur content. Both the effect of ionic liquids and their interface with the porous cathode on cell performance have been investigated in this study. It was found that large pore size and volume of the conductive matrix are greatly important for the performance of batteries using IL electrolytes. It was found that the best composite for IL solvents does not work well for the conventional DOL:DME electrolytes. In addition, lithium(tetraglyme)-

TFSI ([Li(G4)]-[TFSI]) electrolyte viscosity decreased with the addition of ether, which increases ionic mobility while suppressing the PS shuttle mechanism. Thus, the capacity retention of the cells improved from 61.6% to 73.5% [69].

Table 2.1. Literature summary utilizing ionic liquids as electrolytes in Li-S batteries.

Ref.	Encapsulation	S wt.%	S Loading (mg/cm^2)	IL Solvent	C	Peak Capacity (mAh/g)
[70]	NO	57	0.3	[Li(G3)1]-[TFSI]	0.06	1061
[71]	Carbon Black	34	NP	(P13)(TFSI)	0.20	609
				(P13)(TFSI)	0.10	1386
				PMIM(TFSI)	0.10	1178
[72]	Ketjen Black	60	NP	[Li(G3)4][TFS]	0.08	844
		57		[Li(G3)1][TFSI]	0.06	1056
		60		[Li(G4)1][TFSI]	0.08	897
		60		[Li(G4)1][TFSI]/HFE	0.08	1000
[73]	Activated Carbon	35	NP	C4mpyr-TFSI	0.10	688
				C4mpyr-FAP	0.10	439
				C4mpyr-Otf	0.10	515
[74]	NO	40	NP	P1A3TFSI	0.10	1457
[75]	Ketjen Black	60	0.6	[P13][TFSI]	0.08	808
				[P13][BETI]	0.08	641
				[P14][OTf]	0.08	703
				[P13][FSA]	0.08	967
				[DEME]BF4	0.08	891
				[P14][TFSI]	0.08	642
				[P2225][TFSI]	0.08	589
				[PP13][TFSI]	0.08	349
				[C4dmim][TFSI]	0.08	724
				[DEME][TFSI]	0.08	800

NP:Not provided, P13:N-methyl-N-propylpyrrolidinium, PMIM:1-methyl-3-propyl imidazolium, G3:Triglyme, G4:Tetraglyme, HFE:1,1,2,2– tetrafluoroethyl 2,2,3,3–tetrafluoropropyl ether, C4mpyr:1-butyl-1-methylpyrrolidinium, FAP:tris(pentafluoroethyl)trifluorophosphate, P1A3: n-Methyl-n-Allylpyrrolidinium, Otf:trifluoromethanesulfonate , FSA:bis(fluorosulfonyl)amide, BF_4:tetrafluoroborate, P14:N-butyl-N-methylpyrrolidinium, P2225:triethylpentylphosphonium, PP13:N-methyl-N-propyl piperidinium, C4dmim:1-butyl-2,3-dimethylimidazolium, DEME:N,N-diethyl-N-methyl-N-(2- methoxyethyl)ammonium

Lu et al. used the IL 1-ethyl-3-methylimidazolium bis(trifluoromethylsulfonyl)imide ([EMIM]-[TFSI]) as a co-solvent in Li-S batteries. The effect of the addition of 25, 50, and 75 vol.% of fluorinated ether to the IL was investigated. The cathodes were prepared using sulfur and mesoporous carbon (CMK-3) composite with carbon black conductive additive and PVDF binder. The sulfur content and loading of the cathodes were 55 wt.% and 1.6 mg/cm^2, respectively. It was found that there is a synergy between [EMIM]-[TFSI] and

fluorinated ether where the low solubility of the PSs in the electrolyte is supported by the prevention of PS dissolution into the electrolyte. Hence, it was found that the specific capacity of the cells with the IL with 50 vol.% fluorinated ether was 505 mAh/g after 50 cycles. It was suggested that although this result was promising, the vol.% should be further optimized [76].

Wu et al. prepared an electrolyte using ionic liquids containing two lithium salts for high-performance Li-S batteries. N-methoxyethyl-N-methylpyrrolidinium bis (trifluoromethanesulfonyl)imide ([$Pyr_{1,2O1}$]-[TFSI]) and tri(ethylene glycol)dimethyl ether (Tri-EGDME) in a mass ratio of 7:3 was determined to be the best candidate to prevent fast capacity decay and low Coulombic efficiency. [$Pyr_{1,2O1}$]-[TFSI] was preferred due to its ability to prevent crystallization, and its high conductivity and Li_2S_m solubility. Additionally, Tri-EGDME was used as a co-solvent to improve the electrolyte properties further. Moreover, binary salts having lithium difluoro(oxalate)borate (LiODFB) and LiTFSI in a mole ratio of 6:4 further improves the electrolyte properties; they help the formation of a solid electrolyte interface (SEI) layer on the anode and protect both electrodes by preventing the PS shuttle mechanism [77].

2.1.5. Modeling Studies of Li-S Batteries

A one-dimensional (1-D) mathematical model was developed by Kumaresan et al. to determine the underlying reactions resulting in two characteristic discharge plateaus of Li-S cells. The model was performed for low C-rates, and it was observed that Li^+ concentration increases up until 14 hours without any Li^+ gradient during all stages of discharge. With the increase in the sulfide concentration, Li^+ concentration tends to decrease. On the other hand, at 57.7 hours of discharge, a S_4^{2-} concentration gradient was observed from the separator to the cathode, which is attributed to the slower mass transfer rate than the reduction reaction kinetics. In addition, it was proposed that the shape of the discharge curve is related to the concentration gradients of all the species present in the cathode during discharge. At first, solid sulfur present in the cathode starts to dissolve in the electrolyte until it reaches the solubility limit, and then it is reduced. During the first hour of discharge, sulfur reduces to S_8^{2-}, then to S_6^{2-} and S_4^{2-}, which corresponds to the end of the first discharge plateau. In the second plateau, the S_2^{2-} concentration increases, and Li_2S starts to precipitate on the

carbon surface. The voltage of the proposed reactions coincides with the voltage profile of the Li-S batteries [78].

Marinescu et al. proposed a zero-dimensional model that predicts the discharge and charge behavior of Li-S cells. Nernst equation was used to model two electrochemical reactions by including the Butler-Volmer kinetics. By taking the precipitation/dissolution of S_2^- into account, the characteristic charge and discharge plateaus of Li-S cells were obtained. It was found that the precipitation rate does not affect the discharge capacity, whereas dissolution reaction rate can significantly reduce the charge capacity [79]. Fronczek and Bessler also used a 1-D model to perform the elementary kinetic modeling and impedance simulation by taking 5 precipitation/dissolution and 6 electrochemical reactions, including the Li oxidation, into account. It was assumed that the reactions occur only at the electrolyte-solid interface, and there are no side or degradation reactions. The discharge voltage profile was attributed to the variation of the volume fractions of S_8 and Li_2S [16].

Zhang et al. investigated the effects of electrolyte resistance and precipitation kinetics on the voltage loss mechanisms. A lumped model was developed by including electrochemical and precipitation reactions, charge transfer kinetics, and morphology variations in the model. Electrolyte resistance was found to be at its maximum at the transition of the discharge plateaus, and higher electrolyte resistance was obtained at higher current densities. Finally, it was found that activation overpotentials are the second main reason for high cell resistance in Li-S cells [18]. Al-Mahmoud et al. modeled the PS concentration gradients in the cathode and the reaction of PSs with the anode to study the effect of electrolyte volume on the self-discharge behavior of Li-S cells [80]. Furthermore, Mikhaylik and Akridge and Hofmann et al. quantitatively analyzed the PS shuttle mechanism to link the self-discharge, charge-discharge efficiency, and specific capacity of Li-S cells [15], [23].

Erisen et al. modeled the effect of carbon-to-sulfur (C/S) and E/S ratios on the electrochemical performance of Li-S batteries. This one-dimensional model assumed a single electrochemical reaction, hence a single kinetic parameter, cathode exchange current density for each of the two discharge plateaus. Using this single kinetic parameter, cell voltage at 60 % depth of discharge (DoD) was estimated. It was found that the cell voltage

increases significantly with increasing C/S or E/S ratios. It was also suggested that the E/S ratio has a major impact on the kinetic parameter [81]. In another study from the same group, an electrochemical model taking two electrochemical and two dissolution/precipitation reactions into account was proposed [82]. The voltage profile was successfully predicted, including the two discharge plateaus and the voltage dip at the end of the first discharge plateau. Similar to the previous work, cell voltages significantly improved up to a specific value of E/S and C/S ratios, after which the increase was less pronounced [81,82]. Abdulkadiroglu et al. improved this model further by offering a novel definition for the cathode electrochemically active area based on carbon weight fraction and a reference porosity [83].

Although there are various studies on the electrochemical modeling of Li-S batteries, modeling efforts focusing on the prediction of system-level performance metrics are more limited. One of the most important research on material-to-system analysis was performed by Eroglu et al. In this work, the system-level energy density and specific energy, together with the battery price, were determined as a function of critical cathode design and cell parameters. The BatPaC model was taken as the basis to build up the tecno-economic model. A 1-D electrochemical model was developed using the Butler-Volmer kinetics for the anode and the Newman and Tobias model for the porous cathode [84]. Based on the cell design, the sizing of the battery packs was done. The E/S ratio, C/S ratio, excess Li amount, reaction kinetics, and sulfur loading were determined to be the most important factors affecting the system-level performance and price of Li-S batteries. According to the results, excess amounts of Li, electrolyte, and carbon significantly lower the pack-level specific energy and energy density. Moreover, it was found that the electrode loadings should be higher than 8 mAh/cm^2 to have both high energy density and low-cost batteries [65]. This model was further improved in recent years by feeding it with experimental results to investigate the impact of the E/S ratio [85], C/S ratio [86], and S loading and carbon properties [87].

Emerce and Eroglu performed a modeling study to determine the effect of E/S ratio on cell- and system-level performances. The cell voltage at 60% DoD was predicted using a 1-D electrochemical model. Previous works have stated that the E/S ratio has a significant influence on the cathode specific capacity. Hence, to include this effect in the model, the experimental studies reported in the literature were used to obtain a linear empirical equation

that takes the PS solubility limit into account. Using this model, E/S ratios were investigated in the range of 0-30 mL/g at C/S=0.5 and 0.2C. System-level performance results showed that the specific energy and energy density of the cells increase up to E/S=10 mL/g, whereas any further increase in the E/S ratio decreases the system-level performance [88].

Xue et al. emphasized the importance of increasing the volumetric and gravimetric energy densities of Li-S cells to be commercialized in practical applications and electric vehicles. Hence, a model that can predict both volumetric and gravimetric energy densities was proposed, and the effects of various cell variables on them were investigated. The cell stack was designed as a sandwich-structured model where one cell consists of double-sided Al and Cu current collectors, a Li anode, a sulfur cathode, and a separator. It was assumed that the Li metal is non-porous, whereas the porous cathodes contain carbon, sulfur, and 5 wt.% binder. In addition, 70 wt.% sulfur, 10 mg/cm^2 sulfur loading, 30 % cathode porosity, and 50 % excess Li amount were assumed for an ideal Li-S configuration. The exact required amount of electrolyte to fill the pores of the cathodes was used in the ideal cell. According to the model, in the ideal case, Li-S batteries exhibit 720 Wh/kg, whereas LIBs with nickel-manganese-cobalt (NMC) metal provide 421 Wh/kg. On the other hand, the ideal volumetric energy densities were calculated as 1017 and 1300 Wh/L for the Li-S and LIBs, respectively. High void fraction and inactive carbon amounts in the cathode, and excess Li metal in the anode were the main reasons for having lower volumetric energy densities. It was proposed that, in addition to lowering these variables, increasing the sulfur content, loading, and utilization will be required to have larger volumetric energy densities [32].

McCloskey carried out a modeling study focusing on the gravimetric and volumetric energy densities of Li-S cells having protected Li anodes. The Coulombic efficiency of cells can be increased, and the Li dendrite formation can be eliminated by using mechanically stable and Li ion conductive solid state membranes. The required separator thickness, minimum required E/S ratio, and cost were calculated for Li-S batteries. It was assumed in the model that there are not any kinetic or transport limitations. The specific energy was simply calculated by multiplying the active material loading, utilization, and average cell voltage divided by the volume or mass of all the cell components. It was found that the minimum E/S ratio, ideally much less than 11, that can prevent the PS shuttle mechanism should be used in Li-S batteries to have higher specific energies than LIBs. Finally, the

maximum thickness and cost of a protective separator were found to be 100 μm and \$10/m^2, respectively, for the Li metal anodes to be competitive with graphitic anodes [89].

Cleaver et al. showed that only 9% of the Li-S literature has focused on cell mechanisms and modeling [90]. As mentioned above, most of the modeling work in the literature is mainly about understanding the reaction and PS shuttle mechanisms, kinetic determination, effects of resistances on the cell voltages, and capacity fading determination [15–18]. This shows that the modeling studies compared to the experimental work are still limited. In the current literature, modeling studies investigating the cell- and system-level performances using material-to-system modeling of Li-S batteries are scarce.

2.2. Li-O_2 Batteries

2.2.1. Effect of Oxygen Solubility

Kwak et al. worked on the development of new electrolytes for Li-O_2 batteries as a localized high-concentration electrolyte (LHCE) was used. The standard electrolyte consisted of 1 M lithium trifluoromethanesulfonate (LiTf) in tetraethylene glycol dimethyl ether abbreviated as G4, while the proposed electrolyte has 0.84 M LiTf with 1,1,2,2-tetrafluoroethyl ether (OTE) additive salt. The high boiling point and F/H=3 ratio are the reason for selecting the OTE salt. First, the importance of low viscosity and stability were emphasized in 1 mAh/cm^2 capacity limited tests with 0.2 mA/cm^2 areal density as LHCE electrolyte preserved the capacity for 50 cycles without any loss in voltages. In addition, the effect of oxygen solubility was also emphasized as LHCE's oxygen solubility was doubled with the addition of OTE. In deep discharge experiments with a cut-off voltage range of 2.4-5.0 V, only LHCE electrolytes retained the capacity for 25 cycles, whereas, without OTE additive, the other cells failed even after 2 cycles [91].

In the comprehensive work done by Gittleson, the properties of several electrolytes were investigated. Both experimental and molecular modeling studies were performed together, and it was found that oxygen transport is a critical parameter for high-performance Li-air batteries, and the electrolyte solvent determines oxygen transport. On the other hand, oxygen solubility is also critical for battery performance. Oxygen solubility depends on the

presence, types, and amounts of ionic species. The performance tests were performed in a full cell where carbon gas diffusion layers were used in the cathodes. The highest oxygen diffusivity and solubility were obtained for dimethyl sulfoxide (DMSO) electrolytes, which also performed better at high current rates for 1 atm dry air [92].

Xu et al. studied nonaqueous electrolyte properties for lithium/air batteries. Specifically, electrolyte polarity, oxygen solubility, viscosity, and ionic conductivity were studied in this work. It was stated that triphase regions should be formed where dissolved oxygen as active material, electrolyte as Li^+ ion source, and the positive electrode matrix as electron matrix meet. There are two routes for oxygen transport through the pores of the cathode matrix: through electrolytes and through open pores of the matrix, which is several orders of magnitudes larger than the former. Hence, the solvent polarity that is linked to electrolyte wetting is proposed to have higher importance than oxygen solubility, contrary to previous works [93].

Haas et al. discussed the effect of atmospheric gas solubilities in the electrolytes of lithium-air batteries. The fact that dissolved CO_2, N_2, and O_2 strongly affect the discharge mechanism and the stability of the cells. The gas solubilities were measured by gas uptake experiments, whereas the diffusion coefficients were determined by molecular modeling simulations. The commonly used ether electrolytes, namely di-, tri-, and tetraglymes, together with DMSO solvents, were used, and their viscosity and surface tension properties were considered. In addition, the effect of salt presence on the solubilities was also discussed. The experiments showed that the electrolytes have the highest solubility for CO_2 and the lowest solubility for N_2 gas, although the electrolytes have slightly higher O_2 solubilities. In addition, direct linear trends were observed for O_2 and N_2 solubilities with surface tension [94].

Monroe investigated the effect of oxygen transport on the cell voltages of metal-air batteries. The ionic conductivity, electrolyte, and oxygen diffusivity relations were obtained using Newman's concentrated-solution theory and Onsager-Stefan-Maxwell transport equations. Two new properties were defined in this work: the migration coefficient, which is the relation between ionic and oxygen fluxes, and the cross-diffusion, which shows the

relation between salt gradients and oxygen flux. It was stated in this work that the oxygen gradients in metal-air cells have an influence on the nominal voltage [95].

Sergeev et al. studied the effect of both cathode and electrolyte properties on the lithium-air battery properties using a numerical computational method. Oxygen diffusivity, discharge product precipitation, and pore filling of the cathodes were taken into consideration in the model. The positive electrodes were modeled as two neighboring phases: the electronically conductive porous matrix and electrolyte for ion and oxygen sources. The pores were assumed to be fully flooded by the electrolyte, and oxygen solubilities were assumed to be constant. The side reactions and surface passivation by deposition of insulating discharge product were discarded. Three electrolyte solvents, namely acetonitrile, DMSO, and DME, and the effect of electrode material densities were investigated. Fast oxygen diffusivity, stability of the electrolytes, and porous cathodes having short oxygen diffusion paths were identified as critical to having high-performance metal-air batteries [96].

2.2.2. Effect of Positive Electrode Materials and Design

The positive electrodes of metal-air batteries suffer from sluggish kinetics, resulting in ORR/OER overpotentials and mass transfer limitations. Hence, cathode materials that have intrinsic activities and pore structures are essential to increase round-trip efficiencies, Coulombic efficiencies, and cycle lives of metal-air batteries. According to the literature, since aqueous and non-aqueous batteries have different reaction mechanisms, the catalysts of the air electrodes should be designed according to the electrolyte choice. In non-aqueous electrolytes, redox reactions involve two electrons where Li_2O_2 is formed as the discharge product. Carbon materials were excessively used in the literature earlier, but new polar materials having precious metals or transition metal-oxides are more popular in recent years due to better OER/ORR kinetics [97]. Gao et al. developed the Co_3O_4 electrocatalysts on the silver support as a yolk-shell structure using a synchronous reduction technique. Active sites were introduced in the interface of the Ag-Co_3O_4 due to the tuning in electronic structure. In addition, the flower-like Ag structure has high electrical conductivity and a larger surface area. This cathode showed excellent specific capacity, which is 12,000 mAh/g at 200 mA/g current rate, dropping to 4700 mAh/g at 800 mA/g currents based on the cathode mass [98].

Li and Manthiram investigated the single, decoupled, and mixed air electrode configurations on the performances of Li-air batteries. In the decoupled configuration, $NiCo_2O_4$ nanoflakes on nickel foam and Pt/C composite on carbon-fiber paper were used separately as the OER and ORR catalyst electrodes, which are switched during charge and discharge, respectively. In the mixed structure, although two different layers were used, there is not a switch and the current collectors of the two layers are connected. On the other hand, the classical way single-layer structure, both $NiCo_2O_4$ and Pt/C, were grown onto a single carbon-fiber layer. The decoupled electrodes showed better performances, and they had high stability. Switching between the electrodes prevented the high voltages of the ORR layer, hence resulted in better stabilities [99].

Peng et al. studied the ratio of Co_3O_4/Graphene as air electrodes in an aqueous/aprotic hybrid electrolyte. The composites with 33.7 wt.%, 48.2 wt.%, and 62.5 wt.% of Co_3O_4/Graphene were synthesized by a facile hydrothermal method. Afterwards, the catalyst inks were prepared by mixing the composites and PVDF binder in the N-methyl-2-pyrolidone (NMP) solution, and dropped into carbon clothes. The catalyst loading was set to around 1 mg/cm^2. The moderate Co_3O_4 loading was found to be more effective in terms of homogenous distribution over graphene and better balance on the catalytic versus electronic conductivity abilities [100]. Azuma et al. utilized lithium bromide as a redox mediator, which is defined as molecules having redox potentials pretty close to 2.96 V, which is the OCV of lithium-air batteries. The role of a redox mediator is to enable the oxidation of the discharge product of Li_2O_2 at lower charging voltages. In this study, the effect of lithium bromide coating on carbon nanotube electrodes was investigated as the air electrodes. These electrodes increased the capacity to 4 mAh/cm^2, which is almost 2-fold higher than LIBs and a 3-fold higher cycle life [101].

2.3. Machine Learning for Beyond Li-ion Batteries

This section is part of a review article published by authors A. Kilic, B. Oral, D. Eroglu, R. Yildirim. The reviewing part was done by A. Kilic and B. Oral together, whereas the text-mining section of the article was performed by A. Kilic [9].

2.3.1. Machine Learning in LIB Research

The rechargeable energy storage materials and systems have been investigated more extensively in recent years with the increasing use of portable devices and growing demand to utilize renewable electricity in these devices and transportation. As expected, the application of ML, which is another increasingly popularized field, in energy storage systems like LIB [102], flow batteries [103–105], supercapacitors [106], and other rechargeable batteries such as nickel–metal hydride batteries [107] has been also increased in the last few years. In this thesis, we extensively used ML techniques for both Li-S and Li-O_2 batteries; hence the literature survey on the ML application of rechargeable batteries was provided in this section.

2.3.1.1. State of Charge and Health Prediction for Li-ion Batteries. Most of the ML works in literature are related to LIBs, as the already commercialized and extensively used system, and a significant part of these works are on the real-time data modeling and state of charge and health prediction to develop better-functioning battery systems in complicated devices [108–111]; numerous papers, including reviews, on the use of ML to correlate various features (like voltage, current, temperature, capacity) with state of health (SOH) indicators (i.e. capacity decrease, internal resistance increase) have been published in recent years [108], [112]. Various methods such as feedforward artificial neural networks (ANN), recurrent ANN algorithms, classification and regression algorithms, and probabilistic algorithms were used for this purpose [113]. Considering that a large number of publications have covered SOH studies, and we intended to focus on beyond LIBs more, we will not discuss this subject further; instead, we discuss the material and manufacturing related works, which are also relevant for beyond LIBs, in more detail below and move to the new battery technologies.

2.3.1.2. Machine Learning in Li-ion Battery Materials and Manufacturing. The remaining ML works on LIBs are mostly related to the properties or performance of electrode and electrolyte materials; as is true for the other fields, ML is very helpful to establish structure-property-performance relations of materials and to discover new materials with specific properties. Both experimental and computational (mostly generated by density functional theory (DFT)) data were used in these works; while some of the data were generated by the

researchers themselves, the use of data extracted from various material databases has also become more popular in recent years as these databases provide more accurate data for increasing number of materials with an easier access and retrieval of data. For example, Maphanga et al. used deep learning algorithms to estimate the voltage of 4369 DFT-computed structures acquired from the Material Project [114]; they used linear regression (LR), support vector machine (SVM), deep neural network (DNN), RF, and k-Nearest neighbour (kNN) algorithms with 15 features such as crystal lattice type, space group, volume, etc. Wang et al., on the other hand, showed that, for doped spinel LIB cathodes, the discharge performance can be predicted, and the influential material properties can be identified by various ML algorithms (SVM, DNN, decision tree (DT), RF, gradient boosted tree (GBT), least absolute shrinkage and selection operator (LASSO), and ridge regression (RR)) [115].

There are also works that involve the characterization of electrodes, such as Li intercalation to graphite electrodes using ANN [116], the analysis of 3-D tomography images to investigate the microstructures [117] and deformations [118] of cathode materials, the classification of microstructures leading to thermal runaways [119], analysis of X-ray absorption near-edge structure spectra to determine electronic and atomic structures of the positive electrode [120] and analysis of 3-D image data from electron backscatter diffraction to determine the intra-particle grain morphologies [121]. Similarly, ML was used to study the properties of electrolytes [122–124] and to optimize the electrolyte composition [125].

ML has also been used in the manufacturing process of LIBs for analyzing manufacturing parameters and end-product quality [126–130]. Kolodziejczyk et al. used convolutional neural networks and the finite element method to determine the thermal properties of Li-ion battery packs by analyzing 2000 images [131]. Wu et al. developed ANN to predict the specific capacity and power using six controllable manufacturing variables [132]. The optimization of cathode slurries [133] and the determination of the mass load of electrodes by SVM [134] were also studied in the literature. Some representative works on ML applications for LIBs are summarized in Table 2.2; we grouped the publications in terms of cell elements (electrodes represent the works involving both electrodes, while the studies involving only the negative or the positive electrodes are presented as different classes).

Table 2.2. ML for LIBs.

Battery Component	Objective	Data Source & Number	ML Algorithms
Both Electrodes	Prediction of voltages of various battery materials [135]	MP (DFT), 4369	DNN, kNN, LR, RF, SVM
	Prediction of redox potentials of organic materials [136]	DFT, 108	ANN, GBR, KRR, LASSO
	Design of new molecular electrode materials with guessed redox potentials [137]	DFT, 114	ANN
	Prediction of local diffusion barrier [138]	DFT, 48	LR, LASSO
	Classification of specific MXene chemical formula and prediction of electrochemical properties [139]	DFT, 360	RF
Positive Electrode	Prediction of discharge capacities of lithium manganese oxide spinel systems [115]	Experimental, 100	DT, GBM, LASSO, RF, RR, SVM
	Prediction of electronic conductivities of spinel structures and classification based on conductivity [140]	Experimental, 304	XGBoost
	Designing the mesoscale porous structures of electrodes [141]	High-throughput physicochemical model, 2100	ANN with Bayesian optimization
	Prediction of cathode crystal system [142]	DFT,339	ANN, ERT, kNN, RF, SVM
	Prediction of voltages of various materials [143]	DFT, 12 962	Behler–Parrinello NN
	Design and discovery of new doped lithium nickel-cobalt-manganese (NCM) oxide cathodes [144]	Experimental, 168	GBM, kNN, KRR, RF, SVM
	Prediction of diffusion energy barrier of quantum cathode materials for fast charging electrodes [145]	DFT, 7385	KRR, MLP, SVM
	Prediction of Li-ion insertion voltages of organic electrode materials [146]	DFT, 1001	ANN
	Prediction of the initial capacity, capacity retention rate, and amount of residual Li for Ni-rich cathode materials [147]	Experimental, 330	DT, ERT, MLP, RF, RR, SVM
	Prediction of redox potentials of organic redox compounds [148]	Experimental, 6000	RF
Negative Electrode	Modeling of the energetics of lithium intercalation into graphite [116]	DFT, 9189	ANN
	Development of Li-intercalated metal-organic frameworks (iMOFs) [149]	XRD image, 2751	RF
	Identification of outlier structures and their use in anionic reactions via band-gap structure relations [150]	MaterialGo database, 4000	GBR
	Prediction of redox potentials of electrolyte additives [151]	DFT,149	GBR, KRR
Electrolyte	Prediction of electrolyte infiltration in porous NMC electrodes [122]	3D-Tomography image	MLP
	Prediction of redox potentials of electrolyte additives [123]	DFT, 149	GPR
	Prediction of coordination energy of electrolytes [124]	DFT, 103	LR, GPR
	Optimization of aqueous electrolyte mixtures [125]	Experimental, 251	Bayesian optimization
	Prediction of the refractive index and viscosity of ionic liquids [152]	Various studies, 5884	XGBoost

Table 2.2. ML for LIBs. (cont.)

Battery Component	Objective	Data Source & Number	ML Algorithms
Separators	Classification of separators to detect defects [153]	Surface image, 746	DT

KRR: Kernel ridge regression, ERT: Extreme regression tree, NN: Neural network, MLP: Multilayer perceptron, GPR: Gaussian process regressor

2.3.2. Machine Learning in Beyond LIBs

As we mentioned above, ML applications in LIB research typically involve the *state of charge and health prediction, material screening,* and *property or performance prediction*. Since the general structure (anode, cathode, electrode, etc.) of the beyond LIBs is the same as the LIBs, the ML applications are also similar (except for SOH predictions, for which the new technologies are not at that stage yet). From another perspective, we can say that ML studies for the beyond LIBs, as the experimental works in the field, practically aim to develop solutions to the shortcomings of these batteries such as searching alternatives for liquid electrolytes, solving problems like dendrite formation in Li metal anodes or the PSM in sulfur cathodes, or identifying the structural and electrochemical properties required for good intercalation or conversion kinetics.

2.3.2.1. Search for New Electrodes. Indeed, ML has been widely used for the search of compatible materials and predictions of their properties for univalent [154–157] and multivalent [158–160] metal-ion, metal-air [48], [161,162] and Li-S [163–165] batteries. For example, Joshi et al. developed a web accessible tool to predict the voltages of electrode materials for sodium-ion (Na-ion) and potassium-ion (K-ion) batteries using ML (DNN, SVM, and KRR algorithms) [166]; they used a dataset containing 3977 intercalation-based electrode materials from the Materials Project (MP) [114] and 80 features obtained by principle component analysis of 237 features (like active metal concentration, crystal lattice details, space group numbers, and elemental properties). In another example, we used a dataset with 1660 points constructed from the published works to analyze the factors affecting the discharge capacity and cycle life of Li-S batteries [43]. Electrolytes (both liquids and solids) have also been studied extensively to improve the safety and performance of LIBs [167,168] as well as to identify the best electrolyte alternatives for the new battery systems [169]. Jeschke et al. classified Li−S battery electrolytes as either salt-in-solvent,

solvent-in-salt, or solvate IL electrolytes using various classifiers such as k-nearest neighbors and support vector machines. Additionally, a regression model was trained to predict the solubility of PSs in these electrolytes. They combined DFT and statistical mechanics (COSMO-RS) to achieve a quantitative structure-property relationship model for 55 electrolytes containing binary and ternary mixtures of solvents and different Li salts [170]. The SEI is another topic of interest in the computational approach in next-generation batteries. For instance, Ishikawa et al. studied the ion transfer at the electrolyte/electrode interface by creating a predictive model for the coordination energy of five alkali metal ions (Li, Na, K, Rb, and Cs) to the electrolyte solvent using LR, LASSO, and MLR regression methods; they used the properties of the cation and the solvent for this purpose.

Table 2.3. ML for beyond LIBs.

Battery	**Subject**	**Data Source & Number**	**ML Algorithms**
Li-S	Prediction of the discharge capacity and cycle life [43]	Experimental, 1660	ARM
	Prediction of the binding energy of sulfur hosts [163]	DFT, 3295	TL
	Screening of supported single-atom catalysts via investigation of the pattern of PSs adsorption [164]	DFT, 812	CGCNN
	Screening of an AB_2-type sulfur host material [165]	DFT, 1320	XGBoost
	Classification of different electrolytes and prediction of PS solubility [170]	COSMO-RS, 40	kNN, MLR, NB, RF, SVM
	Assessment of the critical materials and cell design factors for Li-S batteries using IL electrolytes [171]	Experimental ,207	ARM
Li-air	Prediction of performance based on capacity [48]		ARM, DT
	Prediction of the solvent effect [162]		ANN
	Analysis of pore size distribution [172]		RF
	Prediction of electrophilicity and nucleophilicity [173]		ANN, LASSO
Na-ion	Prediction of Na-ion diffusion energy barrier [155]		DT, GPR, KRR, SVM
	Screening of anodes for sodium-ion batteries [174]		DT, kNN, RF, SVM
	Real-time prediction of battery life and failure [175]		CNN, MLP, SVM
	Prediction of discharge capacity and cycle life[176]		DT, RF
K-ion	Prediction of crystal stability [157]		RF
	Prediction of capacity [177]		ERT, KRR, SVM
Zn-ion	Prediction of cathodes with high capacity and high voltage [160]	MP and Aflow (DFT), 13 000	CGCNN
Mg-ion	Prediction of average voltage, gravimetric capacity, volumetric capacity, specific energy, and energy density [178]		RF
Other uni- and multi-valent	Prediction of voltages [154]		DNN
	Prediction of electrical property [159]		XGBoost

Table 2.3. ML for beyond LIBs. (cont.)

Battery	Subject	Data Source & Number	ML Algorithms
Other uni- and multi-valent metal-ion	Prediction of average voltages and volume change upon charging and discharging of electrode materials [166]		DNN, KRR, SVR
	Calculations of the coordination energy [179]		MLR, LASSO
Solid state	Conductivity prediction of polymers [180]		GBT
	Na and Li-based SICON compounds [181]		LogR
	Conductivity prediction of ternary crystals [182]		GPR
	Conductivity prediction of Li-ion conducting ceramics [183]		ANN, RF
	Classification of the ionic conductivity of doped LLZO [184]		GBT, RF, SVM
	Prediction of the Li-ion conductivity and phonon-free energy [185]		GPR
	Prediction of the mechanical properties of Na-solid state electrolytes [186]		GBT
	Design of solid–electrolyte-interphase [187]		ERT
	Calculation of bond valence [188]		RF
	Prediction of the mechanical properties of Li-ion conducting solid-state electrolytes [189]		GBT
	Discovery of novel Li-ion conducting solid state electrolyte [190]		GBT, RF
	Investigation of manufacturing conditions on the quality of solid-state electrolytes [191]		k-means, SVM
	Prediction of ionic conductivity for solid-state electrolytes [192]		GBT, kNN, LogR, RF, SVM
	Prediction of activation energy [193]		Partial least squares regression
	Screening of inorganic solid electrolytes for suppression of dendrite formation [194]		CGCNN
	Clustering of Raman map for polymer composite electrolytes [195]		k-means
	Investigation of pore formation [196]		CNN

CGCNN: Crystal graph convolutional neural network, TL:transfer learning, NB: Naïve Bayes, CNN: convolutional neural network, LogR: Logistic regression

2.3.2.2. Search for Solid-State Electrolytes. Solid-state electrolytes received special attention in battery research, including ML applications in all Li batteries [197]. For example, Ahmad et al. screened inorganic solids (both isotropic and anisotropic interfaces) based on their ability to suppress the dendrite formation when in contact with the Li metal anode. They predicted 20 mechanically anisotropic interfaces between the Li metal and four solid electrolytes; elastic constants of the cubic materials and the shear and bulk moduli of the crystalline solid electrolyte materials were projected by gradient boosting, KRR and CGCNN, respectively [194]. In another work, Jo et al. predicted the mechanical properties

of Na-conducting solid-state electrolytes for 12361 materials from the Material Project database using GBT [198]. The ML works on the beyond LIBs are summarized in Table 2.3. The table is organized according to the battery type; this seems to be a more relevant classification to see the trends in new battery technologies. We list the representative works related to the solid-state batteries as a separate group in the table, considering that those works represent a new direction in electrolyte search that may apply to all battery types.

3. MATERIALS AND METHODS

In this chapter, all the details about the experimental techniques, system-level performance model, and ML techniques are given in sections 3.1, 3.2, and 3.3, respectively.

3.1. Experimental Work

The experiments were carried out for only Li-S batteries, and their electrochemical performances were tested. CR2032 coin cell fabrications were carried out for all of the cases. The summary of the experimental procedure is presented in Figure 3.1.

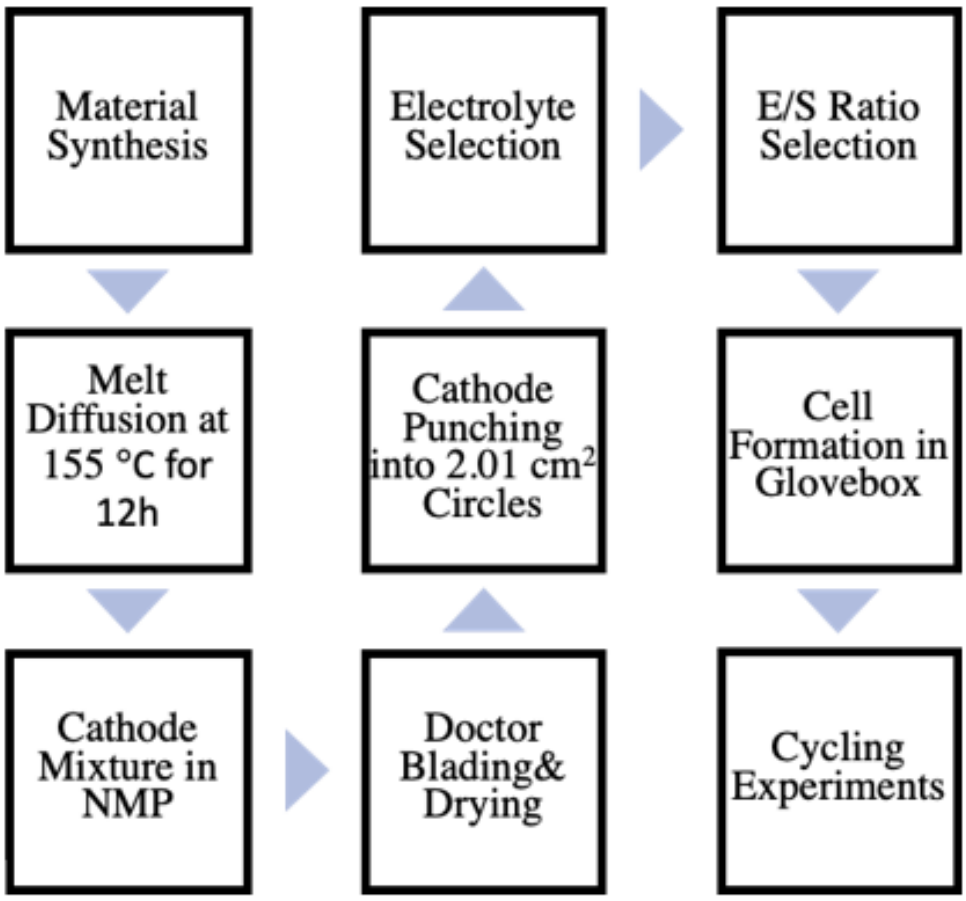

Figure 3.1. The summary of the experimental procedure.

3.1.1. Chemicals and Materials

All the chemicals used in the experiments are listed in Table 3.1. The material purposes are also given in the table.

Table 3.1. The materials used in the construction of Li-S cells.

Material	Function	Source
Carbon Black (Super C65)	Cathode conductive material	MTI
Sulfur	Cathode active material	Sigma Aldrich
PVDF	Cathode binder	MTI
Ketjen Black (EC-600J)	Cathode conductive material	Nanografi
NMP	Cathode solvent	MTI
Aluminum foil (15 µm)	Cathode current collector	MTI
Copper foil (25 µm)	Anode current collector	MTI
Lithium metal foil (170 µm)	Anode	MTI
DOL	Electrolyte solvent	Sigma Aldrich
DME	Electrolyte solvent	Sigma Aldrich
$LiNO_3$	Electrolyte salt	Sigma Aldrich
LiTFSI	Electrolyte salt	Sigma Aldrich
Polymer film (25 µm)	Separator	Celgard
1-butyl-3-methyl-imidazolium hexafluorophosphate ([BMIM]-[PF_6])	IL as electrolyte solvent	Iolitec (99.5 % purity)
1-butyl-3-methyl-imidazolium trifluoromethane-sulfonate ([BMIM]-[CF_3SO_3])	IL as electrolyte solvent	Iolitec (99.5 % purity)
1-butyl-3-methyl-imidazolium methylsulfate ([BMIM]-[$MeSO_4$])	IL as electrolyte solvent	Iolitec (98 % purity)
Tributylmethylammonium bis(trifluoromethane)sulfonimide ([TBMA]-[TFSI])	IL as electrolyte solvent	Iolitec (99 % purity)
[DEME]-[TFSI]	IL as electrolyte solvent	Iolitec (99 % purity)
[PP14]-[TFSI]	IL as electrolyte solvent	Iolitec (99 % purity)

3.1.2. Experimental Details for Selection of Ionic Liquid Electrolytes for High-Performing Lithium-Sulfur Batteries: An Experiment-Guided High-Throughput Machine Learning Analysis

3.1.2.1. Cathode Formation. The composite cathode was prepared using the melt-diffusion strategy. First, sulfur and carbon black (Timcal Super C65, MTI) were mixed with mortar in 70:30 mass ratios for a few minutes and stayed in a vacuum oven at 155 ◦C for 12 hours. After the heat treatment, some of the sulfur evaporated and the final sulfur amount of the

resulting composite was 65.3 wt.%, which is determined by thermal gravimetric analysis (TGA). The cathode powder was prepared by mixing 70 wt.% of this composite with 20 wt. % of additional carbon black (C65) and 10 wt.% PVDF and the slurry was obtained using NMP solvent. The NMP to solid ratio is generally 5 to 6 by mass to obtain honey-like viscosities after overnight mixing. Using the doctor-blade method, the slurries were pasted onto aluminum foil and dried overnight. Finally, the cathodes were punched into the cathodes with 2.01 cm^2 areas and approximately 2 mg/cm^2 sulfur loadings and around 80 μm thicknesses.

3.1.2.2. Coin Cell Fabrication. After the cathode formation, the rest of the steps were carried out inside MBraun Labstar Glovebox with oxygen and water levels below 0.5 ppm. To test the performances of the selected six ionic liquids, two-electrode CR2032 Li-S coin cells were prepared using pure lithium metal as the anode, a polymeric Celgard separator and the composite cathode. As the electrolyte, mixed electrolytes containing 25 vol.% IL and 75 vol.% organic solvent were used. All the electrolyte components were directly used without further treatments. First, the organic electrolyte was prepared by mixing equal volumes of DOL:DME (1:1 vol.%) solvents containing lithium salts as 1 M LiTFSI and 0.1 M $LiNO_3$.

Table 3.2. The experimental details of Section 4.1.3.

Encapsulation Material		Carbon Black (C65)
Encapsulation Condition		C65/S (30/70 wt.%) at 155 °C for 12 h in vacuum
Final Cathode Composite	Encapsulation	C65/S, 70 wt.%
	Conductive	C65, 20 wt.%
	Binder	PVDF, 10 wt.%
Final S wt. %		65.3 x 0.7 = 45.7 wt.%
Sulfur Loading		1 and 2 (mg/cm^2)
Electrolyte (IL:Organic= 25:75 vol%)	Organic	DOL:DME containing 1 M LiTFSI and 0.1 M $LiNO_3$
	IL	BMIM- PF_6
		BMIM-CF_3SO_3
		BMIM-$MeSO_4$
		PP14-TFSI
		DEME-TFSI
		TBMA-TFSI
E/S Ratio		13 mL/g
Current Rate		0.1C and 0.5C

The ILs were obtained from Iolitec company used without further treatment. The selected ionic liquids were: BMIM cation coupled with PF_6, CF_3SO_3 and $MeSO_4$ anions, and TFSI anion paired with PP14, DEME and TBMA cations. Hence, 6 ILs were tested experimentally.13 mL/g E/S ratio was used in all the cells. The cells rested at OCV for 16 h to stabilize the cells and to properly wet the cathodes. For cycling experiments, the current was decided according to the selected current rate, in other words, C-rate, which was calculated using the theoretical capacity of the sulfur. 0.1C is the typically used C-rate, which is the current for 10 hours of discharge theoretically. So, for 0.1C rate for 1 g sulfur-loaded cathode, the corresponding current is 167.5 mA. Accordingly, the cells were cycled at a constant current for at least 100 cycles to observe cycling performances. The experimental variables were summarized in Table 3.2.

3.1.3. Experimental Details for MOF/Graphene Nanoplatelet Composite Increases Rate Performance of Lithium-Sulfur Batteries

3.1.3.1. Synthesis of UiO-66/GNP and UiO-66/GNP-S Composites. The metal-organic framework (UiO-66) presented in Section 4.1.4. was developed by Prof. Şahika Sena Bayazit. A facile hydrothermal method was used for the synthesis of UiO-66 and UiO-66-based materials. An equimolar amount of zirconium chloride ($ZrCl_4$, Sigma Aldrich, purity ≥99.5 %) and terephthalic acid were mixed to synthesize UiO-66. Afterward, graphene nanoplatelets (GNP, XG Science, purity ≥99.5 %) were added to the solution. GNP to $ZrCl_4$ amount was set to 9:1, 7:3, and 5:5, and the samples were defined as UG-1, UG-3, and UG-5, respectively. HCl (Merck Co., 37 %) was added dropwise into the solution, and then the solution was put into a hydrothermal autoclave. The hydrothermal reaction was placed at 120 °C for 16 h. The as-prepared composites were cooled down and washed with dimethylformamide (Sigma Aldrich Co. ≥99.5 %) and ethanol. The final drying was performed in a vacuum at 60 °C.

The encapsulation of sulfur with these composites was done using the standard melt-diffusion method, where the composites (UG-1, UG-3, and UG-5) were mixed with sulfur at a ratio of 30:70 wt.% using a mortar and pestle for five minutes. Finally, the powder was placed in a vacuum oven at 155 ºC for 12 h. UiO-66/GNP/S composites prepared by

incorporating sulfur into UG-1, UG-3, and UG-5 were named UGS-1, UGS-3, and UGS-5, respectively. The sulfur contents in UGS-1, UGS-3, and UGS-5 composites are 57.33, 61.15, and 68.79 wt.%, respectively, determined by elemental analysis (given in Appendix D, in Table D.1). To compare the results, GNP-S and UiO66-S composites were prepared by the same strategy, and their sulfur contents are 66.3 wt.% for the former and 49.4 wt.% for the latter, measured by TGA (Figure D.1).

3.1.3.2. Material Characterization. TGA was performed from room temperature to 500 °C with a 5 °C heat ramp under a nitrogen atmosphere. In addition, elemental analysis was used to determine the sulfur content in UG composites using Thermo Scientific Flash 2000. Scanning electron microscopy (SEM) images were taken using Quanta FEG 250, FEI Company, Netherlands, to observe the morphology changes. Fourier transform infrared spectroscopy (FTIR) and X-ray diffraction spectroscopy (XRD) were also applied to UiO-66/GNP surfaces. The crystal patterns of the composites were determined by XRD with Rigaku D/Max-2200 diffractometer (Cu Kα radiation with $\lambda = 0.15418$ nm). FTIR scans were applied by the KBr method with Bruker Alpha spectrometer. Finally, the surface areas and the pore sizes of the composites were determined by Brunauer-Emmett-Teller (BET) analysis using Micromeritics 3Flex Surface Characterization Analyzer.

3.1.3.3. Cell Preparation and Electrochemical Characterization. The sulfur cathodes were prepared using the synthesized UGS composites, carbon black (Timcal Super C65, MTI), and PVDF binder with 70:20:10 weight % ratios mixed in the NMP solvent. The electrode thicknesses were adjusted using doctor blades, and the cathode slurry was pasted on aluminum foil (15 µm thick, MTI) to get sulfur loadings of 1 mg/cm^2 and 2 mg/cm^2 with a cathode area of 2.01 cm^2. The dried cathode, the polymeric separator (25 µm thick, 3.1 cm^2 area, MTI), and the pure lithium metal anode (170 µm thick, 2.01 cm^2 area, MTI) were used in the preparation of two-electrode CR2032 coin cells. A mixture of DOL:DME (1:1 vol.%) containing 1 M LiTFSI and 0.1 M $LiNO_3$ was used as the organic electrolyte in all cells. The E/S ratio was set to 13 mL/g in all experiments. Afterwards, the electrochemical measurements were performed using these coin cells after resting for 16h at open cell voltage to stabilize cell voltage and to let the electrolyte perfectly wet the cathodes. The galvanostatic cycling and rate capability experiments were carried out in battery cyclers (Neware) at 0.1C

and 0.5C for 1.7-3.0 V voltage window, which are adjusted considering 1675 mAh/g as the theoretical capacity of sulfur. In addition, the rate capability tests were also employed to see how the cells perform under high currents and to determine if they can recover their capacities even after high current rates. Hence, the currents were set to 0.1C, 0.2C, 0.5C, 1C, 0.2C, 0.5C, and 0.1C in sequence for five cycles. The experimental details were given in Table 3.3.

Table 3.3. The experimental details of Section 4.1.4.

Encapsulation Material		UG-1	UG-2	UG-3
Encapsulation Condition		UG/S (30/70 wt.%) at 155 °C for 12 h in vacuum		
Final Cathode Composite	Encapsulation	UGS, 70 wt.%		
	Conductive	Carbon black (C65), 20 wt.%		
	Binder	PVDF, 10 wt.%		
Final S wt. %		57.33x0.7=40.1	61.15x0.7=42.8	68.79x0.7=48.2
Sulfur Loading		1 and 2 (mg/cm^2)		
Electrolyte		DOL:DME containing 1 M LiTFSI and 0.1 M $LiNO_3$		
E/S Ratio		13 mL/g		
Current Rate		0.1C ,0.5C and rate capability		

3.1.3.4. Polysulfide Adsorption Test. The adsorption capacities of the prepared composites were visually detected by the color change of the polysulfide solution. The polysulfide solution was prepared by mixing a 1:5 molar ratio of S_8 and Li_2S in DOL:DME (1:1 vol.%) solution for 24h; the final solution contained 10 mM of Li_2S_6. The adsorption abilities were tested in mixtures containing 20 mL of the polysulfide solution with 10 mg of the prepared UG-1, UG-3, and UG-5 composites. After continuous stirring for 2 hours, the polysulfide solutions rested, and the color change was observed.

3.2. System-Level Performance Model

After finishing the experiments and getting the discharge capacities, average voltages, and cell resistances, system-level performance models were used by following the steps shown in Figure 3.2. This model is based on the BatPaC model developed by Argonne National Laboratory for LIBs [199]. BatPaC model developed for LIBs was modified for Li-

S batteries. Depending on the experimental results, the model calculates the required cell thicknesses, areas, and specific areal capacities. According to these calculations, every component in a Li-S pack was determined and sized by the model. Hence, the system-level performances were calculated as the final outputs of the model using the masses and volumes of all components in Li-S battery packs.

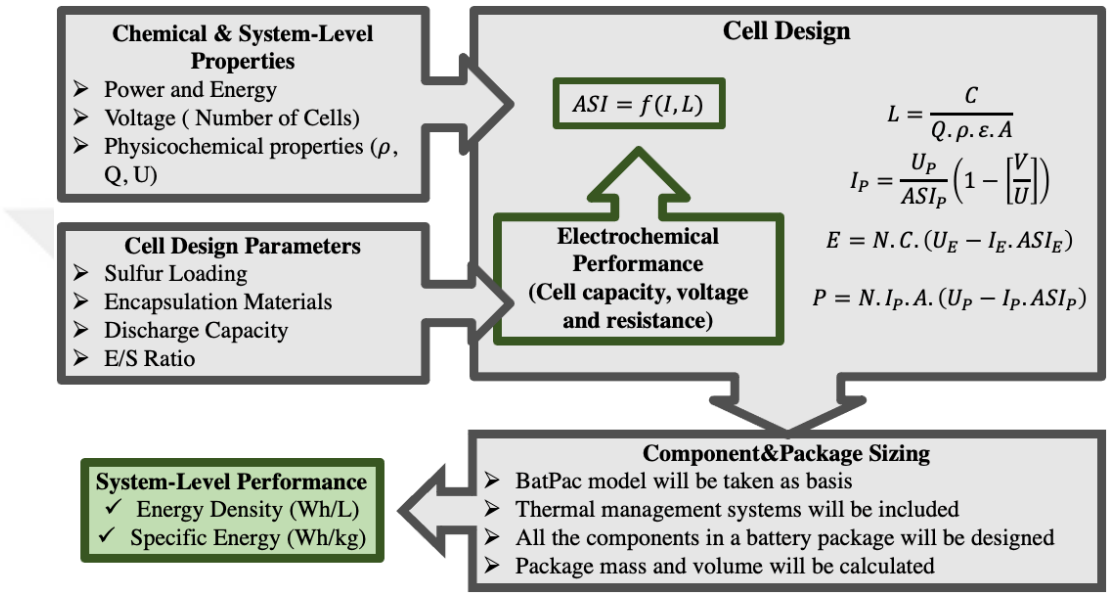

Figure 3.2. Summary of the system-level modeling.

The model reported in this section was originally developed by Eroglu et al. and utilized in this thesis to represent the system-level performances [65]. The model description reported here was published as an original research article in the International Journal of Energy Research by authors A. Kilic, Prof. R. Yildirim, Prof. D. Eroglu [44].

3.2.1. 1-D Electrochemical Model

For developing the system-level performance model, first a 1-D electrochemical model of the Li-S cell predicting the current-voltage relationship for each charge-transfer step was proposed. This model calculates the cell voltage by taking the anode, porous separator, cathode, and both positive and negative current collectors into account. This concentration-

independent, 1-D model calculates the overpotential and area specific impedence (ASI) of the individual components at a specified degree of discharge as illustrated in Figure 3.3.

The sulfur cathode is assumed to be a porous structure consisting of sulfur, carbon, binder, and electrolyte. In addition, it was assumed that there is only one reaction taking place in each discharge plateau as shown

$$\frac{1}{4}S_8^0 + e^- \leftrightarrow \frac{1}{2}S_4^{2-}, \tag{3.1}$$

$$\frac{1}{4}S_4^{2-} + e^- \leftrightarrow \frac{1}{2}S^{2-} + \frac{1}{4}S_2^{2-}. \tag{3.2}$$

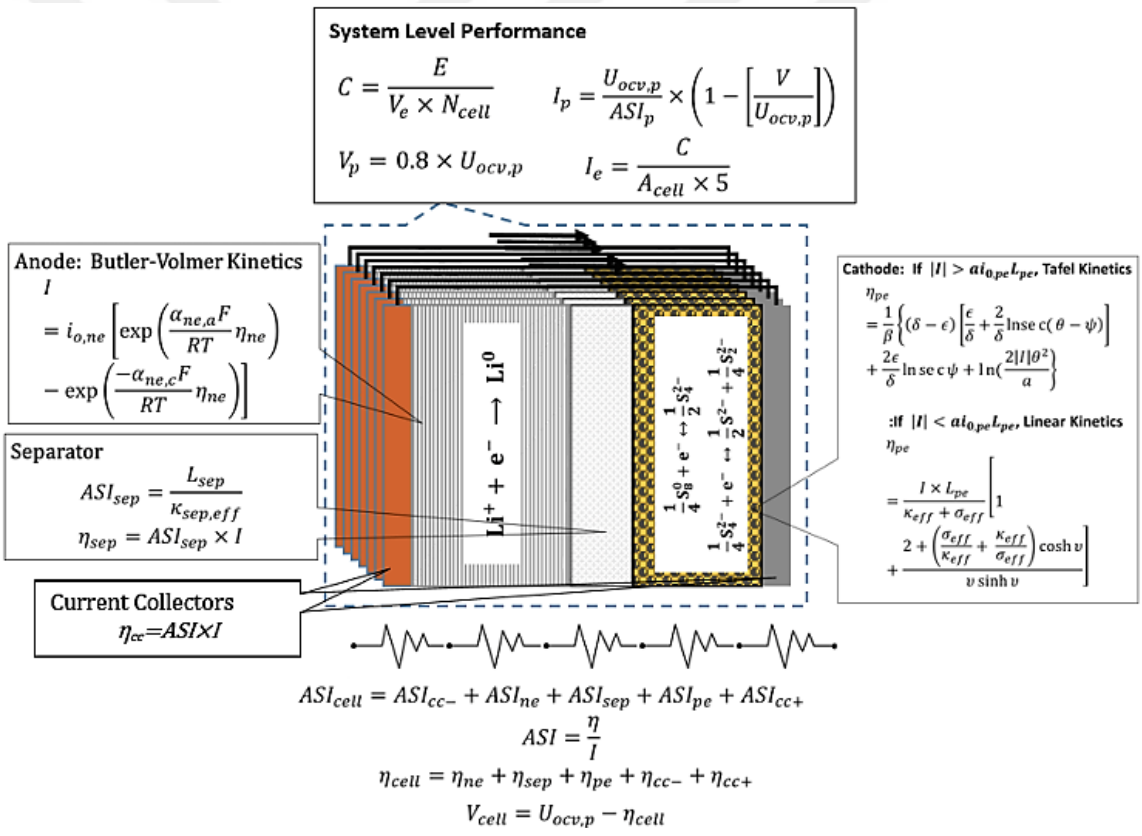

Figure 3.3. Summary of the electrochemical modeling for all cell components.

For the calculation of the cathode overpotential, the porous electrode model developed by Newman and Tobias was used [84], where either Tafel or linear kinetics is applied depending on the current density. For Tafel kinetics, $|I| > ai_{0,pe}L_{pe}$ criteria was used and the overpotential is calculated as

$$\eta_{pe} = \frac{1}{\beta}\left\{(\delta - \epsilon)\left[\frac{\epsilon}{\delta} + \frac{2}{\delta}\ln\sec(\theta - \psi)\right] + \frac{2\epsilon}{\delta}\ln\sec\psi + \ln\left(\frac{2|I|\theta^2}{a}\right)\right\}, \quad (3.3)$$

whereas the cathode overpotential for Linear kinetics, $|I| < ai_{0,pe}L_{pe}$,

$$\eta_{pe} = \frac{I \times L_{pe}}{\kappa_{eff} + \sigma_{eff}}\left[1 + \frac{2 + \left(\frac{\sigma_{eff}}{\kappa_{eff}} + \frac{\kappa_{eff}}{\sigma_{eff}}\right)\cosh\upsilon}{\upsilon\sinh\upsilon}\right], \quad (3.4)$$

where the ASI is calculated from

$$ASI_{pe} = \frac{\eta_{pe}}{I}. \quad (3.5)$$

The oxidation of lithium takes place in the anode during discharge, and the Butler-Volmer equation is used to calculate its kinetics as shown

$$Li^0 \longrightarrow Li^+ + e^-, \quad (3.6)$$

$$I = i_{o,ne}\left[\exp\left(\frac{\alpha_{ne,a}F}{RT}\eta_{ne}\right) - \exp\left(\frac{-\alpha_{ne,c}F}{RT}\eta_{ne}\right)\right], \quad (3.7)$$

$$ASI_{ne} = \frac{\eta_{ne}}{I}. \quad (3.8)$$

Ohm's law is used to calculate the separator resistance and its overpotential with

$$\eta_{sep} = ASI_{sep} \times I, \quad (3.9)$$

$$ASI_{sep} = \frac{L_{sep}}{\kappa_{sep,eff}}. \quad (3.10)$$

The ASI shown in Equation (3.9) and Equation (3.10), is taken as 0.0002 ohm and 0.0005 for negative and positive current collectors, respectively, where the area is 470 cm^2 for both and the overpotentails are calculated using

$$\eta_{cc-} = ASI_{cc-}x\ I, \quad (3.11)$$

$$\eta_{cc+} = ASI_{cc+}x\ I. \quad (3.12)$$

After the total cell overpotential is calculated, cell voltage at constant current density is determined by

$$V_{cell} = U_{ocv,p} - \eta_{cell}, \quad (3.13)$$

$$\eta_{cell} = \eta_{ne} + \eta_{sep} + \eta_{pe} + \eta_{cc-} + \eta_{cc+}, \quad (3.14)$$

$$ASI_{cell} = ASI_{ne} + ASI_{sep} + ASI_{pe} + ASI_{cc-} + ASI_{cc+}. \quad (3.15)$$

Basically, it is calculated using Equation (3.13) by subtracting the total overpotential, Equation (3.14), from the thermodynamic cell voltage where total impedance is calculated by Eqation (3.15).

3.2.2. System-Level Performance Model Adapted for Li-S Batteries

Here, we modified the BatPac model, which was developed by Argonne National Laboratory for the calculation of the system-level performances of LIBs [65], and for the Li-S battery systems to estimate the system-level energy density and specific energy [85]. The 1-D electrochemical model described above calculates the area-specific impedance and overpotential of the cell components; specifically, negative and positive electrodes and their current collectors together with the separator using the experimental inputs including peak discharge capacities (PDCs), cathode wt. percentages, E/S ratios, and sulfur loadings. The cell voltage was determined by subtracting the total overpotential from the open circuit cell potential of 2.2V. Afterward, the battery pack was designed according to the voltage, energy and power requirements. The typical values of 80% and 50% of degree of discharges are determined as the rated power and energy requirements, respectively.

For the system-level calculations, power and energy requirements, denoted as subscript p and e, were used as shown

$$A_{cell} = \frac{P}{I_p \times V_p \times N_{cell}}, \tag{3.16}$$

$$N_{cell} = \frac{U_{batt}}{U_{ocv,p}}, \tag{3.17}$$

$$C = \frac{E}{V_e \times N_{cell}}, \tag{3.18}$$

$$L_{pe} = \frac{C}{A_{cell} \times \varepsilon_{dis} \times \varepsilon_s}, \tag{3.19}$$

$$V_p = 0.8 \times U_{ocv,p}, \tag{3.20}$$

$$I_p = \frac{U_{ocv,p}}{ASI_p} \times \left(1 - \left[\frac{V}{U_{ocv,p}}\right]\right), \tag{3.21}$$

$$I_e = \frac{C}{A_{cell} \times 5}. \tag{3.22}$$

First, the cell area and the number of cells required for pack power were determined using the Equation (3.16) and (3.17), respectively. On the other hand, the energy requirements were used to calculate the cell capacity, Equation (3.18), and thus the cathode thickness, Equation (3.19). Afterwards, iterations were made to get the rated currents (Equation (3.21)) satisfying the rated voltages (Equation (3.20)). Finally, current at rated energy were calculated iteratively using the capacity and cell area requirements (Equation (3.22)).

One crucial issue is related to the thickness of the positive electrode calculation, L_{pe}. It is calculated by the model but practically to have functioning cathodes, it should not exceed 150 μm for the porous cathode. Hence, the cell area was re-calculated using

$$A_{cell} = \frac{C}{L_{pe,max} \times c_{pe}}, \tag{3.23}$$

if the cathode thickness exceeded this maximum electrode thickness.

Table 3.4. The parameters used in the system-level and electrochemical model.

Parameter	Value
Open-circuit cell voltage, $U_{v,p}$ (V)	2.2
Power, P (kW)	80
Energy, E (kWh)	118
Maximum cathode thickness, $L_{pe,\,max}$ (μm)	150
Average battery open-circuit voltage, U_{batt} (V)	360
Target voltage efficiency at rated power, [$V/U_{ocv,p}$]	0.8
Useable state of charge window, (%)	85
Temperature, T (K)	298
Separator thickness, L_{sep} (μm)	20
Separator effective ionic conductivity, $\kappa_{eff,sep}$ (S/cm)	6.5×10^{-4}
Cathode transfer coefficient, $\alpha_{pe,a}$, $\alpha_{pe,c}$	0.5
Anode exchange current density, $i_{0,ne}$ (A/cm^2)	10^{-3}
Anode transfer coefficient, $\alpha_{ne,a}$, $\alpha_{ne,c}$	0.5
Cathode electrochemically active area, a (1/cm)	$A = 650000\ cm^2/g \cdot \rho_c \cdot \varepsilon_c$
Cathode effective ionic conductivity, κ_{eff} (S/cm)	$\kappa_{eff} = \kappa \cdot \varepsilon^{1.5}$
Cathode effective electronic conductivity, σ_{eff} (S/cm)	$\sigma_{eff} = \sigma \cdot \varepsilon_c^{1.5}$
Cathode exchange current density, $i_{0,pe}$ (A/cm^2)	10^{-6}
Cathode electronic conductivity, σ (S/cm)	100
Cathode ionic conductivity, κ (S/cm)	0.01

The parameters together with their symbols used in the models are given in Table 3.4. With the calculation of the required cell area and other cell variables, suitable packaging and

thermal management components were determined. Consequently, the system-level energy densities and specific energies were calculated by taking all the system variables into account. Although material properties such as carbon/electrolyte densities and conductivities are important input variables for the electrochemical model, the system-level performances were found to be rather insensitive to these factors. In fact, the effect of these material properties on the energy density and specific energy is implicitly included in the model since these properties are highly effective on the specific capacities obtained experimentally, and these capacities are the most determinative variable on the system-level performances. Hence, their effects on the system-level performance are taken into account with the variance in the specific capacity value.

The experimental inputs to the system-level model were restricted to the specific capacity, E/S ratio, sulfur loading as well is the cathode sulfur wt. % and binder wt.%. The system-level model were used in two sections: Section 4.1.2 and Section 4.1.5. In Section 4.1.2, the model was applied to literature data. However, among 245 cases, only half of them were providing all of these necessary information whereas the rest did not provide E/S ratios. On the other hand, in Section 4.1.5, the variables shown in Table 3.5 were used.

Table 3.5. The experimental variables used in Section 4.1.5 fed to the system-level model.

E/S ratio (mL/g)	S loading (mg/cm^2)	Additional	KBS	VCKBS	Test Condition
20.1	1.24	Cathode contains 10 wt% PVDF binder and 45 wt% sulfur. Electrolyte is 1 M LiTFSI and 0.1 M $LiNO_3$ in DOL: DME (1: 1 vol%).	803	1329	Group 1, 0.1C, 1st capacity
13.2	2.4		466	1201	Group 2, 0.2C, 1st capacity
20.1	1.24		395	1249	Group 1, 0.1C, 100th capacity
13.2	2.4		142.6	1015	Group 2, 0.2C, 100th capacity
20	0.8		1117	1123	0.1C, 1st capacity
13	0.8		768	973	0.1C, 1st capacity
6	0.8		241	811	0.1C, 1st capacity
20	1.2		962	1285	0.1C, 1st capacity
13	1.2		799	1106	0.1C, 1st capacity
6	1.2		237	965	0.1C, 1st capacity
20	3		279	1009	0.1C, 1st capacity
13	3		219	804	0.1C, 1st capacity
6	3		93	711	0.1C, 1st capacity

3.3. Machine Learning Models

ML models were applied to get the trends and to reveal the hidden relations between battery performances with the materials and design parameters of Li-S and Li-O_2 batteries. The ML steps were given, including the data gathering, data preparation, model development, and analysis of the results, as illustrated in Figure 3.4. Data gathering can be done by collecting literature data as well as using computational modeling or simply using databases that already utilize these techniques. This depends on data availability and applicability for the desired purpose. Data preparation is one of the most important steps for good modeling. On the other hand, the appropriate model depends on the structure and quality of the data. Hence, in this section, the data preparation method as well as the modeling techniques were given for each of the sections utilizing these techniques, namely Sections 4.1.1-3 and Sections 4.2.1-2. In this thesis, a bibliometric analysis was performed by using simple text mining from the data obtained from Web of Science (WOS) database. Apart from that, ARM is the main algorithm utilized in this study as ARM basically works with categorical data; hence it is suitable for the datasets built up in this thesis. ARM gives the single-factor relations between each features and the desired outputs independently. On the other hand, DT is used to get heuristic rules for obtaining the target variables where features are considered altogether to get a rule leading to high class. Finally, the prediction models were built using XGBoost and RF algoritms; both are ensemble tree models where multiple trees were built. Trees were built in parallel and in series in RF and XGBoost, respectively, where the majority of the trees determine the model output whereas trees are built sequentially where each tree improves the latter and the final output is decided. Hence, XGBoost is better to reveal complex non-linear relations but it is slower than RF. In this respect, XGBoost is used in the PS solubility calculations, Section 4.1.3, where only 20 descriptors were used. On the other hand, RF model is used for gas solubility calculations in Section 4.2.2 where more than 400 variables are present.

Figure 3.4. Summary of machine learning steps.

3.3.1. Text mining used in bibliometric analysis of beyond LIBs

A bibliometric analysis was performed, and the results are given in the beginning of Section 4, to see the major patterns and trends involving beyond LIB research [9]. First, a keyword search (with the keyword option) was performed for the articles present in the WOS on 25 June 2023. Alternative battery names were used; for example, we used keywords like *M-ion batter**, *Metal-ion batter*, Metal ion batter*, M-ion cell*, *Metal-ion cell, and Metal ion cell* for metal-ion batteries ("*" is used to account for both singular and plural use of the same word). Likewise, for metal-air batteries, both *oxygen* and *air* keywords were utilized. The "*Title*" option was used as the search criteria to only get the articles in the battery field, assuming that the battery chemistry will always be on the title. Without applying any filtering, all the information of the searched results was exported as Excel files to analyze literature trends. In these Excel files, in addition to the publication information of the articles, *Abstracts*, *Author Keywords, and Keywords Plus* were also listed. Although *Abstracts* can also be used in the text mining analysis, to eliminate the complexity of the modeling process, only the keywords (both author keywords and keywords plus) were used in the text mining analysis. R Studio environment was used for basic text tidying and word frequency analysis with the help of *stringr, tm, plurize,* and *tidytext* libraries [200]. In the modeling process, the data was first cleaned using the basics of text mining commands, eliminating stop words and punctuation, singularization, and handling synonyms. Afterward, the most frequently used keywords were investigated for all beyond LIBs. First, the focus of articles on essential elements (anode, cathode, electrolyte, and separator) was analyzed as the keywords; techno-economic analysis, ML analysis, and other modeling works for the entire battery systems were represented as *modeling* studies. Furthermore, two-word bigram analyses, which are the counts of two-word relations, were also performed for selected words to see the most frequently followed words.

3.3.2. Materials and Methods for Assessment of Critical Materials and Cell Design Factors for High Performance Lithium-Sulfur Batteries using Machine Learning

This section is modified from the original research paper published in the Chemical Engineering Journal by authors A. Kilic, Dr. Ç. Odabaşı, Prof. R. Yildirim, and Prof. D.

Eroglu [43]. The data gathering, preparation, and result analysis were performed in the scope of this thesis by A. Kilic, whereas the ARM analysis was performed by Ç. Odabaşı.

3.3.2.1. Constructing Database. The database was constructed by extracting data from the papers indexed by the WOS database; the papers were decided using relevance search with all possible ways of written *lithium sulfur battery* (word, symbols w/o "-" and so on). Only the articles published between 01.01.2010-18.07.2018 (search day) were used to represent the recent developments in the field. Additionally, the data was extracted from only the experimental research articles; the review articles or other publications were not considered. At the end, a Li-S database having 1660 experimental data from 353 articles was emerged; this dataset should sufficiently represent the literature because it is constituted of about 10 % of the research articles appeared in the WOS database within our search time interval. As given in Section 4.1.1, the data subsets for the Li-S batteries having liquid electrolyte, catholyte, liquid and solid electrolyte together and solid electrolyte only were analyzed separately. Table A.1 includes the structure of the database.

Although the theoretical discharge capacity of the Li-S batteries is known to be 1675 mAh/g [201] this capacity could not be attained in most of the works; instead, how much the experimental results approached to the theoretical capacity is used as a performance indicator of the cells. Therefore, PDC were used normalized to sulfur mass as one of the output (performance) variables in our analysis. Additionally, the cycle life of the battery is also critical for successful commercialization; for instance, a battery should retain 80% of its initial capacity for at least 1000 cycles [65] to be used in an electric vehicle [202]. Hence, the cycle number were also analyzed and compared, at which the battery preserved more than 80% of its PDC, as another performance variable. Here it should be emphasized that energy density and specific energy are also key performance indicators for Li-S batteries. However, they were not considered in this analysis as output variables since the majority of the studies in the literature do not report these values. Yet, in order to evaluate the effect of materials and design factors to achieve high energy density Li-S cells, an additional analysis, in which Li-S cells only with low E/S ratios ($\leq$ 5 mL/g) and high S loadings ($\geq$ 5 mg/cm^2) were considered, was carried out.

Table 3.6. Categorical and numerical variables (factors) used in the analysis.

Factor	Alternatives
Anode Material	Li Metal, Modified Li Anode*
Current Collector	Al Foil, Carbon Coated Al foil, Carbon, Nickel, Others1*, No
Separator	Glass, Polymer, Others2*
Interlayer	Yes, No
Sulfur Type	Sulfur, Sulfur + Others3*, Li_xS_y, Others4*
S Loading (0.02-20 mg/cm^2)	0-1, 1-3, 3-5, Above 5
Sulfur wt.% (0-100 wt.%)	0-25, 25-50, 50-75, 75-100
S Catholyte Conc. (0-12 M)	0-1, 1-5, Above 6
Conductive Material	Carbon Black, Carbon Black + Others5*, Carbon Black + Structured Carbon1*, CNT, Others6*, Structured Carbon2*, Structured Carbon3* + Others7*, No
Carbon wt.% (0-80 wt.%)	0, 0-15, 15-30, Above 30
Encapsulation Material	Activated Carbon, Activated Carbon+Graphene, Carbon Black, Carbon Black + CNT/Graphene / Others8* / PANI/ Porous Carbons1*, CNF, CNF + GO / Others9*, CNT, CNT+GO/GO + Porous Carbons2* /Graphene/Others10*/Porous Carbons3* /Porous Carbons4*+PANI, GO, GO+Hollow Structured Carbon1* /Others11*/Polypyrrole/Porous Carbons5*, Graphene, Graphene+ Hollow Structured Carbon2*/OtherCarbons1*/Others12*/ Polypyrrole/Porous Carbons6*/Porous Carbons7* +Others13*, Hollow Structured Carbon3*, Hollow Structured Carbon4*+Others14*/Polypyrrole, No, Other Carbons2*, Other Carbons3*+Others15*, Others16*, PANI, Polypyrrole, Porous Carbons8*, Porous Carbons9* +Others17*/PANI/Polypyrrole, Structured Carbons4*
Encapsulation wt.% (0-89 wt.%)	0, 0-25, 25-40, Above 40
Doping Type	Nitrogen, Nitrogen+Others18*, Others19*, No
Binder Type	No, PVDF, CMC, Others20, LA, PEO, PTFE, CMC+SBR, PVDF+Others21*, PEO+Others22*
Electrolyte Solvent	DOL:DME, DOL:DME:Others23, DOL:TEGDME, EC:DEC, EC:Others24*, Others25*, TEGDME
Electrolyte Salt	LiTF, LiTFSI, $LiPF_6$, Others26*, $LiClO_4$, No
Electrolyte Additive	Yes, No
Electrolyte Additive Conc. (0-4.65 M)	0-0.1, 0.1-0.2, 0.2-0.5, Above 5
Electrolyte/Sulfur Ratio (0-166 mL/g)	0-5, 5-10, 10-15, 15-30, Above 30

*Detailed descriptions and abbreviations are given in Appendix A. CMC: Carboxymethyl Cellulose, CNF:Carbon Nanofiber, DEC:Diethyl Carbonate, GO:Graphene Oxide, LA:Polymer n-Lauryl Acrylate, PANI:Polyaniline, PEO: Polyethylene Oxide, PTFE:Polytetrafluoroethylene SBR:Styrene-Butadiene Rubber, TEGDME:Tetraethylene Glycol Dimethyl Ether. Slashes show the alternatives for additional materials.

There are various variables (factors) that affect the attained PDC and cycle life of a Li-S cell; the most important continuous and categorical factors with their ranges (for continuous factors) or alternatives (for categorical factors), as extracted from the papers, are shown in Table 3.6. Different names and notations used for the alternatives of discrete variables were combined into a single clear and comparable statement, while the continuous

variables were categorized by dividing into intervals because the ML technique we used required so. The new materials alternatives tested in some of the recent studies were combined under a single factor named as *others* because individual number of data points for these factors were not sufficient to make statistical analysis or compare with the conventional alternatives; the detailed content of *others* is given in Appendix A.

The articles, which do not contain sufficient information for the key input or performance variables, were not used in dataset construction; however, for certain variables that are not critical, the most commonly used materials were assumed if only that information is missing. For instance, if there was no specific information, we assumed "Li metal" for the anode type, "Polymer" as the separator type, "No" for both the conductive additive and doping types. If not given, the cathode area was assumed as 1.6 cm^2 for C-rate estimations and the sulfur loading was taken to be 1 mg/cm^2 for E/S ratio calculations. If the conductive materials and sulfur were pretreated to form a composite before they were used in the cathode preparation, the materials were defined as the "encapsulation materials", whereas they were categorized as "conductive materials" if there was no other treatment of the cathode matrix and sulfur than mechanical mixing.

3.3.2.2. Computational Details. Single factor associations (i.e. relation of performance variables with individual factors) were analyzed using the ARM method to identify the factors leading to high PDC or longer cycle life; *high performance cell classes* were defined, and the factors required to have a cell in these classes were identified using ARM. *Apriori* algorithm was adopted by using *arules* package [203] of *R Studio* software [204]. ARM results were evaluated using three key parameters for this technique: *support*, *confidence* and *lift* values of the parameters. These parameters can be calculated from

$$Support = \frac{A\&B}{N}, \tag{3.24}$$

$$Confidence = \frac{A\&B}{B}, \tag{3.25}$$

$$Lift = \frac{\frac{A\&B}{B}}{\frac{A}{N}}. \tag{3.26}$$

Support is defined as the fraction of batteries made using a specific material (factor) and have defined PDC (in high class) in all data points while *confidence* is the fraction of batteries made with that material in all cells in the high PDC class (calculated by Equation (3.24) and Equation (3.25), respectively). *Lift*, which is the most important parameter to evaluate the ARM results, is the fraction of batteries with that material in high PDC class cells to the fraction of batteries with that materials in total data points, Equation (3.26).

As it will be more apparent in the Section 4.1.1, the lift should be more than one, and higher lift values indicate that the fraction of that material in high performance cells is higher than its fraction in the entire database indicating that the use of that material favors high performance cells. ARM analyses were performed for the PDCs equal to or higher than 1000 mAh/g, 1200 mA/g, 1400 mAh/g and 1600 mAh/g, and the change in lift values was monitored to determine the significance of the individual factors for high performance. The same procedure was also applied to investigate the factor effect on cycle life by analyzing the lift values for the cells retained 80 % of its peak discharge capacity more than 50, 100, 200, 300 and 400 cycles.

3.3.3. Materials and Methods for Assessment of Ionic Liquid Electrolytes for High Performance Lithium-Sulfur Batteries using Machine Learning

This chapter is an edited version of the original article published in the International Journal of Energy Research by authors A. Kilic, Prof. R. Yildirim, and Prof. D. Eroglu [44]. The ARM analysis on peak discharge capacity, system-level specific energy, and energy density was performed in this section as the ML method.

WOS database was used to collect the experimental articles reporting the use of ionic liquids as their liquid electrolytes in Li-S batteries; the application of ILs in solid electrolytes or cathode matrices was excluded. After the data collection step, the dataset was preprocessed to reduce inconsistencies and to select suitable variables (i.e., those widely reported in the literature and influential on the performance) while the rarely reported variables such as electrode thicknesses and material properties were not included to have a statistically reliable result. Similarly, the cells tested at temperatures higher than 30 °C were

not considered here because those data were significantly different than the ones obtained at room temperature, yet not in sufficient numbers to show the temperature effects. In the end, a dataset with 244 data points from 42 articles, including important cell design variables and materials, was built. The data points in the dataset using only molecular solvents (37 data points), reported for comparison reasons, are not used in the analysis either. Consequently, the dataset used in this section was composed of 207 data points; the variables and their alternatives (levels) are given in Table 3.7.

Table 3.7. The variables and levels used in the analysis.

	Factors	**Levels**
Electrolyte Variables	Ionic Liquid	C4dmim_TFSI, DEME_Others1, DEME_TFSI, EMIM_TFSI, Li(G3)_Others1, Li(G3)_TFSI, Li(G4)_Others1, Li(G4)_TFSI, P1,2O1_TFSI, P13_Others1, P13_TFSI, P14_Others1, P14_TFSI, P1A3_TFSI, P2225_TFSI, PMIM_TFSI, PP13_TFSI, PP14_TFSI, TES_TFSI
	Molecular Solvent(MS)	DME, DOL, DOL:DME, Fluorinated Ether, None, Others2, TEGDME
	IL/MS vol.%	<50, 50, >50, 100
	MS Salt	LiTFSI, None, Others3
	MS Additive	Yes, None
	E/S Ratio	0-15.0, 15.0-30.0, >30.0
Cathode Variables	Conductive Material	Acetylene Black, Carbon Black, Ketjen Black, None, Others4
	Encapsulation Material	Activated carbon, Carbon Black, Carbon Nanotube, Graphene Oxide, Ketjen Black, Mesoporous carbon, Nano Carbon, None, Others5, Porous Carbon
	Binder	CMC, None, Others6, PVA, PVDF, SBR/CMC
	Sulfur wt.%	0-50, 50-60, >60
	Conductive wt.%	0, <20, 20, >20
	Encapsulation wt.%	0, 1-20, 20-30, 30-35, >35
	Sulfur Loading (mg/cm2)	0-0.1, 1.0-1.5, 1.5-4.0, >4.0
Others	Anode	Li metal, Modified Li anode
	Separator	Glass, Polymer

Others1:FSI, Nitrate, trifluoromethanesulfonate, BETA, BF4, tris(pentafluoroethyl)trifluorophosphate, tricyanomethanide // Fluoriated Ethers: HFE, TFTFE, TTE // Others2: TEGDME:DOL, TMU, DMSO, ACN, TTE:DOL, DOL:ETFE, Methylisopropylsulfone // Others3: LiFSI, LiBF4, LiPF6, Li[BETA], LiODFB // Others4: Carbon Nanotube+Ketjenblack, Graphene+Carbon Black // Others5: Graphene+magnesium aluminate, N-doped mesoporous carbon // Others6: LiPAA, PAA, SBR, PAA/PVDF, PEDOT/PSS, PEO

As seen in Table 3.7, there are 15 important variables in the dataset. Most of these variables are already categorical by their nature; the originally continuous variables were also categorized into intervals to be able to be used in the ARM analysis, which requires categorical data. The range of the intervals is determined according to the distribution of the

data points to have a statistically significant number of data in each class with the best representation of the patterns in the literature. The rarely used materials were categorized as "others" because no rule can be deduced from the results supported by only a few instances. As it was stated in the Introduction section, due to the insulating nature of sulfur, the conductive materials should be added into the cathodes. If these materials are chemically pretreated with sulfur before the cathode formation, they were reported as "Encapsulation Materials", while physically treated materials were saved as "Conductive Materials". As the performance metric, the *peak discharge capacity (PDC) normalized to sulfur amount (mAh/ g S)* was chosen because it shows *how much of the theoretical capacity of sulfur cathodes is attained*. In addition, the *system-level energy density* (Wh/L) and *specific energy* (Wh/kg), which are more relevant performance indicators in practice, were calculated using the modified version of the Battery Performance and Cost (BatPaC) model as described in Section 3.2.

ARM model was used to identify the single factor associations between each variable and the performance metrics. First of all, the *high* class was defined by setting a minimum performance limit, either PDC, specific energy or energy density, and the levels of each factor, as shown in Table 3.7, that can lead to that high class was analyzed using the ARM results. ARM model was developed using *R Studio* software and its *apriori* algorithm of *arules* package [204]. This algorithm provides *support*, *confidence* and *lift* values calculated from the Equation (3.24) to Equation (3.26) where A shows the count of a specific level of a factor, and B and N show the number of instances in the high class and the total dataset, respectively. Support and confidence show the most direct trends in the dataset where the fraction of a level with high performance in the entire and the high-performance datasets, respectively, were calculated. On the other hand, more complex patterns can be found using lift values, which is calculated by the ratio of the confidence to the fraction of that level in the total dataset [48]; the lift values above one signify positive associations between that level and high performance since it is more frequently found in the high class subset [205]. Furthermore, higher lift values imply higher probability to have better performances; this will be more evident in the next section when it is discussed on specific examples. It should be noted that although cycling performances at high current rates is also important for the Li-S batteries, this data in the literature for ionic liquid electrolytes are not sufficient to get

statistically valid conclusions. Hence, this indicates that the IL electrolytes have some stability problem which should be improved, but this topic is out of the scope of this work. Because of that, ARM analysis was applied to PDC, energy density and specific energy only.

3.3.4. Materials and Methods for Selection of Ionic Liquid Electrolytes for High-Performing Lithium-Sulfur Batteries: An Experiment-Guided High-Throughput Machine Learning Analysis

In this section, the data preparation and ML models for Chapter 4.1.3. is presented; a manuscript detailing these methods are in preparation by authors A. Kilic, O. Abdelaty, Prof. D. A. Uzun, Prof. R. Yildirim, and Prof. D. Eroglu. The COSMO-RS calculations, ML studies and the IL experiments were performed by A. Kilic and presented here. O. Abdelaty also supported the discussions on ML modeling. Here, the dataset was prepared by using the COSMO-RS calculations for solubilities and by using PM3 for feature determination.

3.3.4.1. Solubility and Property Calculations. COSMOThermX software was used for the determination of Li_2S_8 solubility in ILs at 25 ºC using COSMO-RS calculations [206]. The built-in IL database, COSMObaseIL, was used to form the dataset for this study. COSMOThermX uses the σ-profiles calculated using the DFT functional BP and def2-TZVP level. The dataset comprised 98 anions and 370 cations, which adds up to 36,260 pairs of ILs. The long chain Li_2S_8 was used to model the PSs in the system. In accordance with previous reports about Li_2S_8 conformation in the solvents [207,208], the linear conformation of Li_2S_8 was optimized using B3LYP/def2-TZVP then inputted to TMOLEX (v.4.5.3) to generate the standard σ-profile file (*.cosmo* file). The sigma profile and the corresponding surface of the Li_2S_8 molecule are given in Figure C.1

The *IL Screening Module* was used to calculate the PS solubility in ILs at 25 °C via

$$C_i^{\infty} = \frac{1}{\gamma_i^{\infty}} \tag{3.27}$$

where C_i^{∞} and γ_i^{∞} are capacity (mol/mol solubility) and activity coefficient of the PS at infinite dilution, respectively.

The melting point, viscosity, and electrical conductivity were also calculated at 25 °C using the IL Properties Module, which also uses the same σ-profile files for the ions. The densities of ILs were calculated using the molecular volume obtained by the COSMO-RS volume calculations, whereas COSMO-RS enthalpies were used for the melting point calculations. Finally, the same formula utilizing ionic radius and dielectric energies was used for the viscosity and electronic conductivity calculations. The implemented correlation coefficients were naturally different for each calculation**.**

3.3.4.2. Structural Descriptors for ILs. The structures in the COSMObaseIL were reoptimized with Spartan'14 using the PM3 semi-empirical method with the default convergence criteria. Similar to our previous studies [209,210], ten descriptors were calculated for each anion and cation separately: Molecular weight (MW in amu), HOMO and LUMO energies (E_{HOMO}, E_{LUMO} in eV), CPK-area (in $Å^2$) and CPK ovality (O) obtained from the space-filling model, dipole (μ in D), polarizability (m^3), vibrational zero point energy (ZPE in kJ/mol), hydrogen bond donor count (HBD), and hydrogen bond acceptor count (HBA). Consequently, there are 20 descriptors for each IL pair. The distribution of ions in terms of these structural descriptors is given in Figure 3.5.

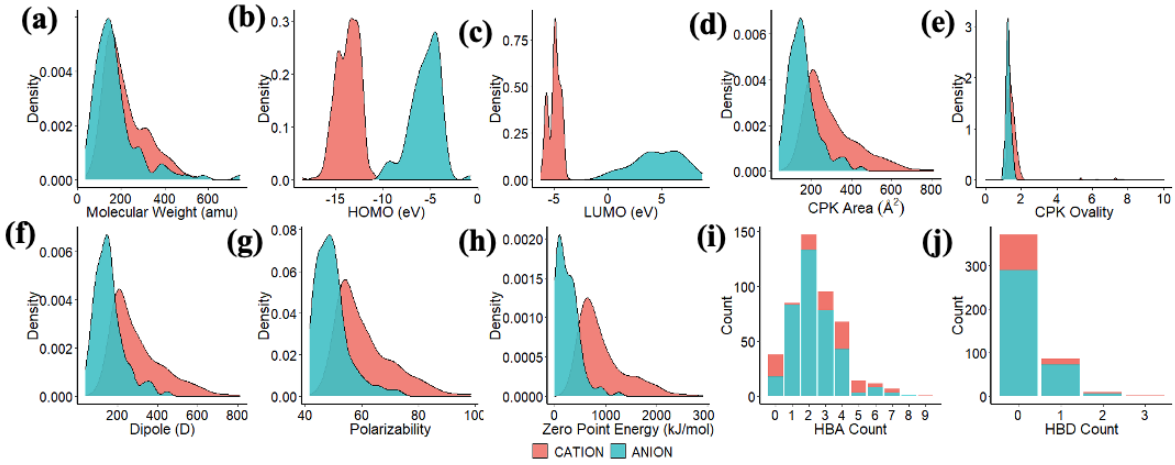

Figure 3.5. The distributions of descriptors; molecular weight (a), HOMO (b), LUMO (c), CPK area (d), CPK Ovality (e), dipole (f), polarizability (g), zero point energy (h), HBA count (i) and HBD count (j), for cations and anions in the dataset.

3.3.4.3. ML Modeling. Distinct prediction models were trained for each IL property of interest: the solubility of Li_2S_8, melting point, viscosity, and electrical conductivity. Random sampling was employed to negate the bias towards the majority class. Afterward, the dataset was partitioned into a training and test set using a 75%-25% split. Given that PS solubility highly depends on anion type, random assignment of the data entries into each subset was avoided as it overfitted the ions in the set and performed poorly on new ions (due to the strong effects of the anions). Therefore, the splitting was done either according to the anion or the cation groups. In practice, this means that a random 25% fraction of anions/cations in each anion/cation group was included in the test set, while the remaining ions were used in the training set. This way, the test set contains new anions/cations not encountered during training or validation. The same strategy was used for 5-fold cross-validation, where 20% of the training ions were selected in the validation sets, and the rest were used for training. Next, the partitioned dataset, along with the respective values of properties calculated by COSMOThermX, were used to train ML models XGBoost algorithm was used in the predictions. The hyperparameters were optimized with a grid search according to the performance criteria of root mean square error (RMSE), which shows the average difference between the predicted and the COSMO-RS calculated values; hence, the lower it is, the better the predictions. In addition, the R-squared (R^2) value, the proportion of the difference between the two, ranging between 0 and 1, is also reported [211]. The optimized hyperparameters for XGBoost are the maximum depth, number of trees, and learning rate (η) values, which were found to be 3, 225, and 0.1, respectively, for the solubility predictions. The descriptor importance was calculated with these hyperparameters over the train set.

After the prediction models were built, the ARM method was utilized to classify the promising anion and cations together with their descriptors. The classification models were trained as binary classifiers: class A and class B are the favorable and non-favorable levels of related properties and solubilities, respectively. The thresholds of these classes were determined according to the experimental results and the desired characteristics of a battery electrolyte. In the case of solubility, a threshold value of -0.7 to 0.1 mol/mol in the log scale was selected as it is comparable to ILs tested in the literature and the performance data obtained in our research [75]. Similarly, limits for the viscosity, conductivity, and melting

point classifications were determined as 100 mPa.s, 2 mS/cm, and 0 ºC, respectively. In the ARM analysis, all these four targets were held to see the most promising ILs as electrolytes of Li-S batteries.

The relationships between the anion/cation groups and their descriptors with the class A in all four criteria were independently analyzed by a single-factor ARM algorithm. Since ARM only works for categorical data, HBA and HBD counts were turned into factors, and the remaining eight numeric descriptors were categorized into ten multiple intervals with a similar number of data points. The performance metrics, support, confidence, and lift, were used together to determine the reliability of a rule. Similar to the previous sections, the lift value was considered the ultimate criterion to assess the association between a descriptor and the solubility, as long as the rule clears the minimum support and confidence thresholds, taken as 0.1 % and 3 %, respectively. All the modeling and figure creation was performed in the R Studio environment.

3.3.5. Materials and Methods for Determining the Key Performance Factors in Lithium-Oxygen Batteries Using Machine Learning

This chapter includes the Materials and Methods part of the original research paper published in the Journal of the Electrochemical Society by authors A. Kilic, Prof. R. Yildirim, and Prof. D. Eroglu [48].

3.3.5.1. Constructing Database. The data were collected from the Web of Science database using various keywords to cover all the possible representations of Li-O_2 and Li-air batteries. Experimental research articles were sorted by their relevance, and reviewed starting from the top; only the papers published after 2010 were considered. 1015 data from 157 papers were collected, and the dataset was divided into two groups as *capacity testing* (773 data points) and *voltage testing* (242 data points), depending on the aim of the study. In the capacity testing group, a cell is discharged at a constant current until a cut-off voltage is attained. On the other hand, for voltage testing group, a cell is discharged until a specific capacity is reached and cut-off voltage is reported. The ML tools were applied to capacity

and voltage testing groups independently, where *discharge specific capacity* and *cut-off voltage* were used as the performance indicators, respectively.

Table 3.8. Description of categorical and numerical variables (factors) used in the analysis.

Factors	Alternatives
Anode	Li Metal, Modified Li Anode
Separator	Glass, Polymeric, Glass+Polymeric, Solid Electrolyte
Reactant	Air, Dry Air, Oxygen, Oxygen:Carbon dioxide
Reactant Pressure (atm)	<1, 1, >1
Gas Diffusion Layer	Carbon, Carbon cloth, Carbon paper, Graphene, No, Filter paper
Bulk Cathode Material	Activated carbon, Carbon black, Carbon black+CNT, Carbon black+Graphene, Carbon black+other carbons1, CNF, CNT, Co oxide, Gold, Graphene, Graphene oxide, Ionic liquid CNT, Mn oxide, N-doped carbons, N-doped CNT, Other carbons2, Others1, Porous carbon, rGO, RuO_2, Ti composite
Cathode Ingredient	Al_2O_3, Al_2O_3+Ag, Al_2O_3+Pd, Au, Au+Pd, AuPt composite, Co oxide, Co oxide+Others2, Co_4N, CoMn oxide, CuCo oxide, LaFe oxide, Mn oxide, Mo compound, $NiCo_2O_4$, NiO+ $NiCo_2O_4$ microspheres, No, Other oxides, Others3, Pd, Pd composite, PdO, Perovskite, Pt, Pt+Au, Pt_3Co, Ru, Ru oxide+Mn oxide, RuO_2
Binder Type	No, PVDF, PTFE, PVDF-HFP, Nafion, Others4
Active Material Loading (0.0-26 mg/cm^2)	0-0.8, 0.8-1.2, 1.2-3.0, Above 3
Active Material wt.% (35-100 wt.%)	39-60, 60-80, 80-90, 90-100, 100
Electrolyte Solvent (E Solvent)	DME, DMSO, EC:DEC, EC:DMC, EC:PC, Ionic Liquid, Others5, PC, PC:Others6, Solid E+Liquid E, Solid Electrolyte, Tetraglyme, Triglyme
Electrolyte Salt (E Salt)	$LiCF_3SO_3$, $LiClO_4$, LiTFSI, $LiPF_6$, Others7, No
Electrolyte Additive (E Additive)	Yes, No

CNT: Carbon Nanotube, CNF: Carbon Nanofiber, rGO: Reduced Graphene Oxide, PVDF: Polyvinylidene Fluoride, PTFE: Polytetrafluoroethylene, PVDF-HFP: Poly(vinylidene fluoride co-hexafluoropropylene)), DME: Dimethyl Ether, DMSO: Dimethyl Sulfoxide, EC: Ethylene Carbonate, DEC: Diethyl Carbonate, DMC: Dimethyl Carbonate, PC: Propylene Carbonate. Further information about the materials is given in Appendix F.

Capacity and voltage of Li-O_2 cells are dependent on various cell design variables (can be also labeled as *factors* or *descriptors*). Due to the nature of ARM and DT methods, only the categorical (discrete) variables were used in the analyses; the continuous variables were discretized to categorical variables by grouping them in terms of intervals [212]. The

categories (for example specific materials), which are not repeated sufficiently large number of times to form a group, merged as *others,* and their contents are given in Appendix F. Additionally, the articles with too many missing variables were not taken into consideration. The variables, which were used in analyses, are listed in Table 3.8. Here it should be mentioned that not all the variables that affect the cell performance, such as the electrode and gas diffusion layer thicknesses, were typically reported in the literature. Hence, only the factors that are widely reported in the literature were included in the analyses. Active material is defined as the total cathode materials excluding the binder, which is taken as a separate variable. Throughout the dataset, all the capacities were normalized to active material masses so that they will signify the effect of the type of active materials on capacities rather than the amount used in the cathodes.

3.3.5.2. Computational Details. R Studio environment was chosen for both data pre-processing and ML implementations. ARM was used first to determine the effect of individual factors on the performance by using *apriori* algorithm of *arules* package [203]. ARM reveals dominant factors (antecedents) leading to higher capacities (consequences) by providing the parameters of *support*, *confidence* and *lift.* For practical applications, cycling stability is also a very important performance criterion for batteries. However, the amount of cycling data of Li-O_2 batteries is limited in the literature. Hence, the analysis was performed only for the initial discharge capacities of the cells in the scope of this work; cycling performance will be modeled in future studies when the literature becomes more mature in terms of the cycling data.

Although multi-factor analyses are also possible using ARM, we used decision tree (DT) because it is more effective and easier to interpret. In order to analyze and compare the cells manufactured and tested under the same testing conditions, we only considered the cells that used oxygen at 1 atm as the reactant and were discharged at 0.1-0.5 mAh/cm^2 for the DT analysis. For this part, the dataset was divided into three classes based on the performance levels (as class A, B, and C) to be able to differentiate the conditions for high performing class from the others. The batteries with capacities higher than or equal to 6000 mAh/g, between 1500-6000 mAh/g and lower than 1500 mAh/g were defined as Class A, Class B, and Class C, respectively. To prevent class imbalance problem, which creates a bias

toward the majority class, random sampling was applied to have equal number of data in each class [212]. However, variables with a small number of datapoints caused a problem when the dataset was divided into training, validation and testing because some values (for example, a specific cathode ingredient) appeared only in one or two of the training, validation or testing sets making the assessment of model fitness unmanageable. To prevent this, rarely found variables were merged as "others" (given in Appendix F). DT analysis was performed by using *dplyr* package of RStudio [213]. In order to prevent any bias, the dataset was randomly divided into two subsets as 75 % for training and validation, and 25 % for testing. First, the DT model was built by applying 5-fold cross validation procedure. The dataset containing 75% of data was further divided into five subsets randomly; the model constructed using four subsets was tested with the remaining set. This procedure was repeated five times by assigning different validation sets in each turn, and the model with the minimum split of 10 and complexity parameter of 0.01 was found to represent the data best (with the lowest validation error). Then, this model was tested using the testing data (25% separated first) to assess its accuracy for the classification of the data not seen before.

The determination of the cut-off voltages for restricted capacities is also widely reported in the literature because high cell voltages are important for the batteries to produce high power. However, the restricted capacity ranges vary significantly from one paper to another; therefore, the comparison of factors (for example, materials) would not be fair unless a specific capacity range was chosen. Consequently, the data generated in two different capacity intervals of [500, 750] mAh/g and (750, 1000] mAh/g were analyzed as two separate datasets considering that these intervals have relatively high number of datapoints as 112 and 130 (total 242 datapoints), respectively. Although DT could not be applied to these datasets due to small number of data, ARM analyses were conducted to identify the critical factors resulting in high cell voltages.

3.3.6. Materials and Methods for Screening of Ionic Liquids as Electrolyte of Metal-Oxygen Batteries using COSMO-RS and Machine Learning

This section includes the Materials and Methods part of the manuscript in preparation, detailing the results reported in Chapter 4.2.2. The manuscript is entitled Screening of Ionic

Liquids as Electrolytes of Metal-Oxygen Batteries using COSMO-RS and ML, and the authors are A. Kilic, A. Uzun, R. Yildirim, and D. Eroglu. Similar to Section 3.3.3, this section uses COSMO-RS calculations for gas solubility calculations. On the other hand, a Python-based free library was used to estimate the molecular features.

3.3.6.1. Solubility and Property Calculations**.** The COSMOthermX program of COSMOlogic software with the C30_1602 version was used for solubility and property calculations of ILs. First, the solubility of oxygen molecule j, in IL i, was calculated using the *Ionic Liquids Screening* module for 36,260 ILs. The solvent solubility at infinite dilution, $C_{i,j}^{\infty}$ was

$$C_{i,j}^{\infty} = \frac{1}{\gamma_{i,j}^{\infty}}, \tag{3.27}$$

where $\gamma_{i,j}^{\infty}$ is the activity coefficient of i at infinite dilution in j and $C_{i,j}^{\infty}$ is the corresponding solubility value calculated in mol/mol.

Although these results can be used to compare oxygen solubilities qualitatively, they are orders of magnitude different from the experimental values reported in the literature. Better estimations can be computed using the *Gas Solubility* calculations in the *Solubility* module, where gas solubilities in ILs are iteratively calculated by varying the mole fraction of each compound j, x_j until the partial pressure of j, p_j

$$p_j = p_j^0 x_j \gamma_j, \tag{3.28}$$

reaches the given pressure value, where p_j^0 and γ_j are the pure compound partial pressure and activity coefficient.

For the TFSI anion, the oxygen solubilities were calculated using both methods, and a perfect linear correlation was obtained. Afterward, the results obtained from the *Ionic Liquid Screening* module were corrected using this correlation. However, this additional conversion was only performed for the oxygen solubility for experimental validation; only manual computing is possible in the *Gas Solubility* module, and it is a computationally more expensive method in terms of both time and computing power. Hence, the *Ionic Liquids Screening* module calculations were used in the rest of the study.

3.3.6.2. Feature Calculations and Selection. Python's Rdkit library of Molecular Operating Environment (MOE) was used for descriptor calculations [214,215]. Rdkit is an open-source cheminformatics library developed for calculating the materials descriptors using 10 million compounds encoded by the SMILES codes [216]. The SMILES codes were used to obtain 123 physicochemical properties (2-dimensional) and the fraction of 85 substructures (the number of benzene or -CO groups) of the ions; 208 variables were calculated for each anion and cation. The complete list of the descriptors can be found in Appendix G.

Although there are 416 features for a single IL, only the relevant features were used in the modeling. In this respect, the *Boruta algorithm,* a random forest-based algorithm showing feature relevance on the outcome*,* was used for the feature selection. Boruta adds the copy of each variable as a shadow variable and compares the Z-score (the difference between a value and the mean divided by the standard deviation, showing how close a value is to the sample mean) of the two-sided equality tests for the actual versus shuffled version of a feature. A feature is found to be unnecessary when the Z-score of the real feature is less than the shuffled version [217]. As a result of the Boruta analysis, 285 out of 416 features were selected for developing ML models.

3.3.6.3. Machine Learning Algorithms. The RF algorithm was used to predict the gas solubilities with the 285 as-selected descriptors. RF is an ensemble-type tree-based method in which training sets and the features used in the modeling are randomly selected in each tree. The outcomes of the random forest predictions are averages of the results obtained in each tree. Since the features and the training sets are randomly selected, the RF algorithm shows more robust results [218]. The model was performed using the "randomForest" library of the RStudio environment. The hyperparameters, ntree and nodesize, were optimized using grid search and 5-fold cross-validation, and the best model was identified using the validation error. The test dataset was determined first by randomly selecting 25% of the anions in an anion group with more than four members. Afterward, the remaining data was further divided into training and validation sets with the criteria of having nearly 20% of each anion group in the validation set. This process was repeated four times to get five training and validation sets where modeling was performed on training sets. The model was validated using validation sets via stratified sampling. The best model was determined

according to the average of the validation error. This was done to reduce the bias towards having identical anions in validation and test sets and to prevent overfitting. Finally, the model was tested on the test set to report the final model performance metrics: root mean square error (RMSE) showing the error between the predicted and the actual values and R-squared (R^2) giving the fraction of variability captured by the model.

4. RESULTS AND DISCUSSION

This chapter presents the results and discussion of the studies conducted in the thesis. First, the results of a bibliometric analysis done for the beyond LIB literature is presented. 24,523 papers obtained from the WOS database, regardless of their research topic, were analyzed with the help of text mining tools to see the major patterns and trends involving beyond LIB research. This part is modified from the review article by A. Kilic, B. Oral, D. Eroglu, and R. Yildirim [9]. A. Kilic conducted the bibliometric analysis presented next. Figure 4.1a presents the number of appearances of the various beyond LIBs in keyword search so far, while Figure 4.1b indicates the change of publications frequency with time so that any increasing (like in Na-ion) and decreasing (like in Li-air) trends could be seen; the less frequently studied systems are also provided in the figure insets. The specific elements explored in these publications are also shown in Figure 4.1c for the most commonly studied beyond LIB systems.

Figure 4.1a suggests that the most widely investigated chemistries are Li-S, Na-ion, Zn-air, Zn-ion, Li-air, and K-ion in decreasing order. Apart from Li-air batteries, they have all shown an increasing trend in the past ten years, and Na-ion and Li-S batteries seem to be at the heart of battery research. Zn-air batteries are the 3rd most commonly investigated battery system (surprisingly, they have become more popular than Li-air batteries) because of lower prices, safer operation, and higher availability of materials. Zn- and K-ion batteries have been studied significantly recently.

Since the anode, cathode, electrolyte, and separator are the four essential elements of a battery cell, any research is expected to focus on at least one of these (or the overall performance of the entire cell) because the optimization of materials and design parameters related to those elements are critical for the commercialization of these beyond LIBs. As is also apparent in Figure 4.1c, the presence of different battery technologies requires a diverse focus of attention because the challenges are different for each system due to the variances in their electrochemistry. For example, the most widely investigated cell section is the anode for Na-ion and K-ion cells, the cathode for Li-S and Zn-ion batteries, whereas it is the electrolyte for air batteries. This indicates that typically the development of the cathode is

critical in conversion chemistries, whereas the anode may be the performance-limiting factor in intercalation chemistries. The number of studies involving the electrolyte is also significant for all major battery types, yet it is the most widely used topic for air batteries. On the other hand, studies working on separators and modeling are very limited in the literature.

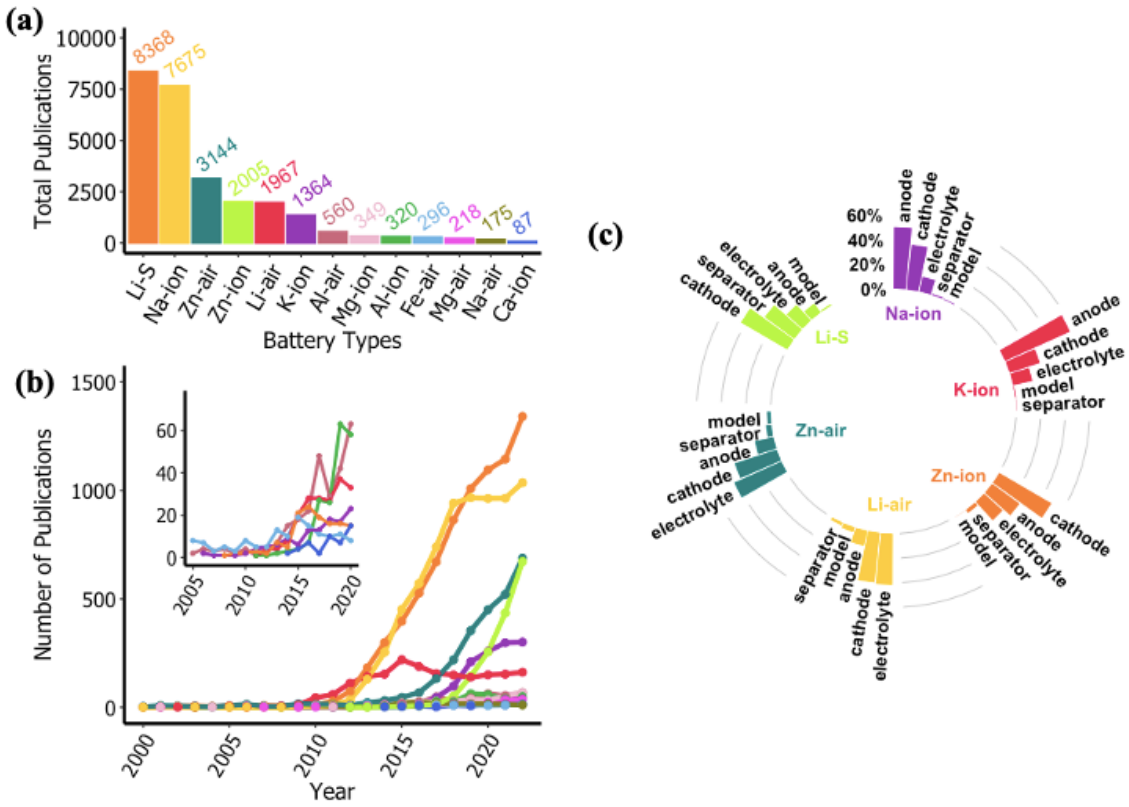

Figure 4.1. Total number of publications of each beyond LIBs (a), year vs. publication number (b), and research interests (c).

Next, the most frequently appearing 15 keywords for each beyond LIB using the WOS were identified without any filtering. The lists of the most frequently appearing keywords for the six most commonly studied LIB chemistries are presented in Figure 4.2a-Figure 4.2f. Apart from the typical battery-related words such as *anode* or *cathode*, the words *graphene* and *carbon* are also frequently encountered in text mining analysis. Since this result may be an indicator for the direction of research in material selection, the investigation was further extended to identify the secondary keywords associated with carbon and graphene by employing bigram analysis of text mining (Figure 4.2g-Figure 4.2h). Indeed, some information related to the most frequently used form of materials, treatment procedure, or

part of the cell involved emerged. For example, as clearly seen in Figure 4.2g, the *nanotube* is the most frequently associated keyword with carbon for almost all batteries (second most frequent after anode in K-ion batteries), while the other forms of carbon also appear in the list.

As expected, the *anode* appears at the top of the Na- and K-ion batteries list. The working mechanisms of Na- and K-ion batteries are very similar to that of LIBs; basically, reversible intercalation reactions of Na-ion (Na^+) and K-ion (K^+) take place in layered materials present in both the negative and positive electrodes [219]. Hence, the pore size and structure of electrode materials should be tailored to accommodate the change in the ion size. Consequently, the *anode* is at the top in Figure 4.2a and Figure 4.2b, while the *cathode* appears in the lower part of the list; the *electrolyte* does not even emerge in the top 12. *Carbon* and *graphene* are the most commonly used material-related words in Na-ion and K-ion batteries. In addition, two-word text mining results show that the carbon is mainly related to *nanotube* and *anode* keywords, and graphene is primarily followed by *oxide* for Na- and K-ion batteries, respectively. Indeed, carbon-based anodes, including graphene oxides, are frequently investigated in univalent metal-ion batteries [219–228]; there are also comprehensive reviews on polyanionic [229], layered [230], and alloyed materials [231] for the anodes of Na-ion batteries. The "oxide" keyword is among the top 15 keywords for Na-ion batteries, showing its popularity for these batteries. P2-Type [232,233], sodium [230], boron-doped [234] sodium, manganese [235], transition metal and P3/O3 [236] integrated layered oxides are investigated for Na-ion batteries. The electrolytes of the Na-ion and K-ion batteries are similar to those of LIBs, where generally, Na-salts or K-salts containing organic liquids are used. Hence, a similar methodology can be used to develop the electrolytes of Na- and K-ion batteries [237].

The working electrode of multivalent batteries should be designed to promote multi-ion redox reactions [238]. Hence, tailored cathodes are needed; *cathode* has appeared at the top of the keyword list for Zn-ion batteries (Figure 4.2c). Since the charge/size ratios of the multivalent ions are higher than the univalent ones, larger solvation shells occur for the multivalent metals in the bulk electrolyte, making these ions more stable. Hence, slow de-solvation kinetics at the electrolyte-electrode interface and the formation of passivation layers are major hurdles in these batteries. Plus, the electrochemical stability of the

electrolytes is low; hence, it is understandable that the new *electrolyte* compositions for multivalent chemistries are also investigated extensively [239]. Aqueous electrolytes (as emerged as *aqueous* and *electrolyte* keywords) were investigated and extensively reviewed for Zn-ion batteries [240–243]. *The oxide* keyword is more frequently used than the *carbon* keyword, and graphene is not listed for Zn-ion batteries; hence, it may represent vanadium and manganese oxides, which are the most common oxide types for these battery systems [244–248]. *Intercalation* cathode materials (among the top 15 keywords) such as *polyanions* and *carbon-based materials* are also studied as working electrodes in the literature [249,250].

The use of air instead of oxygen is the ultimate aim of metal-air batteries, yet, most of the works in the literature use pure oxygen to prevent side reactions due to the humidity and CO_2 in the air. Even with oxygen, the efficiency, stability, and energy density are limited mainly due to poor ORRs [48]. The presence of the *catalyst*, *electrocatalyst,* and *reduction* keywords for Li- and Zn- air (Figure 4.2d and Figure 4.2e) batteries indicates the significance of this problem. The positive electrode of metal-oxygen batteries is mainly porous carbon substrates where the gaseous reactant is distributed. From kinetic and mass transport points of view, it is essential to distribute oxygen homogenously over the cathode surface [251,252]. In addition, catalyst materials are added to the positive electrodes to favor the ORR kinetics. Oxides [253,254] and carbon-based materials [255,256], including graphene, are among the common electrocatalysts. Although electrolytes are the key elements of all kinds of batteries, they should be chosen with extra care for metal-oxygen batteries because the cathode side is open to a gaseous environment [257-259]. The electrolyte should have low vapor pressure to prevent its depletion, while the salts and the solvents making the electrolyte should be electrochemically stable toward the gaseous chemicals. Plus, to promote fast kinetics, these electrolytes should have high oxygen solubility and diffusivity. Similar to other beyond Li-ion battery chemistries, aqueous, non-aqueous, hybrid, and solid-state electrolytes are also possible for metal-oxygen batteries [260]. Aqueous electrolytes have the advantage of safety, low cost, and high ionic conductivity compared to non-aqueous electrolytes [261]. Hence, their adaptation to metal-air batteries is desired [262–264].

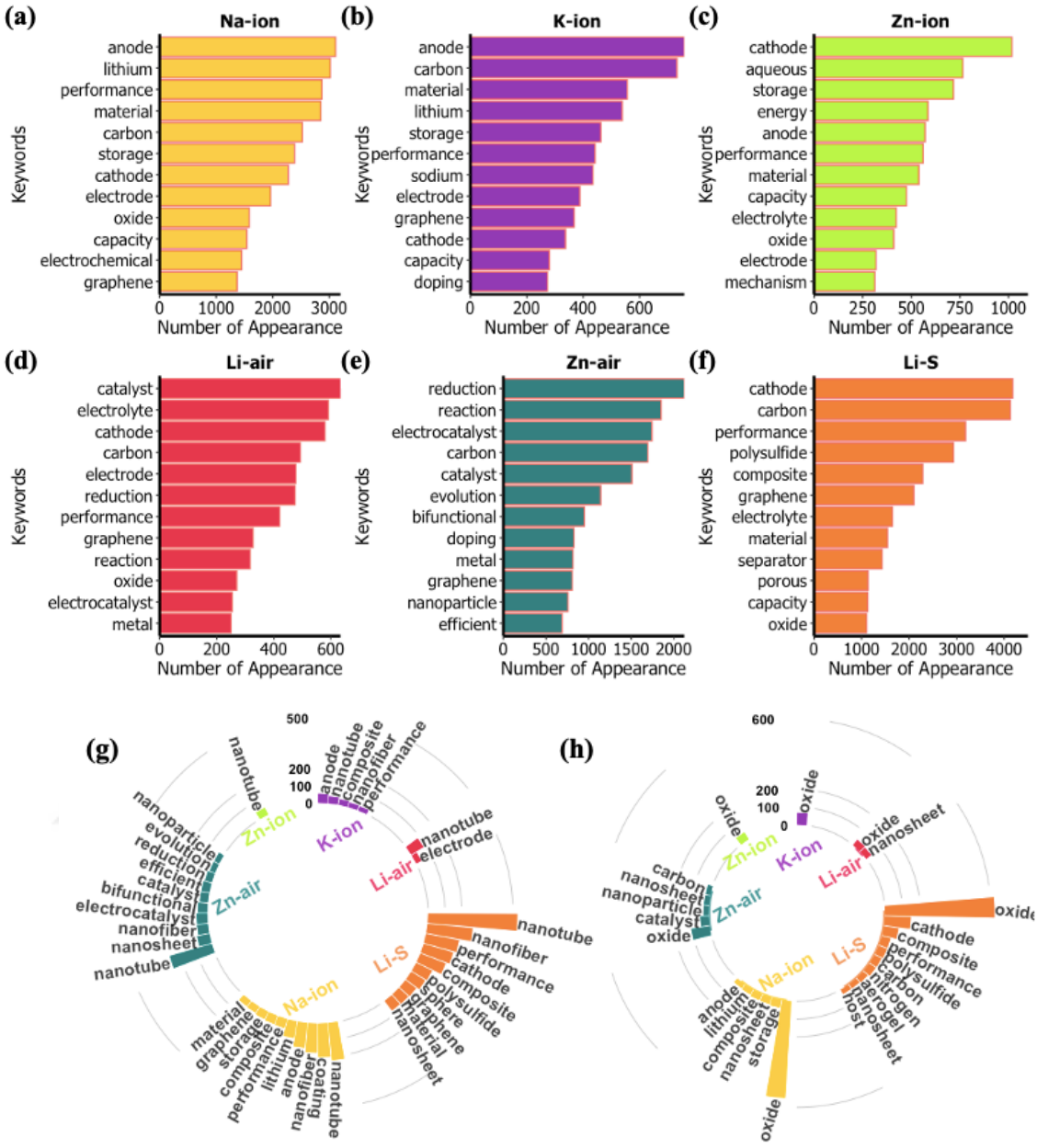

Figure 4.2. Keyword analysis for Na-ion (a), K-ion (b), Zn-ion (c), Li-air (d), Zn-air (e), and Li-S (f) batteries, carbon (g) and graphene (h) bigrams.

The PSM is one of the main problems of the Li-S batteries that many researchers try to decrease the effect of it by using specialized materials in terms of pore size or structure inside the cathode; the encapsulation of sulfur in specialized carbonous nanostructures in the cathode aims to improve the battery performance by trapping the PSs (physically or chemically), increasing the electronic conductivity and accommodating the volume change due to the conversion of sulfur into Li_2S. This is why the keywords *cathode, carbon, PS,* and *composite* are at the top of the keyword list for Li-S batteries (Figure 4.2f). *Graphene* is also

widely utilized in sulfur cathodes with the promise of entrapping PSs and increasing electronic conductivity by providing large surface area and suitable pore structures; the appearance of composites, nitrogen doping, aerogels, and nanosheets in Figure 4.2h indicate various parts of research involving the use of graphene for Li-S batteries. The selection and design of electrolytes is another commonly researched topic on Li-S batteries. The ideal electrolyte should have moderate and low solubility to long and short-order PSs, respectively, while showing excellent Li^+ conductivity [265]. Solid-state electrolytes, carbonate-based organic electrolytes, and fluorinated solvents are among the new alternatives to conventional ether-based electrolytes in Li-S batteries [266–268].

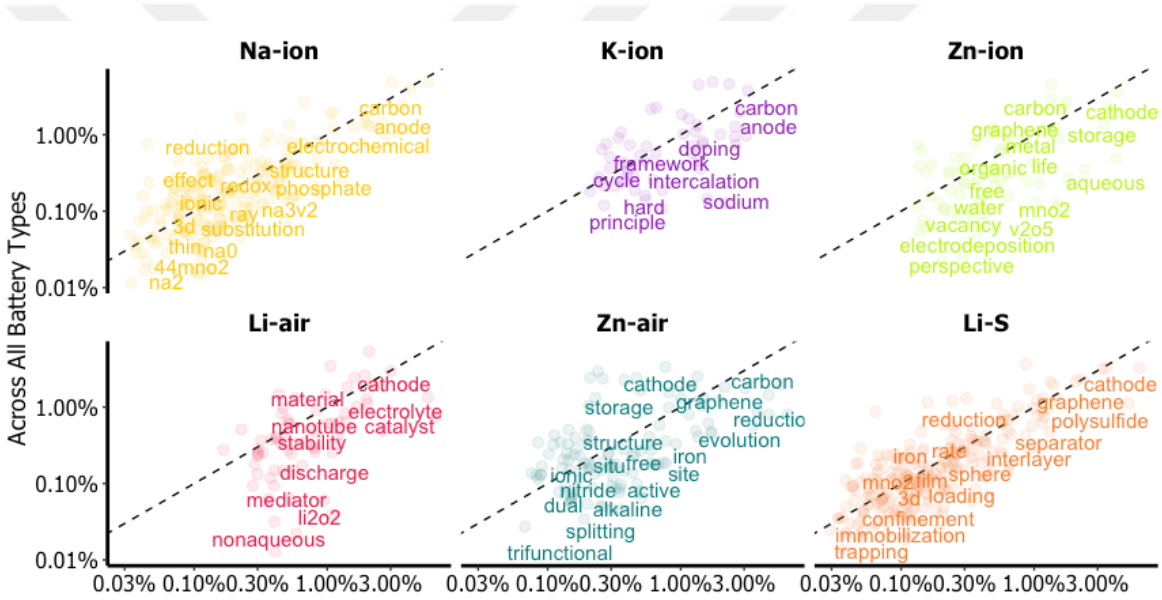

Figure 4.3. Relative frequency of keywords in papers related to specific battery types versus entire beyond LIBs.

To conclude this part, it can be stated that beyond LIBs mostly emerged as a response to the shortcomings of LIBs, such as scarcity of materials, performance problems, and safety concerns; some new solutions lead to new battery designs, while some seem to be relevant for more than one battery type. In principle, a variety of features, performance measures, and challenges among the beyond LIBs may require different approaches in ML applications for each battery type. This is a more serious issue in practice; different research groups focusing on different battery types create different data build up through the years, making ML analysis more difficult as it is mainly based on a statistical analysis of a uniform dataset. Consequently, the analysis and understanding of data structure seem to be especially

important for ML applications in beyond LIBs. To demonstrate the diversity of concepts and focuses of attention in beyond LIBs, we performed a keyword search in literature and analyzed them to identify whether the keywords were repeated more frequently in the publications related to specific battery types by adapting a method used to analyze the characters in a novel series, in Figure 4.3 [200].

In Figure 4.3, the percent of specific keywords in all keywords related to a specific beyond LIB technology is given in the x-axis, while the percent of the same keyword in all keywords of entire beyond LIB literature is in the y-axis in the logarithmic scale. Consequently, the keywords with similar frequency of appearance in all battery types appear near the x=y line, as the fraction in a specific battery type will be the same as the fraction in the entire beyond LIB literature. A keyword appearing more frequently in papers related to a specific battery type will have a higher fraction for that type than the entire beyond LIB literature and appear *below* the x=y line because x will be higher than y. On the other hand, keywords appearing less frequently for that battery type will be above the x=y line because x will be smaller than y. For example, *carbon* is one of the most widely used keywords across all battery types and has a similar frequency in Na-ion batteries; hence it is on the top of the x=y axis. However, *reduction* is less common in Na-ion batteries (it is on the upper side of the x=y line), whereas the *$44MnO_2$* keyword is more frequently used in Na-ion batteries than the other battery types (it is on the lower side of the line). Similarly, *polysulfide* is one of the most frequently found keywords in Li-S batteries; it is less common in the rest of the battery types. Differences in the keywords and their frequency of appearance in literature for a specific battery type are expected because different battery technologies require different materials and processes. However, the variance seems to be more than that; some keywords in Figure 4.3 do not seem to be directly associated with the materials or processes used; they are rather related to the performance and problems, indicating that the focus of attention and even research direction may also be deviating in different batteries (probably due to the differences in the problems encountered). The distance of a keyword from the origin indicates the frequency of that keyword in a specific battery or entire LIB literature. Although this additional information may enrich the analysis, it should be treated cautiously; some keywords may appear more frequently not because they are more important but because they are related to a more frequently studied battery type.

Table 4.1. The summary of the methods used in the sections in Results and Discussion.

		Experiments	System-Level Performance Model	Machine Learning	Ref.
Li-S	4.1.1.	-	-	+	[43]
	4.1.2.	-	+	+	[44]
	4.1.3.	+	-	+	in preperation
	4.1.4.	+	-	-	[45]
	4.1.5.	+	+	-	[46,47]
$Li-O_2$	4.2.1.	-	-	+	[48]
	4.2.2.	-	-	+	in preperation

Among the beyond LIB systems discussed above, the focus is on the development of Li-S and $Li-O_2$ batteries in this thesis, and the results are represented in two main sections: Li-S batteries and $Li-O_2$ batteries. The summary of the methods used in the subsequent sections is given in Table 4.1.

4.1. Li-S Battery Studies

This section includes five different works for the development of Li-S batteries. In Section 4.1.1., ML techniques were used for the assessment of critical materials and cell design factors for high-performance Li-S batteries using the literature data. In the subsequent section, ML tools were applied to the literature data for Li-S batteries with IL electrolytes to determine the critical factors and materials to increase Li-S cell- and system-level performances, specifically for IL electrolyte-containing cells. In the next section, the relation between the PS solubility in the IL, the properties of the IL and battery performance was examined using experimentation, COSMO-RS calculations, and ML techniques to further study IL electrolytes. Next, the effect of encapsulation material properties on the electrochemical performance was evaluated for MOF materials. Likewise, the impact of encapsulated cathodes on the system-level metrics of Li-S battery was reported for the V- and Co-doped ketjen black sulfur composite cathode in the following section.

4.1.1. Assessment of Critical Materials and Cell Design Factors for High Performance Lithium-Sulfur Batteries using Machine Learning

This section is modified from the original research paper published in the Chemical Engineering Journal by authors A. Kilic, Dr. Ç. Odabaşı, Prof. R. Yildirim, and Prof. D. Eroglu [43]. The data gathering, preparation, and results analysis were performed in the scope of this thesis by A. Kilic, whereas the ARM analysis was performed by Ç. Odabaşı.

In Li-S batteries, as a consequence of the highly complex reaction and degradation mechanisms, materials and cell design have a critical impact on the performance. Subsequently, Li-S batteries receive significant research attention. In this section, a comprehensive analysis on the effect of key factors on the battery performance, namely the peak discharge capacity and the cycle life, is conducted using ML. Data for 1660 cells from 353 papers in the literature is collected and analyzed via association rule mining.

4.1.1.1. Pre-Analysis of Data. Because of the complexity of reaction and degradation mechanisms in a Li-S cell, the performance is highly sensitive to a variety of factors as shown in Figure 4.4. In this section, we pre-analyzed the impact of critical variables on the Li-S battery performance to understand the structure of the database and the behavior of the major variables better before starting a more detailed ML analysis.

In Li-S batteries, the discharge current density or the C-rate, which is the current density normalized against the battery capacity, is a critical factor as it defines the battery performance through the cell area-specific impedance and the Li anode surface morphology [65]. Cells have different capacities at different C-rates; typically lower discharge capacities are attained at higher current densities. In Figure 4.5, the comparison of the distribution of the overall data with the data at a specific C-rate (i.e. 0.1C) is presented. It can be seen in the figure that both datasets have the normal distribution and the mean of the overall data is very similar to the mean of the data at 0.1C rate; considering this and the relatively high number of cases in the overall dataset; hence the overall dataset was used in the analysis to have statistically more reliable results.

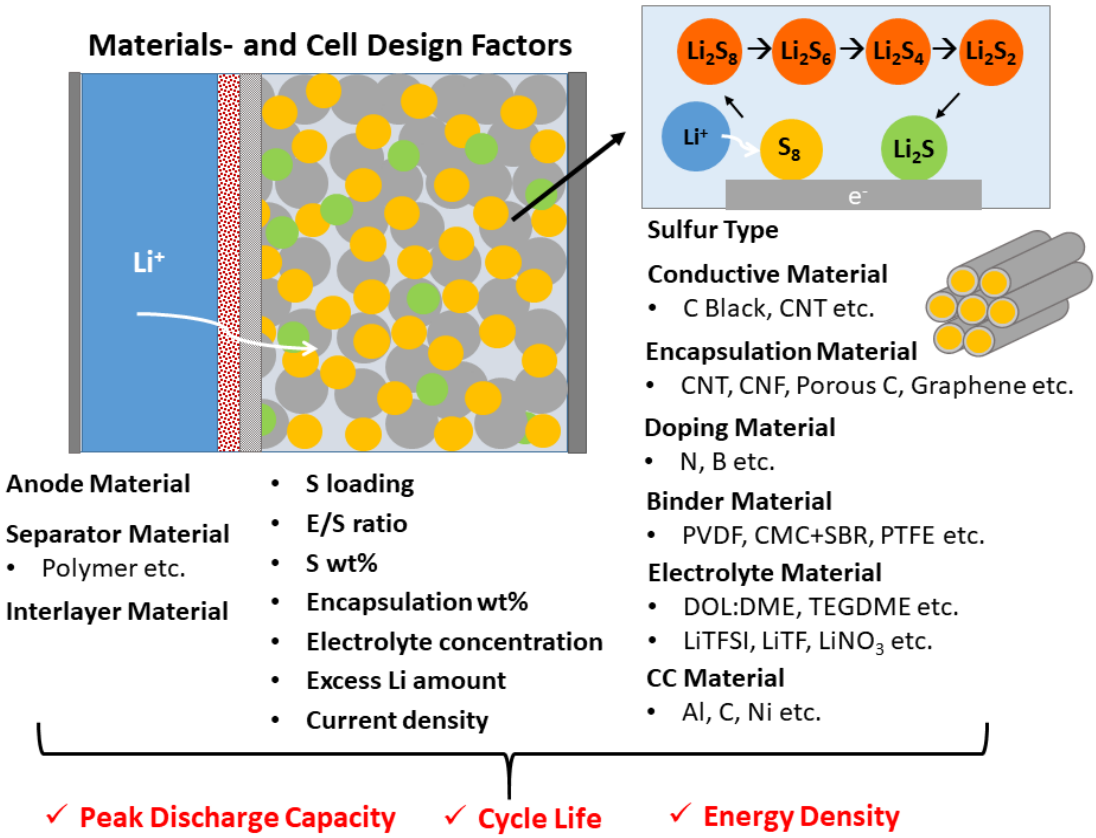

Figure 4.4. Schematic of the materials and cell design factors in a Li-S cell.

Li metal is one of the best candidates as the anode material for beyond LIBs due to its lowest possible molecular weight of 6.94 g/mol and highest possible standard oxidation potential of 3.040 V (vs H_2/H^+). Consequently, Li metal has a very high specific capacity of 3860 mAh/g [10]. However, both the high reactivity of the Li metal with the electrolyte and the dendrite formation in the anode as a result of the changes in surface morphology with cycling prevent achieving the theoretical capacities in the cell. In the literature, there are efforts to solve these problems by forming a stable Li and electrolyte interface by utilizing different electrolyte types, salts and additives. Introducing an interlayer to the anode such as Al_2O_3 layer or impurities as hard carbon or carbon black to strengthen the Li metal are some of the other approaches reported in the literature [269–271]. Since the anode material plays a key role in the battery performance, it is considered a variable in the analysis.

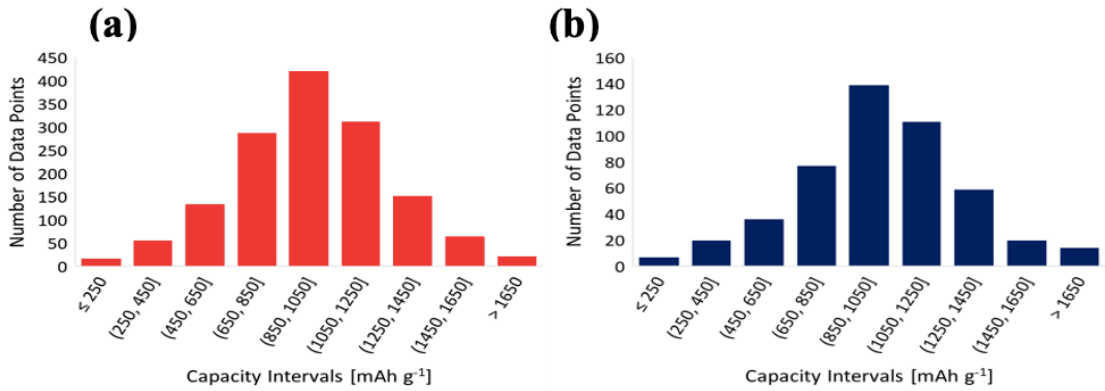

Figure 4.5. Distribution of PDCs for liquid electrolyte cells: entire dataset (average of PDCs = 966 mAh/g) (a), data subset at 0.1C (average of PDCs = 1004 mAh/g) (b).

Excess Li amount in the anode, or negative-to-positive capacity (N/P) ratio, in other words, is also an important design variable. Li-S cells typically contain excess amount of Li in order to prevent the Li depletion in the cell as a result of the side reaction between the anode and the electrolyte. Subsequently, increasing the amount of excess Li in the cell enhances the cycling performance [32], [272]. Even though the excess Li amount is a key variable, the majority of the studies in the literature do not report the anode thickness in the cell. Consequently, its effect on the battery performance is not considered in this section as well.

Elemental sulfur, as the active material in the Li-S cathode, has the advantages of high specific capacity, natural abundance, non-toxicity and low cost [273,274]. During the discharge of a Li-S cell, the transition from the solid-state sulfur to the soluble high-order PSs takes place in the high voltage plateau corresponding to a theoretical capacity of 418 mAh/g [275]. The discharge proceeds with the reduction of the PSs in the low voltage plateau till the formation of the end solid product Li_2S. The majority of the studies in the literature use solid-state sulfur as the cathode active material because of the aforementioned reasons. However, the low electronic conductivity of the sulfur slows down the kinetics and thus limits the active material utilization significantly in the cathode [276,277]. Therefore, studies investigating the soluble PSs and other chemicals, such as $CoMoS_{3.13}$, as the sulfur source are also present in the current literature [278–280]. Consequently, sulfur type is also included in this analysis as a design variable.

As a consequence of the insulating nature of sulfur and Li_2S, Li-S cathodes typically require the addition of a significant amount of conductive material. Thus, the type of the conductive material in the cathode is a vital factor for defining the reaction kinetics through the electronic conductivity and the electrochemically active surface area [13], [281,282] . In this section, conductive materials are defined as the ones, which are mixed with the active material directly without any further treatment. As can be seen in Figure 4.6a, most of the studies in the literature with liquid electrolyte, use carbon black as the conductive material in the Li-S cathode (74.6 %), whereas 14.7 % does not use any conductive material; however the majority of the studies that do not use additional conductive material already have conductive encapsulated S cathodes.

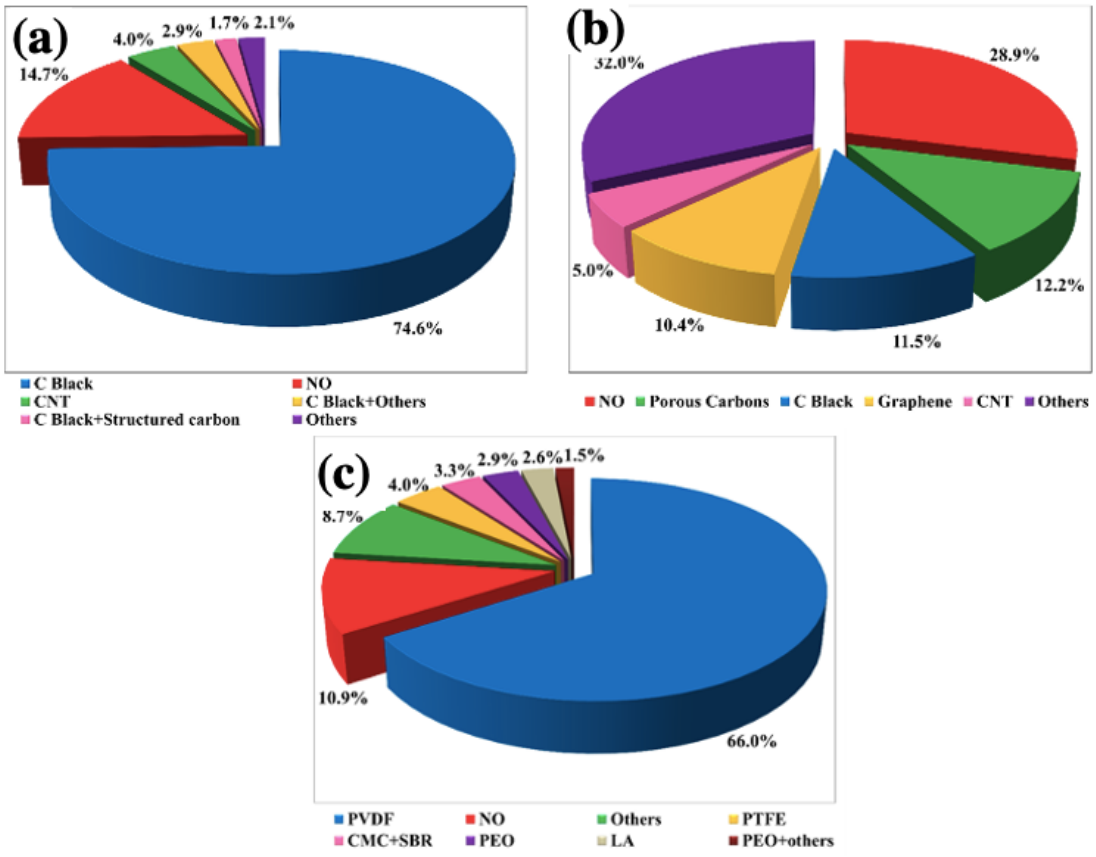

Figure 4.6. Breakdown of conductive material type (a), encapsulation material type (b), and binder type (c) in dataset for cells with liquid electrolyte.

Encapsulation strategy in sulfur cathodes has gained significant attention in the last decade [283,284]. It is a highly successful strategy in preventing the PS shuttle mechanism

by trapping the soluble PSs, enhancing the electronic conductivity of the sulfur cathode and accommodating the volume change in the cathode. Encapsulation strategy improves the sulfur conductive interface and puts extra barriers for the migration of the PSs [285–289]. Indeed, encapsulation cathode materials are among the most widely investigated research areas in the Li-S battery field. Cleaver et al. [90] report in their review that 64% of the research articles in the field are on developing novel materials design for the cathode; consequently, the encapsulation cathode material type is a critical variable.

The conductive materials are incorporated into the cathode either by physically mixing with the active material or by being treated thermally or chemically in various encapsulation methods. In this work, cathodes that are prepared by any treatment of the conductive materials with the sulfur other than physical mixing are defined as encapsulated cathodes and analyzed in this part. As can be seen in Figure 4.6b, only 28.9 % of the cells with liquid electrolyte do not use any encapsulation material in the cathode. The most commonly used encapsulation materials are porous carbons (the details of the alternative materials are given in the Appendix A), carbon black, graphene and carbon nanotubes, while 32.0 % of the cases in the database have used different encapsulation materials. Binder type impacts the performance of the Li-S batteries; it is not only responsible for the contact between the sulfur, cathode matrix and current collectors, but it is also important to prevent the structural deformation due to volume change and active materials dissolution. In addition, an ideal binder should also decrease the PS migration by interacting with the soluble PSs [33].

As can be seen in Figure 4.6c, 89.1 % of the data points have used binder in their cathodes; the most common binder type is PVDF, with 66.0 % in the dataset. PVDF is typically preferred due to its high stability and adhesion properties. However, PVDF needs to be dissolved in NMP solvent, which is toxic and expensive [290]. Therefore, there are some efforts to replace PVDF as the binder in the sulfur cathode; PEO, PTFE, LA, and CBC+SBR are some of the other typical binders used in the literature to have more environmentally friendly and cost-effective batteries. It is apparent in Figure 4.6c that 10.9 % of our database does not use any kind of binder. It should be mentioned that the majority of the binder-free cells again contain encapsulated cathodes.

15-20 wt.% of the total mass of a Li-S cell stems from the current collectors, which account for 10-15% of the total cost. Although Al foil is the most widely used cathode current collector, it is nonporous, and prone to oxidation at high voltages. The electrical contact between the corroded Al foil and sulfur is significantly low and that increases the cell resistance considerably. In this context, developing an appropriate current collector is also important for high cyclability and low cost [291]. Recently, 3-D current collectors have gained significance in Li-S batteries to ensure higher sulfur loadings and areal capacities in the cathode [292–295]. Graphene hierarchical networks, free-standing carbon nanofiber and carbon nanotube papers, and Ni foams are some examples of the newly developed 3-D current collectors in the Li-S battery literature [293–295]. These 3-D structures enable the use of thicker cathodes and thus higher areal capacities in the cell due to a superior electronic conductivity and electrode integration. In addition to favoring much higher sulfur loadings in the cell, these 3-D current collectors are also effective in accommodating the volume change in the cathode. As a result, the positive current collector type is considered as a design variable in the analysis in the following sections. Since there is no emphasis on the development of novel current collectors in the anode, the negative current collector type is not taken into account.

In a Li-S cell, the separator plays a key role in preventing the PS shuttle by blocking the transfer of the PSs to the anode while ensuring high Li-ion conductivity. In addition, the separator in a Li-S cell should suppress the Li dendrite growth to avert any short circuit in the cell that may lead to thermal runaway. Subsequently, the separator type has a high impact on both the cycle life and the capacity retention of a Li-S battery. The most commonly used separators in the literature are polymer-based [296]. However, studies focusing on the improvement of the existing separators by coatings or the development of novel separators are also common in the recent literature [297–299]. Consequently, we treated the separator type as a variable in our analysis.

Interlayers, either between the anode and the separator or between the separator and the cathode, have gained significant attention in recent years in Li-S battery research. These multi-functional interlayer systems are typically carbon- or polymer-based. The interlayer in the cell can block the diffusion of the PSs preventing the loss of the active material to the anode and protect the Li metal. In addition, the interlayer improves the electronic

conductivity and ensures high contact during cycling, which may be otherwise challenging due to the volume change in the cathode. As a result, significantly enhanced electrochemical performances are commonly reported for Li-S cells containing an interlayer [300–302]. Therefore, the presence of an interlayer is considered in this section as a variable.

S loading in the cell, which is controlled by the cathode thickness and the sulfur weight fraction in the cathode, is another key design parameter that determines the areal specific capacity of the cell. As the active material loading in the cathode increases, the energy density of the cell increases remarkably [88]. Despite that, due to the transport limitations in thicker electrodes, the discharge capacity and cycle life of the cell could be affected inversely. Previous studies typically report cathodes with S loadings of 1-3 mg/cm^2 for high discharge capacity Li-S cells [303,304]. However, in order to surpass the commercial LIBs, which have active material loadings of 15-20 mg/cm^2, Li-S batteries should be designed with much higher S loadings. For instance, in their techno-economic analysis, Eroglu et al. conclude that in order to have high energy density Li-S batteries, the S loading in the cathode should be 7 mg/cm^2 at least [65]. Similarly, Chung et al. recommend S loadings higher than 6.5 mg/cm^2 for enhanced system-level performance [6]. The average of sulfur loadings in the cells with liquid electrolytes is 2.4 mg/cm^2 in the database used in this section.

As previously discussed, Li-S cells typically require a high amount of conductive material, mostly carbon, because of the low electronic conductivity of the sulfur. Increasing the carbon ratio enhances the cathode kinetics significantly through increasing the electronic conductivity and the electrochemically active surface area. Consequently, utilization of the active material and thus the discharge capacity of the cell increase considerably. However, after a threshold value, the specific capacity and cell voltage are very similar for cathodes with different carbon wt%, mainly because the kinetic limitations are not dominant anymore. On the other hand, increasing carbon wt% intrinsically means decreasing the S wt% or active material loading in the cathode. Based on the discussion in the previous section, as the S wt% in the cathode is reduced, the energy density of the Li-S battery decreases in a great manner. In fact, S wt% higher than 70wt% are typically suggested for high energy density Li-S batteries, [81], [275], [305,306]. As a consequence of the aforementioned trade-off between the discharge capacity and the energy density, S wt% is one of the most important design parameters in a Li-S cell. In this analysis, S wt%, conductive material wt%, and

encapsulation material wt% are taken as variables, whereas binder wt% is not included as an independent variable since the total of the S, conductive, and encapsulation materials and binder weight percentages should sum up to 100%. In the literature, some papers using encapsulated cathodes gave the targeted S wt% while some others provided the achieved S wt% (typically measured by TGA after the encapsulation procedure); there are also papers that reported both. Since only one of these two related variables should be used in the analyses, a regression model was constructed by Ç. Odabaşı to correlate targeted and achieved S wt% using the data from the papers providing both, and computed the achieved S wt% for those provided only the targeted values; then we used achieved S wt% as the variable in our analysis. The details of regression model used are given in Appendix A; since S wt.% was also categorized with a 25% interval, the model fitness was quite satisfactory for our purpose.

As previously discussed, the encapsulation of sulfur in Li-S cathodes is highly promising in terms of achieving high capacities and cycle lives. The properties of the conductive host material, such as the pore size, pore shape, and architecture, can be tailored successfully with the encapsulation strategy. Likewise, the intrinsic properties of the conductive host material, such as the electronic conductivity, surface chemistry, and polarization, can be tuned by doping with heteroatoms as N, B, P. Nitrogen doping is the most commonly investigated doping type by far in the literature. Previous studies discuss that doping of the conductive host material in encapsulated cathodes enhances the electrochemical performance of a Li-S battery, mainly through an improvement in the electronic conductivity and S activity [307–310]. The relationship between doping and the improvement in the electronic conductivity can be explained by a modification in the electronic structure of the carbon host; heteroatoms offer extra free electrons for the conduction band and thus enhance the electronic conductivity of the carbon framework [310]. Recently, doping with metals as Co, Ni, and metal oxides as TiO_2, MnO_2 has also gained significance in Li-S batteries [311]. These metal and metal oxide dopants improve the cycle life remarkably by suppressing the PSM in the cell; this may be explained by the immobilization of the PSs due to their strong interaction with the dopants. These dopants may also enhance the battery performance by accelerating the redox reactions in the cathode. As a result, the doping material type is taken into consideration in the analysis.

The complicated sulfur kinetics in the cathode involves multiple redox reactions of PS intermediates that are soluble in the electrolyte. The transfer of these PSs to the anode is the main reason of the PSM, as previously mentioned. Consequently, the electrolyte has a major role in the battery performance because of its impact not only on the reaction kinetics but also on the PS shuttle rate and parasitic reactions in the anode. For these reasons, the recent literature focuses on the development of novel electrolytes that have sufficient Li^+ conductivity but can suppress the mobility of the PSs and lead to better Coulombic efficiency in the cycling of the Li metal. Novel organic liquid electrolytes, ionic liquids and solvent-in-salt electrolytes are some examples of the recent research trends in the electrolyte development in Li-S batteries [19], [273]. In the literature, the most typical electrolyte solvent used in a Li-S cell is a mixture of DOL and DME. In this mixture, DME is responsible for the high PS solubility and fast PS reaction kinetics whereas DME accounts for forming a stable solid electrolyte interface on the Li anode surface [19]. However, because of the high solubility and mobility of the PSs in this electrolyte, new electrolyte solvents that can result in better Li-S batteries with slow PS shuttle rate are investigated in the literature [312].

In the selection of the Li salt in a Li-S cell, the most critical concern is the chemical compatibility of the salt with the PSs. The majority of the studies in the literature report the use of LiTFSI as the Li salt in the electrolyte, mainly due to its good thermal stability and compatibility. However, there are several studies in the literature investigating the impact of other salt types on the Li-S battery performance in order to enhance the desired electrolyte properties [19], [31], [313]. In this section, both the solvent and the salt type were considered as design variables. On the other hand, the influence of the salt concentration on the battery performance is not examined since the concentrations used in the literature do not vary significantly, except in solvent-in-salt electrolytes.

Even though the majority of the literature investigates Li-S cells with a liquid electrolyte, solid-state Li-S batteries as well as Li-S cells with catholyte have been reported as promising in the recent literature [314]. Therefore, the electrolyte type (i.e. liquid, catholyte, solid) is also taken into account in the analysis. However, since the design parameters are considerably different in these batteries, they are treated and discussed separately.

The major additive used in Li-S cells is $LiNO_3$, which is commonly added into the electrolyte in order to form a passivating surface film on the anode surface. Previous studies suggest that the addition of $LiNO_3$ in the electrolyte enhances the Coulombic efficiency and cycling performance of the battery in a significant manner due to passivating the anode surface and preventing the PSM [73], [315]. The concentration of the additive is also critical [316,317]. In this analysis, the impact of the presence of an additive and its concentration on the performance is also studied.

The E/S ratio is one of the most critical design parameters in a Li-S cell as it influences both the electrochemical performance and the system-level energy density of the battery significantly. The complex reaction and PS shuttle mechanisms in the cathode are highly sensitive to the E/S ratio through the PS concentration on the electrode surface, which is directly determined by the electrolyte amount in the cell [81], [88]. Previous studies in the literature clearly show that increasing the E/S ratio enhances the discharge capacity considerably by increasing the utilization of the active material. In electrolyte-starved cathodes, high PS concentrations lead to an elevation in the electrolyte viscosity, which may restrict the diffusion of Li^+ and PS. In addition, electrochemical reactions may be inhibited at low E/S ratios due to the solubility limit of the PSs. These all lead to a drastic decrease in the discharge capacity in electrolyte-starved cells. On the other hand, a considerable excess of electrolyte in the cell intensifies the PSM and thus reduces the capacity retention significantly [318–322]. When the impact of the E/S ratio is investigated in terms of the system-level performance, all previous materials-to-system analyses conclude that energy density decreases significantly with increasing electrolyte amount in the cell; E/S ratios lower than 5 mL/g is required for high energy density Li-S batteries [6], [89]. To sum up, as a consequence of all these competing forces, the E/S ratio has a key role in the Li-S battery performance and hence is studied in this section as another variable.

4.1.1.2. Analysis of Peak Discharge Capacity for the Cells with Liquid Electrolyte. First, Entire Liquid Electrolyte Dataset: In this part, ARM analysis were presented on the dataset containing cells with liquid electrolyte achieving PDCs equal to or higher than 1000 mAh/g to determine the important factors for obtaining this capacity. In Table 4.2, ARM results for this analysis are given; the factors are ranked according to the lift values. As discussed in the Material and Methods section, the lift shows the probability of a factor appearing in a

cell with high PDC relative to the total data in the dataset; the lift will be greater than one if a factor appears in cells with high PDCs more frequently compared to the entire dataset. Hence, the higher lift values can be used as an indicator for the positive effect of that particular factor. However, lift is not the only criteria to show the significance of a factor. Support and confidence are the other two statistical properties that should be taken into account, as discussed before. The total number of data points obeying the rules stated in each row in Table 4.2 gives an idea of the statistical significance of the rule in a simpler term, even though that information already exists in support. Since larger counts show more reliable rules, the rows were color-coded depending on the number of counts, and only the rules that were obeyed by at least five cases were discussed. Moreover, if all entries are coming from the same article, the count was marked with "*" to warn the reader.

The use of carbon as the current collector can be used as an example to better understand the meaning of support, confidence, and lift values, as well as the interpretation of Table 4.2. The support, confidence, and lift values for this entry are 0.018, 0.040, and 1.90, respectively, with a count of 27. This indicates that there are 27 cells using carbon as the current collector and achieving PDCs equal to or higher than 1000 mAh/g. Considering that we have 1463 cells in the database, the support is 27/1463=0.018. Because there are 669 cells with PDCs equal to or higher than 1000 mAh/g in the entire database, the confidence is 27/669=0.040. Since a total of 31 cells uses carbon as the current collector (27 of them has high PDC), the lift is (27/669)/(31/1463)=1.90 meaning that the fraction of the cells using carbon as the current collector in those with PDCs equal to or higher than 1000 mAh/g is 1.90 times higher than the fraction of the cells with carbon current collector in the entire database. We can conclude from this result that the use of carbon as a current collector is beneficial.

As can be seen in Table 4.2, most of the high lift entries with statistically sufficient number of counts are associated with the use of encapsulation materials in the cathode. The highest lifts are obtained with the specialized encapsulation materials, i.e. structured carbons such as GO and porous carbon and polymers such as polyaniline. According to the table, the cells utilizing two different types of encapsulation materials together perform better compared to a single encapsulation material. Using graphene oxide with porous carbons, carbon nanotubes with special chemistries or hollow structured carbons lead to higher lift

values. This clearly shows that the development of structured carbons and special chemistries as encapsulation materials in the cathode is key to get higher specific capacities.

Table 4.2. Association rule mining results for cells with liquid electrolyte having PDCs of 1000 mAh/g and above.

RHS	Support	Confidence	Lift	Count
{Encapsulation=Graphene+Hollow Structured Carbon}	0.00068	0.00149	2.19	1
{Encapsulation=Graphene+Porous Carbons+Others}	0.00068	0.00149	2.19	1
{Encapsulation=GO+Hollow Structured Carbon}	0.00068	0.00149	2.19	1
{Encapsulation=Porous Carbons+Others}	0.00137	0.00299	2.19	2
{Encapsulation=Hollow Structured Carbon+Polypyrrole}	0.00205	0.00448	2.19	3
{Encapsulation=C Black+Porous Carbons}	0.00273	0.00598	2.19	4
{Encapsulation=GO+Porous Carbons}	0.00342	0.00747	2.19	5
{Encapsulation=Porous Carbons+PANI}	0.00478	0.01046	2.19	7*
{Encapsulation=C Black+PANI}	0.00547	0.01196	2.19	8*
{Current_Collector=Carbon}	0.01846	0.04036	1.90	27
{Electrolyte_Additive=Others}	0.00615	0.01345	1.79	9
{Encapsulation=Hollow Structured Carbon+Others}	0.00273	0.00598	1.75	4
{Electrolyte_Salt=NO}	0.00273	0.00598	1.75	4
{Seperator=Others}	0.00205	0.00448	1.64	3
{Encapsulation=CNT+Others}	0.01572	0.03438	1.62	23
{Doping=Nitrogen}	0.04033	0.08819	1.54	59
{E_S_Ratio=5--10}	0.04033	0.08819	1.54	59
{Encapsulation=Hollow Structured Carbon}	0.00957	0.02093	1.53	14
{Encapsulation=C Black+Others}	0.00137	0.00299	1.46	2
{Encapsulation=Other Carbons+Others}	0.00684	0.01495	1.46	10
{S_Type=Sulfur+Others}	0.00684	0.01495	1.46	10
{Electrolyte_Salt=Others}	0.00820	0.01794	1.46	12
{C_Type=C Black+Structured carbon}	0.01094	0.02392	1.40	16
{E_S_Ratio=0--5}	0.01162	0.02541	1.38	17
{Binder_Type=PTFE}	0.02529	0.03453	1.37	37
{Encapsulation=CNF}	0.01162	0.03576	1.33	17
{Binder_Type=LA}	0.01572	0.03699	1.32	23
{Binder_Type=CMC+SBR}	0.01982	0.03822	1.32	29
{Encapsulation=Structured Carbons}	0.00410	0.03945	1.31	6
{Encapsulation=CNF+Others}	0.00410	0.04068	1.31	6
{Interlayer=Yes}	0.10663	0.04191	1.30	156
{Binder_Type=PEO+Others}	0.00889	0.04314	1.29	13
{Electrolyte_Solvent=TEGDME}	0.01435	0.04437	1.28	21
{S_wt=0--25}	0.01572	0.04560	1.26	23
{Binder_Type=PVDF+others}	0.00273	0.00598	1.25	4
{Encapsulation=Graphene+Others}	0.01435	0.03139	1.24	21
{Electrolyte_Solvent=Others}	0.02051	0.04484	1.24	30
{Doping=Nitrogen+Others}	0.00615	0.01345	1.23	9

The table also reports high lift values with reasonably high number of counts for the use of carbon current collectors, nitrogen doping and the E/S ratios of 0-10 mL/g in the cathode. As a result, Li-S cells with these factors have higher probability to reach specific capacities equal to or higher than 1000 mAh/g. The other important factors for achieving high PDCs are the conductive material type, electrolyte salt type, sulfur type, binder type, and S weight percentage. In addition, having an interlayer is also beneficial for achieving PDCs equal to or higher than 1000 mAh/g.

Although the ARM analysis for the cells with PDCs equal to or higher than 1000 mAh/g gives valuable information for the effect of various cell materials and compositions, this value is still only the 60 % of the theoretical capacity; PDCs should be much higher for practical applications. For this reason, the ARM analysis were repeated for the cells with PDCs equal to or higher than 1200 mAh/g, 1400 mAh/g and 1600 mAh/g; this way the change in lift with increasing PDC could be also monitored to identify the factors that become more apparent when the desired PDC value is increased. The PDC values were defined cumulatively; for example, the batteries with PDCs equal to or higher than 1000 mAh/g also cover the batteries having PDCs equal to or higher than 1200 mAh/g, 1400 mAh/g and 1600 mAh/g. The results of such analysis are shown in Figure 4.7, for the cathode design parameters as the lift versus discharge capacity bubble graphs, where the bubble size indicates the number of counts obeying that rule (numbers next to the bubbles); only the cases having a minimum of 10 data points were included in the figures related to association rule mining results. Figure 4.7a indicates that carbon black, which is the most common conductive material used, is still the best option since the lift values of all other options are lower (although the lift for C-black with some structured carbon materials is higher at low PDCs, this result cannot be generalized because all these data points are coming from a single article). The amount of conductive material seems to be important, and 15-30 wt.% (intermediate values) is more favorable for high capacity sulfur cathodes (Figure 4.7b).

Thirteen options are present in Figure 4.7c for the effect of encapsulation material type. Although the graph seems to be complex at first look, the general trends are rather simple; the most striking conclusion is that encapsulated cathodes are much better for achieving high PDCs when compared with the no encapsulation case. When the PDC is 1000

mAh/g, all the alternatives overlap even though the lowest lift value is still obtained for the no encapsulation case (represented by the large blue bubble in the figure). Then, the lift values start to differentiate with increasing PDC. For example, C black is one of the most commonly used encapsulation materials; however, its lift is around one, showing that it is not a good material for this purpose. The other materials seem to be better than C black or no encapsulation in general; especially porous carbons appear to be highly effective with the lift of 2.44 at 1600 mAh/g. Likewise, the lift of "others", which is a collection of infrequently used materials (like polyacrylonitrile and covalent organic frameworks doped with boron and oxygen), is much higher (2.57) with the count number of 5 (the count was 10 at 1400 mAh/g). Carbon nanotubes (CNT) with some additives also result in high-capacity cathodes; for instance, CNT with zeolitic ZIF-8 or polyethylenimine may favor capacities over 1400 mAh/g. To sum up, encapsulating sulfur with structured carbons (i.e., CNT, CNF, porous carbons) or developing novel encapsulation materials (i.e., others, other carbons) are highly promising pathways to achieve PDCs over 1400 mAh/g. This may be because the structure and the properties of the encapsulation materials, such as CNT, CNF, porous carbons, etc., can be defined and controlled better compared to C black; for instance, structured carbons typically have higher conductivity and surface area. Therefore, better control of the structure and more refined properties of carbons (or novel materials) may be significant in the success of the encapsulation.

Figure 4.7d shows that high fractions of encapsulation materials (more than 40 wt.%) also improve the cell performance. This may be attributed to the enhanced conductivity and electrochemically surface area of the sulfur electrode leading to higher sulfur utilization. Encapsulation fractions less than 40 wt.% does not seem to have the same effect. When the effect of the binder type on the PDC is considered in Figure 4.7e, it is seen that PVDF, which is the mostly used binder, has a constant lift value around one for all of the capacity intervals. On the other hand, PTFE or LA shows promise for attaining high capacity Li-S batteries. PEO, CMC+SBR, PEO+Others and the other binders that are not listed here are not favorable when the peak specific capacity is considered as the performance indicator. The impact of the sulfur loading in the cathode on the PDC is presented in Figure 4.7f. It is apparent in the figure that the sulfur loading should be smaller than 1 mg/cm^2 to have peak capacities higher than 1400 mAh/g; this is due to the improved sulfur utilization at low loadings as discussed in the previous section.

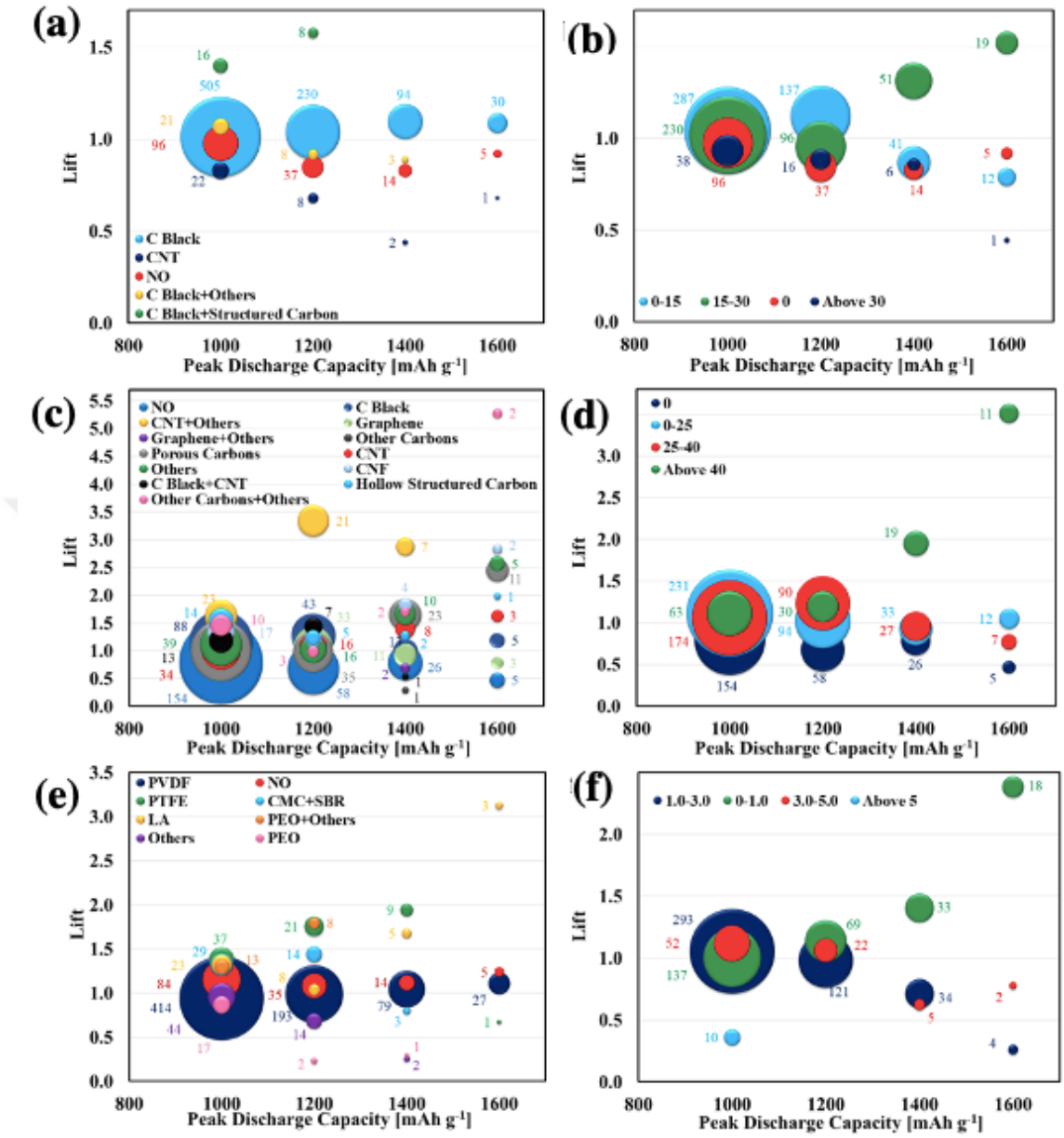

Figure 4.7. Change of lift with peak discharge capacity for materials and design factors in cathode with liquid electrolyte: conductive type (a), conductive weight % (b), encapsulation type (c), encapsulation weight % (d), binder type (e), sulfur loading (mg/cm^2) (f).

Electrolyte materials are also important design factors in a Li-S cell. First, the solvent material type in the electrolyte was considered. As can be seen in Figure 4.8a, most of the works in the literature use DOL:DME as the solvent; hence, this material has a lift value of around one. On the other hand, EC:DEC has a very high lift value of 13.18. Only 20 of 588 data points using DOL:DME achieve PDCs equal to or higher than 1600 mAh/g, while 6 of

10 EC:DEC cases are still in the dataset at 1600 mAh/g capacity, resulting in this very high lift value of 13.18. This, together with the high lift result of TEGDME, shows that the conventional electrolyte solvent can be replaced with new electrolyte solvents to get closer to the theoretical capacity.

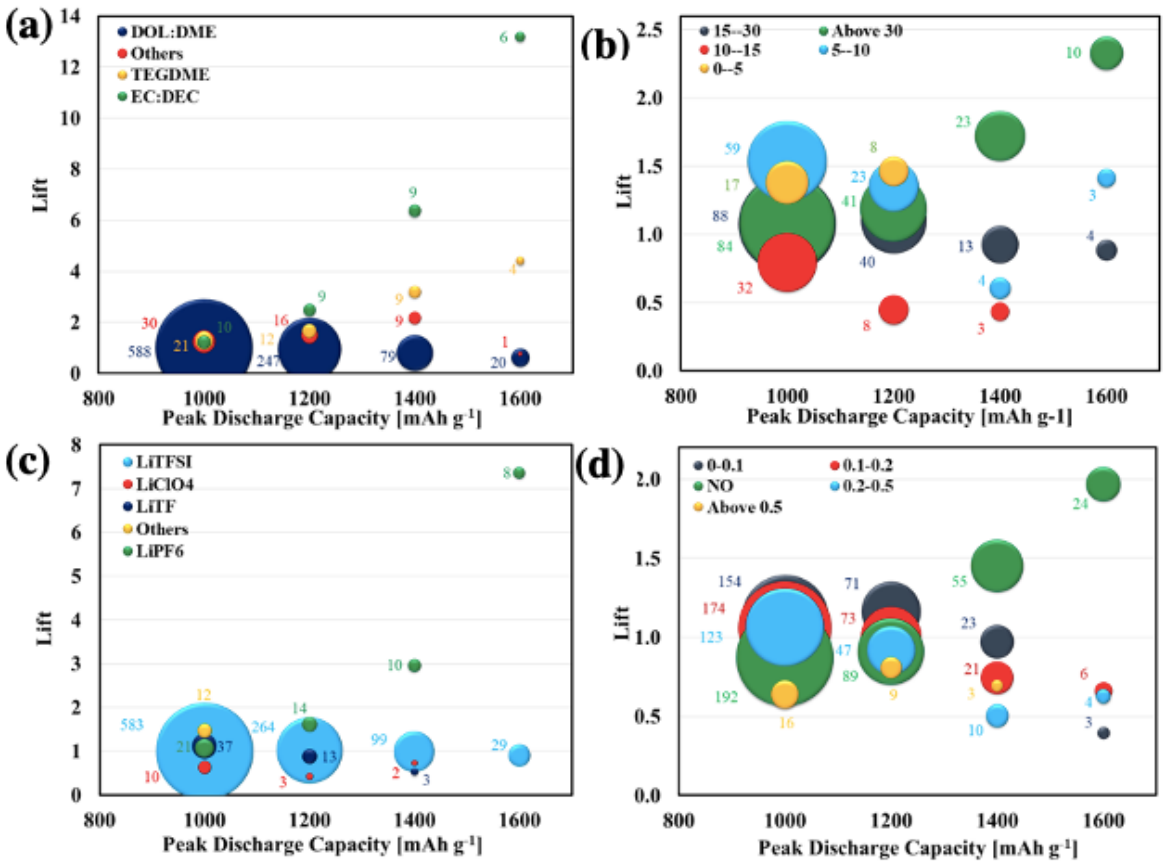

Figure 4.8. Change of lift with PDC for materials and design factors of liquid electrolyte: electrolyte solvent (a), E/S ratio (mL/g) (b), electrolyte salt (c), electrolyte additive concentration (M) (d).

The E/S ratio is another critical factor in our analysis as given in Figure 4.8b. The impact of E/S ratio on the PDC is obvious in the figure. Even though low or moderate E/S ratios (0-5 and 5-10 mL/g) are favorable in attaining capacities of 1000 mAh/g S, E/S ratios higher than 30 mL/g are required to achieve 1600 mAh/g. This clear trend in the figure confirms that very high E/S ratios are needed in the cell when the cell performance is evaluated based on the peak discharge capacity. Electrolyte salt type is also considered together with the electrolyte solvent. As it can be seen in Figure 4.8c, $LiPF_6$ has a very high lift value compared to the most commonly used salt LiTFSI; this trend indicates that using

$LiPF_6$ in the electrolyte is favorable for high capacities. On the other hand, the electrolyte additive, which is mainly $LiNO_3$, does not have any positive effect on the PDC as presented in Figure 4.8d. On the contrary, the electrolyte with no additive seems to be much better for high PDC even though $LiNO_3$ improves the cycle life, as it will be discussed in later in this section.

For Liquid Electrolyte Dataset with E/S Ratio and S Loading Limitations: As previously discussed, even though the majority of the studies in the literature evaluate the Li-S cell performance through the peak discharge capacity, the energy density of the cell is also critical. Since sulfur is the active material in the cathode, high sulfur loadings are desired for high energy densities. Likewise, the amount of the electrolyte in the cell should be limited like all the other inactive materials that do not contribute to the cell capacity. In other words, for high energy density Li-S batteries, the E/S ratio should be low while the sulfur loading in the cathode is high. Consequently, in order to investigate the effect of factors to achieve high energy density cells, ARM analysis was also performed for the cells having sulfur loadings higher than 5 mg/cm^2 (Table 4.3) and E/S ratio of 0-5 mL/g (Table 4.4) with PDCs equal to or higher than 1000 mAh/g. Because of the low number of data in the dataset satisfying both sulfur loading and E/S ratio requirements simultaneously, the analyses for these two factors were conducted individually.

The most significant result in Table 4.3 is that there should be no conductive additive or binder in the cathode for high PDCs at high sulfur loadings. In addition, encapsulation weight percentages should be between 0-25 wt.%. This shows that the development of binder-free cathodes with efficient encapsulation materials at low amounts is key to have high performance at high sulfur loadings. ARM analysis, in which E/S ratio is restricted, also provides valuable information. There are electrolyte starved cells that can achieve peak discharge capacities $\geq$ 1000 mAh/g and ARM analysis can be successfully used to investigate the common materials and cell design factors in these cells. However, because of the low number of data in the dataset for these low E/S ratios, it is not possible to differentiate between E/S ratios of 0-5 mL/g.

Table 4.3. Association rule mining results for cells with liquid electrolyte having PDCs equal to or higher than 1000 mAh/g and S loadings equal to or higher than 5 mg/cm^2.

RHS	Support	Confidence	Lift	Count
{Encapsulation=C Black+PANI}	0.00068	0.100	18.29	1
{Encapsulation=Structured Carbons}	0.00068	0.100	14.63	1
{Electrolyte_Additive=LiNO3+Others}	0.00068	0.100	13.30	1
{Current_Collector=NO}	0.00137	0.200	8.61	2
{S_Type=LixSy}	0.00205	0.300	6.65	3
{Current_Collector=Others}	0.00137	0.200	5.85	2
{S_wt=75--100}	0.00137	0.200	5.23	2
{Binder_Type=NO}	0.00342	0.500	4.57	5
{Encapsulation=Graphene}	0.00273	0.400	3.85	4
{C_Type=NO}	0.00342	0.500	3.40	5
{C_wt=0}	0.00342	0.500	3.40	5
{Encapsulation=CNT}	0.00068	0.100	2.00	1
{Electrolyte_Salt=LiTF}	0.00068	0.100	2.00	1
{Encapsulation_wt=0--25}	0.00410	0.600	1.94	6
{E_S_Ratio=5--10}	0.00068	0.100	1.74	1
{Electrolyte_Add_Conc=0.2--0.5}	0.00205	0.300	1.73	3
{E_S_Ratio=Above 30}	0.00137	0.200	1.72	2
{Encapsulation=Porous Carbons}	0.00137	0.200	1.64	2
{E_S_Ratio=15--30}	0.00137	0.200	1.63	2
{Encapsulation_wt=Above 40}	0.00068	0.100	1.18	1

It can be seen in Table 4.4 that the electrolyte solvents (i.e. Sulfolane and TMS:TTE) other than DOL:DME, TEGDME and EC:DEC are highly effective having lift values higher than 8. This suggests that the development of novel electrolytes may play a critical role in achieving high discharge capacities in electrolyte starved cells. In addition, using CNT or carbon black as encapsulation materials may increase the probability of having PDCs equal to or higher than 1000 mAh/g. Finally, the presence of an interlayer may contribute to the specific capacity of the Li-S cells with lean electrolyte conditions. These results all indicate that materials design is necessary to attain high discharge capacities at low E/S ratios in the cell.

Table 4.4. Association rule mining results for cells with liquid electrolyte having PDCs equal to or higher than 1000 mAh/g and E/S ratios lower than 5 mL/g.

RHS	Support	Confidence	Lift	Count
{Binder_Type=PEO+Others}	0.0021	0.1765	11.74	3
{S_Type=Sulfur+Others}	0.0014	0.1176	11.47	2
{C_Type=C Black+Structured carbon}	0.0021	0.1765	10.33	3
{Electrolyte_Solvent=Others}	0.0034	0.2941	8.12	5
{Binder_Type=PEO}	0.0027	0.2353	8.01	4
{Encapsulation=CNT}	0.0034	0.2941	5.89	5
{Current_Collector=Others}	0.0021	0.1765	5.16	3
{Binder_Type=CMC+SBR}	0.0014	0.1176	3.59	2

Table 4.4. Association rule mining results for cells with liquid electrolyte having PDCs equal to or higher than 1000 mAh/g and E/S ratios lower than 5 mL/g. (cont.)

RHS	Support	Confidence	Lift	Count
{Electrolyte_Salt=LiTF}	0.0021	0.1765	3.54	3
{C_Type=CNT}	0.0014	0.1176	2.97	2
{Encapsulation=C Black}	0.0034	0.2941	2.58	5
{Electrolyte_Salt=LiClO4}	0.0007	0.0588	2.46	1
{Electrolyte_Solvent=TEGDME}	0.0007	0.0588	2.39	1
{Electrolyte_Add_Conc=0.2--0.5}	0.0048	0.4118	2.38	7
{Binder_Type=LA}	0.0007	0.0588	2.26	1
{S_loading=1--3}	0.0109	0.9412	2.26	16
{Interlayer=Yes}	0.0041	0.3529	1.96	6
{C_wt=0--15}	0.0089	0.7647	1.86	13
{Current_Collector=C coated Al foil}	0.0034	0.2941	1.80	5
{S_wt=75--100}	0.0007	0.0588	1.54	1
{Binder_Type=PTFE}	0.0007	0.0588	1.46	1
{S_wt=50--75}	0.0082	0.7059	1.40	12
Encapsulation_wt=0}	0.0041	0.3529	1.22	6
{Encapsulation=NO}	0.0041	0.3529	1.22	6
{Electrolyte_Add_Conc=0--0.1}	0.0027	0.2353	1.14	4

4.1.1.3. Analysis of Cycle Life for the Cells with Liquid Electrolyte. The association rule mining analysis was also performed for the cycle life by using a similar procedure explained for the PDC. Here,the cycle life was defined as the number of cycles a cell retains at least 80% of its PDC. The lift values were calculated for the cells that preserved 80% of their peak capacity for more than 50, 100, 200 and 400 cycles cumulatively (for example 200 cycle data also contains 400 cycle data), and monitored to understand the effect of individual factors on the battery cycle life. The results for the entire dataset are presented in Figure 4.9 and Figure 4.10. Since the end goal is to attain high capacity retention at high PDCs, an additional ARM analysis was also performed for the cycle life of the cells achieving 1000 mAh/g and higher peak capacities only and the results are given in the parenthesis to show how much of the data comes from the cells with the desired PDCs.

According to Figure 4.9a, the cathodes that do not contain any binder perform better than the cathodes having PVDF, CMC+SBR or others. However, it should be noted that, these binder-free cathodes are generally the ones that utilize special encapsulation materials in which an additional binder is not needed. Therefore, a discussion built on encapsulation materials rather than the binder type would be more relevant. The sulfur loading, which is a critical cathode design parameter, has a strong effect on the cycle life (Figure 4.9b). 80 % capacity retention for more than 300 and 400 cycles seems to be more possible if the sulfur loading is between 3-5 mg/cm^2 while higher loadings (above 5 mg/cm^2) are better in lower

cycle numbers. This can be explained that high active material loadings may enhance the PSM and increase the cell resistance with cycling. As seen in the figure, cells with low sulfur loadings (0-1 mg/cm^2) show limited cycle life despite achieving high PDCs as discussed above. This, together with the discussion on the energy density, clearly suggests that low S loaded cathodes are not feasible.

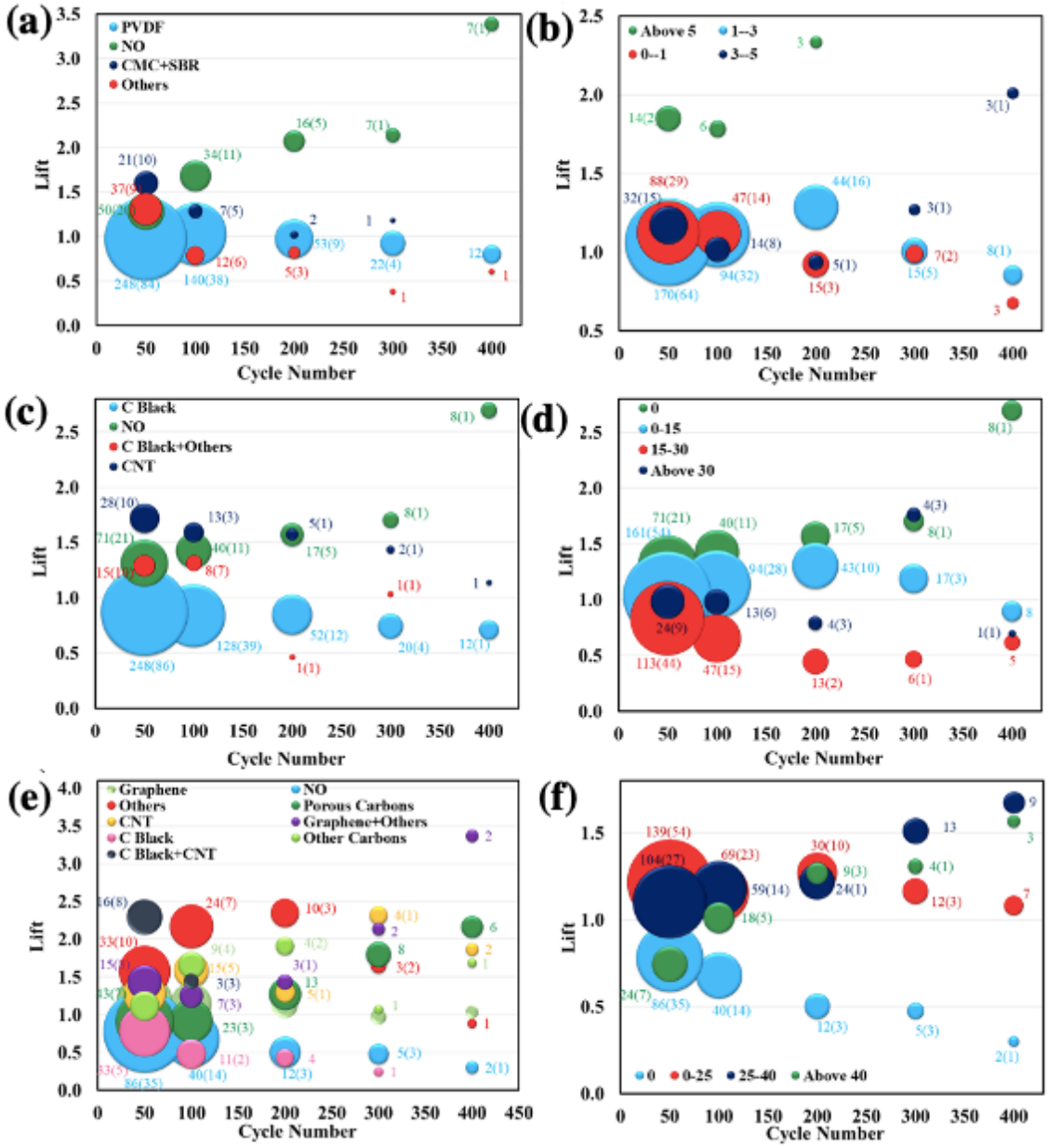

Figure 4.9. Change of lift with cycle number for materials and design factors in cathode with liquid electrolyte: binder type (a), sulfur loading (mg/cm^2) (b), conductive type (c), conductive weight % (d), encapsulation type (e), encapsulation weight (f).

The cells with no conductive additive have the highest lift at high cycle life (Figure 4.9c); this is also apparent in Figure 4.9d that the highest lift was obtained with 0% additive. However, it should be emphasized that these cells are also the ones with specialized encapsulation materials. These results suggest that if the encapsulation materials have large surface area, appropriate pore structure and volume that restrict structural deformations, and provide high conductivity, additional conductive additives and binders are not necessary. Then, it can be said that the type and amount of encapsulation material are the most crucial factors for achieving high capacity retention and thus enhanced cycle life.

When the influence of encapsulation type and amount on the cycle life is considered in Figure 4.9e and Figure 4.9f, respectively, the critical impact of the encapsulation strategy can be clearly comprehended. Cells prepared without any encapsulation (NO in Figure 4.9e and 0% in Figure 4.9f) have the worst cycling performance. Moreover, it is seen that porous carbons, carbon nanotubes, and less frequently used materials collected in the entry of others (i.e., polyacrylonitrile, polydopamine) are good options for high cycle life. Graphene together with various other materials (graphene+others) and other carbons also have high lift values up to 400 cycles. Furthermore, Figure 4.9f suggests that encapsulation wt.% higher than 25% (25-40% and 40-100%) is favorable for enhanced cycle life; this result is consistent with the findings presented above for PDC proposing binder- and conductive-free cathodes for high-performance cells.

When the electrolyte parameters of the cells are considered in Figure 4.10, the only conclusive results come from the E/S ratio and electrolyte additive concentration. Better cyclability is obtained with E/S ratios higher than 30 mL/g while 0.1-0.2 M additive (mostly $LiNO_3$) concentration seems to improve the cycle life. The latter result is expected as $LiNO_3$ is known to passivate the anode; however, it is interesting that intermediate concentrations (0.1-0.2 M) resulted in better cyclability. On the other hand, observing the highest lift values for the highest E/S ratio range was an unexpected finding since it is frequently discussed in the literature that too high electrolyte amounts enhance the PSM in the cell and thus reduce the capacity retention.

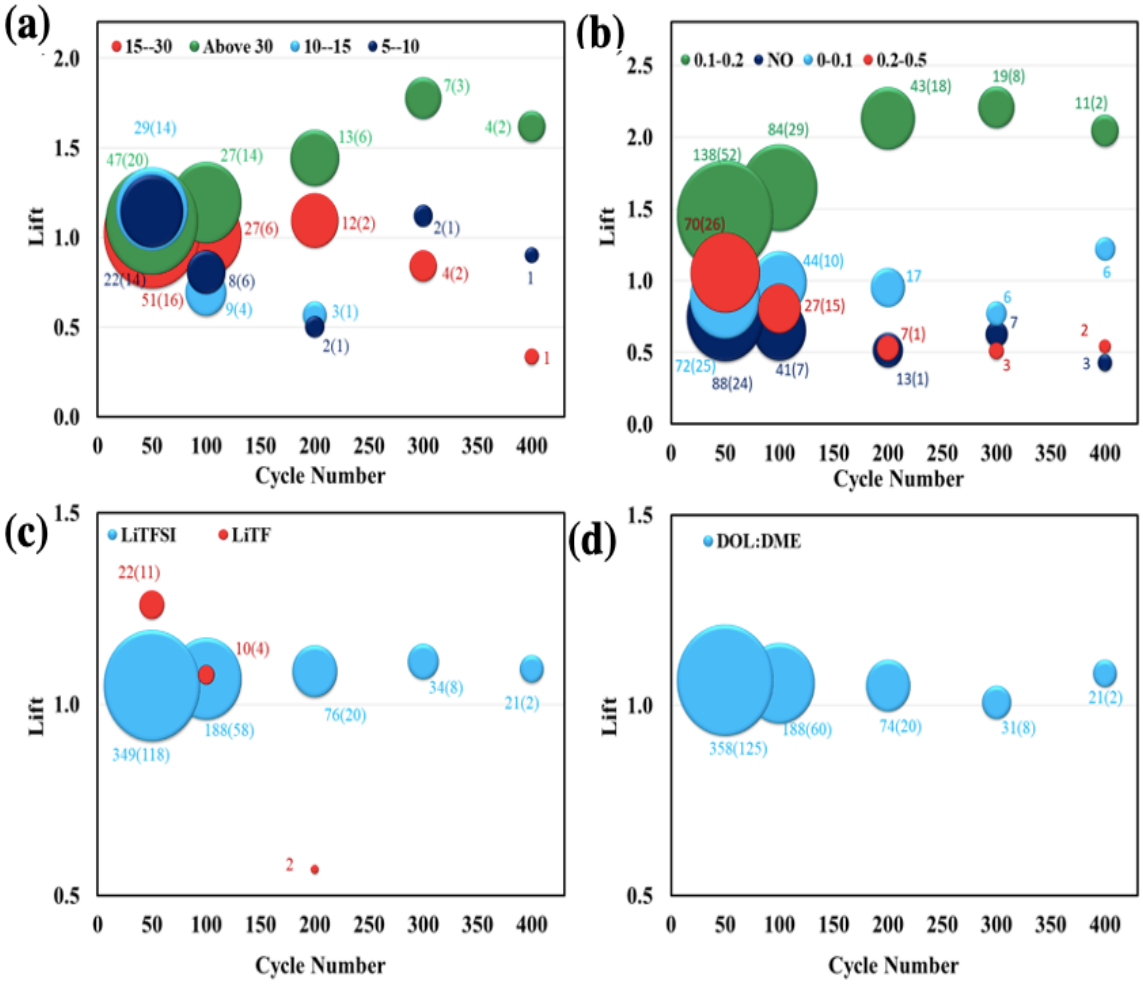

Figure 4.10. Change of lift with cycle number for materials and design factors of liquid electrolyte: electrolyte solvent (a), E/S ratio (mL/g) (b), electrolyte salt (c), electrolyte additive concentration (M) (d).

4.1.1.4. Analysis of Peak Discharge Capacity and Cycle Life for the Cells with Other Types of Electrolyte. Finally, association rule mining was performed for PDC and cycle life of Li-S cells with catholyte and solid electrolyte. However, the number of data points were too small to have a detailed discussion as in the case of liquid electrolyte; instead, PDC and cycle life of three electrolytes were compared in Figure 4.11. The cells with solid electrolyte perform better in PDC analysis while the catholyte is better for long cycle life. Li conductivity in all-solid-state Li-S batteries is already comparable with the conventional electrolytes; hence, they can achieve very high PDCs. However, the interface forming between the anode and the solid electrolyte with cycling causes high interfacial resistance in the cell and thus leads to poor cycle life [323]. On the other hand, cells with catholyte achieve

improved cycling performance, most probably due to reversible and kinetically fast reactions in the presence of additional PSs in the electrolyte [324]. To conclude, since Li-S cells using catholyte and all-solid-state electrolyte are relatively recent in the literature, a future ARM study focusing only on these cells would result in more elaborate conclusions.

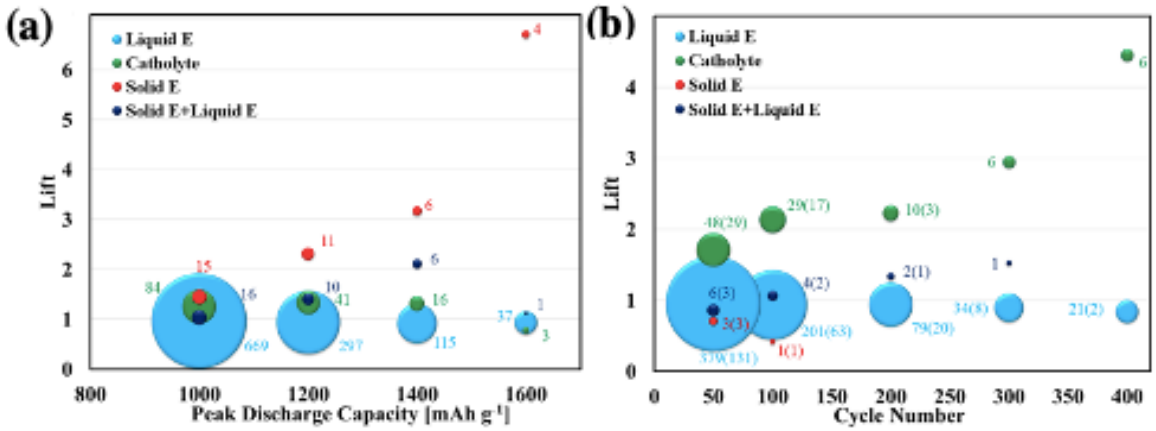

Figure 4.11. Comparison of peak discharge capacity (a) and cyclability of electrolyte types (b) in Li-S cells.

4.1.2. Assessment of Ionic Liquid Electrolytes for High Performance Lithium-Sulfur Batteries using Machine Learning

This chapter is an edited version of the original research article published in the International Journal of Energy Research by authors A. Kilic, Prof. R. Yildirim, and Prof. D. Eroglu [44].

Although Li-S batteries are very promising in terms of their theoretical specific energy, their commercialization is severely hindered by the multi-step reaction and various degradation mechanisms. The PSM is one of the big challenges associated with these batteries that results in irreversible capacity loss and low efficiencies. To realize the full potential of the Li-S batteries, the shuttling of PS intermediates between the electrodes should be prevented. Additionally, to increase the system-level energy density of the Li-S battery, the dead mass inside the battery pack should be minimized. In this respect, ionic liquids (IL) are getting increasing attention as they can reduce the PS shuttle mechanism with their limited PS solubility and their functionality at lean electrolyte conditions. In this

section of the thesis, a dataset is constructed from the experimental literature data, which uses ILs as their electrolytes, to analyze the important cell variables and promising ILs for both high system- and cell-level performances using association rule mining.

4.1.2.1. ARM Results for Peak Discharge Capacity. The lowest capacity limit for the *high-capacity* subset was chosen as 800 mAh/g, and its ARM results are given in Table 4.5. This table was ranked with respect to the lift values as higher lift values present stronger associations between that factor and the high-class cells, while lift values below 1 imply negative correlations. Confidence and support are also given together with the count value, which is the number of cases satisfying the rule, as a more practical measure to see the significance of the results. Indeed, some of the entries with the highest lift have only a few cases; hence, they cannot be generalized with high confidence as a rule to follow. The calculation of support, confidence, and lift can be shown for EMI_TFSI as an example to better understand the results. The total number of data points in the dataset is 207 while only 125 of them have PDCs ≥ 800 mAh/g, high class subset. On the other hand, 7 data points contain EMI_TFSI in their electrolytes and 6 of them give high performances (count). Hence, support, confidence and lift values are found as 6/207=0.029, 6/125=0.0480 and 0.0480/(7/207)=1.42, respectively. As seen in the table, the electrolyte parameters, specifically the IL type, are at the top of the table, indicating that they are very effective for providing high-capacity Li-S batteries.

The rules or conclusions deduced for the factor effects can be refined further with a slightly different use of ARM as follows; the lower limits of high performance data can be set to a different level (such 800 mAh/g to 1000 mAh/g, and so on) and ARM analysis is performed for each case. Since the number of data will decrease with increasing lower limit (tighter performance requirement), the lift of a level promoting high performance should increase because the number of data satisfying this condition, should remain constant or at least should decrease less than the others. Hence, the increasing trend in the lift can be used as a further indicator of the positive effect of that level. Therefore, the limits for the high-capacity class were increased from 800 mAh/g to 1000 mAh/g, 1200 mAh/g and 1400 mAh/g and the trend for the lift of each factor was analyzed separately. The results, as lift versus capacity limit, are presented in bubble graphs, where the bubble size represents the number of data points satisfying the conditions. Since the capacities are cumulative (for

example if a PDC is greater than 1400 mAh/g, it is also greater than 800 mAh/g), the size of the bubbles are expected to decrease, while the lift of the promising factor will increase.

Table 4.5. ARM results for PDCs ≥800 mAh/g.

Factors	Levels	Support	Confidence	Lift	Count
IL_Abbreviation	DEME_Others1	0.0048	0.0080	1.66	1
IL_Abbreviation	PMIM_TFSI	0.0048	0.0080	1.66	1
IL_Abbreviation	P1A3_TFSI	0.0097	0.0160	1.66	2
Encapsulation_Material_Categorized	Carbon Black	0.0097	0.0160	1.66	2
Conductive_Material_Categorized	Others4	0.0097	0.0160	1.66	2
Anode_Categorized	Modified Li anode	0.0145	0.0240	1.66	3
IL_Abbreviation	Li(G3)_TFSI	0.0145	0.0240	1.66	3
Binder_Categorized	CMC	0.0386	0.0640	1.47	8
IL_Abbreviation	EMI_TFSI	0.0290	0.0480	1.42	6
IL_Abbreviation	P13_Others1	0.0290	0.0480	1.42	6
E/S_Ratio_Categorized	0-15.0	0.1111	0.1840	1.41	23
Encapsulation_Material_Categorized	Carbon Nanotube	0.0821	0.1360	1.41	17
S_Loading_Cat	>4.0	0.0966	0.1600	1.38	20
IL_Abbreviation	Li(G4)_TFSI	0.1159	0.1920	1.32	24
IL/Solvent_vol.%_Categorized	<50	0.1353	0.2240	1.32	28
Molecular_Solvent_Categorized	DOL:DME	0.1449	0.2400	1.31	30
Conductive_Material_Categorized	Acetylene black	0.1256	0.2080	1.30	26
IL_Abbreviation	P13_TFSI	0.0483	0.0800	1.27	10
Molecular_Solvent_Categorized	Fluorinated ether	0.0483	0.0800	1.27	10
Binder_Categorized	None	0.0435	0.0720	1.24	9
Conductive_Material_Categorized	Ketjen Black	0.0435	0.0720	1.24	9

Figure 4.12 presents the ARM results showing the effect of IL type on the PDC. The lift values are very close for all ILs at PDCs ≥ 800 mAh/g, meaning that most of the ILs work well for this capacity range. However, when the capacity limits are increased, promising ILs become more apparent as they differentiate with higher lifts. For example, P13_Others1, EMI_TFSI, and P13_TFSI seem to be much better for PDCs ≥ 1400 mAh/g, while P1,201_TFSI shows promise for PDCs ≥ 1200 mAh/g. Although P1A3_TFSI has high lift values, since it has a low count, we cannot deduce a conclusion. On the other hand, there are many examples of SILs, which have Li(triglyme) or Li(tetraglyme) cations and TFSI or other various anions in the literature. However, an association between these ionic liquids and high performance is not observed for PDCs ≥ 1200 mAh/g; the true ionic liquids performed better in terms of high PDCs. As presented in Table 3.7, there are 19 different ionic liquids, which are combinations of 14 cation and 2 anion groups in the dataset; 92 %

of ionic liquids uses TFSI as their anion group and there are only a few studies investigating the effect of the anion group on the performance [325,326]. The main reason for this preference is probably the known low PS solubility of TFSI anionic group as compared to other organic solvents [326]. However, further analysis of the ARM results shows that the use of different anion groups (BETA, FSI) for P13 cation may be beneficial considering that the lift is almost tripled with the increasing performance measure (higher limits for the high-performance class); in other words, the use of the different anionic groups (BETA, FSI) resulted in high PDCs if P13 was used as the cation. This may be suggesting that the other anion groups should also be investigated for the other cations in addition to TFSI, which seems to be a default anion.

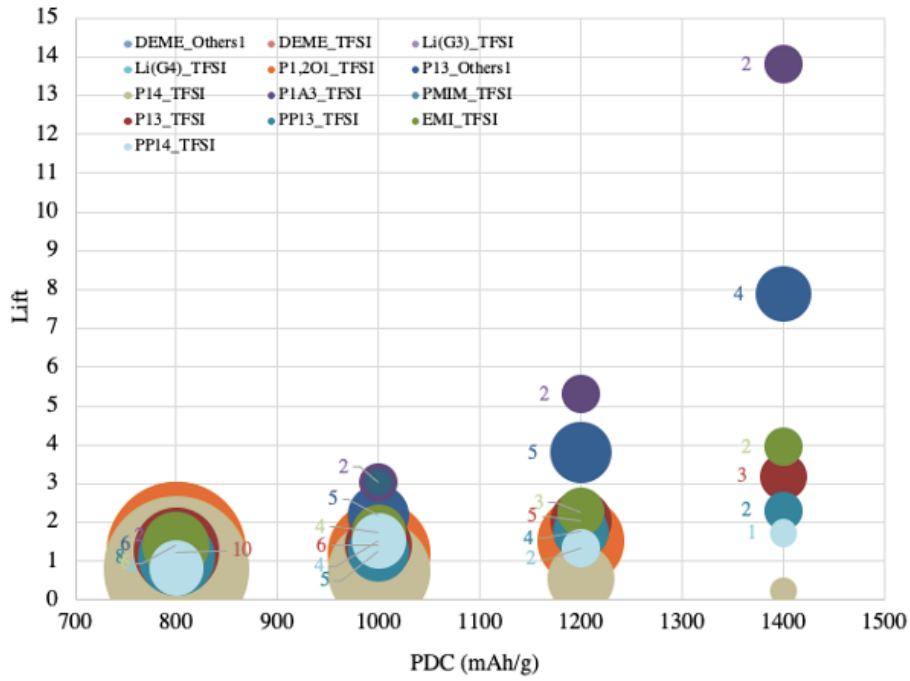

Figure 4.12. Lift vs. peak discharge capacity of ionic liquids as electrolytes.

Rather than using pure IL electrolytes, most of the data points in the dataset uses additional molecular solvents (MS), which are generally organic solvents with certain salts [327,328]. In fact, 64% of the data uses these solvents to decrease the viscosity of ILs to facilitate Li^+ ion transfer in general. However, Figure 4.13a and Figure 4.13b do not seem to support this practice; the use of suitable pure IL electrolytes works better as "None" level has the highest lift at the highest capacity limit. On the other hand, if a MS is needed, DOL:DME solvent mixture should be used with the condition that IL/MS vol.% should not

exceed 50 vol.%. It was also found that the addition of various salts, other than LiTFSI, favors high PDCs, whereas $LiNO_3$ decreases the probability of having high PDCs in IL electrolytes (Figure B.3).

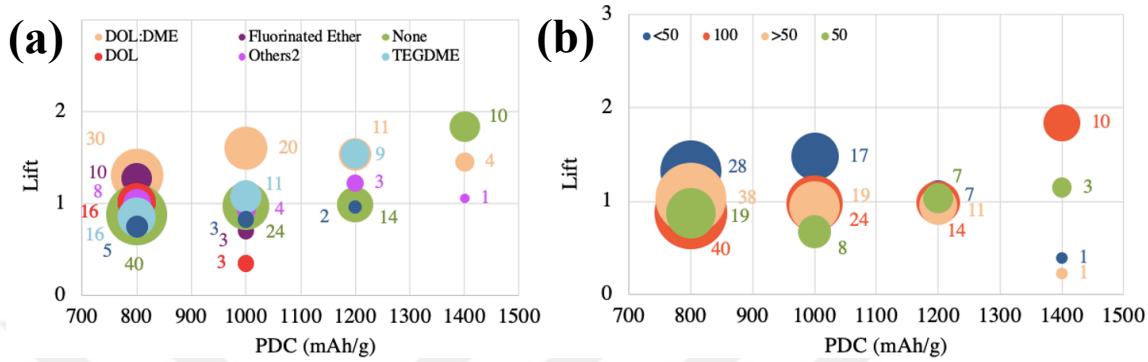

Figure 4.13. Lift vs. peak discharge capacity of molecular solvents as electrolytes (a) and IL/MS vol.% in the electrolyte (b).

In Figure 4.14 and Figure 4.15, the effect of E/S ratio and sulfur loading on the PDC of Li-S batteries with IL electrolytes are compared with the Li-S cells with molecular solvent electrolytes using the dataset we created in the previous section [43]. In Figure 4.14a, it is shown that low E/S ratios are more favorable for reaching higher PDCs in IL electrolytes (Figure 4.14a); on the other hand, high E/S ratios are needed for high performance for non-IL electrolytes (Figure 4.14b).

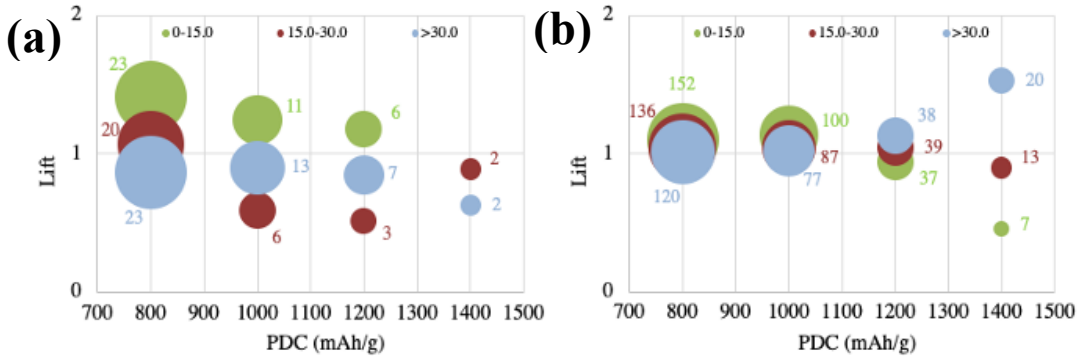

Figure 4.14. Lift vs. peak discharge capacity of E/S ratio for IL (a) and molecular solvent (b) electrolytes.

Figure 4.15 indicates that ILs work well with high sulfur loadings, whereas Li-S cells with molecular solvents fail at high sulfur loadings. Figure 4.14 and Figure 4.15 support that

the use of IL electrolytes is beneficial in Li-S batteries; high PDCs can be achieved at low E/S ratios and high S loadings for these cells. These positive improvements may be attributed to the limited PS solubility with the utilization of the IL electrolytes [329].

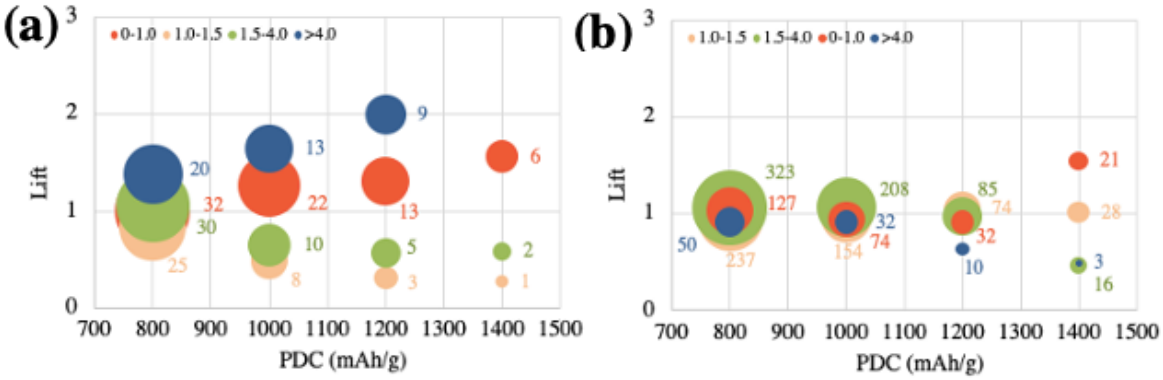

Figure 4.15. Lift vs. peak discharge capacity of sulfur loading (mg/cm^2) for IL (a) and molecular solvent (b) electrolytes

The ARM results of the other variables are given in Appendix B. It is found that the encapsulation of sulfur cathodes is still desired for high PDCs to further suppress the PSM and to increase the electronic conductivity (Figure B4.a). Carbon black and activated carbons should be used as encapsulation materials in the presence of the IL electrolytes. In addition, graphene/$MgAl_2O_4$ and N-doped mesoporous carbon seem to have a positive effect on the improvement of the Li-S cell performance.

4.1.2.2. ARM Results for System-Level Performance. Although having a high PDC is important for a Li-S cell, more relevant performance indicators for practical applications of batteries are system-level gravimetric and volumetric energy densities [65], [32], [330]. Especially, for applications like electric vehicles, the gravimetric energy density of the battery should be higher than 400 Wh/kg [331]. However, studies that investigate the system-level performance of Li-S batteries are very limited [332,333]. Hence, in this section we modified the BatPac model to estimate the system-level energy density and specific energy of the Li-S batteries using the experimental PDCs and design factors such as the E/S ratio, sulfur loadings, S/C/binder wt% etc. in the dataset. However, only half of the dataset reported these variables; hence, the total number of data points decreased from 207 to 102 for this analysis.

Table 4.6. ARM results for specific energies ≥ 60 Wh/kg.

Factors	Levels	Support	Confidence	Lift	Count
Conductive_Material_ Categorized	Others4	0.010	0.067	6.80	1
Binder_Categorized	CMC	0.059	0.400	4.53	6
E/S_Ratio_Categorized	0-15.0	0.137	0.933	3.53	14
Conductive_Material_ Categorized	None	0.059	0.400	3.40	6
Encapsulation_wt%_ Categorized	30-35	0.059	0.400	3.40	6
Conductive_wt%_Categorized	0	0.059	0.400	2.40	6
S_Loading_Cat	>4.0	0.049	0.333	2.27	5
S_wt%_Categorized	>60	0.088	0.600	2.19	9
IL_Abbreviation	Li(G4)_TFSI	0.059	0.400	2.15	6
Encapsulation_Material_Categorized	Graphene Oxide	0.049	0.333	2.13	5
Encapsulation_Material_Categorized	Ketjen Black	0.059	0.400	1.94	6
Encapsulation_Material_Categorized	Mesoporous carbon	0.029	0.200	1.70	3
Electrolyte_Salt_ Categorized	None	0.059	0.400	1.70	6
IL/Solvent_vol.%_ Categorized	100	0.059	0.400	1.70	6
Molecular_Solvent_ Categorized	None	0.059	0.400	1.70	6
Molecular_Solvent_Categorized	DOL:DME	0.078	0.533	1.60	8
IL/Solvent_vol.%_Categorized	50	0.049	0.333	1.55	5
Electrolyte_Additive_Categorized	Yes	0.049	0.333	1.48	5
S_Loading_Cat	1.5-4.0	0.088	0.600	1.42	9
Conductive_wt%_Categorized	20	0.049	0.333	1.36	5
Separator_Categorized	Polymer	0.118	0.800	1.36	12
Encapsulation_wt%_Categorized	0-20	0.039	0.267	1.30	4
Binder_Categorized	Others6	0.029	0.200	1.28	3
IL_Abbreviation	P14_TFSI	0.078	0.533	1.21	8

Table 4.6 and Table B.1 report the ARM analysis results for Specific Energy ≥ 60 Wh/kg and Energy Density ≥ 60 Wh/L, respectively. As seen in the table, the cell design parameters are also effective on the system-level performances. Since the IL type is not appeared frequently in the Table 4.6 and the entire dataset used in the analysis is constructed with ILs, we may say that cell design variables are more important in terms of system-level energy density rather than the type of the IL. As supported with the Table 4.6, the dead mass of the cell should be minimized to provide high energy density Li-S battery systems.

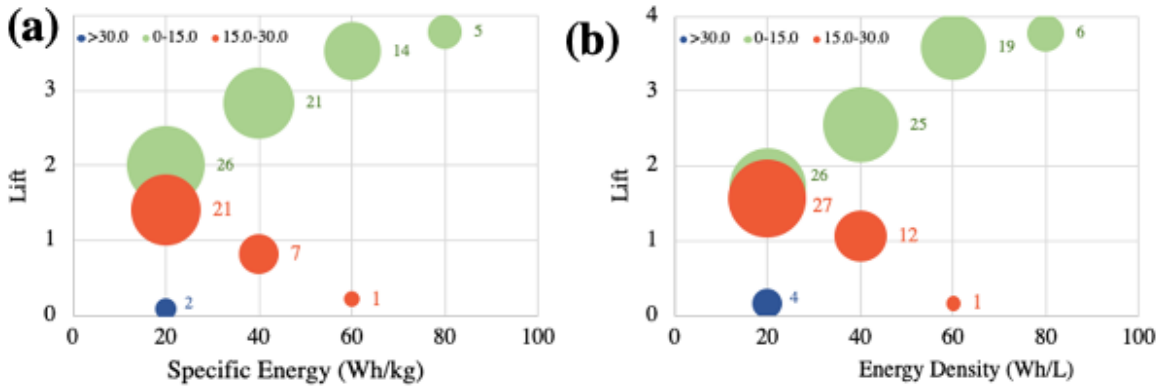

Figure 4.16. Lift vs. specific energy (Wh/kg) (a) and energy density (Wh/L) (b) of E/S ratio for IL electrolytes.

On the other hand, one of the highest lifts is obtained with E/S=0-0.15 ml/g and sulfur loading higher than 4 mg/cm^2 where we proved ILs are improving PDCs at these conditions. Hence, we may still conclude that ILs have a critical effect on the improvement of the system-level performance. In addition, with lift values higher than 1, Li(G4)_TFSI and P14_TFSI are found to be the best options for high system-level performance metrics. In addition, graphene oxide, ketjen black and mesoporous carbons should be utilized as encapsulation materials when IL electrolytes are used.

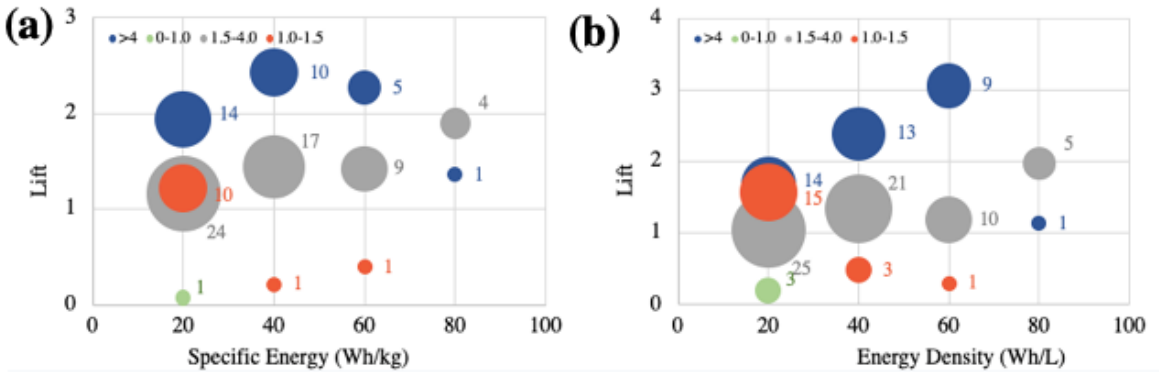

Figure 4.17. Lift vs. specific energy (Wh/kg) (a) and energy density (Wh/L) (b) of sulfur loading (mg/cm^2) for IL electrolytes.

As seen in Figure 4.16 and Figure 4.17, the estimated energy densities are far below the requirements for the commercial applications. However, in order to develop some insight to build relatively high energy density Li-S cells, the ARM analysis was still conducted. The ARM analysis shows that low E/S ratios and high sulfur loadings are needed to increase the

energy density and specific energy at the system level for Li-S batteries with an IL electrolyte; this conclusion is in parallel with the discussions for the Li-S cells using regular electrolytes [334,335].

4.1.3. Selection of Ionic Liquid Electrolytes for High-Performing Lithium-Sulfur Batteries: An Experiment-Guided High-Throughput Machine Learning Analysis

A manuscript detailing the results presented in this section is in preparation by authors A. Kilic, O. Abdelaty, Prof. A. Uzun, Prof. R. Yildirim, and Prof. D. Eroglu. The COSMO-RS calculations, ML studies and the experiments were performed by A. Kilic and presented here. O. Abdelaty supported the discussions on ML modeling.

The PSM is one of the most significant challenges of Li-S batteries in achieving high capacity and cyclability. One way to minimize the shuttle effect is to limit the PS solubilities in the battery electrolyte. IL are particularly suited as electrolyte solvents because of their tunable physical and chemical properties. In this chapter, thousands of ILs are screened to narrow down potentially viable candidates to be used as electrolytes in Li-S batteries. To that end, COSMO-RS calculations are performed over more than 36000 ILs. An extensive database containing PS solubilities and other relevant properties is constructed at 25 °C. First, the effectiveness of the COSMO-RS calculations is experimentally tested with 6 ILs with a wide range of solubility and viscosity values. After specifying the target limits for promising ILs using the experimental battery performance data, ML tools are used to predict and identify the relationship between IL properties and PS solubilities and structural and molecular descriptors of ILs.

4.1.3.1. Pre-analysis of the Dataset. In this screening section, we aimed to use a dataset representative of most ILs commonly used and studied, as well as the rare ones in the battery literature. Hence, our dataset spans several cation groups, including imidazolium, pyridinium, and ammonium, in addition to anions of different types, including fluorinated, chlorinated, carboxylates, oxyanions, amino acids, etc., and more commonly investigated anions in IL electrolytes such as $[BF_4]^-$, $[PF_6]^-$ and $[TFSI]^-$. The complete lists of the cations and anions groups are given in Table 4.7. The table shows that the most crowded groups are imidazolium and pyridinium for cations, while amino acids and carboxylates for the anions.

Table 4.7. The list of cation and anion groups present in the dataset.

Cation Group	Cation Count	Anion Group	Anion Count
Ammonium	49	Amino acid	16
Choline	1	Bis_imide	4
Guanidinium	20	Borate	12
Imidazolium	134	Carboxylate	16
Morpholinium	9	Cyano	3
Others	4	Halo_elemental_complexes	7
Phosphonium	28	Halogen	4
Piperidinium	9	Nonmetal oxide	5
Pyrazolium	4	Others	6
Pyridinium	67	Phosphate/ Phosphinate[1]	9
Pyrrolidinium	19	Sulfate	9
Quinolinium	15	Sulfonate	7
Sulfonium	5		
Thiazolium	3		
Uronium	3		
Total	370	Total	98

[1]Abbreviated as Phosp./Phosphin.

The COSMO-RS solubility screening results, including solubility, viscosity, conductivity, and melting points, are shown in Figure 4.18 depending on anion groups, whereas the distributions on the cation groups are presented in Figure C.3. When these distributions are compared, solubilities and properties show similar distributions and ranges regardless of the cation groups. On the other hand, noticeable differences are observed when anion groups are considered. This clearly indicates anionic effect dominance on the properties of the ILs.

Figure 4.18a shows that solubility values obtained from the calculations span a wide scale of many orders of magnitude from 10^{-9} to almost 10^{20} in mol/mol units. This is expected primarily when the difference between the solute (Li_2S_8) and the solvents (ILs) results in larger deviations of the activity coefficients. Still, the calculations can compare small and larger values, but the extreme calculations should be treated cautiously [336,337]. When ILs with extremely low and high PS solubilities are analyzed, it is seen that some anions give these abnormal solubility values regardless of the cation types. This may indicate COSMO-RS's failure to predict the properties of these anions. According to the graph, most amino acids, carboxylates, halogens, non-metal oxides, and phosphines fall into the extreme solubility ranges, below 10^{-3} and above 10^{3} mol/mol, and should be treated cautiously. On the other hand, bis_imide, borate, halo-elemental, and others (the rare ones that do not belong to any of the anion groups listed) anion groups show reasonable solubility values.

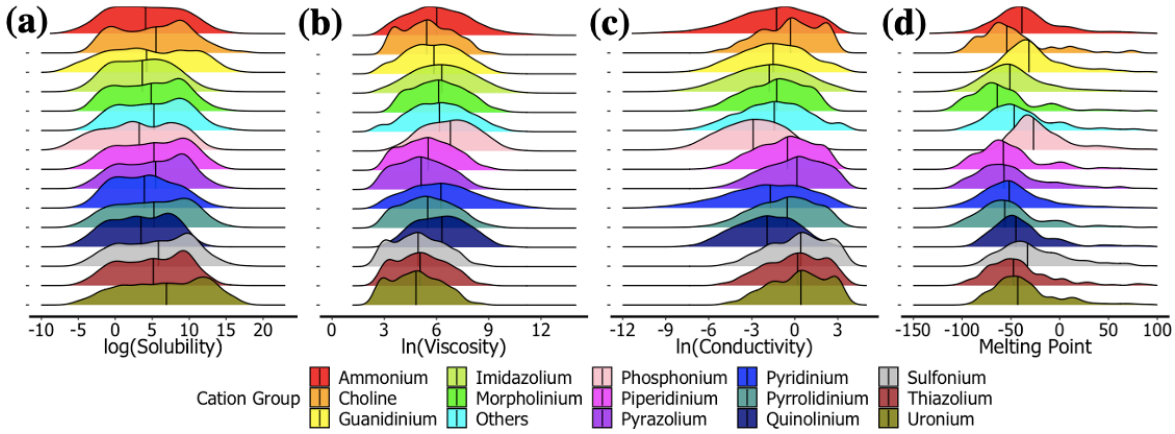

Figure 4.18. The distribution of solubility (a), ln(viscosity(mPa.s)) (b), ln(conductivity(mS/cm)) (c), and melting point(°C) (d), depending on the anion group.

PS solubility is not the only criterion when selecting electrolytes for Li-S batteries. Other properties are also essential in the screening process of ILs in search of suitable electrolytes for Li-S batteries; the melting point, viscosity, and conductivity are all significant criteria in Li-S cell electrolyte selection to ensure smooth cell operation. This way, utilization of highly viscous IL electrolytes must be avoided to allow for appreciable Li^+ diffusion. 1 M Li salt containing DOL:DME electrolyte has a 1.6 mPa.s viscosity value and shows sufficient ionic conductivity [338]. In the dataset, the lowest viscosity value calculated from the COSMO-RS is 9.1 mPa.s, which is almost 5-fold higher than that of DOL:DME electrolytes and only 25 % of 36,260 ILs have viscosity values below 134 mPa.s. On the other hand, around 15 % and 7 % of the dataset do not have melting points below 0 °C and ln(electronic conductivity) values below 2, respectively.

The anion and cation descriptors have been shown to strongly correlate with target properties in previous studies, including the solubility of water and C4 hydrocarbons in various ILs and the physicochemical properties of ILs [209,210]. The descriptors are simple yet essential structural, electronic, and energetic factors. CPK area and ovality are related to the geometry of ions calculated based on the space-filling model, which is a crucial indicator of the area of potential interactions with other ions or the PSs. Naturally, the higher the area is, the stronger the interactions in the solution are. However, the ovality effect also plays an important role in the space fitting of ions surrounding the PSs and each other. Dipole and polarizability represent ions' charge distribution and susceptibility of that distribution to

deformation when interacting with other molecules. These are highly important in studying solvation energy and solubility because they directly relate to the interactions during solvation. The potential for hydrogen bond formation is given by the hydrogen bond donor (HBD) and acceptor count (HBA) [339]. PSs are all known to be weak bases, in other words, hydrogen bond acceptors [340]. However, this also indicates the potential for the cation and anion to be attracted to each other, which will also affect the solubility.

Other important descriptors include electronic and energetic ones, which may affect the solubility less directly. The values of HOMO and LUMO energies calculated by simple DFT calculations contain important information related to ion stability, its potential for electronic interactions, and bond strength. The vibrational Zero-point energy is the lowest vibrational energy level and determines the flexibility or stiffness of the bonds in the molecule to stretching and bending. This property describes the flexibility of ions to structural deformation during the solvation process [341,342]. Finally, the molecular weight of ions is also useful as it gives information about ion diffusion coefficients, density, and viscosity, which indirectly affect solubility.

4.1.3.2. IL Requirements for High-Performance Li-S Batteries. To see if there is a correlation between PS solubilities and IL properties calculated using the COSMO-RS method and Li-S battery performance, as hypothesized, six ILs listed in Table 4.8 are tested experimentally (the experimental details are provided in Appendix C). As seen in the table, three different cations with $[TFSI]^-$ and three different anions with $[BMIM]^+$, 1-butyl-3-methyl-imidazolium, which are one of the most common anions and cations in the literature, are used in the experiments. These ILs are commercially available, hence easily accessible, and have low/high solubility and viscosity values (melting point and electrical conductivity are only used to confirm the suitable liquid phase of the electrolyte and to ensure no electron flow through the electrolyte). Hence, four of these ILs are projected to have low solubilities (PP14-TFSI, DEME-TFSI, TBMA-TFSI, BMIM-PF_6), whereas the other two (BMIM-CF_3SO_3 and BMIM-$MeSO_4$) have extremely high values. Moreover, ILs with low and high viscosities also have both high and low solubility cases. Hence, it is possible to identify the effect of COSMO-RS predicted viscosity and solubility values on the performance of Li-S batteries.

Table 4.8. Experimentally tested six ionic liquids.

Cation	Anion	COSMO-RS PS Solubility (mol/mol)	COSMO-RS Viscosity (mPa.s)
PP14	TFSI	0.20	65
DEME	TFSI	0.38	54
TBMA	TFSI	0.04	107
BMIM	PF_6	1.29	223
BMIM	CF_3SO_3	847	56
BMIM	$MeSO_4$	182635	146

The results presented in Figure 4.19 supported the discussion on the importance of low solubility but also highlighted the effect of viscosity on the Li-S cell performance. Although high viscosity may also suppress the PSM by restricting PS movement, it also prevents the diffusion of Li^+ ions. In this respect, the ILs of PP14-TFSI and DEME-TFSI with both low solubility and viscosity show the best cycling performance. On the other hand, Li-S cells with ILs (TBMA-TFSI, BMIM-PF_6) with low PS solubility but higher viscosity performed moderately. Finally, BMIM-CF_3SO_3 and BMIM-$MeSO_4$ showed almost zero capacity over cycling. These ILs are predicted to have high solubility, indicating that even though low viscosity is required for high performance, low PS solubility is a more critical property. For instance, BMIM-CF_3SO_3 performs poorly, even though it has low viscosity, proving that mostly PS solubility determines the performance.

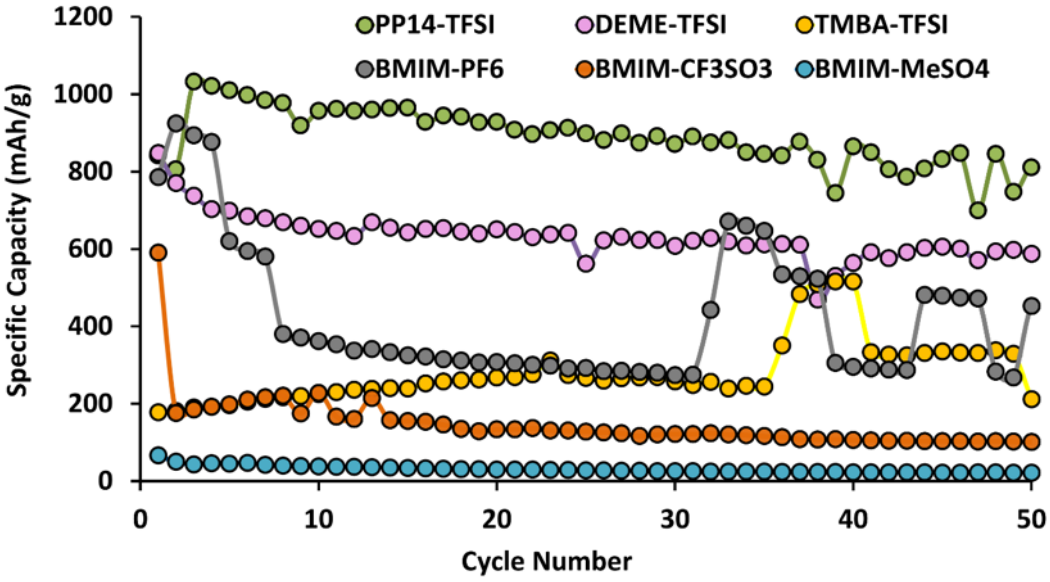

Figure 4.19. The cycling performances of six ILs tested at 0.1C.

The experimental results show that it is possible to use the COSMO-RS predictions for assessing Li-S battery performances. However, these results are only limited to 6 ILs, and the validation of COSMO-RS results is still needed. Unfortunately, a sufficiently comprehensive experimental study to evaluate the predictions made by the COSMO-RS model is excessively difficult, necessitating a comparison with the available data in the literature. The few studies regarding solubility had limited scope due to difficulties discussed previously. Among them, Park et al. reported PS solubilities for various ILs. The experimentally measured PS solubilities account for a mixture of PSs in the solution due to *disproportionation reactions* and the subsequent cascade of PS reactions. This difference is partially responsible for the departure of predictions of Li_2S_8 solubility from experimental measurements of all PSs. Indeed, the measured solubilities are the sum of solubilities of all PS species with various chain lengths and are provided in terms of total atomic sulfur concentration. Despite this and other simplifying assumptions, the COSMO-RS model results showed an excellent correlation with the experimental measurements, as shown in Figure 4.20. Although there is a significant numerical difference between the COSMO-RS calculated absolute solubility values and experimental ones, the resulting linear correlation has an R^2 score of 0.97, showing the success of our method.

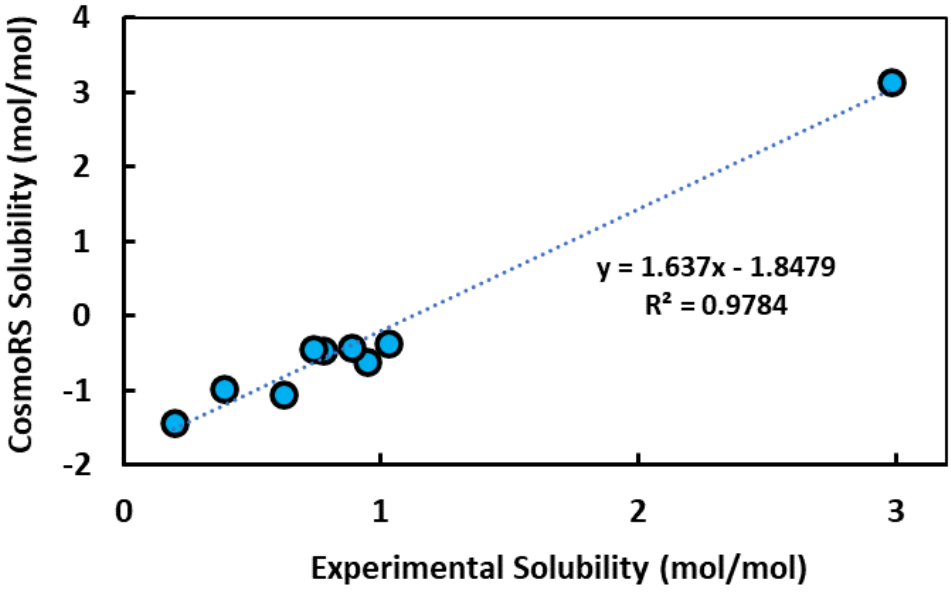

Figure 4.20. Experimental PS solubility plotted against the predicted solubility values by COSMO-RS *in log scale*. The dotted line is the best-fit line. (The experimental data was obtained from [75].

Determining the limits for PS solubility for high performance should also be done according to the COSMO-RS calculated values. Hence, the six experimental results with Park et al. performance data are used together. When the 50th cycle capacities of this experimental set are considered, a clear solubility limit for high specific capacity can be determined, as shown in Figure 4.21. The underlying reason is sluggish reaction kinetics and sulfur loss from cathode in extremely low and high PS solubilities, respectively [75]. Therefore, determining the solubility limits is very critical to assess whether an IL will perform well or not as the electrolytes of Li-S batteries. According to Figure 5, the solubility limit should be between -0.7 to 0.1 mol/mol in log scale.

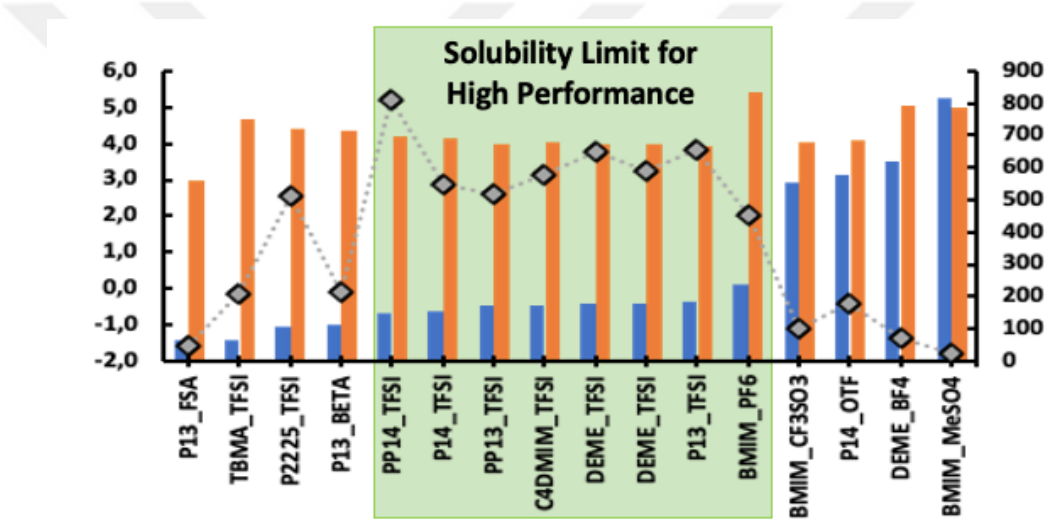

Figure 4.21. The 50th cycle capacity of experimental results (mAh/g) together with Park et al. results with COSMO-RS results.

All these discussions show the importance of solubilities and properties in selecting suitable ILs for Li-S battery applications and the success of the COSMO-RS calculations. However, thousands of ILs are present, and many more are possible, and it takes too much time to experimentally test all the ILs. The COSMO-RS calculations made it possible to calculate the properties of thousands of ILs using '.cosmo" files using special packages like COSMOthermX. On the other hand, once the dataset is constructed, it is valuable to have ML methods that can predict IL properties using the IL descriptors calculated from more conveniently found methods compared to generating .cosmo files and using special packages. In addition, hidden relations between ILs and their properties can be identified. In this respect, ML models for predicting PS solubility and the IL properties are developed with

a dataset consisting of 36260 ILs and 20 IL descriptors, computed from PM3 semi-empirical calculations, in the search for promising ILs for Li-S battery electrolytes. In addition, using the limits for high performances obtained from experimental results, the factors leading to desired properties are obtained.

4.1.3.3. Solubility and Property Predictions. The ML models are trained to further understand the trends and heuristics of the solubility correlation with the specified descriptors and to make predictions for new ILs without using the COSMO-RS software. The training of the XGBoost model on randomly chosen combinations of anions and cations performs nearly perfectly with a 5-fold cross-validation R-squared (R^2) score of 0.99. It is essential to note the excessive dependence of the predictions on the anion descriptors and the fact that randomly splitting the data generally means that the same anions are present in both training and validation sets. To avoid such overlap, which may lead to the model "memorizing" the anions instead of learning descriptor correlation, the data was split such that randomly chosen anions from each anion group are only present in the validation set. For example, there are 4 bis_imide anions including TFSI in the dataset. Knowing that anions are more dominant over solubility, once the solubility of TFSI is seen by the model, it will automatically determine the solubility of IL containing TFSI without paying attention to the cation types in the validation set. However, restricting TFSI to only train set while putting bis(fluorosulfonyl)imide (FSI) in validation set, make the model more robust. This way, the training model learns from similar but not identical anions. The XGBoost model performance R^2 score dropped to 0.98 with a root-mean-square-error (RMSE) of 1.4, which still indicates an excellent performance on the available data and eliminates the risk of bias due to data overlap. Meanwhile, the RMSE of the test set increases to 3.05, which shows that the model can capture the PS solubilities in an order of magnitude scale.

These results are somewhat similar to water solubility prediction results [209], in the sense that the anion properties are more dominant over the solubilities. However, in this work, the effect of cation properties were also found to be important. This is clear from Figure 4.22, showing the descriptor importance obtained from the analysis of XGBoost results. Some cation descriptors, such as the CPK area and dipole, have noticeable importance. While the anions can still roughly estimate the solubilities, the cations refine these results. The top 3 descriptors having a dominant effect on PS solubility were electronic

HUMO-LUMO levels and dipoles of the anions. The HUMO-LUMO levels were also found to have a significant contribution to ML models on the CO_2 solubility [343].

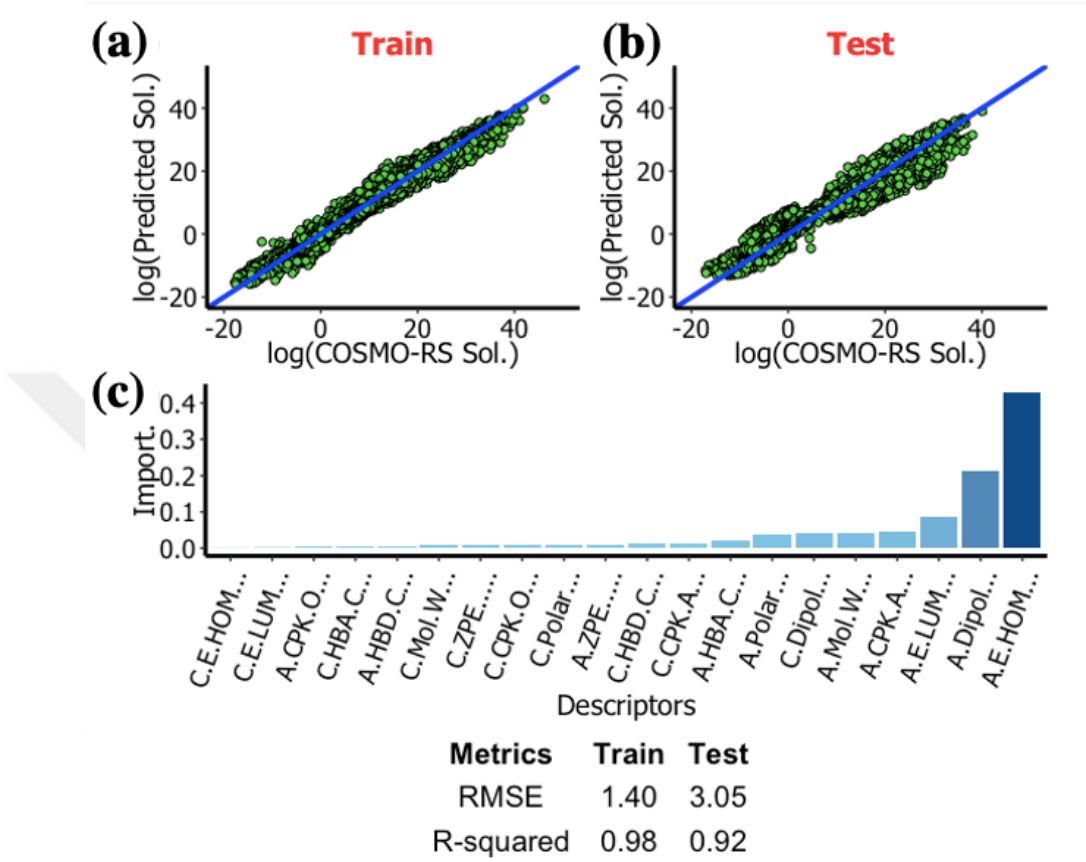

Metrics	Train	Test
RMSE	1.40	3.05
R-squared	0.98	0.92

Figure 4.22. The prediction results for ln(COSMO-RS Solublity (mol/mol)) for train (a), test (b) sets and relative importance (c) of the descriptors in the determinative power of the model.

Literature review indicates that ML techniques have been repeatedly used to predict different IL properties, including melting point, density, viscosity, ionic conductivity, and even surface tension [344,345]. Nevertheless, the property prediction models based on our descriptors were also trained to a high degree of success. Herein, the sampling in the training of these predictions was also anion-based rather than cation-based, as in the solubility classifier. This is because the results vary significantly according to the anion groups in these predictions, and the cation group-based distributions have similar distributions (Figure C.3). The anion-based sampling also used for melting point, viscosity, and conductivity performed well with RMSE score values of 19.4, 0.48, and 1.80, respectively. The descriptor importance plots are given for each property prediction in Appendix C, along with each

model's performance metrics. In the prediction of IL properties of the interest, the cationic properties have found more significance in comparison to solubility predictions. The most significant cation descriptors were found to be MW, dipole, and HOMO level. In parallel with our findings, Zheng et al. also found that the alkyl chain lengths of ILs having different imidazolium cations with $[TFSI]^-$ anion, therefore, MW and dipole, considerably affect the viscosities [346]. Another study found that the anion and cation properties both affect the final IL properties [347].

4.1.3.4. Identifying Promising ILs for Li-S Batteries using ARM. Lastly, the descriptor-property and solubility correlations are analyzed using ARM. ARM method needs both categorical descriptors and outcomes; hence, most descriptors were divided into ten intervals to see the characteristics of desired ILs, while the HBA and HBD counts were defined as factors. The limits for both solubility and viscosity values were set according to the experimental findings reported in Section 4.1.3.2. In this respect, the solubility was categorized into binary classes, as mentioned before, and the results for low solubility (class A, the log(solubility)) limits between -0.7 and 0.1 mol/mol as determined from experimental results reported in Figure 4.21. On the other hand, viscosities lower than 100 mPa.s were decided to be class A. 100 mPa.s, which is not too rigid a condition for IL viscosity, was also set to avoid severe Li^+ ion resistance problems. In addition, since the potential applications of Li-S batteries include daily applications, in other words they will be prone to various climate conditions, the melting point of ILs should be low enough so that the cell remains functional in cold climates. Towards that end, ILs with melting points below 0 □C are desired, and fortunately, 86.1% of the dataset satisfies this condition. Finally, the electronic conductivity limit is taken as 2 mS/cm. This rough estimation allows us to exclude ILs with considerable electronic conductivity. With these four criteria in place, the number of potential IL candidates drops to only 650 from 36260 data points. All the selection process are illustrated in Figure 4.23.

First, associations between anion or cation groups or cation-anion pairs and the desired properties were investigated. After refining the generated rules using the support and confidence thresholds, the lift value was used to extract rules with the highest correlation, and the table was sorted according to the lift values. Although the definitions of support, confidence, and lift are already provided in the previous sections, one example is provided

to understand the results better. The dataset used in the ARM analysis contained 36260 total data, with only 650 of them having class A solubility and property (viscosity, melting point, and conductivity). On the other hand, there are 1480 ILs having the bis_imide anion group, and only 194 (count value in Table C4) of them have class A for the four criteria. Hence, the support, confidence, and lift values are calculated as 194/36260 = 0.005, 194/650 = 0.298, and (194/650)/(1480/36260) = 7.31, respectively. As seen in Figure 4.24, most rules satisfying the confidence and support thresholds with the highest three lifts correlate with the anion group, indicating the trends in anion descriptors are more reliable and determinative than cation descriptors. These trends can be seen in Figure 4.24a for cation and anion groups and Figure 4.24b for cation-anion pairs. The bis_imide group is found to be the most promising one with the highest lift, but borates and "others" groups are also good candidates for both cases. However, although imidazolium and pyridinium groups have lower lifts than piperidinium and pyrrolidinium, their synergistic effects are stronger with the anion groups of borates and bis_imides. Specifically, imidazolium_borate and imidazolium_bis_imide ILs are around 10 and 5 times more favorable than other ILs for Li-S batteries, respectively.

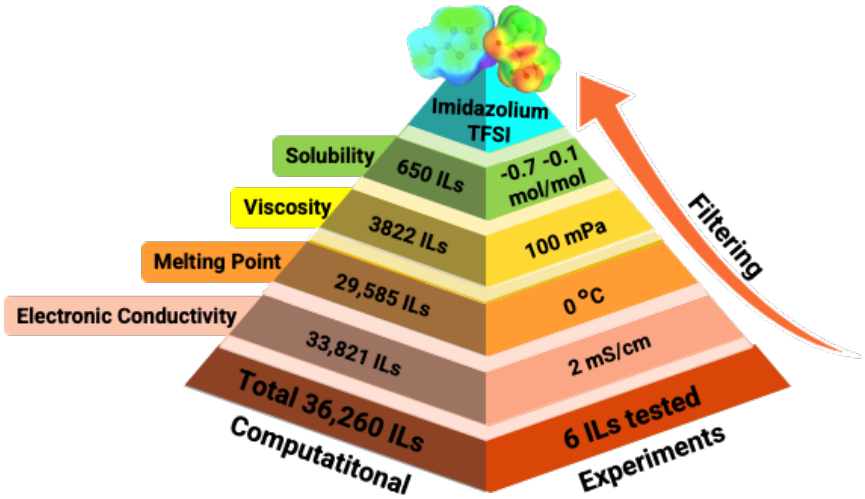

Figure 4.23. The determination of suitable ILs with the help of experimental results.

Imidazolium and $[TFSI]^-$ are the most common cation and anion in the Li-S literature, respectively [348]. In addition, it has been found that combining them improves the Li metal ion morphology and, therefore, increases the cycle life [349]. Given that pyridinium and imidazolium are similar in the completely delocalized aromatic rings [349], pyridinium is

the second promising cation group paired with borates. On the other hand, the borate anion group has 12 anions in total, including $[BF_4]^-$, which is reported as reactive towards PSs [75]. Fortunately, this anion is not present in the promising IL list. Although no additional articles use ILs with borate anions, in some studies, borate anions, specifically bisoxalatoborate [350–352], are used in Li salts, which positively affect the capacities.

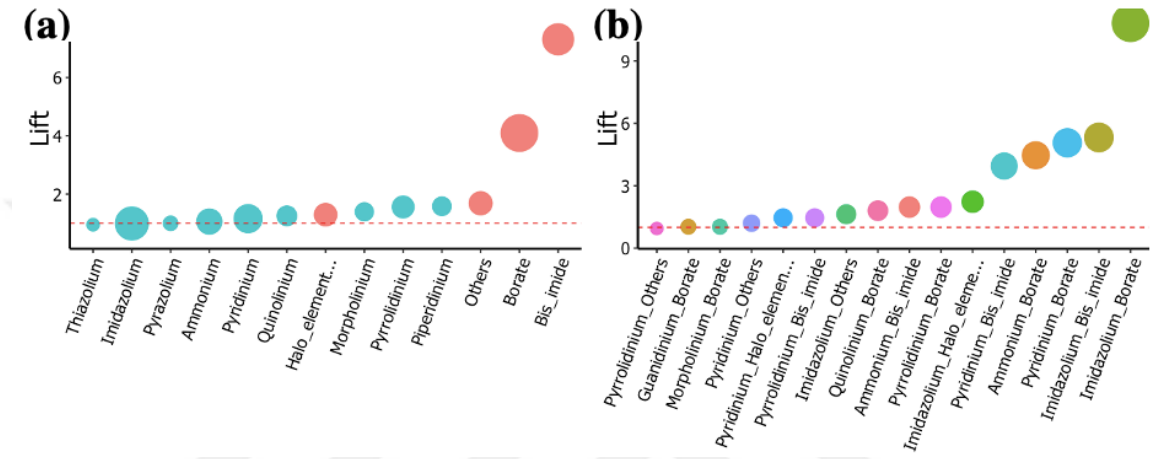

Figure 4.24. ARM results for anion and cation groups independently (a) and anion-cation pairs (b) for low solubility and viscosity.

Now that the promising groups are identified, we discuss the ARM results on a descriptor basis to identify the rules ending up with favorable ILs. To better extract the trends, Figure 4.25 summarizes the ARM results for the anions more concisely. Upon examining the results, the most pronounced rule concerns the anion HOMO energy value. In the database, low-lying anion HOMO energies in the range of (-7.5):(-6.7) eV result in a nearly five times more chance of having low solubility of Li_2S_8 and viscosity values. This lift drops significantly to slightly over 2.5 times if the HOMO value dips lower than -7.5 going to -9.9 eV. However, the correlation stands that low HOMO values correlate strongly with low solubility. A similar yet less strong correlation can be seen for the other properties. The other rules indicate that desirable anions for low PS solubility and viscosity are more likely to have moderately low LUMO energy, no HBD sites, relatively high MW but moderate CPK area, and moderate polarizability.

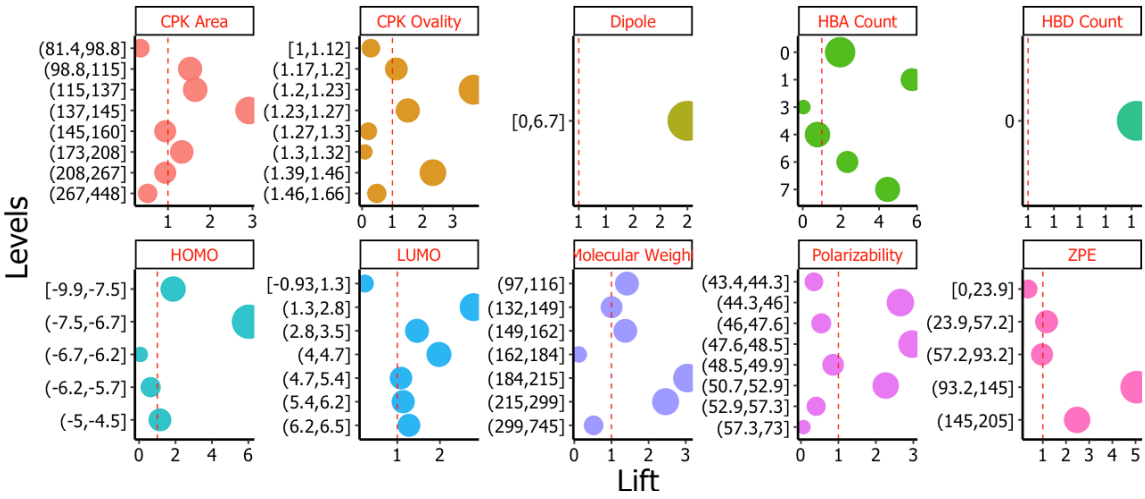

Figure 4.25. ARM results for anion descriptors; each point size correlates with support.

Figure 4.26 shows that cation descriptors have clear trends for low solubility and viscosity; lift values above one are obtained for low values of each descriptor, except HBA, HBD, and LUMO. It is important to emphasize that these trends imply an increased likelihood rather than a confident prediction. Can et al. [209] reported similar results about the dominance of anion descriptors in the ARM analysis when examining the association between water solubility in ILs and molecular descriptors. However, the importance of each descriptor differs significantly from the results reported here. That is to be expected because water and Li_2S_8 have different solvation processes. On the contrary, the solubility of hydrocarbons in imidazolium-based ILs showed a strong correlation with both anion and cation descriptors [210].

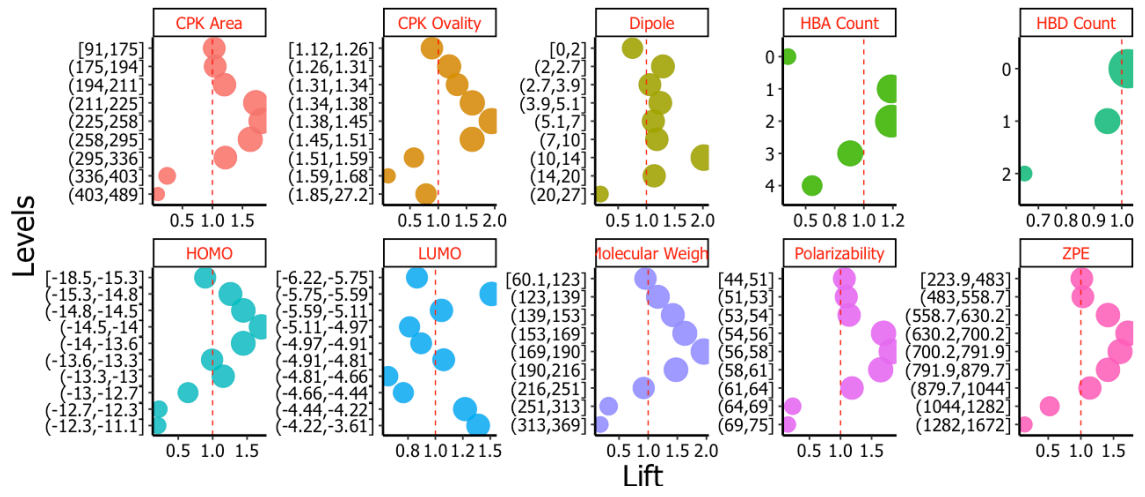

Figure 4.26. ARM results for cation descriptors; each point size correlates with support.

4.1.4. MOF/Graphene Nanoplatelet Composite Increases Rate Performance of Lithium-Sulfur Batteries

This section is modified from an original research article with authors A. Kilic, Ş. S. Bayazit, and D. Eroglu [45]. The preparation of the cathodes, the development of Li-S cells, and electrochemical performance tests were performed by A. Kilic, whereas MOF composites were synthesized by Ş. S. Bayazit.

The PSM is one of the biggest problems of Li-S batteries, resulting in fast capacity fading and low Coulombic efficiency. Due to electrostatic interactions, polar materials can adsorb the PS intermediates on their surfaces, decreasing the PSM effect. These polar materials should also have high electronic conductivity and surface area to be used in sulfur cathodes of Li-S batteries. In this respect, metal-organic frameworks (MOF) and their derivatives have gained significant attention. In this section, UiO-66/Graphene nanoplatelet (GNP)/sulfur composites are prepared with different MOF/GNP ratios to investigate the effect of MOF amount on the electrochemical performance of Li-S batteries.

The SEM images of the synthesized UiO-66, UG-1, UG-3, and UG-5 composites are given in Figure D.2 and Figure 4.27, respectively. As seen in Figure D.2a, UiO-66 nanoparticles have an octahedral crystal structure [353]. According to the scale of the SEM images, the sizes of UiO-66 nanoparticles are determined to be approximately 20-30 nm in UiO-66/GNP composites. On the other hand, the sizes of the attached UiO-66 nanoparticles on the GNP plates, clearly seen as two-dimensional sheets in Figure 4.27a, are measured to be 32-45 nm. Similar structures and particle sizes are observed for UG-5 in Figure 4.27b. It can be discussed that the particles are evenly distributed in the composites, especially in UG-5 (Figure 4.27b).

The surface areas and pore volumes of each composite are measured by the BET analysis, and the results are presented in Figure 4.27**c**. As seen in the figure, the BET area of GNP is significantly improved by the addition of UiO-66 into the structure, while the pore volume is reduced considerably. In other words, as pores of GNPs are filled with UiO-66 particles, the surface area of GNP increases remarkably, but the pore volume decreases simultaneously.

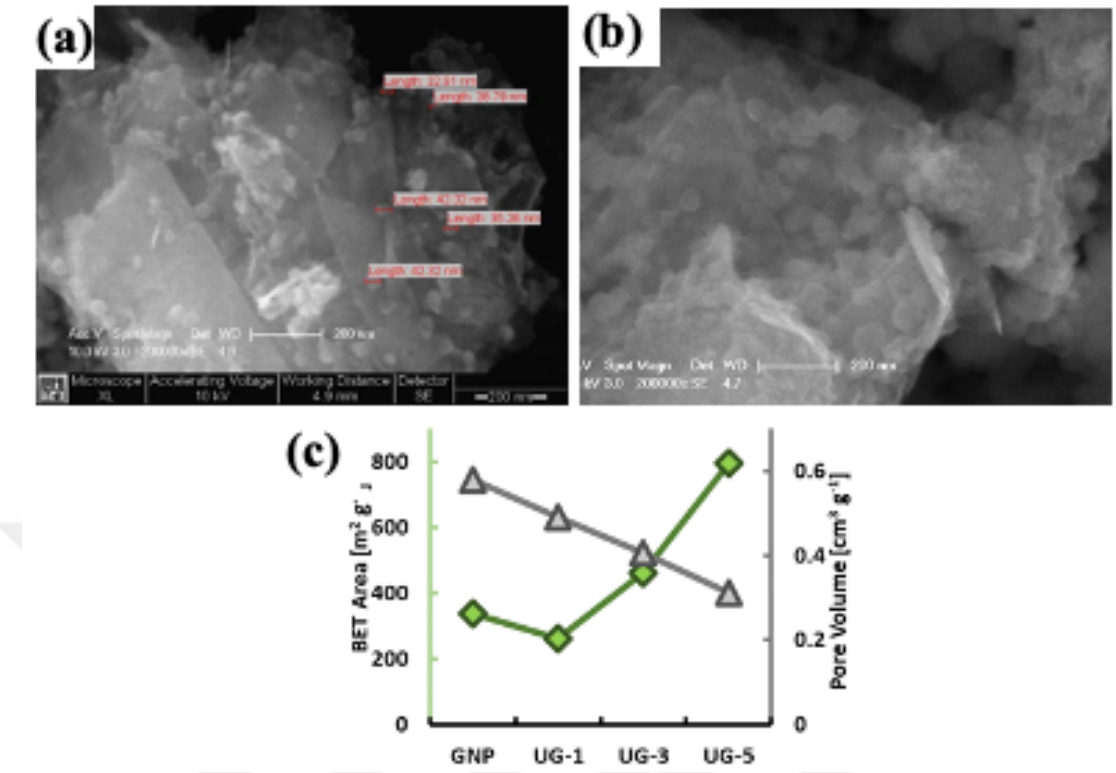

Figure 4.27. SEM images of UG-3 (a) and UG-5 (b) and BET surface area (◊) and pore volume (Δ) measurements (c).

The XRD patterns of UiO-66, UG-1, UG-3, and UG-5 are given in Figure D.3. XRD patterns of all composites were scanned between 2-60 degrees. The characteristic peaks of UiO-66 crystals can be seen at 7.46°, 8.66°, and 25.94°; these 2θ degrees are compatible with the literature [354]. As seen in the figure, the patterns of UG-3 and UG-5 composites are analogous to the UiO-66 nanoparticles. The 26.7° peak associated with GNP is also seen (which is not seen in the XRD pattern of UiO-66). The intensity of this peak in UG-3 is higher than in UG-5 since there is 70% GNP in UG-3 and 50% in UG-5. When the XRD pattern of UG-1 is examined, the intensity of the peaks belonging to UiO-66 is too low to be noticed; the intensity of the GNP peak prevents the appearance of UiO-66 characteristic peaks when there is 10% MOF in the composite.

The FTIR plots of UiO-66 and UiO-66/GNP are presented in Figure D.4. The asymmetric O=C=O stretching vibrations at 1399 cm^{-1} and symmetric carboxylate groups at 1576 cm^{-1} are observed in the figure. These peaks belong to the terephthalic acid, the organic linker in UiO-66. Terephthalic acid has benzene rings as seen at 1507 cm^{-1}. In

general, the peaks of the UiO-66/GNP composite are compatible with UiO-66. However, two peaks, -CH- stretching peaks at 2926 and 2855 cm^{-1}, have disappeared, and the intensity of the -OH peak at 3432 cm^{-1} has increased after the composite formation.

PS adsorption tests are also performed to see if MOF addition improves the PS chemisorption. As seen in Figure 4.28, a significant color change is observed for UG-5, and a slighter change is observed for UG-3, whereas the rest remains at a similar color to the blank solution. The solution with UG-5 being almost colorless clearly proves the binding of the PSs with the MOF-containing composite only if enough MOF is present in the composite to capture the PSs effectively.

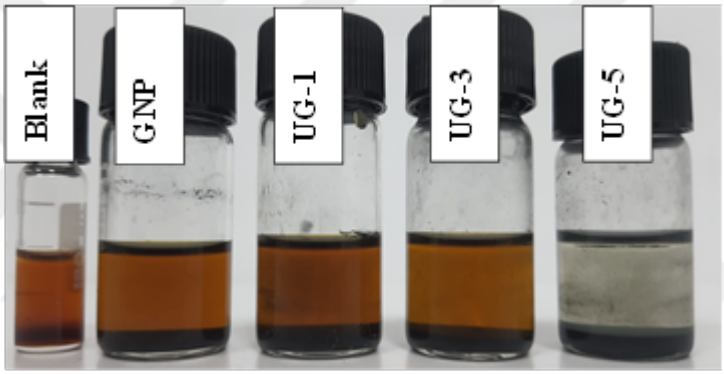

Figure 4.28. PS adsorption capabilities of GNP, UG-1, UG-3, and UG-5, respectively.

Electrochemical characterization tests are performed to determine the effect of MOF/GNP ratios on the electrochemical performance of Li-S cells. First, the measurements are performed for a low sulfur loading of 1 mg/cm^2. Cycling performances of the UGS composites, bare UiO66-S, and GNP-S at 0.1C are given in Figure 4.29a. As the figure shows, apart from the UiO66-S composite, all cells performed similarly. Significantly lower capacities obtained for the cells with UiO66-S-based cathodes can be attributed to the low electronic conductivity of the MOF, hindering the electrochemical reactions. This result indicates that the presence of GNP in the composite is required to achieve high cycling performance.

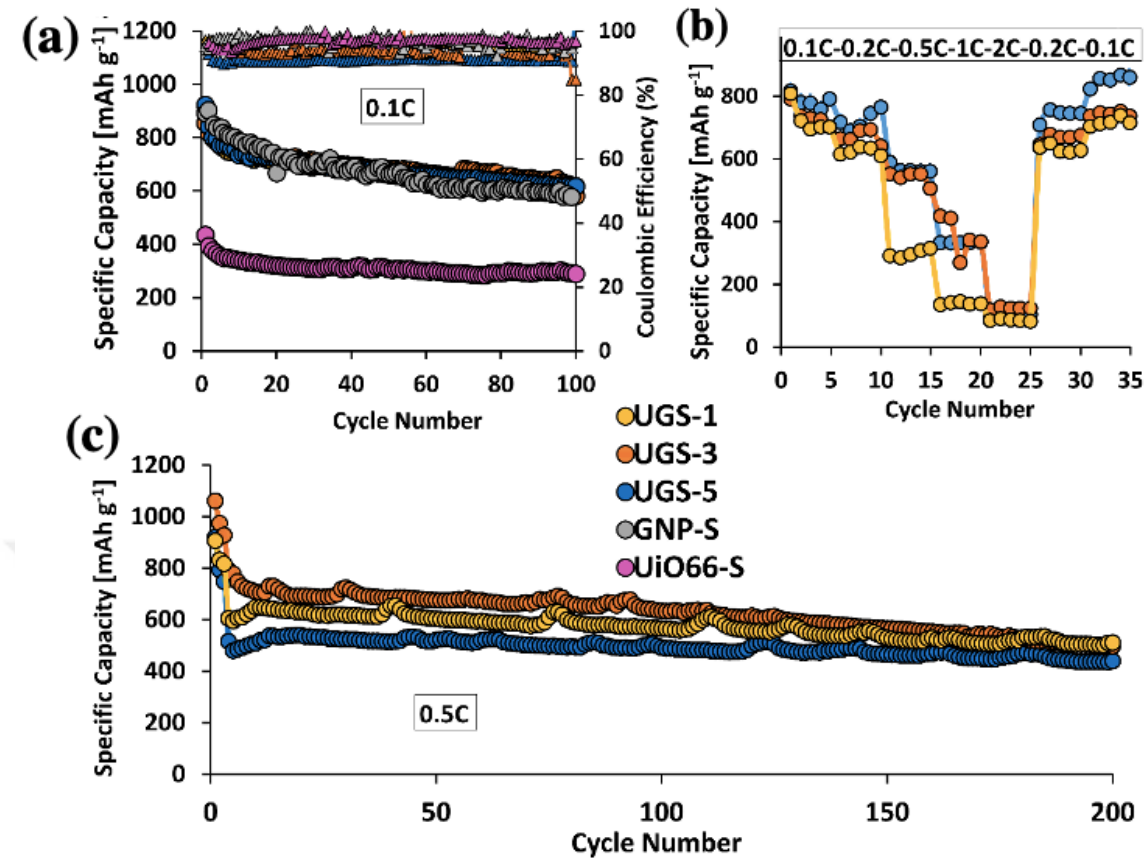

Figure 4.29. For Li-S cells with an S loading of 1 mg/cm^2: cycling performance at 0.1 C (a), rate performance (b), and cycling performance at 0.5 C (c).

The rate performance results in Figure 4.29b show that although MOF/GNP composites perform similarly at 0.1C and 0.5C, UGS-1 is less successful in retaining its capacity at higher C-rates. Nevertheless, cells with all three composites show remarkable rate capability, returning to the original capacities when the cycling rate is returned to 0.1C. These results are also confirmed by a longer cycling test, conducted at a higher C-rate of 0.5C, given in Figure 4.29c. When the C-rate increases to 0.5C, the composites show slightly different capacities at the earlier cycles, UGS-3 containing cell, showing the highest capacities. However, after 200 cycles, all composites end up displaying similar capacities.

The effect of MOF/GNP weight ratio on the cell performance is more apparent when the sulfur loading is increased to 2 mg/cm^2; the results are given in Figure 4.30. The first striking result is that GNP-S containing Li-S cells, which show similar performance to the MOF-containing ones at low S loadings in Figure 4.30a, display the worst performance for higher S-loaded cells, proving the necessity of MOF addition into the composite for

achieving better cycling performance. Moreover, the UGS-1 cathode performs the worst among the UiO66/GNP composites in all testing conditions from both the capacity and the capacity retention perspectives. UGS-3 and UGS-5 lead to better cell performances at higher sulfur loadings and C-rates. For instance, the UGS-5-containing Li-S cell shows an excellent rate performance. The PS adsorption ability of UiO-66 can explain this observation. When the sulfur loading is higher, the adsorption of PSs gains more importance as the PS concentration in the electrolyte will be higher. Hence, the loading of polar UiO-66 should be higher to preserve the PSs on the cathode surface, thereby retaining the specific capacity. This is probably why GNP cathodes fail at capacity retention; a drastic decrease in the specific capacities is observed after a few cycles. Figure 4.30b and Figure 4.30c show that a MOF loading of 50 wt.% is needed for 0.5C and 1C rates; however, 30 wt.% also performs well at 0.5C. Hence, a minimum of 30 wt.% MOF should be added to the composite for improved performance.

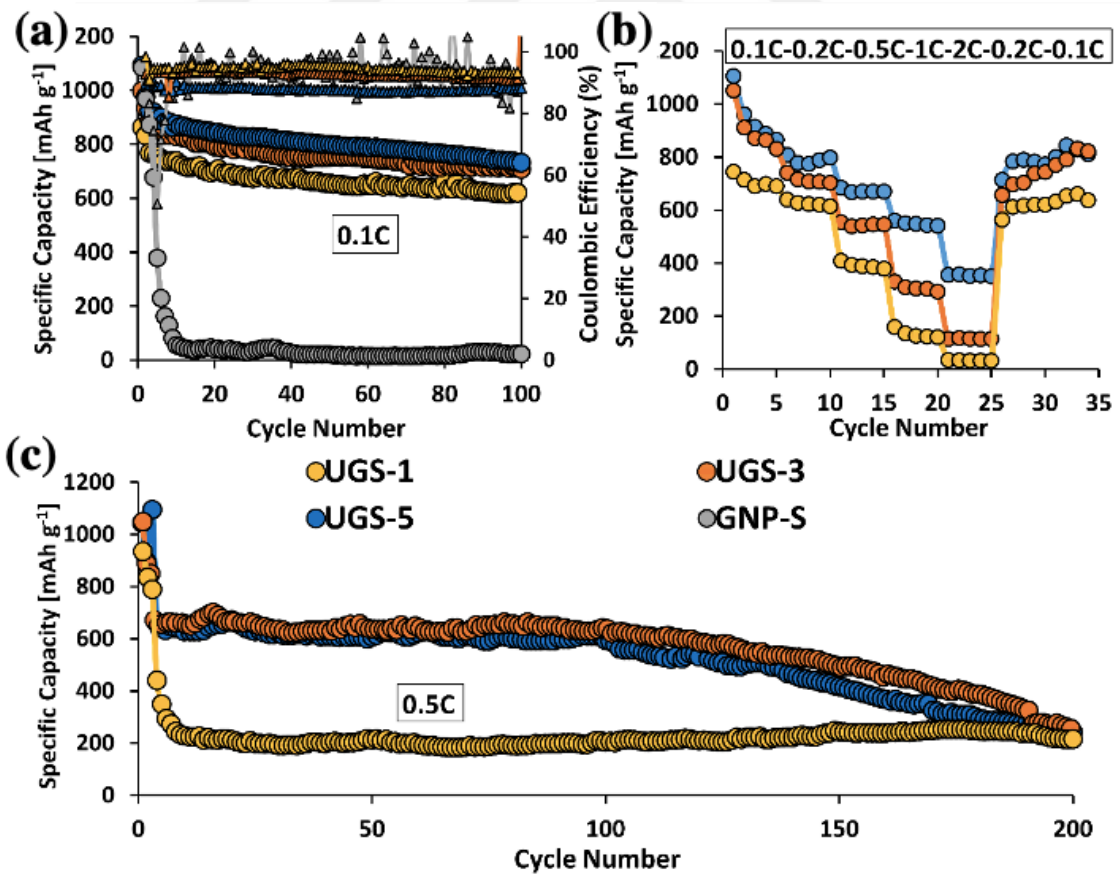

Figure 4.30. For Li-S cells with an S loading of 2 mg/cm^2: cycling performance at 0.1 C (a), rate performance (b), and cycling performance (c) at 0.5 C.

4.1.5. Effect of Atomic Vanadium- and Cobalt-Modified Ketjen Black-Sulfur Cathode, Sulfur Loading and Electrolyte-to-Sulfur Ratio on the System-Level Performances of Li-S Batteries

This section includes a modified version of the original research paper written by authors Hira Fazal, Damla Eroglu, Aysegul Kilic, Nazakat Ali, Changyu yan, Zai Jiantao, Xuefeng Qian [46]. The experimental studies were performed by H. Fazal and the system-level model application was performed by A. Kilic. It also contains the results of a proceeding study, which investigates the effect of the E/S ratio and sulfur loading on Li-S battery performance and system-level properties with the proposed material, where the latter was also performed by A. Kilic [47].

In this chapter, sulfur was encapsulated with atomic vanadium (V) and cobalt (Co) modified Ketjen black (VCKBS) to hinder the shuttle mechanism and enhance the redox kinetics in Li-S batteries. The synthesized composite provided plenty of interfacial active sites and assured smooth electron transfer, which assisted in attaining the balance of the enhanced catalytic activity due to Co and the adsorption ability mainly derived from V. Consequently, the Li-S cells having an optimized composition presented alleviated shuttle effect, enhanced sulfur utilization and conversion efficiency, and showed stable cycling performance and an outstanding rate performance with an initial capacity of 1329 mAh/g, which was maintained as 1249 mAh/g after 100 cycles. Due to impressive experimental specific capacities, the system-level specific energies and energy densities were also predicted for the 1^{st} and 100^{th} discharges. In the following study, we investigated the effect of cathode material by preparing two different cathodes: by encapsulating sulfur (S) with pure Ketjen black (KBS) and with VCKBS. In addition to the cathode material, the influence of crucial cell design parameters, namely the electrolyte-to-sulfur (E/S) ratio and sulfur loading, on the battery performance was also compared. A system-level performance model was used to estimate the system-level specific energies and energy densities.

4.1.5.1. Effect of Cathode Material on System-Level Performance of Li-S Batteries.

Insufficient electrolyte amounts or low electrolyte-to-sulfur ratios (E/S ratios) often lead to inadequate wetting of the electrode surface and continuous depletion of the electrolyte throughout the discharge-charge cycle, resulting in decreased capacity and low cycle life of

the Li-S battery. Conversely, excessive amounts of electrolyte result in a substantial increase in the overall weight/volume of the cell, thereby causing a reduction in the gravimetric/volumetric energy densities [85]. Similarly, S loading in the cathode controls the battery performance through discharge capacity, cycling performance, and system-level metrics. Moderate S loadings enhance the discharge capacity and cycle life, while high loadings are essential to improve the battery's energy density [86]. Consequently, to reach high performance, all other than the active materials should be minimized in the cell along with maximized specific capacity and cycle life. Hence, two groups of Li-S cells (Group 1: E/S ratio=20 mL/g, S loading=1.24 mg/cm^2 cycled at 0.1C, Group 2: E/S ratio=13 mL/g and S loading= 2.4 mg/cm^2 cycled at 0.2C) are compared to see the impact of the newly developed material on the energies of the Li-S cells and packs. To assess the cell- and system-level energy densities and specific energies of the Li-S batteries developed with the materials presented here, a modified version of the BatPaC model [199] developed by Argonne National Laboratory, is used with the experimental inputs, including capacity based on sulfur mass, the E/S ratio and sulfur loading. The summary of the model is given in Section 3.2 where the underlying equations and parameters of the model can be seen in detail. Battery pack system parameters, the number of modules, module configurations, and cell numbers in each module are assumed to be similar to a Li-ion battery pack. In contrast, a 1-dimensional, concentration-independent electrochemical model was implemented to determine the cell's voltage-current relationship. This model can estimate cell- and system-level energy densities (Wh/L) and specific energies (Wh/kg) as a function of materials properties and cell design parameters. The system-level specific energies and energy densities, given in Figure 4.31, are predicted using the experimental capacities for both the 1st and 100th discharge for Groups 1 and 2.

Energy densities of all cathodes for the 1st and 100th discharges are presented in Figure E.1. The superiority of VCKBS cathodes is already shown for both groups when the specific discharge capacities are compared; the percent increase of the initial discharge capacities by the introduction of VCKBS cathodes is 66 % and 158 % for Groups 1 and 2, respectively (Figure 4.31a). As seen in Figure 4.31 VCKBS cathodes significantly improve the system-level specific energies and energy densities as well. For instance, when the system-level metrics based on the initial capacities are compared in Figure 4.31b and Figure 4.31c, significant improvements are obtained, prominently for predicted specific energies. Since

VCKBS cathodes retain their capacity with cycling, when the 100th discharge capacities (Figure 4.31d) are used in the calculations, the percent increase in the specific energies and energy densities is more substantial than the ones based on the 1st discharge capacity. For instance, introducing VCKBS cathodes lead to 353% and 1342% improvement in the specific energies and 203% and 568% improvement in the energy densities for Groups 1 and 2, respectively (Figure 4.31e and Figure 4.31f). It is apparent that the enhancement in the system-level performance metrics is more prominent at the higher S loading and the lower E/S ratio (Group 2). This indicates that VCKBS cathodes synthesized in a facile manner would be advantageous for higher sulfur loadings at electrolyte-depleted cells; this is further investigated in the next section.

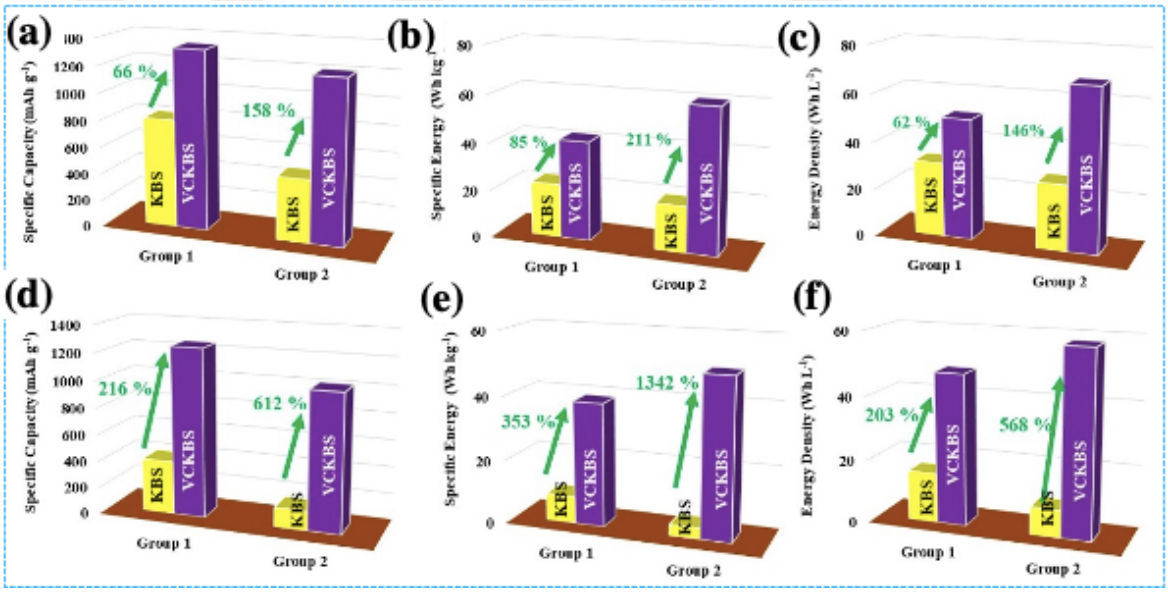

Figure 4.31. Specific capacities, system-level specific energies, and energy densities of KBS and VCKBS cathodes (Group 1: S loading=1.24 mg/cm^2, E/S ratio=20 mL/g, at 0.1C, Group 2: S loading=2.40 mg/cm^2, E/S ratio=13 mL/g, at 0.2C) for 1st discharge (a)-(c) and for 100th discharge (d)-(f).

4.1.5.2. Effect of E/S Ratio and S Loading on the System-Level Performance of Li-S Batteries with VCKBS and KBS Cathodes. Previous studies [355–357] often discuss optimal values for the S loading and the E/S ratio in a battery, maximizing the discharge capacity of the Li-S batteries. The cycling performance of Li-S cells with KBS or VCKBS cathodes (Table E.2) with E/S ratios= 6, 13, and 20 mL/g and S loadings of 0.8, 1.2, and 3 mg/cm^2 are compared in Figure E.2. For both cathodes, E/S ratio=6 mL/g and S loading=3 mg/cm^2

result in the poorest cell performance, which may be explained by the high internal resistance at lower E/S ratios and higher S loadings in the cell.

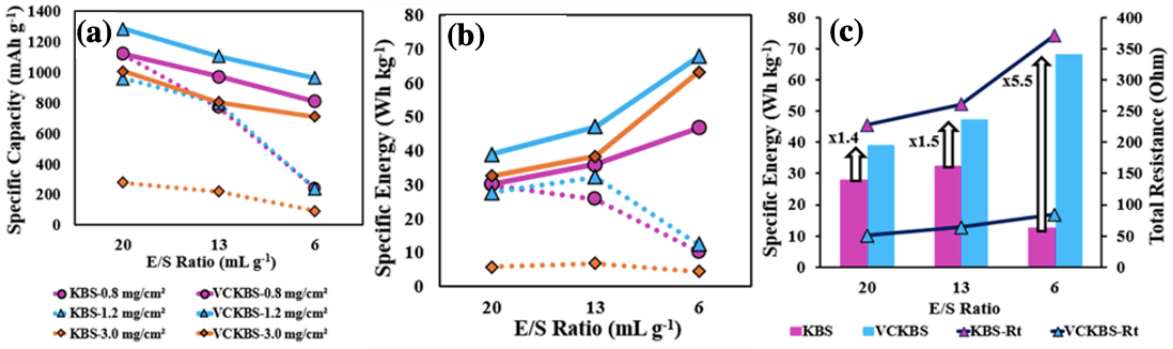

Figure 4.32. Experimentally measured initial discharge capacities (a), predicted system-level specific energies for various sulfur loadings and E/S ratios (b), and the relation between cell resistance and specific energies for sulfur loading = 1.2 mg/cm^2 (c).

Although high cell-level specific capacities and cycling performances are essential, system-level specific energy is a more viable performance metric for assessing the commercialization of Li-S batteries [358,359].A modified BatPaC model was used to estimate the system-level performance metrics with the experimentally obtained specific capacities, S loadings, and E/S ratios. Figure 4.32a shows a decreasing trend in specific capacity for lower E/S ratios and higher S loadings for KBS cathodes. In contrast, maximum capacity is obtained with an S loading= 1.2 mg/cm^2 for VCKBS cathodes. In contrast, corresponding system-level specific energies of Li-S cells containing VCKBS cathodes show an opposite trend to the specific capacity. Lowering the E/S ratio drastically increases the specific energies, with the highest specific energy obtained with a moderate S loading. In contrast, in Li-S batteries with KBS cathodes, the decrease in the specific capacity with decreasing E/S ratio and increasing S loading is too high, and the reduction in the cells' dead mass does not compensate for obtaining higher specific energies. Finally, Figure 4.32c summarizes the superiority of the VCKBS cathodes over KBS ones, presenting the higher specific energies obtained for these novel cathodes, especially at low E/S ratios. To sum up, tailoring cathode properties is critical for improved battery performance. The co-doping of Co and V elements boosts the catalytic ability of Co and the absorption ability of V simultaneously. The effect strengthens the intrinsic ability of the active sites. Thus, active sites in the modified KB can accommodate higher S loadings in the cathode. Moreover, since

cathode kinetics for the PS transfer are enhanced, lower E/S ratios and higher S loadings can be tolerated.

4.2. Li-O_2 Battery Studies

4.2.1. Determining the Key Performance Factors in Lithium-Oxygen Batteries Using Machine Learning

This part is modified from the original research paper published in the Journal of the Electrochemical Society by authors A. Kilic, Prof. R. Yildirim, and Prof. D. Eroglu [48].

Lithium-oxygen (Li-O_2) batteries are among the most prominent alternative battery chemistries to lithium-ion batteries with their high theoretical capacities. However, attaining their high theoretical capacity is difficult due to the poor cell design and insufficient cell materials. In this section, ML algorithms are used to determine the effective cell design factors and the most promising materials for reaching high discharge capacities and voltages.

4.2.1.1. Pre-Analysis of Data. Before presenting the results of the ML algorithms, the effect of materials- and cell-design factors are analyzed in this section using simple descriptive statistics to see the basic trends in the dataset. As mentioned in Introduction, Li-O_2 batteries are severely affected by the side reactions and degradation mechanisms. Hence, the utilization of specialized materials and designs are essential for reaching high capacity Li-O_2 batteries; in this section, the main materials groups covered in the dataset were discussed.

Having the highest standard oxidation potential of 3.040 V and the lowest molecular weight, Li metal is a promising anode material, which provides a specific capacity of 3860 mAh/g [10]. The main disadvantage of a Li anode is the high reactivity of the lithium metal. The reaction of lithium with oxygen and water, and the formation of lithium dendrites as a result of its interactions with the electrolyte are the major challenges that cause low Coulombic efficiency and poor cycling performance [360]. To protect the lithium anode and to prevent the formation of dendrites, special surface treatments or coatings are employed in the literature [361–363]. Since the stability of the lithium anode is essential for improved battery performance, anode material is taken into consideration in the analysis. “Modified

Li anode" category is defined if there is any additional treatment or material employed on the lithium metal. Only 46 datapoints are in the Modified Li anode category, whereas 969 datapoints use pure lithium metal.

The conventional separators used in the batteries are porous structures with pore sizes of hundreds of nanometers. Polyolefins are accepted as the ideal separators for the LIBs, which provide high stability with low cost. However, post lithium-ion technologies need further improvement in the separator materials to achieve durability in the harsh working conditions [34]. Li-O_2 batteries use pure oxygen or air as the reactant in the cathodes. Due to safety and efficiency reasons, reaching of these gaseous reactants to the Li anode should be prevented [364]. With this respect, separator type is taken as one of the variables in this analysis. In the dataset used in this section, 59 % of the data uses glass separator, whereas 23 % uses polymeric separator; various separator materials are employed in the remaining cells.

One of the main advantages of the Li-O_2 batteries is that they do not require to store the active material inside the cell. Li-O_2 batteries can operate with either pure oxygen or air taken from outside. Although oxygen is used in most of the cases in the dataset, probably the use of air will be preferred in future because it will be more practical and safer. Yet, if the oxygen is supplied from air, impurities like H_2O and CO_2 can also penetrate into the cells and cause side reactions both in the cathode and the anode, and consequently, may result in cell failure and safety problems [365]. These problems and the underlying mechanisms are analyzed in the literature to some extent. However, the majority of the studies use pure oxygen as the reactant to eliminate the possible side reactions in lab-scale Li-O_2 cells; indeed, the percentages of the use of oxygen and air in the dataset are 80.2 % and 9.5 % (remaining 9.0 % is dry air and 1.4 % is O_2:CO_2 mixture), respectively. Finally, to further simplify the process 91 % of the data use 1 atm as the reacting pressure.

In this section, cathode support is defined as the "bulk cathode material", which generally provides electrochemically active surface area in the cathode, whereas a common name "cathode ingredient" is given for the additional materials, which typically show catalytic activity. Since the active material is gaseous in Li-O_2 batteries, it should spread homogenously over the positive electrode and be reduced with the upcoming electrons from

the anode. In this respect, a solid network is provided in the cathode by using porous materials with high surface area and electronic conductivity. Moreover, this network should be stable enough against the electrolyte and the operating conditions of these batteries [366, 367]. In some papers, additional metals or metal oxides are used in the cathodes for catalytic purposes. It is reported in the literature that electrocatalysts strongly determine the power density and cyclability of the battery by affecting the oxygen reaction mechanisms [38]. Hence, these two variables are included in the analysis. The distributions of bulk cathode and ingredient materials in our dataset are shown in Figure 4.33; as it is seen, carbon black is used in more than half of the dataset as the bulk cathode material, which is followed by CNT and graphene. On the other hand, 60.2 % of the dataset does not use any additional materials in their cathodes. Among the cathode ingredients, Mn oxides and Co oxides are the most preferred materials.

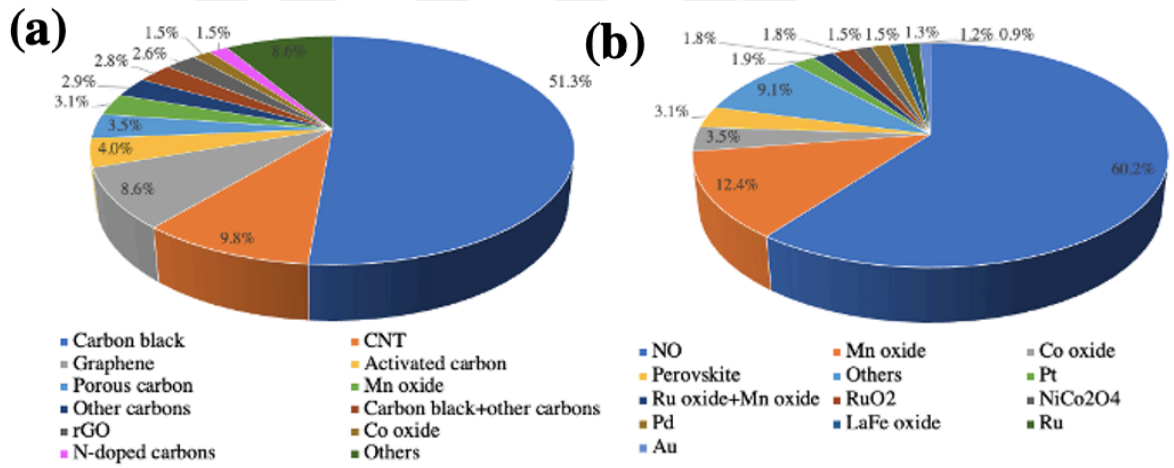

Figure 4.33. Distribution of active materials (a) and ingredients (b) used in the cathode.

The stability of a Li-O_2 battery also depends on the binder used in the cathode. Conventional binders such as PVDF may react with super oxides to give by-products since they are present on the surface of the cathode rather than in the bulk [368]. These by-products eventually react with metal oxides leading to the formation of LiOH, which may accumulate in the cells [369–371]. Hence, choosing a stable binder is critical for improved cycling behavior of Li-O_2 batteries. Figure 4.34 shows that 37% of the data in our dataset uses PVDF as a binder, whereas 20 % does not use any binder in the cell.

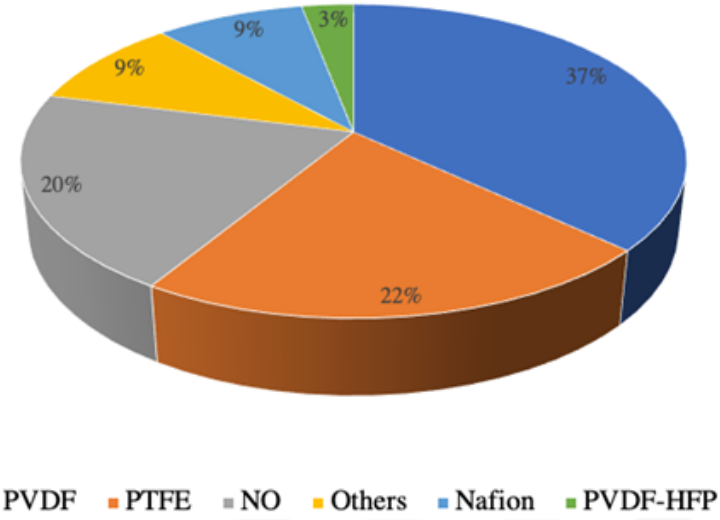

Figure 4.34. Distribution of binder materials in the cathode.

As stated in the above, a typical cathode consists of a bulk cathode material, an ingredient and a binder in a Li-O_2 battery. Although using a binder in the cathode improves the structural integrity and the physical stability of the cathode, it also increases the dead mass of the cell. Moreover, using too much binder can decrease the porosity of the cathode [372]. Hence, the ratio of the active material to the binder should be optimized to provide high surface area for the electrochemical reactions while achieving high cathode stability. Similarly, sufficient active material loadings should be supplied to the cells for high electronic conductivity and active surface area [373]. In order to examine this critical connection, both active material loadings and percentages in the cathode are taken into consideration in our analysis. In this section, the gas diffusion layer is defined as the additional porous medium, which is typically carbon paper that is placed in between the cathode and the current collector. Since efficient and homogeneous diffusion of oxygen into the cathode is crucial for enhanced performance, the use of a gas diffusion layer in the cell improves the cell performance [39,40]. Therefore, the effect of gas diffusion layer on the battery performance is also investigated here.

The electrolyte system plays a key role in Li-O_2 batteries for enhanced capacities. Since these batteries are exposed to oxygen environments, several criteria such as low vapor pressure of solvents, high electrochemical stability of salts and solvents in the presence of oxygen, high dielectric constants and high oxygen solubility and diffusivity should be met for an electrolyte system to be considered as promising [374]. Hence, selecting an ideal

electrolyte is important for achieving high cycling stability and rate capability in Li-O_2 batteries.

Depending on the electrolyte selected, Li-O_2 batteries can be divided into four as aqueous, non-aqueous, solid state and hybrid. There is a vast difference between these batteries in terms of stability, oxygen solubility and diffusivity. The literature mainly consists of cells with non-aqueous solvents since these electrolytes perform better than the others in terms of the aforementioned characteristics [35–37]. Figure 4.35a shows that tetraglyme, DMSO and DME are the most widely used electrolyte solvents in the literature. Electrolyte salts are also determinative of the final oxygen solubility, electrolyte viscosity and wettability [375,376]. Figure 4.35b presents the distribution of salts used in the electrolytes in this dataset; LiTFSI is the most commonly used electrolyte salt. In addition, some papers use additional salts or redox mediators to increase the stability of electrolytes [377,378]. These are all included in the electrolyte additive group. However only the presence of the additives is taken into account (6.7% of data contains an additive) in the analyses; specific types of the additives are not considered due to their large variety with rare appearance.

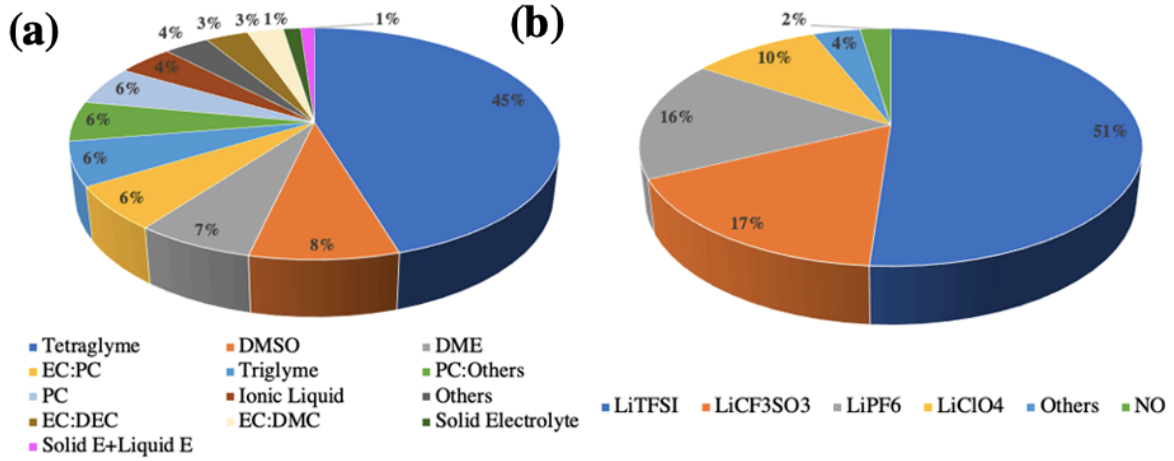

Figure 4.35. Distribution of electrolyte solvents (a) and salts (b).

4.2.1.2. Discharge Capacity Analysis with ARM. The ARM results, in which the factor categories (antecedents) leading to capacities equal to or higher than 3000 mAh/g (consequents) with descending order in terms of lift, are presented in Table 4.9. By definition, lift values higher than one signify that the corresponding categories have higher

probabilities to provide the desired capacities than that of entire dataset. However, there should also be sufficient number of data points for statistical significance; hence, the other parameters (support, confidence and count) are also important. Additionally, we provide the number of data points obeying the rule in each row as count in the last column. Only the rows (i.e. factor categories) having more than five data points are presented and discussed here for the statistically significant conclusions; the complete results of ARM analysis are given in Table F.3 for the readers who are also interested in less frequently employed materials with high lifts as the new but potentially promising materials appear so. Moreover, the categories are marked by "*" in the table if all data is extracted from a single article to warn the reader for the possibility of experimental bias.

In Table 4.9, it is shown that the highest lift with a sufficient count number is obtained for the cathode ingredients and bulk cathode materials. Among them, LaFe oxide can be given as an example to better understand the table. In our dataset, there are 8 LaFe oxide datapoints, which provide capacities higher than or equal to 3000 mAh/g. The total number of datapoints used in this analysis is 773, and only 269 of those provide high capacities. The support is 8/773 =0.0103 (i.e. the number of cases that use LaFe oxide and have high capacities divided by the total number of datapoints in capacity testing set); the confidence is 8/269=0.0297 (i.e. the number of datapoints using LaFe oxide and have high capacities divided by the total number of high capacity data in capacity testing group). Since the total number of datapoints using LaFe oxide as the ingredient is 10 in the entire data set, the lift can be calculated as (8/269)/(10/773) leading to the value of 2.30. From the formula presented, it can be easily seen that the fraction of the cells using LaFe oxide in the high capacity data is 2.30 times higher than the fraction of the cases with LaFe oxide in the entire dataset. Here, a lift value of one indicates the lack of a correlation between two variables (i.e. the use of a factor versus capacity), while values higher than one indicate a positive correlation (higher the lift, stronger the correlation is). On the other hand, lift values between one and zero imply negative correlations. Consequently, lift indicates the possible positive correlations and the strength of the correlation, while support (how much of the total data supports the rule) and confidence (how much of the cases containing that input variable supports the rule) reveal the reliability of the rule.

Table 4.9. ARM results for capacity testing group for capacities higher than or equal to 3000 mAh/g with count numbers greater than or equal to 5.

Descriptors	Support	Confidence	Lift	Count
{Bulk_Cathode_Categorized=N-doped carbons}	0.0078	0.0223	2.87	6
{Ingredient_Categorized=NiO+$NiCo_2O_4$ microspheres }	0.0091	0.0260	2.87	7*
{Ingredient_Categorized=LaFe oxide}	0.0103	0.0297	2.30	8*
{Salt_E_Categorized=Others}	0.0259	0.0743	1.98	20
{Bulk_Cathode_Categorized=Graphene}	0.0556	0.1599	1.96	43
{Ingredient_Categorized=Perovskite}	0.0246	0.0706	1.88	19
{E_Solvent_Categorized=Triglyme}	0.0466	0.1338	1.88	36
{Bulk_Cathode_Categorized=Graphene oxide}	0.0091	0.0260	1.83	7
{E_Solvent_Categorized=DMSO}	0.0530	0.1524	1.79	41
{Bulk_Cathode_Categorized=Porous carbon}	0.0233	0.0669	1.78	18
{Reactant_Categorized=Others}	0.0103	0.0297	1.77	8
{Gas_Diffusion_Layer_Categorized=Carbon paper}	0.1164	0.3346	1.71	90
{Bulk_Cathode_Categorized=Carbon black+other carbons}	0.0129	0.0372	1.69	10
{Ingredient_Categorized=Others}	0.0103	0.0297	1.64	8
{Salt_E_Categorized=NO}	0.0103	0.0297	1.53	8
{Active_Material_Loading_Categorized=[0.8-1.2)}	0.0802	0.2305	1.50	62
{Bulk_Cathode_Categorized=N-doped CNT}	0.0078	0.0223	1.44	6*
{E_Solvent_Categorized=Tetraglyme}	0.1889	0.5428	1.41	146
{Active_Material_Loading_Categorized=(0-0.8)}	0.1100	0.3160	1.30	85
{Bulk_Cathode_Categorized=rGO}	0.0116	0.0335	1.29	9
{Binder_Categorized=PVDF}	0.1617	0.4647	1.28	125

The ARM results show that the selection of the cathode material is the most determining factor on the capacities of the Li-O_2 batteries. The use of special oxide materials such as LaFe oxide, Ni oxide or perovskite as cathode ingredients and N-doped carbons, graphene and graphene oxide as bulk cathode materials have led to high capacities. The choice of DMSO or triglyme as the electrolyte with specialized salts seems to be also beneficial. To refine the rules for high capacities better, the ARM analysis is also performed by defining additional (stricter) limits for high capacity class (A) as equal to or higher than 5000 mAh/g, 7000 mAh/g and 10000 mAh/g. Since these definitions are cumulative (i.e. equal to or higher than 5000 mAh/g class also contains 7000 mAh/g and 10000 mAh/g classes), the total number of datapoints is decreasing with the increasing limits; hence, the increase of lift for a factor category indicates that the number of high capacity data having

that factor decreases less than the total number of datapoints. This may be used as a further indicator (in addition to the results in Table 4.9) for the potential benefit of that factor category. The results are presented as the high capacity class limits versus the lift in Figure 4.36, where the bubble size demonstrates the count (number of datapoints obeying that rule).

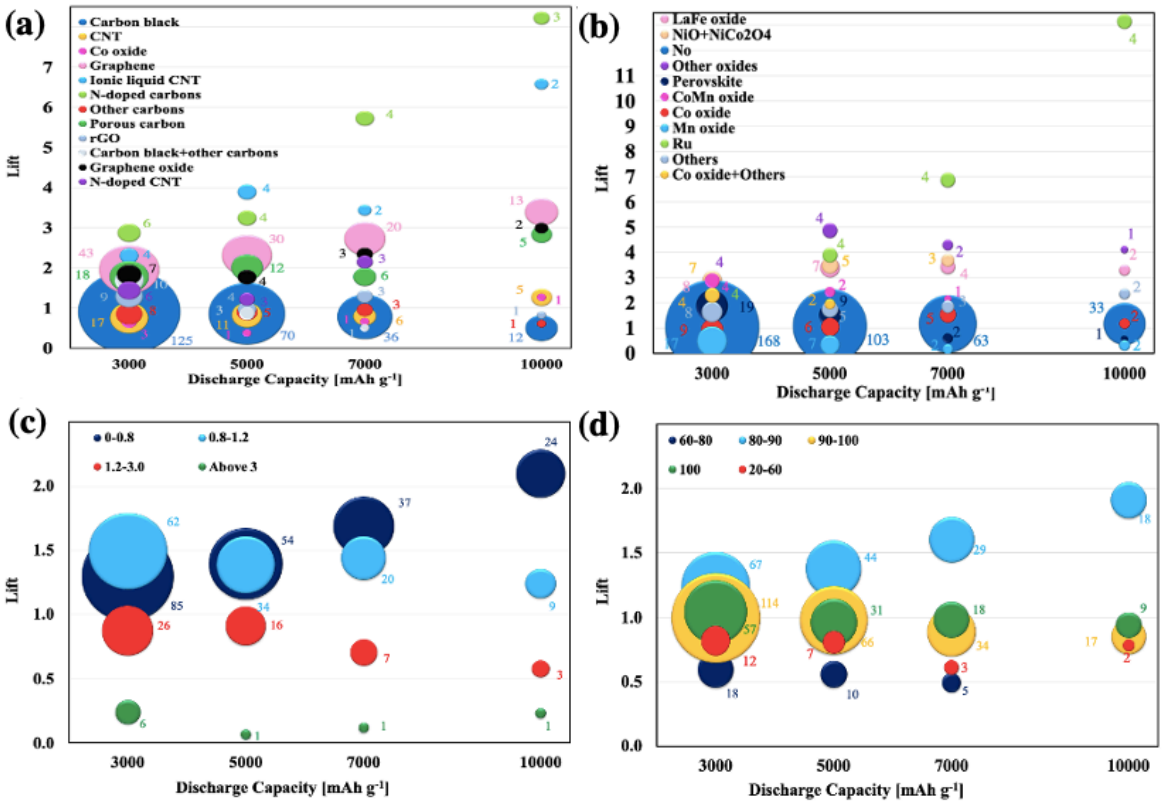

Figure 4.36. Change of lift with changing limits of high discharge capacity for bulk cathode materials (a), cathode ingredient materials (b), active material loadings (mg/cm^2) (c), and active material weight percentages (d) in the cathode.

As seen in Figure 4.36a, carbon black is one of the most widely used bulk cathode material in Li-O_2 batteries; however, having a lift around one that does not change with increasing capacity limits, shows that other (likely new) cathode materials may be leading to higher capacities. Indeed, there are eleven options other than carbon black, and among them, N-doped carbons, graphene, graphene oxide and porous carbons seem to be working better. Since, the IL CNT category comes from a single article, its effect cannot be generalized at this stage even though this material also seems to be promising. The results of the analysis show that combined use of carbon black with other carbon structures such as graphene or CNT also provide capacities higher than 3000 mAh/g. However, this increase

could not be attained with increasing class limits, as it is evident from the decrease of the lift values even lower than that of carbon black alone in Figure 4.36a.

Although the majority of the papers did not use additional cathode ingredients, the ones that did cannot be ignored because such additives seem to have significant effects on the capacities as it is shown in Figure 4.36b. Mn oxide and Co oxide are the most widely used cathode ingredients (as shown in Figure 4.33) However, other oxides seem to provide better performances (different oxides mixed with Co oxides also improve the capacity). For example, LaFe oxides, Ni oxides and Ru are the most promising cathode ingredient materials.

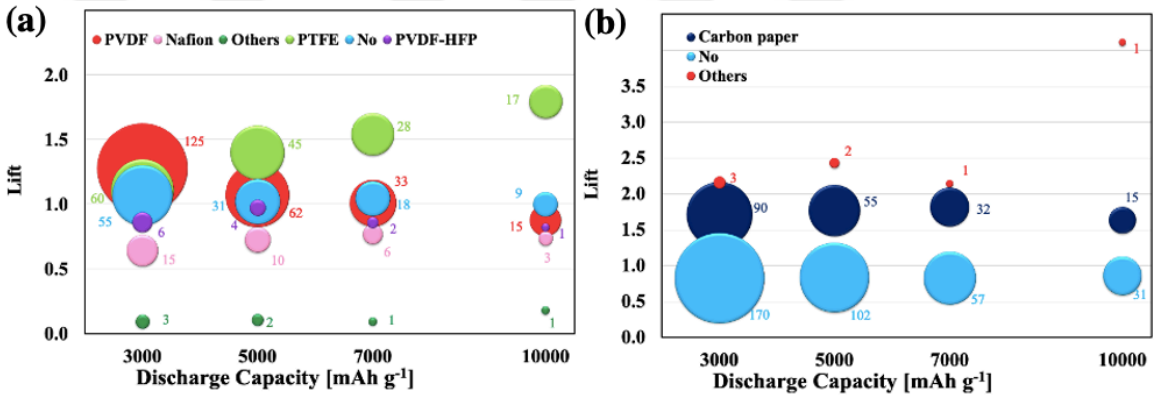

Figure 4.37. Change of lift with changing limits of high discharge capacity for binder type (a) and gas diffusion layer materials (b) in the cathode.

As stated in the pre-Analysis section, active materials are defined in this study as the bulk cathode support and the ingredient. The binder is not considered as an active material in the cathode; it is treated separately as discussed later. Although sufficient amount of active material is important to provide enough surface area for the oxidation and reduction mechanisms and the precipitation of the discharge product Li_2O_2, apparently, there is a limit for this. Figure 4.36c shows that the active material loadings should be no more than 1.2 mg/cm^2; the probability to have low capacities seems to increase at higher loadings. This may be due to limited oxygen transport and increased oxygen gradient in thick cathodes; the limited active material utilization at high cathode loadings may result in low capacities [379]. Figure 4.36d presents that the cathode should contain a binder for high performance batteries. On the other hand, the use of an excess amount of binder can also lead to low

performance; to achieve high capacities, binder weight percentage should be around 10-20 % (i.e. active material should be around 80-90 %). PVDF, which is the most widely used binder in the literature, seems to have a decreasing lift with increasing capacity limits, whereas PTFE shows a continuously increasing trend suggesting its effectiveness (Figure 4.37**a**). PVDF-HFP, Nafion and the other binder materials, which are not presented here, do not have positive effects on the capacity. Finally, it can be stated that the use of an additional carbon paper next to the current collector as the gas diffusion layer improves the battery capacity (Figure 4.37b).

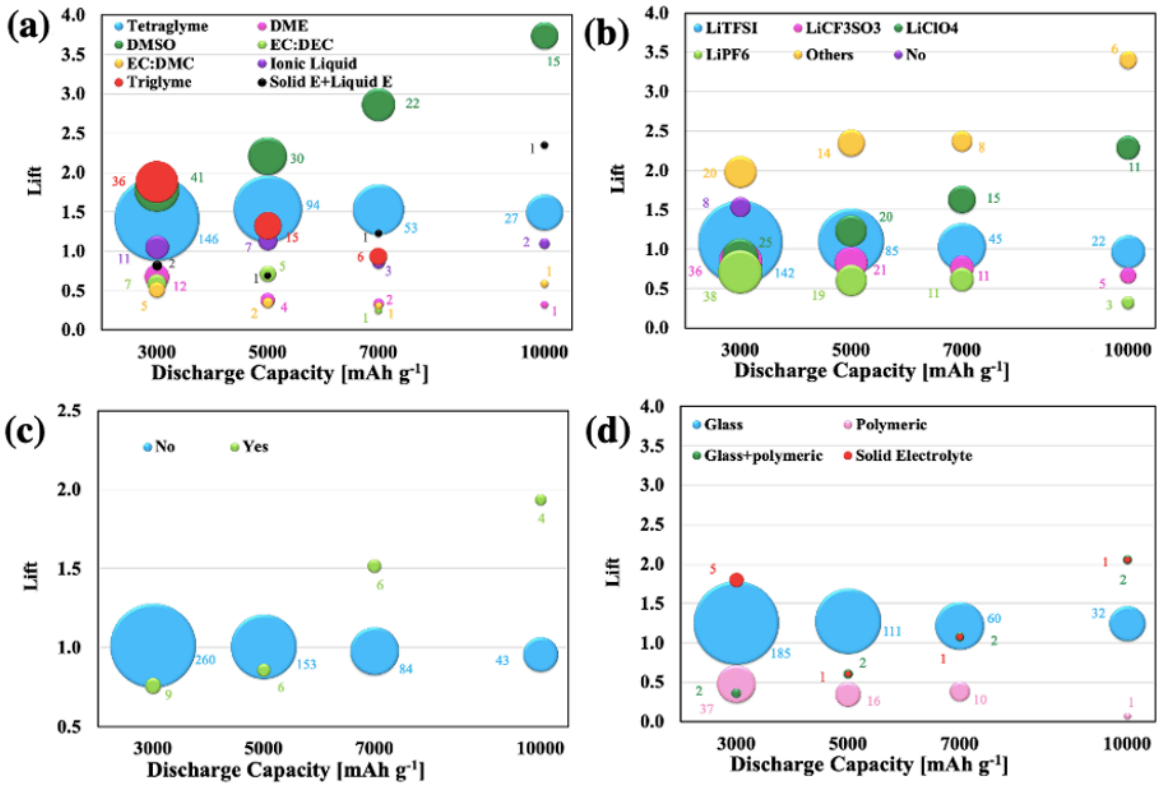

Figure 4.38. Change of lift with changing limits of high discharge capacity for electrolyte solvent type (a), salt type (b), the presence of an additive (c), and separator type (d).

Another important component of the Li-O_2 batteries is the electrolyte, which consists of the solvent, salt, and additives. Since non-aqueous batteries are more common and therefore constitute the entire dataset used in the analysis, their comparison with aqueous solvents is not possible here. However, the electrolyte ingredients could still be compared with each other. As seen in Figure 4.38a, DMSO is by far the best candidate for obtaining high capacities providing lift values more than 3.5 at a capacity target of 10000 mAh/g;

hence, it can be used to replace the conventional electrolyte, tetraglyme, which has lift values slightly higher than one. The other alternatives are not effective as seen in Figure 4.38a**.** The ARM results suggest the use of $LiClO_4$ and some other alternative salts (including LiTFSA, LiTFI and Li[NTf2]) instead of more commonly used LiTFSI, $LiCF_3SO_3$ and $LiPF_6$ (Figure 4.38b). When an electrolyte salt is not used, obtaining capacities higher than 3000 mAh/g does not seem possible. The addition of electrolyte additives into the electrolyte also improves the specific capacities as expected because they are generally redox mediators, which decrease the parasitic reactions in the cell (Figure 4.38c). Finally, the glass separator seems to be a better option compared to the polymeric alternatives (Figure 4.38d).

4.2.1.3. DT Analysis for Combined Factor Effect. ARM, as implemented in the previous section, is helpful to see the individual effects of the individual factors; however, these factors, for example materials, will be employed together as combinations (i.e. as the electrolyte solvent and salt together). Hence, it is also important to investigate and understand their best combinations to improve the battery performance. In this respect, the DT analysis was used to generate heuristic rules for the selection of these combinations for the Li-O_2 batteries with higher capacities. As stated in the Materials and Methods section, the dataset was divided into three classes according to the specific capacities as Class A, B and C for *high* (≥6000 mAh/g), *intermediate* (6000-1500 mAh/g) and *low* (<1500 mAh/g) capacities, respectively. As also mentioned in computational details, we restrict our DT analysis to the data obtained for cells discharged at 0.1-0.5 mg/cm^2 and uses oxygen at 1 atm as the reactant.

The optimum tree structure is given in Figure 4.39. The overall classification accuracy for training is 78%, which is an acceptable value, indicating that the tree correctly classifies 78 % of the total data. The recall for individual classes (fraction of data in class X that was correctly classified as class X) are given in the confusion table in Appendix F together with the class precisions (fraction of actual class X cases in the data that were classified as class X). For example, recall of class A is 74%, while its precision is 88 %; both are relatively high for reliable generalizations. Likewise, the recall and precision of class C are 89% and 75%, respectively while the recall and precision of class B are 73% and 72%, respectively. The DT model was also tested using the testing data that was not used during the model construction; the overall testing accuracy was 76 %, which is quite good. Similarly, the

testing recall and precision of class A (83% and 77 %, respectively) and class C (79% and 77 %, respectively) are also quite satisfactory. Relatively low recall and precision for class B (both are 65%) are expected due to the leaks from both sides; however, this should not be a problem because one usually wants to know the rules for high (to know what to do) or low (to know what to avoid) performances, not the intermediate.

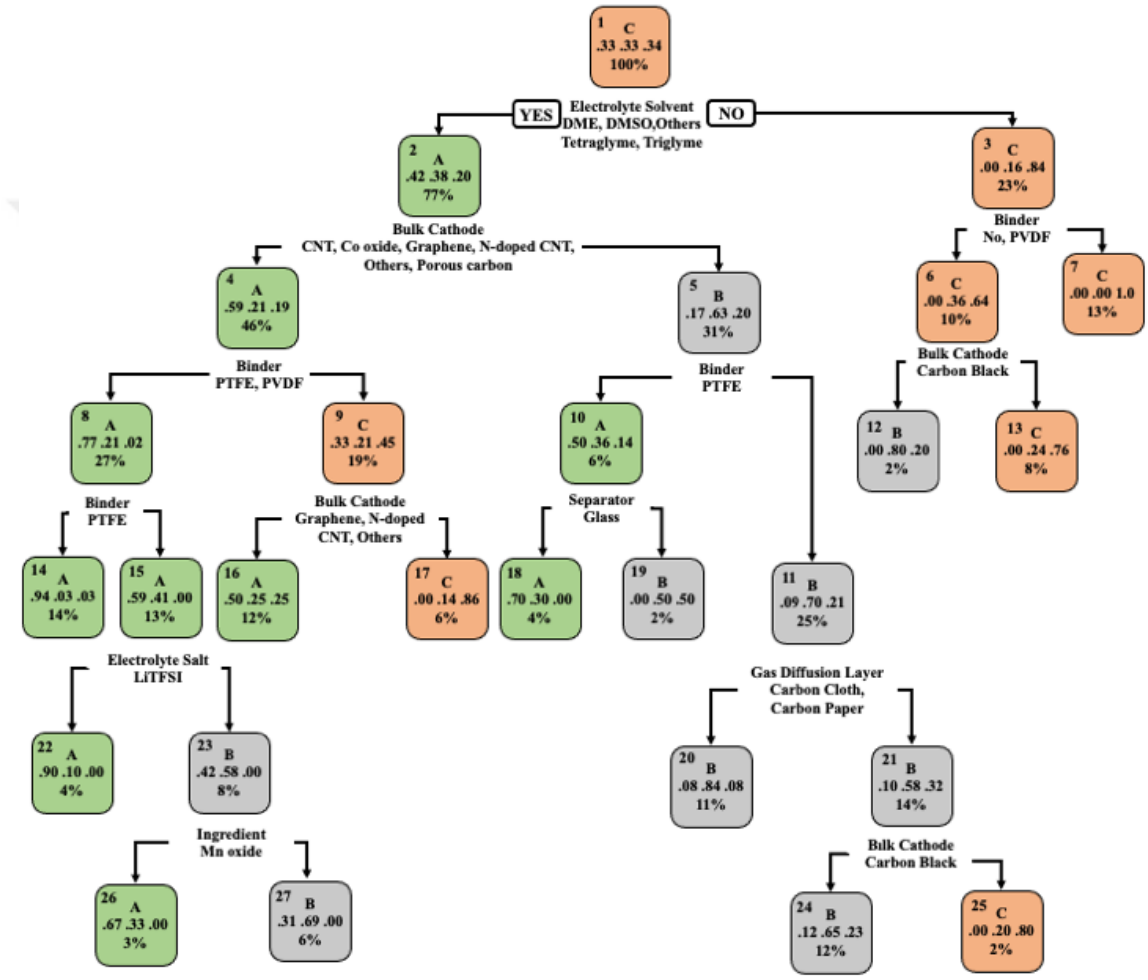

Figure 4.39. Decision tree analysis for Li-O_2 batteries.

Since we use DT to deduce heuristic rules for high performance, the high precision of class A is important because it indicates whether *apparently* favorable set of variables is indeed favorable for class A performance (requiring high precision). Failure to identify one good set of variables may not harm if we find another one to work on (as contrary to the fact that labeling an unfavorable set as favorable will lead to wrong actions). Hence, the heuristic

rules for class A, especially the ones those derived from the terminal nodes having large number of cases with high purity in class A, as explained below, should be reliable.

The numbers at the bottom of each node in Figure 4.39 indicate the fraction of total data obeying the conditions stated so far in that branch, while the fractions in the middle line show the fractions of class A, B, and C (from left to right). The letter and the color represent the dominant class in each node for visualization. Naturally, the top node contains 100 % of data with almost equal fractions of classes, and the total number of data in the nodes decreases with each split, while the fraction of one class increases (purification). The division criteria used by the tree from the top node to a terminal node in a branch can be considered as a heuristic rule to have similar results to those in that terminal node. To have a reliable rule or heuristics, the number of cases in a terminal node should be sufficiently large and the purity of the node (i.e. fraction of one class) should be as high as possible.

The first division is based on the electrolyte solvent; the data with DME, DMSO, Others, tetraglyme and triglyme are sent to the left while the other electrolyte solvents are sent to the right (the data in Class A will likely to be purified in the left nodes while the Class C will be mostly on the right). After the first node, the DT uses the bulk cathode materials showing that the presence of CNT, Co oxide, graphene, N-doped CNT, others and porous carbon lead to Node 4 on the left containing 46% of data with 59% purity in A. This node is further purified into the first terminal (Node 14) by selecting first PVDF and PTFE and then PTFE as binder. This is the most important rule obtained from this tree since both the node size (14 percent of total data) and purity (94%) in class A are sufficiently high to generalize the decision criteria used to reach this node. The remaining data in this branch is divided more using LiTFSI as the electrolyte salt. This rule resulted in Node 22, which still has a reasonably high purity (90%) close to that of the first terminal node (Node 14); hence, this can be also used as another heuristic rule. The conditions leading to the rightmost terminal node (Node 7) may also be used for *not to do* because it contains 13 % of data with 100% purity in the low capacity class (class C). The results in this node indicate that the use of carbonate electrolytes such as PC, EC:DEC and EC:DMC with PTFE or nafion as binders results in very low capacities; hence, the combination of these materials should be avoided in Li-O_2 batteries.

The aim here was to develop heuristic rules for high capacity batteries, and the tree is quite successful for this; however, some additional information can also be extracted related to the relative importance of the individual factors by inspecting their utilization frequencies during the construction of the tree. Although it is not an absolute rule, the most frequently used variables (especially if they are used close to the top node) should be relatively more influential for the capacity. Indeed, electrolyte solvent, bulk cathode material and gas diffusion layer are the most influential three variables for this tree; these variables were also found to have high lifts in the ARM analysis (Table 4.9) as expected.

4.2.1.4. Cut-Off Voltage Analysis with ARM. ARM analysis is also performed for the cut-off voltage dataset to determine the important factors for achieving voltages higher than 2.75 V. The results for capacity range of 750-1000 mAh/g and 500-750 mAh/g are presented in Table F.4 and Table F.5**,** respectively, in Appendix F; the same factors were found to be significant in both cases even though their exact orders slightly changed. This dataset contains less number of data (242 points) compared to discharge capacity dataset (773 points) discussed in the previous section; hence, counts in ARM for the factors are much lower (meaning that the reliability is also lower). However, the performance of various alternative materials can still be compared. For instance, the bulk cathode materials and ingredients seem to be the most effective factors on the cell voltage with their high lift values (this was also the case for the capacity testing group). In addition, PTFE as a binder, DMSO as an electrolyte solvent and 0-0.8 mg/cm^2 active material loading can lead to enhanced cell performance of Li-O_2 batteries.

4.2.2. Screening of Ionic Liquids as Electrolyte of Metal-Oxygen Batteries using COSMO-RS and Machine Learning

Designing an efficient electrolyte system is critical for commercializing metal-air batteries where ionic conductivity and gas solubilities, especially oxygen, are the primary concerns. Among various alternatives, due to their safe nature and tailorable properties, ionic liquids (ILs) have the potential to be used as electrolytes of metal-air batteries. Since many ILs are possible, assessing their gas solubilities before using them in batteries is essential. This section focuses on building ML models for predicting the gas solubilities of ionic liquids (ILs) and screening promising candidates for metal-air battery electrolytes.

COnductor-like Screening MOdel for Realistic Solvents (COSMO-RS) method, using the COSMOThermX program, is utilized first for quick screening of gas solubilities, including oxygen, water, nitrogen, and carbon dioxide, in addition to physical properties of ILs. The structural descriptors and molecular fingerprints, calculated using RDKit, an open-source cheminformatics software, are used to build predictive models for gas solubilities.

4.2.2.1. Importance of Gas Solubilities on Metal-Air Cells. Figure 4.40 shows a metal-air cell structure during discharge and presents the electrolyte's role; here, an IL electrolyte with an anion-cation pair is illustrated. First, atmospheric gas is distributed over the cathode by passing through a gas diffusion layer and dissolving in the electrolyte solution. Meanwhile, metal ions (M^{+n}) coming from the negative electrode through the electrolyte medium and dissolved oxygen react with the help of a catalyst on the surface of the positive electrode with the electrons supplied through the outer circuit. Oxygen only participates in the electrochemical reactions if dissolved in the electrolyte, providing reversible capacity gain. Hence, high electrolyte oxygen solubility is critical for metal-air batteries [380]. In contrast, low solubility to the other atmospheric gases, including carbon dioxide, nitrogen, and water, is necessary to prevent side reactions in the metal-air battery cathode. It is stated in the literature that CO_2 and H_2O in the air may cause side reactions where LiOH and Li_2CO_3 are produced, and when the concentration of these side products increases, the cell suffers from high over-potential and short cycle life. N_2 solubility should also be restricted to preserve the stability of the solid-electrolyte interphase layer in the anode; the lithium anode may deteriorate in the presence of nitrogen [94].

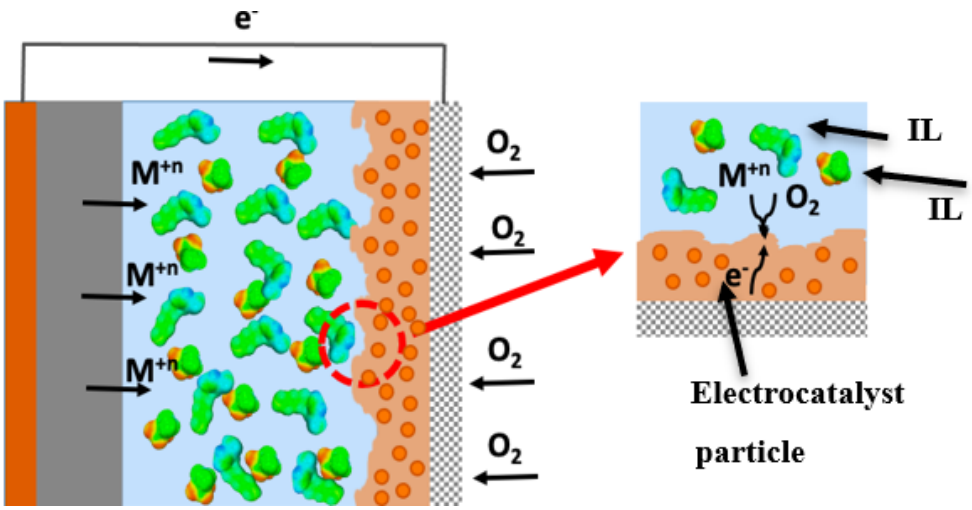

Figure 4.40. Schematic of metal-oxygen cells with IL electrolytes.

4.2.2.2. Description of the Dataset. The IL dataset presented in this section includes the results for the cation-anion pairs obtained from the combination of 370 anions and 84 cations in the COSMOthermX program. In addition to gas (oxygen, carbon dioxide, water, and nitrogen) solubilities, the dataset includes previously calculated in Section 4.1.3, viscosity, melting point, and electronic conductivity values. The distributions of the selected properties and gas solubilities are given in Figure 4.41. The viscous nature of the ILs is visible in Figure 4.41a, as the scale goes up to e^{15} and the mean is around e^{7} mPa.s. On the other hand, luckily, the melting points of these ILs are low, meaning lower than 0 °C, which is essential for stable liquid electrolytes in metal-air batteries. When the gas solubilities are considered, it is observed that all gases except water have similar solubilities, although CO_2 has slightly higher values among the selected atmospheric gases. This is why suppressing CO_2 solubility is essential even though CO_2 partial pressure is low in ambient air. On the other hand, the water solubility spans large intervals from 10^{-2} mol/mol to 10^{4} mol/mol. Hence, extra caution must be exercised according to the water solubility values.

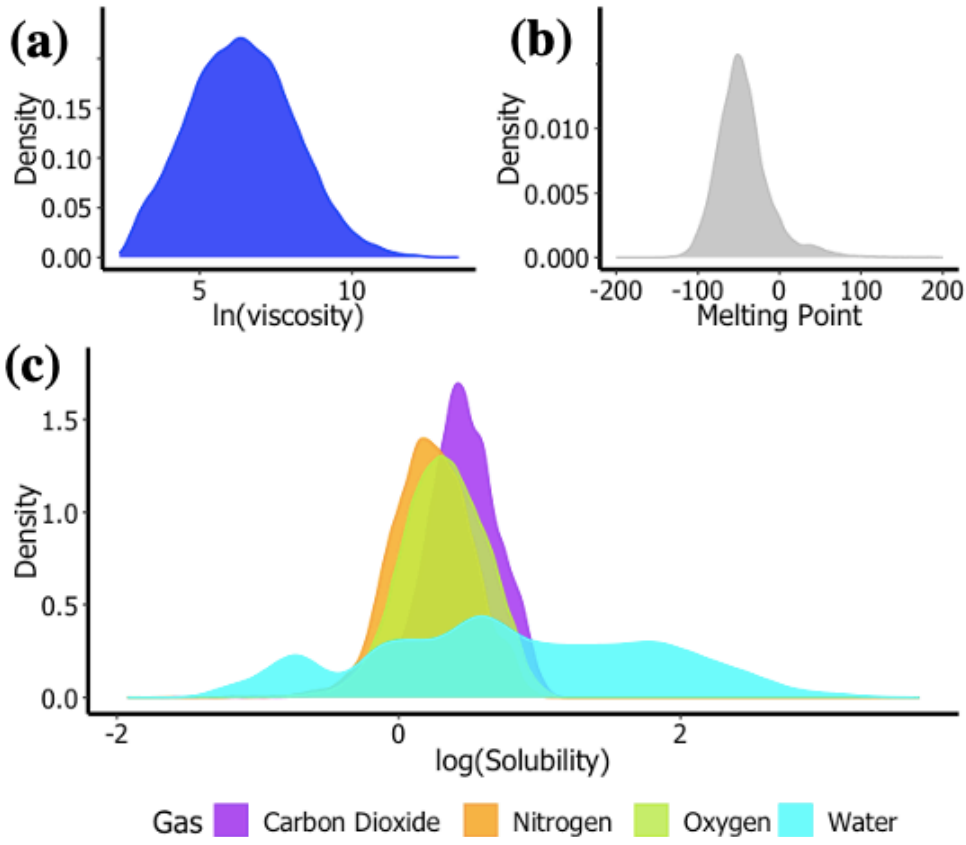

Figure 4.41. Distribution of melting points (a), viscosities (b), melting points (c), and gas solubilities of the whole dataset.

To further extend the analysis, the gas solubility distributions of atmospheric gases for oxygen and other gases based on anion groups are given in Figure 4.42. In parallel to Figure 4.41c, similar solubility distributions are obtained for all three gases except water; most solubilities lie in the range of 0.1-10 mol/mol, whereas extreme values are obtained in both low and high ends for water solubility. Halo_elemental_complex, cyano, borates, and bis_imide groups have the lowest water solubilities; however, halo_elemental_complex is found to be less suitable for metal-air batteries due to higher nitrogen solubility and bis_imide as the most suitable one with the most increased oxygen solubility. On the other hand, the solubility values based on cation groups are given in Figure G.1; the highest oxygen solubilities are obtained for guanidinium, phosphonium, and quinolinium cation groups, respectively. Another noticeable trend is that guanidinium and phosphonium groups have larger solubility values for all gases with larger spread values than the others. Although high oxygen solubility is advantageous for these ILs, high solubilities for other gases may also be problematic. On the other hand, the figure shows that the cation groups do not affect water solubility, as no peaks and no significant trends were observed. Although these results are valuable, no solid conclusions for the most promising anion and cation groups are obtained, showing the need for calculation/prediction of individual ILs. Hence, a low-cost method is provided in this work by building RF models using features calculated by the RDKit free chemical informatics library.

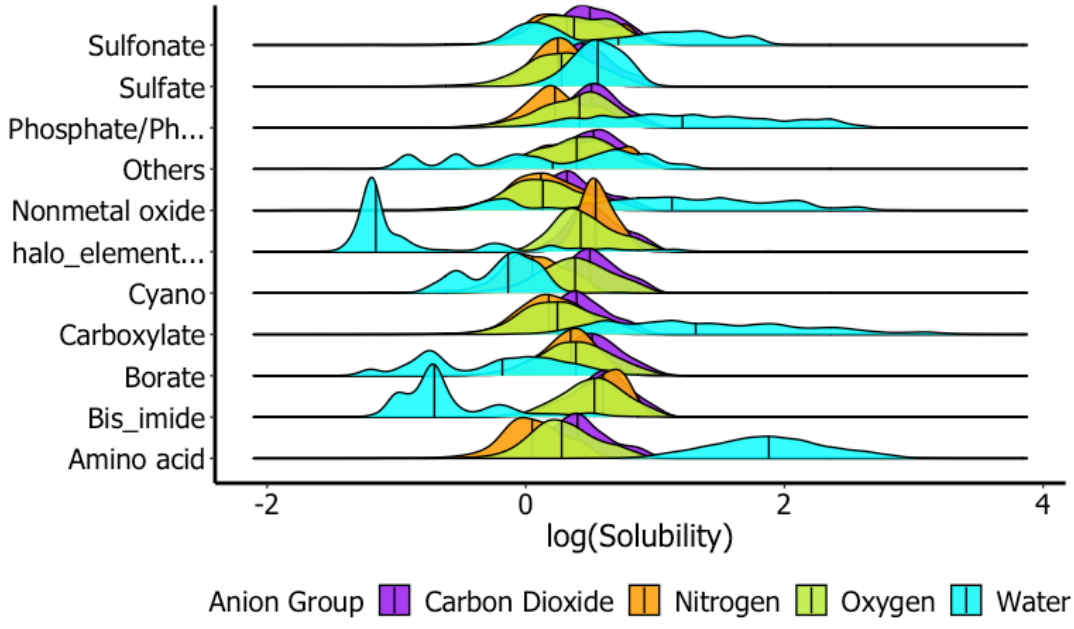

Figure 4.42. Distribution of gas solubilities for anion groups.

RF models were built to predict the gas solubilities using molecular and structural descriptors. The chemical structure is the first consideration when the properties of a molecule are discussed. The qualitative discussions on the system are defined as a structure-activity relationship (SAR) and depend on scientists' experiences and interpretabilities. Because of this variability, the need for numerical representation of the chemical structures, even in the year 1991, was identified. Quantitative structure-activity relationships (QSAR) or structure-property relationships (QSPR) are defined as necessary for representing a molecule [381]. Hence, the molecules were represented using several indexes. In this respect, the RDKit library is developed to provide enough quantitative information on the molecules using only the SMILES, Simplified Molecular Input Line Entry System, codes of molecules. Various indexes are essential since it is impossible to represent a molecule with a single index showing atom and bond types and shapes of molecules. For example, the alkanes can be modeled with total atom count, but it is not essential for complex molecules with many heteroatoms. In the case of ILs, large and bulky molecules containing various atoms and bonding types are present, and many more molecules can be synthesized [381]. Hence, various indexed should be used to account for differences in the IL molecules.

In this respect, the RDKit library provides adequate sets of descriptors, specifically, 125 structural descriptors and multiple topological/electronic indexes utilizing several published works in addition to 85 variables showing the frequency of the fragments in a molecule. The complete list of the descriptors is given inTable G.1. Hall and Kier developed several indexes and features in our context, using a molecular connectivity approach where both topological and electronic characters (explicitly) of atoms or molecules are taken into consideration[381]. These are Chi for structural attributes, Kappa for molecular shapes, and the HallKierAlpha index for atom type information. Labute also reported important descriptors in the RDkit library. There are 35 descriptors calculated by Labute[382], which are LabuteASA (1), PEOE_VSAx ($1 \leq x \leq 14$), SMR_VSAy ($1 \leq x \leq 10$), SlogP_VSAz ($1 \leq x \leq 12$). LabuteASA shows the van der Waals surface area (VSA) of molecules and is also used in calculating latter descriptors. The rest of the three descriptors are calculated for specific ranges on the properties determined over a database where the interval is equally populated. PEOE(sum of partial equalization of orbital theory)_VSA, SMR(sum of molecular refractivity)_VSA, and SlogP(sum of the log of partition of octanol/water)_VSA were used to quantify the effects of hydrophilicity, polarizability and finally electrostatic

interactions. It is stated that there is no correlation between these three sets of descriptors, and several molecular properties are successfully calculated by using only their descriptors. Morgan fingerprint (FpDensityMorganx, 1≤≤x≤3) is a way of representing the chemical structure of a molecule by a two-dimensional vector containing only 0 and 1's where 1 is attributed to specific structural features [383]. Apart from these works, other topological indexes such as BalabanJ [384], BertzCT [385], and Ipc [386] values are reported in the RDKit library. All these topological indexes aim to represent the molecular structure, but their basis of the calculations is different. The best and most relevant kinds of indexes depend on the dataset itself.

The original dataset has 416 for a single IL, making the dataset relatively large. However, working with such a large dataset is disadvantageous given the long computational time and low performance. It is stated in the literature that the optimal set of features should be determined before the ML modeling to prevent these shortcomings. The optimum set of features changes according to the structure of the dataset [387]. Hence, Boruta analysis was performed to reduce non-relevant features or features with no information. Most of the removed features were related to the number of fragments in the molecules as most contain only 0's; only nine cationic and eight anionic features are related to other indexes. Hence, the features used in the modeling were reduced to 285.

4.2.2.3. Machine Learning Analysis. This work uses RF to predict gas solubilities of ILs calculated at 25 °C. Firstly, the dataset is divided into train and test sets as 75% and 25% of the total data with a restriction of different anions in these sets. Modeling is performed using a grid search with 5-fold cross-validation on the train set using the stratified sampling explained in the Materials and Methods section in the validation set; optimum hyperparameters are determined according to validation RMSE. After that, the testing set is used to judge the model's ability to make predictions, and the resulting solutions are shown in Figure 4.43. The optimized hyperparameters of oxygen models are 3 for the maximum depth and 10 for the number of trees. The final model is based on these hyperparameters built for training and test sets. The RF model is found to be quite successful not only for training but also for test sets. In Figure 4.43, the model's estimation accuracy for the testing set is satisfactory, with R^2 and RMSE of 0.95 and 0.34, respectively (0.997 and 0.106 for the training set). It is expected to see better fits on the training set since the model is built on

these data; however, the model does not see the anions present in the test set when it learns from the data.

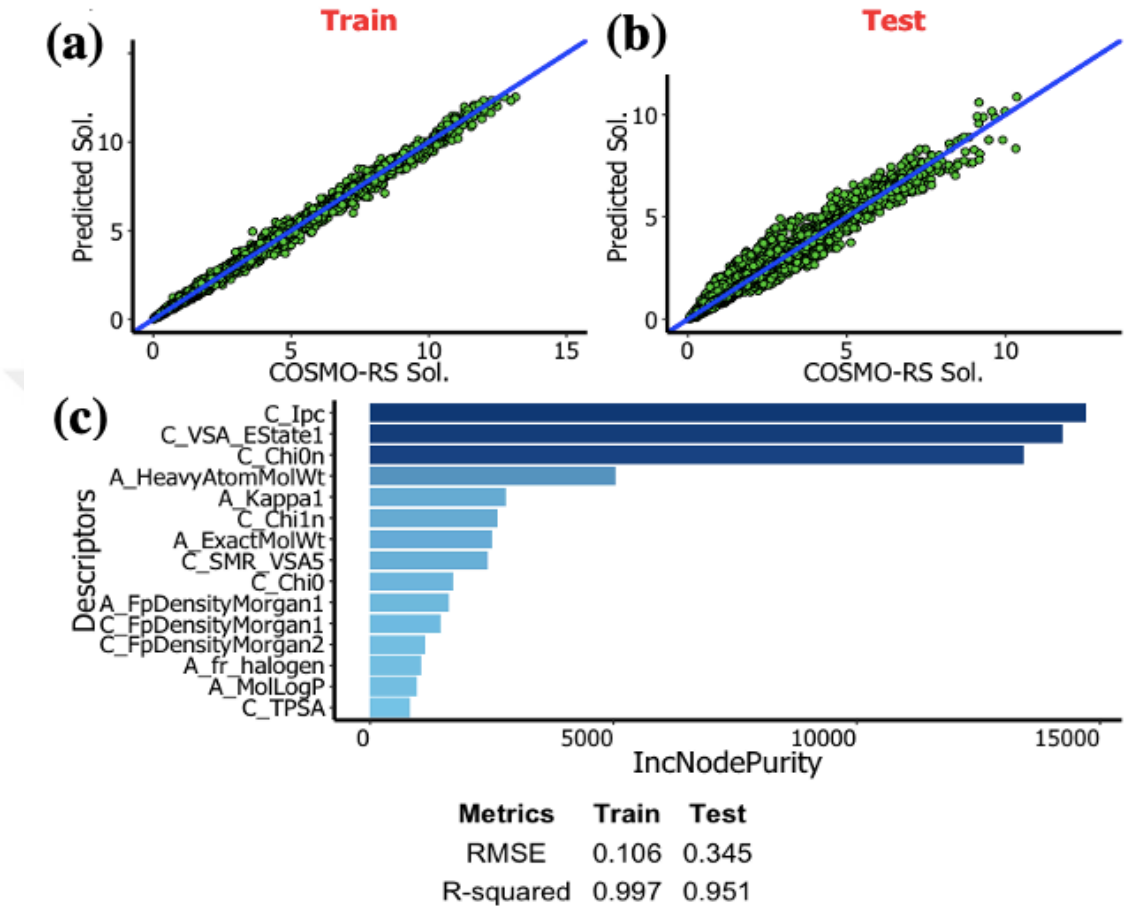

Figure 4.43. ML results on the oxygen solubilities for training (a), test (b) sets with importance (c) values, the performance metrics are provided.

Variable importance analysis is also performed to see the effect of descriptors on the oxygen solubility predictions. Both anion and cation features are present in the importance plot, showing the influence of both parts on the final IL properties, Figure 4.43c. The most important feature was the Ipc value of the cations of ILs. Ipc is the information obtained from characteristic polynomials of a molecule [215]. It is a topological feature reported to be effective in representing the branching [386]. The effect of cation branching was already investigated experimentally in the literature for carbon dioxide solubility in ILs, and it was found that branched cations illustrated as sponge-like structures are determinative in ILs solubility due to favorable interactions of the branched section [388]. Hence, it is expected to have the Ipc value as the top descriptor for gas solubility predictions. The other visible

descriptors are VSA_Estate, Chi values, molecular weights (MolWt), Kappa values, SMR_VSA5, and finally, Morgan fingerprints. Indeed, Morgan fingerprints are used in the ML predictions on ILs properties like refractive indexes and viscosities.[389] In another work, carbon dioxide solubilities [390] of ILs were wellpredicted by using only Morgan fingerprints that represent the ILs successfully. The Kappa1 values showing the sphericity of anions are found to be necessary. The lower Kappa1 values are attributed to high sphericity, and when the molecule is linear, the Kappa value equals the number of atoms. Hence, the structure can also be characterized by the Kappa values, which are essential in modeling. Finally, among 10 SMR_VSA values presented as features, only the moderately polarizable cations value of C_SMR_VSA5 affects the model significantly.

Similar analyses were performed for carbon dioxide, nitrogen, and water solubilities using the hyperparameters in Table G.2. However, as seen in Figure 4.42c, the scale of water solubility is too large. Hence, the model is performed on the logarithmic scale rather than the actual value. The RMSE of these tree models are 0.32 mol/mol, 0.37 mol/mol, and 0.79 mol/mol, as represented in Figure G.6, Figure G.7, and Figure G.8 for carbon dioxide, nitrogen, and log(water) solubilities, respectively. The performances of the predictions are quite similar to each other except for water. The most significant deviation between the predicted and the real value was obtained for saccharinate anion, which belongs to the *Others* family of anions, meaning that the structure is unique in the dataset. However, compared to other gases, water solubilities are less widely reported, but experiments have proved that the anionic effect is dominant in the final water solubilities [391]. Anionic properties were also found to be more critical in the water solubility reported in our previous study, with 20 descriptors calculated by PM3 semi-empirical models [209]. In parallel, our importance plot in Figure G.8. ML results on the water solubilities in natural logarithm scale for train (a), test (b) sets with importance (c) values, the performance metrics are provided at the bottom also supports this discussion with the anionic descriptors on top. The anionic effect is less pronounced for other gases as both anionic and cationic structural and electronic properties are found to be necessary, as well as the molecular weights as they show the complexity of the anion and cation structures. Finally, prediction models are performed for the viscosity and melting points of ILs with the provided descriptor set. The models are quite successful for most of the dataset except glutamate and borate anions. When their features are analyzed, it is seen that these anions have very dissimilar features leading to similar properties. Hence,

the model is limited in accounting for this difference and cannot accurately predict these two anions' properties.

To sum up, the descriptors obtained from the RDKit library can be used to build ML models to predict the gas solubilities and the physical properties of ILs. These predictions can be used to assess the suitability of an IL for metal-air batteries as multiple concerns are considered. The ideal IL electrolyte should have high oxygen solubility, low solubility of the other gases, and low melting point and viscosity. For the restriction of melting point and ln(viscosity) lower than 0 ºC and 6 mPa.s and oxygen solubilities higher than 2 mol/mol, only 19% of ILs satisfy these criteria. Hence, this dataset and models can be used as first-initial guesses when synthesizing new ILs.

4.2.2.4. Validation of COSMO-RS Solubilities with Literature. Although the ML models perform well with gas solubilities calculated by the COSMO-RS method, experimental validation of the computed gas solubilities is still needed. The validation of water [209] and carbon dioxide [392,393] solubilities with the COSMO-RS method was already performed in the literature. In contrast, it was not completed for nitrogen solubilities due to a lack of experimental data. Hence, the validation of oxygen solubility was performed in this work. As explained in the Materials and Method section, there are two methods in the COSMOThermX software to compute the solubilities: gas solubility and IL screening modules. In both ways, the solubilities are initially reported in the mol/mol unit, but they are converted to mM using densities and molecular weights calculated by COSMO-RS. Figure 4.44a gives the oxygen solubilities obtained from the gas solubility module vs. the IL module for ILs having the $[TFSI]^+$ anion. As seen from the figure, the results obtained in these two approaches are an order of magnitude different. However, a perfect linear fit can be obtained where experimentally reported oxygen solubilities are close to the ones calculated using the gas solubility module (Figure 4.44b). Hence, the results obtained in the IL screening module are further improved using the correlation equation presented in Figure 4.44a. However, some deviations are still observed. This is expected because, unfortunately, the experimental methods, techniques, and even equipment calibration change in every research group. For instance, for 1-butyl-1-methyl-pyrrolidinium $[TFSI]^+$ (P13-TFSI), the experimentally measured oxygen solubility changes from 0.73 to 13.6 mM where the COSMO-RS predicts an oxygen solubility of 8.8 mM. Still, the calculated solubility is in the experimentally

reported range. This problem also shows the importance of having a single and reliable method to screen thousands of ILs in terms of gas solubilities for comparative analysis.

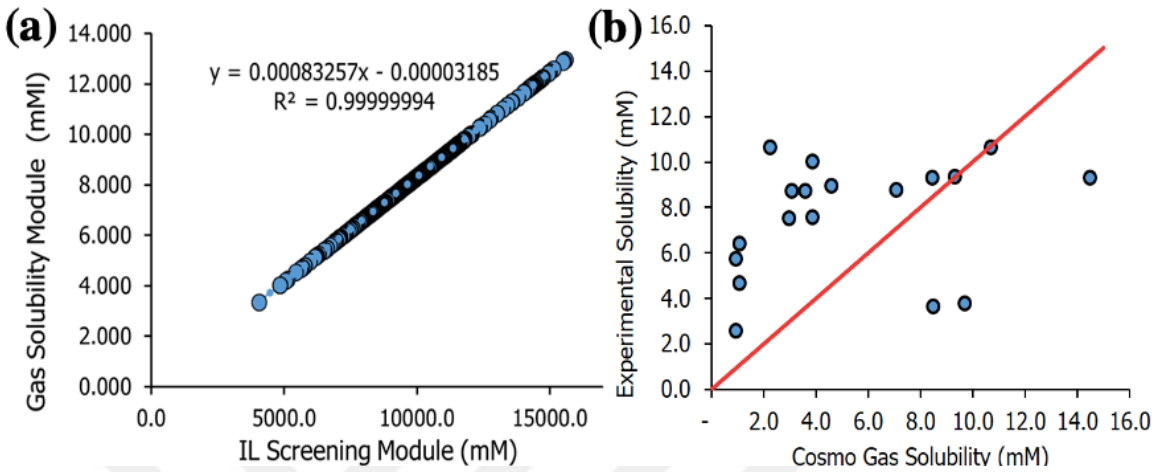

Figure 4.44. The solubility values calculated from COSMO-RS (a) and the comparison between experimental and gas solubility values (b).

5. CONCLUSION

5.1. Conclusions

This thesis aims to increase the performances of Li-S and Li-O_2 batteries by discovering the most promising materials and determining optimum cell parameters. In this respect, galvostatic cycling, system-level modeling, and machine learning are the main techniques used in this study. In the first 5 sections, Li-S batteries were studied using all three methods, whereas only ML tools were used in Li-O_2 battery studies, described in the following two sections. The conclusions of each study are given in this section.

In Section 4.1.1, a dataset having 1660 data from 353 papers in the literature were collected to analyze the effect of critical materials and cell design parameters on the Li-S battery performance using ML. Association rule mining analysis was conducted to determine the single factor effects. The impact of critical factors on both peak discharge capacity and cycle life of a Li-S cell has been discussed; these effects are highly prominent especially for cells achieving peak discharge capacities of 1400 mAh/g and higher and cycle numbers of 200 and higher. The most important conclusions of this section are summarized below:

- Cells with encapsulated cathodes perform significantly better both in terms of the PDC and the cycle life of the battery, importantly for the electrolyte-starved cathodes (E/S<5mL/g). Structured carbons (i.e. porous carbons, CNT) and specialized new materials are highly promising encapsulation materials. High amounts of encapsulation material in the cathode (above 40%) are typically favorable.
- Binder type has a considerable impact on the PDC; PTFE and LA are promising materials for enhanced performance. However, binder- and conductive-free encapsulated cathodes are essential for enhanced cycling performance.
- Electrolyte materials are critical for improved PDCs, especially at low E/S ratios. EC:DEC or TEGDME as the solvent and $LiPF_6$ as the salt perform superiorly compared to the conventional electrolytes. The impact of the electrolyte materials on the cycling performance is less pronounced.

- Even though low S loadings in the cathode (0-1 mg/cm^2) are beneficial for high PDCs, higher S loaded cathodes perform better in terms of the cycle life and the energy density.
- Cells with carbon current collectors or interlayers can achieve higher PDCs, particularly at low E/S ratios.
- Cells achieve PDCs higher than 1400 mAh/g and cycle numbers more than 200 predominantly at very high E/S ratios (above 30 mL/g).
- All-solid-state Li-S batteries are promising in terms of attaining high PDCs while cells with catholyte perform better in terms of cyclability.

To sum up, materials design, specifically design of encapsulation materials and electrolyte, are critical both for high capacities and enhanced cycle life. The most promising pathways forward are the development of encapsulated cathodes that do not require additional binder and conductive material and the design of novel electrolytes that could succeed at low E/S ratios. In addition to proposing favorable pathways for high performance Li-S batteries, this comprehensive analysis also proves that ML is a highly valuable tool, especially for such highly complex systems. To conclude, this analysis confirms that the biggest challenge Li-S batteries face today in competing with the Li-ion technology is to achieve and retain high discharge capacities at high active materials loadings and low electrolyte amounts in the cell.

In Section 4.2.2., 207 data collected from 42 experimental articles were analyzed, which use ILs as their liquid electrolytes, to identify the patterns and hidden relations between the cell variables and both system- and cell-level performances of Li-S batteries using ARM. It was found that IL materials are very important in terms of achieving high PDCs, energy densities and specific energies. This study also showed the importance of IL electrolytes for Li-S batteries with their effectiveness at lean electrolyte conditions and high sulfur loadings.

In section 4.1.3, a large-scale screening of ILs was conducted in search of potential IL electrolytes with low PS solubility to limit the shuttle effect and low viscosity, electronic conductivity, and melting point for application as liquid electrolytes of Li-S batteries. The screening was performed using a COSMO-RS model on the COSMObaseIL dataset of over

36000 ion pairs to produce rough estimations of the solubility of Li_2S_8 as the model PS and IL properties. The predictive model developed by XGBoost algorithm was quite successful indicating that the solubility can be easily predicted for new ILs. Ten descriptors were also analyzed for each anion and cation along with the solubility estimations using association rule mining to find valuable correlations between solubility and property and IL structural properties; solubility limits, which were use as selection criterion for high performance, were determined experimentally. The results showed that the anion descriptors correlate more strongly with PS solubility than the cation descriptors. The ML models showed significant overfitting when exposed to the same anions in both training and test sets. This further provides evidence of the strong correlation between the COSMO-RS-predicted PS solubility/property and anions descriptors. The feature importance analysis also showed that anion descriptors are leading in solubility prediction, with anion LUMO and HUMO energies, dipole, and CPK area being the most important. A comparison with some limited results in the literature showed reasonable agreement. Although calculating the descriptors is comparable in terms of computational cost to the COSMO-RS solubility calculation, the model requires the generation of .cosmo files and the use of COSMO thermodynamic software. In contrast, these descriptors are more readily available and easier to set up on a larger scale. In addition, experiments show optimum solubility and viscosity ranges for high-performing Li-S batteries, whereas melting point and conductivity are only used to ensure the appropriateness of the liquid ILs as the electrolytes. Hence, according to the results, imidazolium and pyridinium were the most suitable cations, whereas borates and bis_imides were determined to be the anion choices for high-performing Li-S batteries. To conclude, this section offers not only ML models that can be easily utilized to identify promising IL electrolytes for Li-S batteries by an original integrated methodology coupling high-throughput COSMO-RS and DFT calculations and experimental characterization but also a better understanding of the structure-solubility-performance relation for IL electrolytes.

In Section 4.1.4, UiO-66-based graphene nanoplatelet composites with three different MOF/GNP ratios (UGS-1, UGS-3, and UGS-5 corresponding to MOF/GNP ratios of 10:90, 30:70, and 50:50 wt.%, respectively) were prepared and used as the conductive encapsulation network for Li-S battery cathodes. A facile strategy is followed in the cathode preparation step. Although no significant performance improvement is observed with the addition of UiO-66 into the composite for a sulfur loading of 1 mg/cm^2, for higher sulfur

loadings (2 mg/cm^2) and current densities, MOF addition is critical for the reversibility of electrochemical reactions and sulfur utilization. For instance, Li-S cells with UGS-5 presented superior rate capability due to the superior surface area and PS adsorption ability of the UG-5 composite. Hence, it can be concluded that the synergistic effect between GNP and MOF favors high-performance Li-S batteries even at high C-rates and sulfur loadings.

In Section 4.1.5, the system-level performance modeling of Li-S batteries with a novel VCKBS composite cathode was done. Li-S cells with VCKBS cathodes exhibited excellent cycling and rate performances with an initial capacity of 1329 mAh g^{-1} at 0.1 C. Even under a higher S loading (2.4 mg cm^{-2}), significant capacity retention of 85 % was accomplished after 200 cycles at 0.2 C. Due to impressive experimental specific capacities, the system-level specific energies and energy densities were predicted for both the 1st and 100th discharges. Compared to KBS, VCKBS cathodes showed 1342% and 568% improvement in the system-level specific energies and energy densities for the 100th discharge, respectively. In both cases, the VCKBS cathode significantly improves system-level performances. In addition, the E/S ratio, S loading, and cathode material characteristics significantly affect the system-level metrics. It was found that VCBKS cathodes with lower E/S ratios excel at specific energies. In pursuing a low-cost Li-S battery with superior energy density and specific energy, the investigation of the VCKBS cathodes at higher sulfur loadings and lower E/S ratios will be critical.

In Section 4.2.1, a dataset containing 1015 experimental data on Li-O_2 batteries was used for ML analysis to identify the most prominent materials and cell design factors combinations for high performance Li-O_2 batteries. ARM and DT were used throughout the study; the factors found to be leading to high cell performance are summarized below:

- Bulk cathode materials, cathode ingredients and electrolyte solvents are found as the most important variables for both high discharge capacities and voltages.
- N-doped carbons, graphene and porous carbons seem to be better options as bulk cathode materials.
- LaFe oxides, Ni oxides and Ru are shown to be good candidates as cathode ingredients.
- The discharge capacities are negatively affected by the active material loadings higher than 1.2 mg/cm^2.

- Cells with PTFE, DMSO, and $LiClO_4$ as the binder, electrolyte solvent and salt, respectively, provide high discharge capacities.
- The use of some electrolyte solvents (DME, DMSO, tetraglyme and triglyme) without a salt or with salts like $LiClO_4$ likely result in capacities higher than or equal to 3000 mAh/g with high probability.
- Mo containing compounds and Ru as ingredients, and N-doped carbons as bulk cathode materials seem to be good for high cell voltages.

Identifying the important correlations between the input and output variables (via ARM), and developing heuristic rules involving more than one variable (via DT) using the data reported in the literature may help to refine the experience gained in the field and make significant contributions to the future works. However, this approach has an important limitation: all the models and conclusions drawn are valid within the limits of the dataset (i.e. data gained from the past studies reported in the literature); hence, it cannot suggest any completely new material types or combinations. To do that, the material characteristics should be also included in the analysis, and significant properties contributing to the battery performance should be identified for the search of new materials or material combinations having similar properties.

In the section 4.2.2., COSMO-RS calculations were used for fast screening of ILs regarding gas solubilities and physical properties to assess if they are suitable as electrolytes of metal-air batteries. The calculations were performed for a dataset of around 30,000 ILs at 25 ºC. Afterward, this dataset was further utilized in an ML algorithm for building predictive models using the structural and electronic features of anions and cations obtained from free software using only the SMILES codes. ML models with low RMSE scores proved that these features are sufficient to represent the IL's properties and solubilities; hence, structure-property relations can be drawn. It was found that both cationic and anionic features influence the gas solubilities other than water. On the other hand, cationic properties have a slight effect on the water solubilities, where anion structures roughly determine the magnitude of the solubilities. It was found that only 19% of ILs are suitable with the restrictions of melting point and ln(viscosity) lower than 0 ºC and 6 mPa.s and oxygen solubilities higher than 2 mol/mol.

5.2. Recommendations

In this thesis, a comprehensive material-to-system analysis was conducted for Li-S and Li-O_2 batteries by applying an integrated research methodology involving experimental characterization, system-level performance modeling, and ML. These studies can be extended in the future by the following recommendations:

- The development of better and more comprehensive battery material databases
- Using better text-mining methods to analyze the trends and results in the literature in a more effective way
- Developing electrochemical models that take material properties into account

REFERENCES

1. Liu C., Z. G. Neale, and G. Cao, "Understanding Electrochemical Potentials of Cathode Materials in Rechargeable Batteries", *Materials Today*, Vol. 19, No. 2, pp. 109–123, 2016.

2. Strauss B. H., S. Kulp, and A. Levermann, "Carbon Choices Determine US Cities Committed to Futures Below Sea Level", *Proceedings of the National Academy of Sciences*, Vol. 112, No. 44, pp. 13508–13513, 2015.

3. Bruce P. G., S. A. Freunberger, L. J. Hardwick, and J.-M. Tarascon, "Li-O_2 and Li-S Batteries with High Energy Storage", *Nature Materials*, Vol. 11, No. 1, pp. 19–29, 2012.

4. Suganthi L. and A. A. Samuel, "Energy Models for Demand Forecasting-A Review", *Renewable and Sustainable Energy Reviews*, Vol. 16, No. 2, pp. 1223–1240, 2012.

5. Hagen M., D. Hanselmann, K. Ahlbrecht, R. Maça, D. Gerber, and J. Tübke, "Lithium-Sulfur Cells: The Gap Between the State-Of-The-Art and the Requirements for High Energy Battery Cells", *Advanced Energy Materials*, Vol. 5, No. 16, p. 1401986, 2015.

6. Chung S., C. Chang and A. Manthiram, "Progress on the Critical Parameters for Lithium–Sulfur Batteries to Be Practically Viable", *Advanced Functional Materials*, Vol. 28, No. 28, p. 1801188, 2018.

7. Geng D., N. Ding, T.S.A. Hor, S.W. Chien, Z. Liu, D. Wuu, X. Sun, and Y. Zong, "From Lithium-Oxygen to Lithium-Air Batteries: Challenges and Opportunities, *Advanced Energy Materials,* Vol. 6, No. 9, p. 1502164, 2016.

8. Wang K.-X., Q.-C. Zhu, and J.-S. Chen, “Strategies Toward High-Performance Cathode Materials for Lithium–Oxygen Batteries”, *Small*, Vol. 14, No. 27, p. 1800078, 2018.

9. Kilic A., B. Oral, D. Eroglu, and R. Yildirim, “Machine Learning for Beyond Li-Ion Batteries: Powering the Research”, *Journal of Energy Storage*, Vol. 73, p. 109057, 2023.

10. Liu Y., D. Lin, P.Y. Yuen, K. Liu, J. Xie, R.H. Dauskardt, and Y. Cui, “An Artificial Solid Electrolyte Interphase with High Li-Ion Conductivity, Mechanical Strength, and Flexibility for Stable Lithium Metal Anodes”, *Advanced Materials*, Vol. 29, No. 10, p. 1605531, 2017.

11. Zhu J., J. Zou, H. Cheng, Y. Gu, and Z. Lu, “High Energy Batteries Based on Sulfur Cathode”, *Green Energy and Environment*, Vol. 4, No. 4, pp. 345–359, 2019.

12. Manthiram A., S. Chung, and C. Zu, “Lithium–Sulfur Batteries: Progress and Prospects”, *Advanced Materials*, Vol. 27, No. 12, pp. 1980–2006, 2015.

13. Liang J., Z.-H. Sun, F. Li, and H.-M. Cheng, “Carbon Materials for Li–S Batteries: Functional Evolution and Performance Improvement”, *Energy Storage Materials*, Vol. 2, pp. 76–106, 2016.

14. Guo J. and J. Liu, “A Binder-Free Electrode Architecture Design for Lithium–Sulfur Batteries: A Review”, *Nanoscale Advances*, Vol. 1, No. 6, pp. 2104–2122, 2019.

15. Hofmann A. F., D. N. Fronczek, and W. G. Bessler, “Mechanistic Modeling of Polysulfide Shuttle and Capacity Loss in Lithium–Sulfur Batteries”, *Journal of Power Sources,* Vol. 259., pp. 300–310, 2014.

16. Fronczek D. N. and W. G. Bessler, “Insight Into Lithium–Sulfur Batteries: Elementary Kinetic Modeling and Impedance Simulation”, *Journal of Power Sources*, Vol. 244, pp. 183–188, 2013.

17. Risse S., S. Angioletti-Uberti, J. Dzubiella, and M. Ballauff, “Capacity Fading in Lithium/Sulfur Batteries: A Linear Four-State Model”, *Journal of Power Sources*, Vol. 267, pp. 648–654, 2014.

18. Zhang T., M. Marinescu, L. O’Neill, M. Wild, and G. Offer, “Modeling the Voltage Loss Mechanisms in Lithium-Sulfur Cells: The Importance of Electrolyte Resistance and Precipitation Kinetics”, *Physical Chemistry Chemical Physics*, Vol. 17, No. 35, pp. 22581–22586, 2015.

19. Zhang S. S., “Liquid Electrolyte Lithium/Sulfur Battery: Fundamental Chemistry, Problems, and Solutions”, *Journal of Power Sources*, Vol. 231, pp. 153–162, 2013.

20. Fotouhi A., D. J. Auger, L. O’Neill, T. Cleaver, and S. Walus, “Lithium-Sulfur Battery Technology Readiness and Applications-A Review”, *Energies,* Vol. 10, No. 12, p. 1937, 2017.

21. Urbonaite S. and P. Novák, “Importance of ‘Unimportant’ Experimental Parameters in Li–S Battery Development”, *Journal of Power Sources*, Vol. 249, pp. 497–502, 2014.

22. Diao Y., K. Xie, S. Xiong, and X. Hong, “Shuttle Phenomenon – The Irreversible Oxidation Mechanism of Sulfur Active Material in Li–S Battery”, *Journal of Power Sources*, Vol. 235, pp. 181–186, 2013.

23. Mikhaylik Y. V and J. R. Akridge, “Polysulfide Shuttle Study in the Li/S Battery System”, *Journal of the Electrochemical Society*, Vol. 151, No. 11, pp. A1969–A1976, 2004.

24. Gu S., C. Sun, D. Xu, Y. Lu, J. Jin, and Z. Wen, “Recent Progress in Liquid Electrolyte-Based Li–S Batteries: Shuttle Problem and Solutions”, *Electrochemical Energy Reviews*, Vol. 1, No. 4, pp. 599–624, 2018.

25. Gupta A. and S. Sivaram, “Separator Membranes for Lithium–Sulfur Batteries: Design Principles, Structure, and Performance”, *Energy Technology*, Vol. 7, No. 6, p. 1800819, 2019.

26. Xu Z.-L., J.-K. Kim, and K. Kang, “Carbon Nanomaterials for Advanced Lithium Sulfur Batteries”, *Nano Today*, Vol. 19, pp. 84–107, 2018.

27. Park J., S.-H. Yu, and Y.-E. Sung, “Design of Structural and Functional Nanomaterials for Lithium-Sulfur Batteries”, *Nano Today*, Vol. 18, pp. 35–64, 2018.

28. Xu W., J. Wang, F. Ding, X. Chen, E. Nasybulin, Y. Zhang, and J.-G. Zhang, “Lithium Metal Anodes for Rechargeable Batteries”, *Energy & Environmental Science*, Vol. 7, No. 2, pp. 513–537, 2014.

29. Zhu Y., X. He, and Y. Mo, “Strategies Based on Nitride Materials Chemistry to Stabilize Li Metal Anode”, *Advanced Science*, Vol. 4, No. 8, p. 1600517, 2017.

30. Fang R., S. Zhao, Z. Sun, D.-W. Wang, H.-M. Cheng, and F. Li, “More Reliable Lithium-Sulfur Batteries: Status, Solutions and Prospects”, *Advanced Materials*, Vol. 29, No. 48, p. 1606823, 2017.

31. Scheers J., S. Fantini, and P. Johansson, “A Review of Electrolytes for Lithium–Sulphur Batteries”, *Journal of Power Sources*, Vol. 255, pp. 204–218, 2014.

32. Xue W., L. Miao, L. Qie, C. Wang, S. Li, J. Wang, and J. Li, “Gravimetric and Volumetric Energy Densities of Lithium-Sulfur Batteries”, *Current Opinion in Electrochemistry*, Vol. 6, No. 1, pp. 92–99, 2017.

33. Urbonaite S., T. Poux, and P. Novák, “Progress Towards Commercially Viable Li–S Battery Cells”, *Advanced Energy Materials*, Vol. 5, No. 16, p. 1500118, 2015.

34. Pan Y., S. Chou, H. K. Liu, and S. X. Dou, “Functional Membrane Separators for Next-Generation High-Energy Rechargeable Batteries”, *National Science Review*, Vol. 4, No. 6, pp. 917–933, 2017.

35. Guo H., W. Luo, J. Chen, S. Chou, H. Liu, and J. Wang, “Review of Electrolytes in Nonaqueous Lithium-Oxygen Batteries”, *Advanced Sustainable Systems*, Vol. 2, No. 8–9, p. 1700183, 2018.

36. Balaish M., A. Kraytsberg, and Y. Ein-Eli, “A Critical Review on Lithium–Air Battery Electrolytes”, *Physical Chemistry Chemical Physics,* Vol. 16, No. 7, pp. 2801–2822, 2014.

37. Li Y., X. Wang, S. Dong, X. Chen, and G. Cui, “Recent Advances in Non-Aqueous Electrolyte for Rechargeable Li–O_2 Batteries”, *Advanced Energy Materials*, Vol. 6, No. 18, p. 1600751, 2016.

38. Shao Y., S. Park, J. Xiao, J.-G. Zhang, Y. Wang, and J. Liu, “Electrocatalysts for Nonaqueous Lithium–Air Batteries: Status, Challenges, and Perspective”, *ACS Catalysis*, Vol. 2, No. 5, pp. 844–857, 2012.

39. Li Y., Z. Zhang, D. Duan, Y. Han, K. Wang, X. Hao, J. Wang, S. Liu, and F. Wu, “An Integrated Structural Air Electrode Based on Parallel Porous Nitrogen-Doped Carbon Nanotube Arrays for Rechargeable Li-Air Batteries”, *Nanomaterials,* Vol. 9, No. 10, p. 1412, 2019.

40. Wang C., Y. Yu, J. Niu, Y. Liu, D. Bridges, X. Liu, J. Pooran, Y. Zhang, and A. Hu, “Recent Progress of Metal–Air Batteries—A Mini Review”, *Applied Sciences*, Vol. 9, No. 14., p. 2787, 2019.

41. Zhang P., M. Ding, X. Li, C. Li, Z. Li, and L. Yin, “Challenges and Strategy on Parasitic Reaction for High-Performance Nonaqueous Lithium–Oxygen Batteries”, *Advanced Energy Materials*, Vol. 10, No. 40, p. 2001789, 2020.

42. Liu Y., L. Wang, L. Cao, C. Shang, Z. Wang, H. Wang, L. He, J. Yang, H. Cheng, J. Li, and Z. Lu, "Understanding and Suppressing Side Reactions in Li–Air Batteries", *Materials Chemistry Frontiers*, Vol. 1, No. 12, pp. 2495–2510, 2017.

43. Kilic A., Ç. Odabaşı, R. Yildirim, and D. Eroglu, "Assessment of Critical Materials and Cell Design Factors for High Performance Lithium-Sulfur Batteries Using Machine Learning", *Chemical Engineering Journal*, Vol. 390, p. 124117, 2020.

44. Kilic A., R. Yildirim, and D. Eroglu, "Assessment of Ionic Liquid Electrolytes for High-Performance Lithium-Sulfur Batteries Using Machine Learning", *International Journal of Energy Research*, Vol. 46, No. 15, pp. 21716–21726, 2022.

45. Kilic A., Ş. S. Bayazit, D. Eroglu, "Metal-Organic Framework/Graphene Nanoplatelet Composite Increases Rate Performance of Lithium-Sulfur Batteries", *Energy Technology*, p. 2301452, 2024.

46. Fazal H., D. Eroglu, A. Kilic, B. Dong, N. Ali, J. Zai, and X. Qian, "Atomic V- and Co-Modified Ketjen Black–Sulfur Composite for High-Performance Lithium–Sulfur Batteries", *ACS Applied Energy Materials*, Vol. 6, No. 12, pp. 6721–6731, 2023.

47. Fazal H., D. Eroglu, A. Kilic, N. Ali, C. Yan, J. Zai, X. Qian, "Electrochemical Impedance Spectroscopy of Li-S Batteries: Effect of Atomic Vanadium-and Cobalt-Modified Ketjen Black-Sulfur Cathode, Sulfur Loading, and Electrolyte-to-Sulfur Ratio", *ChemElectroChem*, p. e202300781, 2024.

48. Kilic A., D. Eroglu, and R. Yildirim, "Determining the Key Performance Factors in Lithium-Oxygen Batteries Using Machine Learning", *Journal of the Electrochemical Society*, Vol. 168, No. 9, p. 090544, 2021.

49. Schneider A., C. Suchomski, H. Sommer, J. Janek, and T. Brezesinski, "Free-Standing and Binder-Free Highly N-Doped Carbon/Sulfur Cathodes with Tailorable Loading for High-Areal-Capacity Lithium-Sulfur Batteries", *Journal of Materials Chemistry A*, Vol. 3, No. 41, pp. 20482–20486, 2015.

50. Doan T. N. L., D. Gosselink, T. K. A. Hoang, and P. Chen, “The Effect of Sulfur Loading on the Electrochemical Performance of a Sulfur–Polymer Composite Cathode Coated on Aluminium Foil”, *Physical Chemistry Chemical Physics*, Vol. 16, No. 27, pp. 13843–13848, 2014.

51. Sun K., H. Liu, and H. Gan, “Cathode Loading Effect on Sulfur Utilization in Lithium–Sulfur Battery”, *Journal of Electrochemical Energy Conversion and Storage*, Vol. 13, No. 2, pp. 21002–21009, 2016.

52. Hu Y., W. Chen, T. Lei, Y. Jiao, J. Huang, A. Hu, C. Gong, C. Yan, X. Wang, and J. Xiong, “Strategies Toward High-Loading Lithium–Sulfur Battery”, *Advanced Energy Materials*, Vol. 10, No. 17, p. 2000082, 2020.

53. Zhong Y., X. Xu, Y. Liu, W. Wang, and Z. Shao, “Recent Progress in Metal–Organic Frameworks for Lithium–Sulfur Batteries”, *Polyhedron*, Vol. 155, pp. 464–484, 2018.

54. Liu X., S. Wang, A. Wang, Z. Wang, J. Chen, Q. Zeng, P. Chen, W. Liu, Z. Li, and L. Zhang, “A New Cathode Material Synthesized by a Thiol-Modified Metal–Organic Framework (MOF) Covalently Connecting Sulfur for Superior Long-Cycling Stability in Lithium–Sulfur Batteries”, *Journal of Materials Chemistry A*, Vol. 7, No. 42, pp. 24515–24523, 2019.

55. Wang Z., J. Shen, J. Liu, X. Xu, Z. Liu, R. Hu, L. Yang, Y. Feng, J. Liu, Z. Shi, L. Ouyang, Y. Yu, and M. Zhu, “Self-Supported and Flexible Sulfur Cathode Enabled via Synergistic Confinement for High-Energy-Density Lithium–Sulfur Batteries”, *Advanced Materials*, Vol. 31, No. 33, p. 1902228, 2019.

56. Wang Z., X. Li, Y. Cui, Y. Yang, H. Pan, Z. Wang, C. Wu, B. Chen, and G. Qian, “A Metal–Organic Framework With Open Metal Sites for Enhanced Confinement of Sulfur and Lithium–Sulfur Battery of Long Cycling Life”, *Crystal Growth & Design,* Vol. 13, No. 11, pp. 5116–5120, 2013.

57. Zheng J., J. Tian, D. Wu, M. Gu, W. Xu, C. Wang, F. Gao, M.H. Engelhard, J.-G. Zhang, J. Liu, and J. Xiao, "Lewis Acid–Base Interactions between Polysulfides and Metal Organic Framework in Lithium Sulfur Batteries", *Nano Letters*, Vol. 14, No. 5, pp. 2345–2352, 2014.

58. Yuan Y., Z. Chen, H. Yu, X. Zhang, T. Liu, M. Xia, R. Zheng, M. Shui, and J. Shu, "Heteroatom-Doped Carbon-Based Materials for Lithium and Sodium Ion Batteries", *Energy Storage Materials*, Vol. 32, pp. 65–90, 2020.

59. Huang J., N. Wang, J. Wang, N. Huang, M. Bayati, and T. Xiaoteng Liu, "Nitrogen, Phosphorus Co-Doped Porous Carbon Originated from Egg White for Advanced Lithium-Sulfur Battery", *Journal of Electroanalytical Chemistry*, Vol. 894, p. 115362, 2021.

60. Yuan Z., H.-J. Peng, J.-Q. Huang, X.-Y. Liu, D.-W. Wang, X.-B. Cheng, and Q. Zhang, "Hierarchical Free-Standing Carbon-Nanotube Paper Electrodes with Ultrahigh Sulfur-Loading for Lithium–Sulfur Batteries", *Advanced Functional Materials*, Vol. 24, No. 39, pp. 6105–6112, 2014.

61. Jin-Young H., P. Soo-Jin, K. Seok, and C. Sungwook, "Facile Preparation of Electrodes Derived from Graphene Oxide@Metal Organic Framework Hybrid Materials and Their Electrochemical Property", *Carbon Letters*, Vol. 25, pp. 113–116, 2018.

62. Li G., X. Wang, M.H. Seo, M. Li, L. Ma, Y. Yuan, T. Wu, A. Yu, S. Wang, J. Lu, and Z. Chen, "Chemisorption of Polysulfides Through Redox Reactions with Organic Molecules for Lithium–Sulfur Batteries", *Nature Communications*, Vol. 9, No. 1, p. 705, 2018.

63. Zhou W., H. Chen, Y. Yu, D. Wang, Z. Cui, F.J. DiSalvo, and H.D. Abruña, "Amylopectin Wrapped Graphene Oxide/Sulfur for Improved Cyclability of Lithium–Sulfur Battery", *ACS Nano*, Vol. 7, No. 10, pp. 8801–8808, 2013.

64. Zhou X., F. Chen, and J. Yang, “Core@Shell Sulfur@Polypyrrole Nanoparticles Sandwiched in Graphene Sheets as Cathode for Lithium–Sulfur Batteries”, *Journal of Energy Chemistry*, Vol. 24, No. 4, pp. 448–455, 2015.

65. Eroglu D., K. R. Zavadil, and K. G. Gallagher, “Critical Link Between Materials Chemistry and Cell-Level Design for High Energy Density and Low Cost Lithium-Sulfur Transportation Battery”, *Journal of the Electrochemical Society*, Vol. 162, No. 6, pp. A982–A990, 2015.

66. Chung S. and A. Manthiram, “Rational Design of Statically and Dynamically Stable Lithium–Sulfur Batteries with High Sulfur Loading and Low Electrolyte/Sulfur Ratio”, *Advanced Materials*, Vol. 30, No. 6, p. 1705951, 2018.

67. Brückner J., S. Thieme, H. T. Grossmann, S. Dörfler, H. Althues, and S. Kaskel, “Lithium–Sulfur Batteries: Influence of C-Rate, Amount of Electrolyte and Sulfur Loading on Cycle Performance”, *Journal of Power Sources*, Vol. 268, pp. 82–87, 2014.

68. Yuan L. X., J. K. Feng, X. P. Ai, Y. L. Cao, S. L. Chen, and H. X. Yang, “Improved Dischargeability and Reversibility of Sulfur Cathode in a Novel Ionic Liquid Electrolyte”, *Electrochemistry Communications*, Vol. 8, No. 4, pp. 610–614, 2006.

69. Zhang S., A. Ikoma, Z. Li, K. Ueno, X. Ma, K. Dokko, and M. Watanabe, “Optimization of Pore Structure of Cathodic Carbon Supports for Solvate Ionic Liquid Electrolytes Based Lithium–Sulfur Batteries”, *ACS Applied Materials & Interfaces,* Vol. 8, No. 41, pp. 27803–27813, 2016.

70. Seki S., N. Serizawa, K. Takei, Y. Umebayashi, S. Tsuzuki, and M. Watanabe, “Long-Cycle-Life Lithium-Sulfur Batteries with Lithium Solvate Ionic Liquids”, *Electrochemistry*, Vol. 85, No. 10, pp. 680–682, 2017.

71. Yan, Y., Y. Yin, Y. Guo, and L.-J. Wan, “Effect of Cations in Ionic Liquids on the Electrochemical Performance of Lithium-Sulfur Batteries”, *Science China Chemistry*, Vol. 57, No. 11, pp. 1564–1569, 2014.

72. Dokko K., N. Tachikawa, K. Yamauchi, M. Tsuchiya, A. Yamazaki, E. Takashima, J.-W. Park, K. Ueno, S. Seki, N. Serizawa, and M. Watanabe, “Solvate Ionic Liquid Electrolyte for Li-S Batteries”, *Journal of the Electrochemical Society*, Vol. 160, No. 8, pp. A1304-A1310, 2013.

73. Barghamadi M., A.S. Best, A.I. Bhatt, A.F. Hollenkamp, P.J. Mahon, M. Musameh, and T. Rüther, “Effect of $LiNO_3$ Additive and Pyrrolidinium Ionic Liquid on the Solid Electrolyte Interphase in the Lithium–Sulfur Battery”, *Journal of Power Sources*, Vol. 295, pp. 212–220, 2015.

74. Yan Y., Y.-X. Yin, S. Xin, J. Su, Y.-G. Guo, and L.-J. Wan, “High-Safety Lithium-Sulfur Battery with Prelithiated Si/C Anode and Ionic Liquid Electrolyte”, *Electrochimica Acta*, Vol. 91, pp. 58–61, 2013.

75. Park J.-W., K. Ueno, N. Tachikawa, K. Dokko, and M. Watanabe, “Ionic Liquid Electrolytes for Lithium–Sulfur Batteries”, *The Journal of Physical Chemistry C*, Vol. 117, No. 40, pp. 20531–20541, 2013.

76. Lu H., Z. Chen, H. Du, K. Zhang, J. Wang, Z. Hou, and J. Fang, “The Enhanced Performance of Lithium Sulfur Battery with Ionic Liquid-Based Electrolyte Mixed with Fluorinated Ether”, *Ionics*, Vol. 25, No. 6, pp. 2685–2691, 2019.

77. Wu F., Q. Zhu, R. Chen, N. Chen, Y. Chen, Y. Ye, J. Qian, and L. Li, “Ionic Liquid-Based Electrolyte with Binary Lithium Salts for High Performance Lithium–Sulfur Batteries”, *Journal of Power Sources*, Vol. 296, pp. 10–17, 2015.

78. Kumaresan K., Y. Mikhaylik, and R. E. White, “A Mathematical Model for a Lithium-Sulfur Cell”, *Journal of the Electrochemical Society*, Vol. 155, No. 8, pp. A576–A582, 2008.

79. Marinescu M., T. Zhang, and G. J. Offer, “A Zero Dimensional Model of Lithium–Sulfur Batteries During Charge and Discharge”, *Physical Chemistry Chemical Physics*, Vol. 18, No. 1, pp. 584–593, 2016.

80. Al-Mahmoud S. M., J. W. Dibden, J. R. Owen, G. Denuault, and N. Garcia-Araez, “A Simple, Experiment-Based Model of the Initial Self-Discharge of Lithium-Sulphur Batteries”, *Journal of Power Sources*, Vol. 306, pp. 323–328, 2016.

81. Erisen N., N. B. Emerce, S. C. Erensoy, and D. Eroglu, “Modeling the Effect of Key Cathode Design Parameters on the Electrochemical Performance of a Lithium-Sulfur Battery”, *International Journal of Energy Research*, Vol. 42, No. 8, pp. 2631–2642, 2018.

82. Erisen N. and D. Eroglu, “Modeling the Discharge Behavior of a Lithium-Sulfur Battery”, *International Journal of Energy Research*, Vol. 44, No. 13, pp. 10599–10611, 2020.

83. Abdulkadiroglu B., H. Bektas, and D. Eroglu, “How to Model the Cathode Area in Lithium-Sulfur Batteries?”, *ChemElectroChem*, Vol. 9, No. 4, p. e202101553, 2022.

84. Newman J. S. and C. W. Tobias, “Theoretical Analysis of Current Distribution in Porous Electrodes”, *Journal of the Electrochemical Society*, Vol. 109, No. 12, p. 1183, 1962.

85. Bilal H. M. and D. Eroglu, “Assessment of Li-S Battery Performance as a Function of Electrolyte-to-Sulfur Ratio”, *Journal of the Electrochemical Society*, Vol. 168, No. 3, p. 30502, 2021.

86. Bilal H. M. and D. Eroglu, “Carbon-to-Sulfur Ratio in the Cell Controls the Discharge Capacity, Cycling Performance and Energy Density of a Lithium-Sulfur Battery”, *International Journal of Energy Research*, Vol. 46, No. 11, pp. 15926–15937, 2022.

87. Bilal H. M., K. Yuksel, and D. Eroglu, “Influence of Sulfur Loading on Lithium-Sulfur Battery Performance for Different Cathode Carbon Types”, *ChemistrySelect*, Vol. 8, No. 12, p. e202203944, 2023.

88. Emerce N. B. and D. Eroglu, “Effect of Electrolyte-to-Sulfur Ratio in the Cell on the Li-S Battery Performance”, *Journal of the Electrochemical Society*, Vol. 166, No. 8, pp. A1490–A1500, 2019.

89. McCloskey, B. D., “Attainable Gravimetric and Volumetric Energy Density of Li–S and Li-ion Battery Cells with Solid Separator-Protected Li Metal Anodes”, *The Journal of Physical Chemistry Letters*, Vol. 6, No. 22, pp. 4581–4588, 2015.

90. Cleaver T., P. Kovacik, M. Marinescu, T. Zhang, and G. Offer, “Commercializing Lithium Sulfur Batteries: Are We Doing the Right Research?”, *Journal of the Electrochemical Society*, Vol. 165, No. 1, pp. A6029–A6033, 2018.

91. Kwak W.-J., S. Chae, R. Feng, P. Gao, J. Read, M.H. Engelhard, L. Zhong, W. Xu, and J.-G. Zhang, “Optimized Electrolyte with High Electrochemical Stability and Oxygen Solubility for Lithium–Oxygen and Lithium–Air Batteries”, *ACS Energy Letters*, Vol. 5, No. 7, pp. 2182–2190, 2020.

92. Gittleson F. S., R. E. Jones, D. K. Ward, and M. E. Foster, “Oxygen Solubility and Transport in Li–Air Battery Electrolytes: Establishing Criteria and Strategies for Electrolyte Design”, *Energy & Environmental Science*, Vol. 10, No. 5, pp. 1167–1179, 2017.

93. Xu W., J. Xiao, D. Wang, J. Zhang, and J.-G. Zhang, “Effects of Nonaqueous Electrolytes on the Performance of Lithium/Air Batteries”, *Journal of the Electrochemical Society*, Vol. 157, No. 2, p. A219, 2010.

94. Haas R., M. Murat, M. Weiss, J. Janek, A. Natan, and D. Schröder, “Understanding the Transport of Atmospheric Gases in Liquid Electrolytes for Lithium–Air Batteries” *Journal of the Electrochemical Society*, Vol. 168, No. 7, p. 070504, 2021.

95. Monroe C. W., “Does Oxygen Transport Affect the Cell Voltages of Metal/Air Batteries?”, *Journal of the Electrochemical Society*, Vol. 164, No. 11, pp. E3547–E3551, 2017.

96. Sergeev A. V., A. V. Chertovich, D. M. Itkis, E. A. Goodilin, and A. R. Khokhlov, “Effects of Cathode and Electrolyte Properties on Lithium–Air Battery Performance: Computational Study”, *Journal of Power Sources*, Vol. 279, pp. 707–712, 2015.

97. Wang H.-F. and Q. Xu, “Materials Design for Rechargeable Metal-Air Batteries”, *Matter*, Vol. 1, No. 3, pp. 565–595, 2019.

98. Gao R., Z. Yang, L. Zheng, L. Gu, L. Liu, Y. Lee, Z. Hu, and X. Liu, “Enhancing the Catalytic Activity of Co_3O_4 for Li–O_2 Batteries through the Synergy of Surface/Interface/Doping Engineering”, *ACS Catalysis*, Vol. 8, No. 3, pp. 1955–1963, 2018.

99. Li L. and A. Manthiram, “Decoupled Bifunctional Air Electrodes for High-Performance Hybrid Lithium-Air Batteries”, *Nano Energy*, Vol. 9, pp. 94–100, 2014.

100. Peng S.-H., T.-H. Chen, C.-H. Lee, H.-C. Lu, and S. J. Lue, “Optimal Cobalt Oxide (Co_3O_4): Graphene (Gr) Ratio in Co_3O_4/Gr as Air Cathode Catalyst for Air-Breathing Hybrid Electrolyte Lithium-Air Battery”, *Journal of Power Sources*, Vol. 471, p. 228373, 2020.

101. Azuma S., M. Sano, I. Moro, F. Ozawa, M. Saito, and A. Nomura, “Redox Mediator-Coated Air-Electrodes for High-Capacity Cycle Operation of Lithium–Air Batteries”, *Journal of Physical Chemistry C*, Vol. 127, No. 15, pp. 7087–7094, 2023.

102. Mao J., J. Miao, Y. Lu, and Z. Tong, “Machine Learning of Materials Design and State Prediction for Lithium Ion Batteries”, *Chinese Journal of Chemical Engineering*, Vol. 37, pp. 1-11, 2021.

103. Li T., F. Xing, T. Liu, J. Sun, D. Shi, H. Zhang, and X. Li, “Cost, Performance Prediction and Optimization of a Vanadium Flow Battery by Machine-Learning”, *Energy & Environmental Science*, Vol. 13, No. 11, pp. 4353–4361, 2020.

104. Li T., W. Lu, Z. Yuan, H. Zhang, and X. Li, “A Data-Driven and DFT Assisted Theoretic Guide for Membrane Design in Flow Batteries”, *Journal of Materials Chemistry A*, Vol. 9, No. 25, pp. 14545-14552, 2021.

105. Wan S., X. Liang, H. Jiang, J. Sun, N. Djilali, and T. Zhao, “A Coupled Machine Learning and Genetic Algorithm Approach to the Design of Porous Electrodes for Redox Flow Batteries”, *Applied Energy*, Vol. 298, p. 117177, 2021.

106. Su H., S. Lin, S. Deng, C. Lian, Y. Shang, and H. Liu, “Predicting the Capacitance of Carbon-Based Electric Double Layer Capacitors by Machine Learning”, *Nanoscale Advances*, Vol. 1, No. 6, pp. 2162-2166, 2019.

107. Junping W., C. Quanshi, and C. Binggang, “Support Vector Machine Based Battery Model for Electric Vehicles”, *Energy Conversion and Management*, Vol. 47, No. 7–8, pp. 858-864, 2006.

108. Sui X., S. He, S. B. Vilsen, J. Meng, R. Teodorescu, and D. I. Stroe, “A Review of Non-Probabilistic Machine Learning-Based State of Health Estimation Techniques for Lithium-Ion Battery”, *Applied Energy*, Vol. 300, p. 117346, 2021.

109. Fei Z., F. Yang, K. L. Tsui, L. Li, and Z. Zhang, “Early Prediction of Battery Lifetime via a Machine Learning Based Framework”, *Energy*, Vol. 225, p. 120205, 2021.

110. Hu X., Y. Che, X. Lin, and S. Onori, “Battery Health Prediction Using Fusion-Based Feature Selection and Machine Learning”, *IEEE Transactions on Transportation Electrification*, Vol. 7, No. 2, 2021.

111. Samanta A., S. Chowdhuri, and S. S. Williamson, “Machine Learning-Based Data-Driven Fault Detection/Diagnosis of Lithium-Ion Battery: A Critical Review”, *Electronics*, Vol. 10, No. 11, p. 1309, 2021.

112. Ng M. F., J. Zhao, Q. Yan, G. J. Conduit, and Z. W. Seh, “Predicting the State of Charge and Health of Batteries Using Data-Driven Machine Learning”, *Nature Machine Intelligence*, Vol. 2, No. 3, pp. 161–170, 2020.

113. Shu X., S. Shen, J. Shen, Y. Zhang, G. Li, Z. Chen, and Y. Liu, “State of Health Prediction of Lithium-Ion Batteries Based on Machine Learning: Advances and Perspectives”, *iScience*, Vol. 24, No. 11, p. 103265, 2021.

114. Jain A., S.P. Ong, G. Hautier, W. Chen, W.D. Richards, S. Dacek, S. Cholia, D. Gunter, D. Skinner, G. Ceder, and K.A. Persson, “Commentary: The Materials Project: A Materials Genome Approach to Accelerating Materials Innovation”, *APL Materials*, Vol. 1, No. 1, p. 011002, 2013.

115. Wang G., T. Fearn, T. Wang, and K. L. Choy, “Insight Gained from Using Machine Learning Techniques to Predict the Discharge Capacities of Doped Spinel Cathode Materials for Lithium-Ion Batteries Applications”, *Energy Technology*, Vol. 9, No. 5, p. 2100053, 2021.

116. Babar M., H. L. Parks, G. Houchins, and V. Viswanathan, “An Accurate Machine Learning Calculator for the Lithium-Graphite System”, *Journal of Physics: Energy*, Vol. 3, No. 1, p. 14005, 2020.

117. Jiang Z., J. Li, Y. Yang, L. Mu, C. Wei, X. Yu, P. Pianetta, K. Zhao, P. Cloetens, F. Lin, and Y. Liu, “Machine-Learning-Revealed Statistics of the Particle-Carbon/Binder Detachment in Lithium-Ion Battery Cathodes”, *Nature Communications*, Vol. 11, No. 1, p. 2310, 2020.

118. Li J., S. Li, Y. Zhang, Y. Yang, S. Russi, G. Qian, L. Mu, S.-J. Lee, Z. Yang, J.-S. Lee, P. Pianetta, J. Qiu, D. Ratner, P. Cloetens, K. Zhao, F. Lin, and Y. Liu,

"Multiphase, Multiscale Chemomechanics at Extreme Low Temperatures: Battery Electrodes for Operation in a Wide Temperature Range", *Advanced Energy Materials*, Vol. 11, No. 37, p. 2102122, 2021.

119. Petrich L., D. Westhoff, J. Feinauer, D.P. Finegan, S.R. Daemi, P.R. Shearing, and V. Schmidt, "Crack Detection in Lithium-Ion Cells Using Machine Learning", *Computational Materials Science*, Vol. 136, pp. 297–305, 2017.

120. Li J., B. Mei, H. Liu, X. Li, S. Gu, J. Ma, X. Yu, and Z. Jiang, "In Situ X-Ray Absorption Near-Edge Structure Calculation and Machine Learning Analysis of the Structural Evolution in Lithium-Ion Battery Cathode Materials", *The Journal of Physical Chemistry C*, Vol. 125, No. 34, pp. 18979–18987, 2021.

121. Furat O., D. P. Finegan, D. Diercks, F. Usseglio-Viretta, K. Smith, and V. Schmidt, "Mapping the Architecture of Single Lithium Ion Electrode Particles in 3D, Using Electron Backscatter Diffraction and Machine Learning Segmentation", *Journal of Power Sources*, Vol. 483, p. 229148, 2021.

122. Shodiev A., M. Duquesnoy, O. Arcelus, M. Chouchane, J. Li, and A. A. Franco, "Machine Learning 3D-Resolved Prediction of Electrolyte Infiltration in Battery Porous Electrodes", *Journal of Power Sources*, Vol. 511, p. 230384, 2021.

123. Zhang Y. and X. Xu, "Machine Learning Properties of Electrolyte Additives: A Focus on Redox Potentials", *Industrial and Engineering Chemistry Research*, Vol. 60, No. 1, pp. 343–354, 2021.

124. Nakayama T., Y. Igarashi, K. Sodeyama, and M. Okada, "Material Search for Li-Ion Battery Electrolytes Through an Exhaustive Search With a Gaussian Process", *Chemical Physics Letters*, Vol. 731, p. 136622, 2019.

125. Dave A., J. Mitchell, K. Kandasamy, H. Wang, S. Burke, B. Paria, B. Póczos, J. Whitacre, and V. Viswanathan, "Autonomous Discovery of Battery Electrolytes With

Robotic Experimentation and Machine Learning", *Cell Reports Physical Science*, Vol. 1, No. 12, p. 100264, 2020.

126. Turetskyy A., J. Wessel, C. Herrmann, and S. Thiede, "Battery Production Design Using Multi-Output Machine Learning Models", *Energy Storage Materials*, Vol. 38, pp. 93–112, 2021.

127. Drakopoulos S.X., A. Gholamipour-Shirazi, P. MacDonald, R.C. Parini, C.D. Reynolds, D.L. Burnett, B. Pye, K.B. O'Regan, G. Wang, T.M. Whitehead, G.J. Conduit, A. Cazacu, and E. Kendrick, "Formulation and Manufacturing Optimization of Lithium-Ion Graphite-Based Electrodes via Machine Learning", *Cell Reports Physical Science*, Vol. 2, No. 12, p. 100683, 2021.

128. Niri M.F., K. Liu, G. Apachitei, L.A.A. Román-Ramírez, M. Lain, D. Widanage, and J. Marco, "Quantifying Key Factors for Optimised Manufacturing of Li-Ion Battery Anode and Cathode via Artificial Intelligence", *Energy and AI*, Vol. 7, p.100129, 2022.

129. Faraji Niri M., K. Liu, G. Apachitei, L. Roman-Ramirez, M. Lain, D. Widanalage, and J. Marco, "Machine-Learning for Li-Ion Battery Capacity Prediction in Manufacturing Process", *ECS Meeting Abstracts*, Vol. Ma2021-02, No. 3, 2021.

130. Liu K., Z. Wei, Z. Yang, and K. Li, "Mass Load Prediction for Lithium-Ion Battery Electrode Clean Production: A Machine Learning Approach", *Journal of Cleaner Production*, Vol. 289, p. 125159, 2021.

131. Kolodziejczyk F., B. Mortazavi, T. Rabczuk, and X. Zhuang, "Machine Learning Assisted Multiscale Modeling of Composite Phase Change Materials for Li-Ion Batteries' Thermal Management", *International Journal of Heat and Mass Transfer*, Vol. 172, p. 121199, 2021.

132. Wu, S. Han, K. G. Shin, and W. Lu, “Application of Artificial Neural Networks in Design of Lithium-Ion Batteries”, *Journal of Power Sources*, Vol. 395, pp. 128–136, 2018.

133. Lombardo T., J.-B. Hoock, E. N. Primo, A. C. Ngandjong, M. Duquesnoy, and A. A. Franco, “Accelerated Optimization Methods for Force-Field Parametrization in Battery Electrode Manufacturing Modeling”, *Batteries & Supercaps*, Vol. 3, No. 8, pp. 721–730, 2020.

134. Chen T., M. Song, H. Hui, and H. Long, “Battery Electrode Mass Loading Prognostics and Analysis for Lithium-Ion Battery–Based Energy Storage Systems”, *Frontiers in Energy Research*, Vol. 9, p. 754317, 2021.

135. Maphanga R. R., T. Mokoena, and M. Ratsoma, “Estimating DFT Calculated Voltage Using Machine Learning Regression Models”, *Materials Today: Proceedings*, Vol. 38, pp. 773–778, 2021.

136. Allam O., R. Kuramshin, Z. Stoichev, B. W. Cho, S. W. Lee, and S. S. Jang, “Molecular Structure–Redox Potential Relationship for Organic Electrode Materials: Density Functional Theory–Machine Learning Approach”, *Materials Today Energy*, Vol. 17, p. 100482, 2020.

137. Allam O., B. W. Cho, K. C. Kim, and S. S. Jang, “Application of DFT-Based Machine Learning for Developing Molecular Electrode Materials in Li-Ion Batteries”, *RSC Advances,* Vol. 8, No. 69, pp. 39414–39420, 2018.

138. Chang J. H., P. B. Jørgensen, S. Loftager, A. Bhowmik, J. M. G. Lastra, and T. Vegge, “On-The-Fly Assessment of Diffusion Barriers of Disordered Transition Metal Oxyfluorides Using Local Descriptors”, *Electrochimica Acta*, Vol. 388, p. 138551, 2021.

139. Li S. and A. S. Barnard, “Inverse Design of Mxenes for High-Capacity Energy Storage Materials Using Multi-Target Machine Learning”, *Chemistry of Materials*, Vol. 34, No. 11, pp. 4964–4974, 2022.

140. Wang Z., H. Zhang, and J. Li, “Accelerated Discovery of Stable Spinels in Energy Systems via Machine Learning”, *Nano Energy*, Vol. 81, p. 105665, 2021.

141. Takagishi Y., T. Yamanaka, and T. Yamaue, “Machine Learning Approaches for Designing Mesoscale Structure of Li-Ion Battery Electrodes”, *Batteries*, Vol. 5, No. 3, p. 54, 2019.

142. Attarian Shandiz M.and R. Gauvin, “Application of Machine Learning Methods for the Prediction of Crystal System of Cathode Materials in Lithium-Ion Batteries”, *Computational Materials Science*, Vol. 117, pp. 270–278, 2016.

143. Houchins G. and V. Viswanathan, “An Accurate Machine-Learning Calculator for Optimization of Li-Ion Battery Cathodes”, *The Journal of Chemical Physics*, Vol. 153, No. 5, p. 54124, 2020.

144. Wang G., T. Fearn, T. Wang, and K.-L. Choy, “Machine-Learning Approach for Predicting the Discharging Capacities of Doped Lithium Nickel–Cobalt–Manganese Cathode Materials in Li-Ion Batteries”, *ACS Central Science*, Vol. 7, No. 9, pp. 1551–1560, 2021.

145. Wu W., S. Wang, and Q. Sun, “Topological Quantum Cathode Materials for Fast Charging Li-Ion Battery Identified by Machine Learning and First Principles Calculation”, *Advanced Theory and Simulations*, Vol. 5, No. 3, p. 2100350, 2022.

146. Carvalho R. P., C. F. N. Marchiori, D. Brandell, and C. M. Araujo, “Artificial Intelligence Driven In-Silico Discovery of Novel Organic Lithium-Ion Battery Cathodes”, *Energy Storage Materials*, Vol. 44, pp. 313–325, 2022.

147. Min K., B. Choi, K. Park, and E. Cho, “Machine Learning Assisted Optimization of Electrochemical Properties for Ni-Rich Cathode Materials”, *Scientific Reports*, Vol. 8, No. 1, p. 15778, 2018.

148. Xu S., J. Liang, Y. Yu, R. Liu, Y. Xu, X. Zhu, and Y. Zhao, “Machine Learning-Assisted Discovery of High-Voltage Organic Materials for Rechargeable Batteries”, *The Journal of Physical Chemistry C*, Vol. 125, No. 39, pp. 21352–21358, 2021.

149. Hazama H., D. Murai, N. Nagasako, M. Hasegawa, and N. Ogihara, “Optimization of Material Composition of Li-Intercalated Metal–Organic Framework Electrodes Using a Combination of Experiments and Machine Learning of X-Ray Diffraction Patterns”, *Advanced Materials Technologies*, Vol. 5, No. 9, p. 2000254, 2020.

150. Jie J., Z. Hu, G. Qian, M. Weng, S. Li, S. Li, M. Hu, D. Chen, W. Xiao, J. Zheng, L.-W. Wang, and F. Pan, “Discovering Unusual Structures From Exception Using Big Data and Machine Learning Techniques”, *Science Bulletin*, Vol. 64, No. 9, pp. 612–616, 2019.

151. Okamoto Y. and Y. Kubo, “Ab Initio Calculations of the Redox Potentials of Additives for Lithium-Ion Batteries and Their Prediction Through Machine Learning”, *ACS Omega*, Vol. 3, No. 7, pp. 7868–7874, 2018.

152. Ding Y., M. Chen, C. Guo, P. Zhang, and J. Wang, “Molecular Fingerprint-Based Machine Learning Assisted QSAR Model Development for Prediction of Ionic Liquid Properties”, *Journal of Molecular Liquids*, Vol. 326, p. 115212, 2021.

153. Huber J., C. Tammer, S. Krotil, S. Waidmann, X. Hao, C. Seidel, and G. Reinhart, “Method for Classification of Battery Separator Defects Using Optical Inspection”, *Procedia CIRP*, Vol. 57, pp. 585–590, 2016.

154. Moses, R. P. Joshi, B. Ozdemir, N. Kumar, J. Eickholt, and V. Barone, “Machine Learning Screening of Metal-Ion Battery Electrode Materials”, *ACS Applied Materials and Interfaces*, Vol. 13, No. 45, pp. 53355–53362, 2021.

155. Wu W. and Q. Sun, “Screening Topological Quantum Materials for Na-Ion Battery Cathode”, *ACS Materials Letters*, Vol. 4, No. 1, pp. 175–180, 2022.

156. Liu X., T. Wang, T. Ji, H. Wang, H. Liu, J. Li, and D. Chao, “Using Machine Learning to Screen Non-Graphite Carbon Materials Based on Na-Ion Storage Properties”, *Journal of Materials Chemistry A*, Vol. 10, No. 14, pp. 8031–8046, 2022.

157. Park S., S. Park, Y. Park, M. H. Alfaruqi, J. Y. Hwang, and J. Kim, “A New Material Discovery Platform of Stable Layered Oxide Cathodes for K-Ion Batteries”, *Energy & Environmental Science,* Vol. 14, No. 11, pp. 5864-5874, 2021.

158. Deng M., L. Wang, B. Vaghefinazari, W. Xu, C. Feiler, S. V. Lamaka, D. Höche, M.L. Zheludkevich, and D. Snihirova, “High-Energy and Durable Aqueous Magnesium Batteries: Recent Advances and Perspectives”, *Energy Storage Materials*, Vol. 43., pp. 238-247, 2021.

159. Cai J., Z. Wang, S. Wu, Y. Han, and J. Li, “A Machine Learning Shortcut for Screening the Spinel Structures of Mg/Zn Ion Battery Cathodes With a High Conductivity and Rapid Ion Kinetics”, *Energy Storage Materials*, Vol. 42, pp. 277-285, 2021.

160. Zhou L., A. M. Yao, Y. Wu, Z. Hu, Y. Huang, and Z. Hong, “Machine Learning Assisted Prediction of Cathode Materials for Zn-Ion Batteries”, *Advanced Theory and Simulations*, Vol. 4, No. 9, p. 2100196, 2021.

161. Loechte A., I. R. Ruiz, and P. Gloesekoetter, “Battery State Estimation With ANN and SVR Evaluating Electrochemical Impedance Spectra Generalizing DC Currents”, *Applied Sciences*, Vol. 12, No. 1, p. 274, 2022.

162. Wang A., Z. Zou, D. Wang, Y. Liu, Y. Li, J. Wu, M. Avdeev, and S. Shi, “Identifying Chemical Factors Affecting Reaction Kinetics in Li-Air Battery via Ab Initio Calculations and Machine Learning”, *Energy Storage Materials*, Vol. 35, pp. 595-601, 2021.

163. Zhang H., Z. Wang, J. Ren, J. Liu, and J. Li, "Ultra-Fast and Accurate Binding Energy Prediction of Shuttle Effect-Suppressive Sulfur Hosts for Lithium-Sulfur Batteries Using Machine Learning", *Energy Storage Materials*, Vol. 35, pp. 88-98, 2021.

164. Lian Z., M. Yang, F. Jan, and B. Li, "Machine Learning Derived Blueprint for Rational Design of the Effective Single-Atom Cathode Catalyst of the Lithium-Sulfur Battery", *Journal of Physical Chemistry Letters*, Vol. 12, No. 29, pp. 7053-7059, 2021.

165. Zhang H., Z. Wang, J. Cai, S. Wu, and J. Li, "Machine-Learning-Enabled Tricks of the Trade for Rapid Host Material Discovery in Li-S Battery", *ACS Applied Materials and Interfaces*, Vol. 13, No. 45, pp. 53388-53397, 2021.

166. Joshi R. P., J. Eickholt, L. Li, M. Fornari, V. Barone, and J. E. Peralta, "Machine Learning the Voltage of Electrode Materials in Metal-Ion Batteries", *ACS Applied Materials and Interfaces*, Vol. 11, No. 20, pp. 18494–18503, 2019.

167. Chidiac J., L. Timperman, and M. Anouti, "Small Dissymmetry, Yet Large Effects On the Transport Properties of Electrolytes Based on Imide Salts: Consequences on Performance in Li-Ion Batteries", *Journal of Energy Chemistry*, Vol. 65, pp. 352–366, 2022.

168. Joraleechanchai N., R. Donthongkwa, N. Phattharasupakun, S. Duangdangchote, P. Chiochan, K. Homlamai, and M. Sawangphruk, "Free Carbonate-Based Molecules in the Electrolyte Leading to Severe Safety Concerns of Ni-Rich Li-Ion Batteries", *Chemical Communications*, Vol. 58, No. 6, pp. 779–782, 2022.

169. Thangadurai V. and B. Chen, "Solid Li- and Na-Ion Electrolytes for Next Generation Rechargeable Batteries", *Chemistry of Materials*, Vol. 34, No. 15, pp. 6637–6658, 2022.

170. Jeschke S. and P. Johansson, “Supervised Machine Learning-Based Classification of Li−S Battery Electrolytes”, *Batteries & Supercaps*, Vol. 4, No. 7, pp. 1156–1162, 2021.

171. Kilic A., R. Yildirim, and D. Eroglu, “Assessment of Ionic Liquid Electrolytes for High-Performance Lithium-Sulfur Batteries Using Machine Learning”, *International Journal of Energy Research*, Vol. 46, No. 15, pp. 21716–21726, 2022.

172. Su Z., V. De Andrade, S. Cretu, Y. Yin, M.J. Wojcik, A.A. Franco, and A. Demortière, “X-Ray Nanocomputed Tomography in Zernike Phase Contrast for Studying 3D Morphology of Li-O_2 Battery Electrode” *ACS Applied Energy Materials*, Vol. 3, No. 5, pp. 4093–4102, 2020.

173. Lee A., J. Yoo, and K. Kang, “Predicting the Chemical Reactivity of Organic Materials Using a Machine-Learning Approach”, *Chemical Science*, Vol. 11, No. 30, pp. 7813–7822, 2020.

174. Kiselyova N. N., V. A. Dudarev, V. V. Ryazanov, O. V. Sen’ko, and A. A. Dokukin, “Predictions of Chalcospinels With Composition ABC_4 (X = S or Se)”, *Inorganic Materials: Applied Research*, Vol. 12, No. 2, pp. 328–336, 2021.

175. Chen X., L. Ye, Y. Wang, and X. Li, “Beyond Expert-Level Performance Prediction for Rechargeable Batteries by Unsupervised Machine Learning”, *Advanced Intelligent Systems,* Vol. 1, No. 8, p. 1900102, 2019.

176. Oral B., B. Tekin, D. Eroglu, and R. Yildirim, “Performance Analysis of Na-Ion Batteries by Machine Learning”, *Journal of Power Sources*, Vol. 549, p. 232126, 2022.

177. Manna S., D. Roy, S. Das, and B. Pathak, “Machine Learning As a Tool for Specific Capacity Prediction of Prospective Potassium Battery Electrodes”, *Energy*, 2022.

178. Torp S., *Prediction of Battery Materials Properties With Machine Learning: Developing Algorithms To Discover Electrodes for Li-Ion and Mg-Ion Batteries*, MSc Thesis, University of Oslo, 2020.

179. Ishikawa A., K. Sodeyama, Y. Igarashi, T. Nakayama, Y. Tateyama, and M. Okada, "Machine Learning Prediction of Coordination Energies for Alkali Group Elements in Battery Electrolyte Solvents", *Physical Chemistry Chemical Physics*, Vol. 21, No. 48, pp. 26399-26405, 2019.

180. Hatakeyama-Sato K., T. Tezuka, Y. Nishikitani, H. Nishide, and K. Oyaizu, "Synthesis of Lithium-Ion Conducting Polymers Designed by Machine Learning-Based Prediction and Screening", *Chemistry Letters*, Vol. 48, No. 2, pp. 130–132, 2019.

181. Xu Y., Y. Zong, and K. Hippalgaonkar, "Machine Learning-Assisted Cross-Domain Prediction of Ionic Conductivity in Sodium and Lithium-Based Superionic Conductors Using Facile Descriptors", *Journal of Physics Communications*, Vol. 4, No. 5, p. 55015, 2020.

182. Hajibabaei A. and K. S. Kim, "Universal Machine Learning Interatomic Potentials: Surveying Solid Electrolytes", *Journal of Physical Chemistry Letters*, Vol. 12, No. 33, pp. 8115–8120, 2021.

183. Verduzco J. C., E. E. Marinero, and A. Strachan, "An Active Learning Approach for the Design of Doped LLZO Ceramic Garnets for Battery Applications", *Integrating Materials and Manufacturing Innovation*, Vol. 10, No. 2, pp. 299–310, 2021.

184. Adhyatma A., Y. Xu, N. H. Hawari, P. Satria Palar, and A. Sumboja, "Improving Ionic Conductivity of Doped $Li_7La_3Zr_2O_{12}$ Using Optimized Machine Learning With Simplistic Descriptors", *Materials Letters*, Vol. 308, p. 131159, 2022.

185. Sumita M., R. Tamura, K. Homma, C. Kaneta, and K. Tsuda, "Li-Ion Conductive Li_3PO_4-Li_3BO_3-Li_2SO_4 Mixture: Prevision Through Density Functional Molecular

Dynamics and Machine Learning", *Bulletin of the Chemical Society of Japan*, Vol. 92, No. 6, pp. 1100-1106, 2019.

186. Jo J., E. Choi, M. Kim, and K. Min, "Machine Learning-Aided Materials Design Platform for Predicting the Mechanical Properties of Na-Ion Solid-State Electrolytes", *ACS Applied Energy Materials*, Vol. 4, No. 8, pp. 7862–7869, 2021.

187. Fitzhugh W., X. Chen, Y. Wang, L. Ye, and X. Li, "Solid-Electrolyte-Interphase Design in Constrained Ensemble for Solid-State Batteries", *Energy & Environmental Science*, Vol. 14, No. 8, pp. 4574-4583, 2021.

188. Katcho N.A., J. Carrete, M. Reynaud, G. Rousse, M. Casas-Cabanas, N. Mingo, J. Rodríguez-Carvajal, and J. Carrasco, "An Investigation of the Structural Properties of Li and Na Fast Ion Conductors Using High-Throughput Bond-Valence Calculations and Machine Learning", *Journal of Applied Crystallography*, Vol. 52, pp. 148-157, 2019.

189. Choi A., J. Jo, W. Kim, and K. Min, "Searching for Mechanically Superior Solid-State Electrolytes in Li-Ion Batteries via Data-Driven Approaches", *ACS Applied Materials and Interfaces*, Vol.13, No. 36, pp. 42590–42597, 2021.

190. Honrao S.J., X. Yang, B. Radhakrishnan, S. Kuwata, H. Komatsu, A. Ohma, M. Sierhuis, and J.W. Lawson, "Discovery of Novel Li SSE and Anode Coatings Using Interpretable Machine Learning and High-Throughput Multi-Property Screening", *Scientific Reports*, Vol. 11, No. 1, pp. 1–14, 2021.

191. Chen Y.T., M. Duquesnoy, D.H.S. Tan, J.M. Doux, H. Yang, G. Deysher, P. Ridley, A.A. Franco, Y.S. Meng, and Z. Chen, "Fabrication of High-Quality Thin Solid-State Electrolyte Films Assisted by Machine Learning", *ACS Energy Letters*, Vol. 6, No. 4, pp. 1639-1648, 2021.

192. Shao H., J. Pu, Y. Zhu, B. Gao, Z. Zhu, and Y. Rao, “Visual Analysis on Machine Learning Assisted Prediction of Ionic Conductivity for Solid-State Electrolytes”, IEEE Pacific Visualization Symposium, China, 2021.

193. Zhao Q., M. Avdeev, L. Chen, and S. Shi, “Machine Learning Prediction of Activation Energy in Cubic Li-Argyrodites With Hierarchically Encoding Crystal Structure-Based (HECS) Descriptors”, *Science Bulletin*, Vol. 66, No. 14, pp. 1041-1048, 2021.

194. Ahmad Z., T. Xie, C. Maheshwari, J. C. Grossman, and V. Viswanathan, “Machine Learning Enabled Computational Screening of Inorganic Solid Electrolytes for Suppression of Dendrite Formation in Lithium Metal Anodes”, *ACS Central Science*, Vol. 4, No. 8, pp. 996–1006, 2018.

195. Yang G., M.L. Lehmann, S. Zhao, B. Li, S. Ge, P.F. Cao, F.M. Delnick, A.P. Sokolov, T. Saito, and J. Nanda, “Anomalously High Elastic Modulus of a Poly(Ethylene Oxide)-Based Composite Electrolyte”, *Energy Storage Materials*, Vol. 35, pp. 431-442, 2021.

196. Dixit M.B., A. Verma, W. Zaman, X. Zhong, P. Kenesei, J.S. Park, J. Almer, P.P. Mukherjee, and K.B. Hatzell, “Synchrotron Imaging of Pore Formation in Li Metal Solid-State Batteries Aided by Machine Learning” *ACS Applied Energy Materials*, Vol. 3, No. 10, pp. 9534–9542, 2020.

197. Liu B., J. Yang, H. Yang, C. Ye, Y. Mao, J. Wang, S. Shi, J. Yang, and W. Zhang, “Rationalizing theInterphase Stability of Li doped-$Li_7La_3Zr_2O_{12}$: via Automated Reaction Screening and Machine Learning”, *Journal of Materials Chemistry A*, Vol. 7, No. 34, pp. 19961-19969, 2019.

198. Jo J., E. Choi, M. Kim, and K. Min, “Machine Learning-Aided Materials Design Platform for Predicting the Mechanical Properties of Na-Ion Solid-State Electrolytes”, *ACS Applied Energy Materials*, Vol. 4, No. 8, pp. 7862-7869, 2021.

199. Nelson P. A., S. Ahmed, K. G. Gallagher, and D. W. Dees, *Modeling thePerformance and Cost of Lithium-Ion Batteries for Electric-Drive Vehicles*, Third Edition, Argonne National Laboratory, Chicago, 2019.

200. UC Business Analytics R Programming Guide, "Text Mining: Creating Tidy Text", 2021, http://uc-r.github.io/tidy_text, accessed on January 3, 2024.

201. Kumar R., J. Liu, J.-Y. Hwang, and Y.-K. Sun, "Recent Research Trends in Li–S Batteries", *Journal of Materials Chemistry A,* Vol. 6, No. 25, pp. 11582–11605, 2018.

202. Ramoni M. O. and H.-C. Zhang, "End-of-Life (EOL) Issues and Options for Electric Vehicle Batteries", *Clean Technologies and Environmental Policy*, Vol. 15, No. 6, pp. 881–891, 2013.

203. Hahsler M., B. Gruen, and K. Hornik, "Arules -- {A} Computational Environment for Mining Association Rules and Frequent Item Sets", *Journal of Statistical Software*, Vol. 14, No. 15, pp. 1–25, 2005.

204. Allaire J.J., "Rstudio: Integrated Development Environment for R", 2016, https://www.r-project.org/conferences/useR-2011/abstracts/180111-allairejj.pdf, accessed on January 5, 2024.

205. Hussein N., A. Alashqur, and B. I. Sowan, "Using the Interestingness Measure Lift To Generate Association Rules", *Journal of Advanced Computer Science and Technology,* Vol. 4, No. 1, pp. 156–162, 2015.

206. Klamt A., F. Eckert, and J. Reinisch, "Cosmothermx Version C30_1601", 2023, http://www.solventextract.org/Organization/COSMOlogic-GmbH-Co-kG, accessed on November 15, 2023.

207. Sgroi M. F., D. Pullini, and A. I. Pruna, "Lithium Polysulfide Interaction With Group III Atoms-Doped Graphene: A Computational Insight", *Batteries*, Vol. 6, No. 3, p. 46, 2020.

208. Vijayakumar M., N. Govind, E. Walter, S.D. Burton, A. Shukla, A. Devaraj, J. Xiao, J. Liu, C. Wang, A. Karim, and S. Thevuthasan, "Molecular Structure and Stability of Dissolved Lithium Polysulfide Species", *Physical Chemistry Chemical Physics*, Vol. 16, No. 22, pp. 10923–10932, 2014.

209. Can E., A. Jalal, I. G. Zirhlioglu, A. Uzun, and R. Yildirim, "Predicting Water Solubility in Ionic Liquids Using Machine Learning Towards Design of Hydro-Philic/Phobic Ionic Liquids", *Journal of Molecular Liquids*, Vol. 332, p. 115848, 2021.

210. Jalal A., E. Can, S. Keskin, R. Yildirim, and A. Uzun, "Selection Rules for Estimating the Solubility of C4-Hydrocarbons in Imidazolium Ionic Liquids Determined by Machine-Learning Tools", *Journal of Molecular Liquids*, Vol. 284, pp. 511–521, 2019.

211. Alexander L. J., A. Tropsha, and D. A. Winkler, "Beware of R^2:Simple, Unambiguous Assessment of the Prediction Accuracy of QSAR and QSPR Models", *Journal of Chemical Information and Modeling*, Vol. 55, No. 7, pp. 1316–1322, 2015.

212. Krawczyk A., "Learning From Imbalanced Data: Open Challenges and Future Directions", *Progress in Artificial Intelligence*, Vol. 5, No. 4, pp. 221–232, 2016.

213. Wickham H., R. François, L. Henry, and K. Müller, "Dplyr:A Grammar of Data Manipulation", 2018, https://dplyr.tidyverse.org, accessed on December 15, 2023.

214. Chemical Computing Group, "Molecular Operating Environment", 2023, https://www.chemcomp.com/Products.htm, accessed on December 15, 2023.

215. "Rdkit: Open-Source Cheminformatics Software", 2023, http://www.rdkit.org, accessed on December 20, 2023.

216. Lovrić M., J. M. Molero, and R. Kern, "Pyspark and Rdkit: Moving Towards Big Data in Cheminformatics", *Molecular Informatics*, Vol. 38, No. 6, p. 1800082, 2019.

217. Kursa B. and W. R. Rudnicki, “Feature Selection With the Boruta Package”, *Journal of Statistical Software*, Vol. 36, No. 11, pp. 1-13, 2010.

218. Breiman L., “Random Forests”, *Machine Learning*, Vol. 45, No. 1, pp. 5–32, 2001.

219. Min X., J. Xiao, M. Fang, W. (Alex) Wang, Y. Zhao, Y. Liu, Amr.M. Abdelkader, K. Xi, R.V. Kumar, and Z. Huang, “Potassium-Ion Batteries: Outlook on Present and Future Technologies”, *Energy & Environmental Science*, Vol. 14, No. 4, pp. 2186–2243, 2021.

220. Yuan F., W. Zhang, D. Zhang, Q. Wang, Z. Li, W. Li, H. Sun, B. Wang, and Y.A. Wu, “Recent Progress in Electrochemical Performance of Carbon-Based Anodes for Potassium-Ion Batteries Based on First Principles Calculations”, *Nanotechnology*, Vol. 32, No. 47, p. 472003, 2021.

221. Zhou J. and S. Guo, “Carbon-Based Anode Materials for Potassium-Ion Batteries: From Material, Mechanism to Performance”, *SmartMaterials*, Vol. 2, No. 2, pp. 176–201, 2021.

222. Wang J., H. Wang, X. Zang, D. Zhai, and F. Kang, “Recent Advances in Stability of Carbon-Based Anodes for Potassium-Ion Batteries”, *Batteries & Supercaps,* Vol. 4, No. 4, pp. 554–570, 2021.

223. Wu X., Y. Chen, Z. Xing, C.W.K. Lam, S.S. Pang, W. Zhang, and Z. Ju, “Advanced Carbon-Based Anodes for Potassium-Ion Batteries”, *Advanced Energy Materials*, Vol. 9, No. 21, p. 1900343, 2019.

224. Zhao L.-F., Z. Hu, W.-H. Lai, Y. Tao, J. Peng, Z.-C. Miao, Y.-X. Wang, S.-L. Chou, H.-K. Liu, S.-X. Dou, L.-F.Z. Zhao, -C Miao, L.-F. Zhao, Z. Hu, W.-H. Lai, Y. Tao, J. Peng, Y.-X. Wang, S.-L.H. Chou, -K Liu, and S.-X. Dou, “Hard Carbon Anodes: Fundamental Understanding and Commercial Perspectives for Na-Ion Batteries Beyond Li-Ion and K-Ion Counterparts”, *Advanced Energy Materials,* Vol. 11, No. 1, p. 2002704, 2021.

225. Palomares V., N. Nieto, and T. Rojo, “Negative Electrode Materials for High-Energy Density Li- and Na-Ion Batteries”, *Current Opinion in Electrochemistry*, Vol. 31, p. 100840, 2022.

226. Yang G., P.R. Ilango, S. Wang, M.S. Nasir, L. Li, D. Ji, Y. Hu, S. Ramakrishna, W. Yan, and S. Peng, “Carbon-Based Alloy-Type Composite Anode Materials Toward Sodium-Ion Batteries”, *Small*, Vol. 15, No. 22, p. 1900628, 2019.

227. Hong Z., H. Maleki, T. Ludwig, Y. Zhen, M. Wilhelm, D. Lee, K.H. Kim, and S. Mathur, “New Insights Into Carbon-Based and Mxene Anodes for Na and K-Ion Storage: A Review”, *Journal of Energy Chemistry*, Vol. 62, pp. 660–691, 2021.

228. Zhao R., N. Sun, and B. Xu, “Recent Advances in Heterostructured Carbon Materials As Anodes for Sodium-Ion Batteries”, *Small Structures*, Vol. 2, No. 12, p. 2100132, 2021.

229. Liu Y., W. Li, and Y. Xia, “Recent Progress in Polyanionic Anode Materials for Li (Na)-Ion Batteries”, *Electrochemical Energy Reviews*, Vol. 4, No. 3, pp. 447–472, 2021.

230. Wei Z., L. Wang, M. Zhuo, W. Ni, H. Wang, and J. Ma, “Layered Tin Sulfide and Selenide Anode Materials for Li- and Na-Ion Batteries”, *Journal of Materials Chemistry A,* Vol. 6, No. 26, pp. 12185–12214, 2018.

231. Li G., S. Guo, B. Xiang, S. Mei, Y. Zheng, X. Zhang, B. Gao, P.K. Chu, and K. Huo, “Recent Advances and Perspectives of Microsized Alloying-Type Porous Anode Materials in High-Performance Li- and Na-Ion Batteries”, *Energy Materials*, Vol. 2, No. 3, p. 200020, 2022.

232. Luo A., A. Langrock, X. Fan, Y. Liang, and C. Wang, “P2-Type Transition Metal Oxides for High Performance Na-Ion Battery Cathodes”, *Journal of Materials Chemistry A*, Vol. 5, No. 34, pp. 18214–18220, 2017.

233. Liu Z., J. Shen, S. Feng, Y. Huang, D. Wu, F. Li, Y. Zhu, M. Gu, Q. Liu, J. Liu, and M. Zhu, "Ultralow Volume Change of P2-Type Layered Oxide Cathode for Na-Ion Batteries With Controlled Phase Transition by Regulating Distribution of Na^{+}", *Angewandte Chemie*, Vol. 133, No. 38, pp. 21128–21137, 2021.

234. Guo Y.J., P.F. Wang, Y. Bin Niu, X.D. Zhang, Q. Li, X. Yu, M. Fan, W.P. Chen, Y. Yu, X. Liu, Q. Meng, S. Xin, Y.X. Yin, and Y.G. Guo, "Boron-Doped Sodium Layered Oxide for Reversible Oxygen Redox Reaction in Na-Ion Battery Cathodes", *Nature Communications*, Vol. 12, No. 1, pp. 1–11, 2021.

235. De la Llave E., E. Talaie, E. Levi, P.K. Nayak, M. Dixit, P.T. Rao, P. Hartmann, F. Chesneau, D.T. Major, M. Greenstein, D. Aurbach, and L.F. Nazar, "Improving Energy Density and Structural Stability of Manganese Oxide Cathodes for Na-Ion Batteries by Structural Lithium Substitution", *Chemistry of Materials*, Vol. 28, No. 24, pp. 9064–9076, 2016.

236. Kanwade A., S. Gupta, A. Kankane, M.K. Tiwari, A. Srivastava, J.A. Kumar Satrughna, S. Chand Yadav, and P.M. Shirage, "Transition Metal Oxides As a Cathode for Indispensable Na-Ion Batteries", *RSC Advances*, Vol. 12, No. 36, pp. 23284–23310, 2022.

237. Åvall G., J. Mindemark, D. Brandell, and P. Johansson, "Sodium-Ion Battery Electrolytes: Modeling and Simulations", *Advanced Energy Materials*, Vol. 8, No. 17, p. 1703036, 2018.

238. Xie J. and Q. Zhang, "Recent Progress in Multivalent Metal (Mg, Zn, Ca, and Al) and Metal-Ion Rechargeable Batteries With Organic Materials as Promising Electrodes", *Small*, Vol. 15, No. 15, p. 1805061, 2019.

239. Ponrouch A., J. Bitenc, R. Dominko, N. Lindahl, P. Johansson, and M. R. Palacin, "Multivalent Rechargeable Batteries", *Energy Storage Materials*, Vol. 20, pp. 253–262, 2019.

240. Jia H., Z. Wang, B. Tawiah, Y. Wang, C.Y. Chan, B. Fei, and F. Pan, “Recent Advances in Zinc Anodes for High-Performance Aqueous Zn-Ion Batteries”, *Nano Energy*, Vol. 70, p. 104523, 2020.

241. Li M., Z. Li, X. Wang, J. Meng, X. Liu, B. Wu, C. Han, and L. Mai, “Comprehensive Understanding of the Roles of Water Molecules in Aqueous Zn-Ion Batteries: From Electrolytes to Electrode Materials”, *Energy & Environmental Science*, Vol. 14, No. 7, pp. 3796–3839, 2021.

242. Zuo S., X. Xu, S. Ji, Z. Wang, Z. Liu, and J. Liu, “Cathodes for Aqueous Zn-Ion Batteries: Materials, Mechanisms, and Kinetics”, *Chemistry – A European Journal,* Vol. 27, No. 3, pp. 830–860, 2021.

243. Huy V. P. H., L. T. Hieu, and J. Hur, “Zn Metal Anodes for Zn-Ion Batteries in Mild Aqueous Electrolytes: Challenges and Strategies”, *Nanomaterials*, Vol. 11, No. 10, p. 2746, 2021.

244. Gao X., H. Zhang, X. Liu, and X. Lu, “Flexible Zn-Ion Batteries Based on Manganese Oxides: Progress and Prospect”, *Carbon Energy*, Vol. 2, No. 3, pp. 387–407, 2020.

245. Bensalah N. and Y. De Luna, “Recent Progress in Layered Manganese and Vanadium Oxide Cathodes for Zn-Ion Batteries”, *Energy Technology*, Vol. 9, No. 5, p. 2100011, 2021.

246. Zhao Y., Y. Zhu, and X. Zhang, “Challenges and Perspectives for Manganese-Based Oxides for Advanced Aqueous Zinc-Ion Batteries”, *InfoMat*, Vol. 2, No. 2, pp. 237–260, 2020.

247. Yi T. F., L. Qiu, J. P. Qu, H. Liu, J. H. Zhang, and Y. R. Zhu, “Towards High-Performance Cathodes: Design and Energy Storage Mechanism of Vanadium Oxides-Based Materials for Aqueous Zn-Ion Batteries”, *Coordination Chemistry Reviews*, Vol. 446, p. 214124, 2021.

248. Zhao Q., A. Song, S. Ding, R. Qin, Y. Cui, S. Li, F. Pan, Q. Zhao, A. Song, S. Ding, R. Qin, Y. Cui, S. Li, and F. Pan "Preintercalation Strategy in Manganese Oxides for Electrochemical Energy Storage: Review and Prospects", *Advanced Materials*, Vol. 32, No. 50, p. 2002450, 2020.

249. Chen S., D. Zhao, L. Chen, G. Liu, Y. Ding, Y. Cao, and Z. Chen, "Emerging Intercalation Cathode Materials for Multivalent Metal-Ion Batteries: Status and Challenges", *Small Structures*, Vol. 2, No. 11, p. 2100082, 2021.

250. Zuo S., X. Xu, S. Ji, Z. Wang, Z. Liu, and J. Liu, "Cathodes for Aqueous Zn-Ion Batteries: Materials, Mechanisms, and Kinetics", *Chemistry – A European Journal*, Vol. 27, No. 3, pp. 830–860, 2021.

251. Cao R., J.-S. Lee, M. Liu, and J. Cho, "Recent Progress in Non-Precious Catalysts for Metal-Air Batteries", *Advanced Energy Materials*, Vol. 2, No. 7, pp. 816–829, 2012.

252. Sun Y., X. Liu, Y. Jiang, J. Li, J. Ding, W. Hu, and C. Zhong, "Recent Advances and Challenges in Divalent and Multivalent Metal Electrodes for Metal–Air Batteries", *Journal of Materials Chemistry A*, Vol. 7, No. 31, pp. 18183–18208, 2019.

253. Dai Y., J. Yu, M. Ni, and Z. Shao, "Rational Design of Spinel Oxides as Bifunctional Oxygen Electrocatalysts for Rechargeable Zn-Air Batteries", *Chemical Physics Reviews*, Vol. 1, No. 1, p. 011303, 2020.

254. Wang Z. L., D. Xu, J. J. Xu, and X. B. Zhang, "Oxygen Electrocatalysts in Metal–Air Batteries: From Aqueous to Nonaqueous Electrolytes", *Chemical Society Reviews*, Vol. 43, No. 22, pp. 7746–7786, 2014.

255. Hu C., Y. Lin, J.W. Connell, H.-M. Cheng, Y. Gogotsi, M.-M. Titirici, L. Dai, C. Hu, L. Dai, Y. Lin, J.W. Connell, H.-M. Cheng, A.Y.J. Gogotsi, and M.-M. Titirici, "Carbon-Based Metal-Free Catalysts for Energy Storage and Environmental Remediation", *Advanced Materials*, Vol. 31, No. 13, p. 1806128, 2019.

256. Zhang J., Z. Xia, and L. Dai, “Carbon-Based Electrocatalysts for Advanced Energy Conversion and Storage”, *Science Advances*, Vol. 1, No. 7, p. E1500564, 2015.

257. Balaish M., A. Kraytsberg, and Y. Ein-Eli, “A Critical Review on Lithium–Air Battery Electrolytes”, *Physical Chemistry Chemical Physics*, Vol. 16, No. 7, p. 2801, 2014.

258. Mainar A.R., E. Iruin, L.C. Colmenares, A. Kvasha, I. de Meatza, M. Bengoechea, O. Leonet, I. Boyano, Z. Zhang, and J.A. Blazquez, “An Overview of Progress in Electrolytes for Secondary Zinc-Air Batteries and Other Storage Systems Based on Zinc”, *Journal of Energy Storage*, Vol. 15, pp. 304–328, 2018.

259. Egan R., C. Ponce de León, R. J. K. Wood, R. L. Jones, K. R. Stokes, and F. C. Walsh, “Developments in Electrode Materials and Electrolytes for Aluminium–Air Batteries”, *Journal of Power Sources*, Vol. 236, pp. 293–310, 2013.

260. Lai J., Y. Xing, N. Chen, L. Li, F. Wu, and R. Chen, “Electrolytes for Rechargeable Lithium–Air Batteries”, *Angewandte Chemie*, Vol. 59, No. 8, pp. 2974–2997, 2020.

261. Wang L., D. Snihirova, M. Deng, B. Vaghefinazari, W. Xu, D. Höche, S. V. Lamaka, and M.L. Zheludkevich, “Sustainable Aqueous Metal-Air Batteries: An Insight into Electrolyte System”, *Energy Storage Materials*, Vol. 52, pp. 573–597, 2022.

262. Liu Q., Z. Pan, E. Wang, L. An, and G. Sun, “Aqueous Metal-Air Batteries: Fundamentals and Applications”, *Energy Storage Materials*, Vol. 27, pp. 478–505, 2020.

263. Xu M., D. G. Ivey, Z. Xie, and W. Qu, “Rechargeable Zn-Air Batteries: Progress in Electrolyte Development and Cell Configuration Advancement”, *Journal of Power Sources*, Vol. 283, pp. 358–371, 2015.

264. Hosseini S., S. Masoudi Soltani, and Y. Y. Li, “Current Status and Technical Challenges of Electrolytes in Zinc–Air Batteries: An In-Depth Review”, *Chemical Engineering Journal*, Vol. 408, p. 127241, 2021.

265. Manthiram A., Y. Fu, S.-H. Chung, C. Zu, and Y.-S. Su, “Rechargeable Lithium–Sulfur Batteries”, *Chemical Reviews*, Vol. 114, No. 23, pp. 11751–11787, 2014.

266. Yu X. and A. Manthiram, “Electrode–Electrolyte Interfaces in Lithium–Sulfur Batteries With Liquid or Inorganic Solid Electrolytes”, *Accounts of Chemical Research*, Vol. 50, No. 11, pp. 2653–2660, 2017.

267. Jiang M., Z. Zhang, B. Tang, T. Dong, H. Xu, H. Zhang, X. Lu, and G. Cui, “Polymer Electrolytes for Li-S Batteries: Polymeric Fundamentals and Performance Optimization”, *Journal of Energy Chemistry*, Vol. 58, pp. 300–317, 2021.

268. Li S., W. Zhang, J. Zheng, M. Lv, H. Song, L. Du, S.L. Li, W.F. Zhang, J.F. Zheng, M.Y. Lv, H.Y. Song, and L. Du, “Inhibition of Polysulfide Shuttles in Li–S Batteries: Modified Separators and Solid-State Electrolytes”, *Advanced Energy Materials*, Vol. 11, No. 2, p. 2000779, 2021.

269. Zhao H., N. Deng, J. Yan, W. Kang, J. Ju, Y. Ruan, X. Wang, X. Zhuang, Q. Li, and B. Cheng, “A Review on Anode for Lithium-Sulfur Batteries: Progress and Prospects”, *Chemical Engineering Journal*, Vol. 347, pp. 343–365, 2018.

270. Fan K., Y. Tian, X. Zhang, and J. Tan, “Application of Stabilized Lithium Metal Powder and Hard Carbon in Anode of Lithium–Sulfur Battery”, *Journal of Electroanalytical Chemistry*, Vol. 760, pp. 80–84, 2016.

271. Jing H.-K., L.-L. Kong, S. Liu, G.-R. Li, and X.-P. Gao, “Protected Lithium Anode With Porous Al_2O_3 Layer for Lithium-Sulfur Battery”, *Journal of Materials Chemistry A*, Vol. 3, No. 23, pp. 12213–12219, 2015.

272. Nanda S., A. Gupta, and A. Manthiram, “A Lithium–Sulfur Cell Based on Reversible Lithium Deposition From a Li_2S Cathode Host Onto a Hostless-Anode Substrate”, *Advanced Energy Materials*, Vol. 8, No. 25, p. 1801556, 2018.

273. Fan L., N. Deng, J. Yan, Z. Li, W. Kang, and B. Cheng, “The Recent Research Status Quo and the Prospect of Electrolytes for Lithium Sulfur Batteries”, *Chemical Engineering Journal*, Vol. 369, pp. 874–897, 2019.

274. Mukra T., Y. Horowitz, I. Shekhtman, M. Goor, S. Drvarič Talian, L. Burstein, J. Kasnatscheew, P. Meister, M. Grünebaum, M. Winter, H.-D. Wiemhöfer, D. Golodnitsky, and E. Peled, “Disiloxane With Nitrile End Groups as Co-Solvent for Electrolytes in Lithium Sulfur Batteries – A Feasible Approach to Replace $LiNO_3$”, *Electrochimica Acta*, Vol. 307, pp. 76–82, 2019.

275. Ding N., S. W. Chien, T. S. A. Hor, Z. Liu, and Y. Zong, “Key Parameters in Design of Lithium Sulfur Batteries”, *Journal of Power Sources*, Vol. 269, pp. 111–116, 2014.

276. Ma Z., F. Jing, Y. Fan, J. Li, Y. Zhao, and G. Shao, “High Electrical Conductivity of 3D Mesporous Carbon Nanocage as an Efficient Polysulfide Buffer Layer for High Sulfur Utilization in Lithium-Sulfur Batteries”, *Journal of Alloys and Compounds*, Vol. 789, pp. 71–79, 2019.

277. Dörfler S., M. Hagen, H. Althues, J. Tübke, S. Kaskel, and M. J. Hoffmann, “High Capacity Vertical Aligned Carbon Nanotube/Sulfur Composite Cathodes for Lithium–Sulfur Batteries”, *Chemical Communications*, Vol. 48, No. 34, pp. 4097–4099, 2012.

278. Fan L., H. L. Zhuang, K. Zhang, V. R. Cooper, Q. Li, and Y. Lu, “Chloride-Reinforced Carbon Nanofiber Host as Effective Polysulfide Traps in Lithium–Sulfur Batteries”, *Advanced Science*, Vol. 3, No. 12, p. 1600175, 2016.

279. Gao X.-C., Y.-J. Shen, L.-L. Xing, Q. Wang, and X.-Y. Xue, "High Electrochemical Performance of Hierarchical $CoMoS_{3.13}/SnO_2$ Nanocomposites as Lithium-Sulfur Battery Cathode", *Materials Letters*, Vol. 183, pp. 413–416, 2016.

280. Yuan Z., H.-J. Peng, T.-Z. Hou, J.-Q. Huang, C.-M. Chen, D.-W. Wang, X.-B. Cheng, F. Wei, and Q. Zhang, "Powering Lithium–Sulfur Battery Performance by Propelling Polysulfide Redox at Sulfiphilic Hosts", *Nano Letters*, Vol. 16, No. 1, pp. 519–527, 2016.

281. Barchasz C., J.-C. Leprêtre, F. Alloin, and S. Patoux, "New Insights Into the Limiting Parameters of the Li/S Rechargeable Cell", *Journal of Power Sources*, Vol. 199, pp. 322–330, 2012.

282. Wang D.-W., Q. Zeng, G. Zhou, L. Yin, F. Li, H.-M. Cheng, I.R. Gentle, and G.Q.M. Lu, "Carbon–Sulfur Composites for Li–S Batteries: Status and Prospects", *Journal of Materials Chemistry A,* Vol. 1, No. 33, pp. 9382–9394, 2013.

283. Wang J., S.Y. Chew, Z.W. Zhao, S. Ashraf, D. Wexler, J. Chen, S.H. Ng, S.L. Chou, and H.K. Liu, "Sulfur–Mesoporous Carbon Composites in Conjunction With a Novel Ionic Liquid Electrolyte for Lithium Rechargeable Batteries", *Carbon*, Vol. 46, No. 2, pp. 229–235, 2008.

284. Ji X. and L. F. Nazar, "Advances in Li-S Batteries", *Journal of Materials Chemistry*, Vol. 2, No. 44, pp. 9821–9826, 2010.

285. Moon S., Y. H. Jung, W. K. Jung, D. S. Jung, J. W. Choi, and D. K. Kim, "Encapsulated Monoclinic Sulfur for Stable Cycling of Li–S Rechargeable Batteries", *Advanced Materials*, Vol. 25, No. 45, pp. 6547–6553, 2013.

286. Zhou G., Y. Zhao, and A. Manthiram, "Dual-Confined Flexible Sulfur Cathodes Encapsulated in Nitrogen-Doped Double-Shelled Hollow Carbon Spheres and Wrapped With Graphene for Li–S Batteries", *Advanced Energy Materials*, Vol. 5, No. 9, p. 1402263, 2015.

287. Zheng G., Y. Yang, J. J. Cha, S. S. Hong, and Y. Cui, “Hollow Carbon Nanofiber-Encapsulated Sulfur Cathodes for High Specific Capacity Rechargeable Lithium Batteries”, *Nano Letters*, Vol. 11, No. 10, pp. 4462–4467, 2011.

288. Zhang B., X. Qin, G. R. Li, and X. P. Gao, “Enhancement of Long Stability of Sulfur Cathode by Encapsulating Sulfur Into Micropores of Carbon Spheres”, *Energy & Environmental Science*, Vol. 3, No. 10, pp. 1531–1537, 2010.

289. Xin S., Y.-X. Yin, L.-J. Wan, and Y.-G. Guo, “Encapsulation of Sulfur in a Hollow Porous Carbon Substrate for Superior Li-S Batteries With Long Lifespan”, *Particle & Particle Systems Characterization*, Vol. 30, No. 4, pp. 321–325, 2013.

290. Bao W., Z. Zhang, Y. Gan, X. Wang, and J. Lia, “Enhanced Cyclability of Sulfur Cathodes in Lithium-Sulfur Batteries With Na-Alginate as a Binder”, *Journal of Energy Chemistry,* Vol. 22, No. 5, pp. 790–794, 2013.

291. Xu G., B. Ding, J. Pan, P. Nie, L. Shen, and X. Zhang, “High Performance Lithium–Sulfur Batteries: Advances and Challenges”, *Journal of Materials Chemistry A*, Vol. 2, No. 32, pp. 12662–12676, 2014.

292. Babu G., K. Ababtain, K. Y. S. Ng, and L. M. R. Arava, “Electrocatalysis of Lithium Polysulfides: Current Collectors as Electrodes in Li/S Battery Configuration”, *Scientific Reports*, Vol. 5, p. 8763, 2015.

293. Hu G., C. Xu, Z. Sun, S. Wang, H.-M. Cheng, F. Li, and W. Ren, “3D Graphene-Foam–Reduced-Graphene-Oxide Hybrid Nested Hierarchical Networks for High-Performance Li–S Batteries”, *Advanced Materials*, Vol. 28, No. 8, pp. 1603–1609, 2016.

294. Peng H.-J., W.-T. Xu, L. Zhu, D.-W. Wang, J.-Q. Huang, X.-B. Cheng, Z. Yuan, F. Wei, and Q. Zhang “3D Carbonaceous Current Collectors: The Origin of Enhanced Cycling Stability for High-Sulfur-Loading Lithium–Sulfur Batteries”, *Advanced Functional Materials*, Vol. 26, No. 35, pp. 6351–6358, 2016.

295. Chung S.-H. and A. Manthiram, “Lithium–Sulfur Batteries With Superior Cycle Stability by Employing Porous Current Collectors”, *Electrochimica Acta*, Vol. 107, pp. 569–576, 2013.

296. Huang J.-Q., Q. Zhang, and F. Wei, “Multi-Functional Separator/Interlayer System for High-Stable Lithium-Sulfur Batteries: Progress and Prospects”, *Energy Storage Materials*, Vol. 1, pp. 127–145, 2015.

297. Zhu J., M. Yanilmaz, K. Fu, C. Chen, Y. Lu, Y. Ge, D. Kim, and X. Zhang “Understanding Glass Fiber Membrane Used as a Novel Separator for Lithium–Sulfur Batteries”, *Journal of Membrane Science*, Vol. 504, pp. 89–96, 2016.

298. Deng N., W. Kang, Y. Liu, J. Ju, D. Wu, L. Li, B.S. Hassan, and B. Cheng, “A Review on Separators for Lithium Sulfur Battery: Progress and Prospects”, *Journal of Power Sources*, Vol. 331, pp. 132–155, 2016.

299. Xu R., Y. Sun, Y. Wang, J. Huang, and Q. Zhang, “Two-Dimensional Vermiculite Separator for Lithium Sulfur Batteries”, *Chinese Chemical Letters*, Vol. 28, No. 12, pp. 2235–2238, 2017.

300. Jeong Y. C., J. H. Kim, S. Nam, C. R. Park, and S. J. Yang, “Rational Design of Nanostructured Functional Interlayer/Separator for Advanced Li–S Batteries”, *Advanced Functional Materials*, Vol. 28, No. 38, p. 1707411, 2018.

301. Li C., A. L. Ward, S. E. Doris, T. A. Pascal, D. Prendergast, and B. A. Helms, “Polysulfide-Blocking Microporous Polymer Membrane Tailored for Hybrid Li-Sulfur Flow Batteries”, *Nano Letters*, Vol. 15, No. 9, pp. 5724–5729, 2015.

302. Xiao Z., Z. Yang, L. Wang, H. Nie, M. Zhong, Q. Lai, X. Xu, L. Zhang, and S. Huang, “A Lightweight TiO_2/Graphene Interlayer, Applied as a Highly Effective Polysulfide Absorbent for Fast, Long-Life Lithium–Sulfur Batteries”, *Advanced Materials*, Vol. 27, No. 18, pp. 2891–2898, 2015.

303. Cha E., M. D. Patel, T. Y. Choi, and C. Wonbong, “Lithium-Sulfur Batteries: The Effect of High Sulfur Loading on the Electrochemical Performance”, *ECS Transactions,* Vol. 85, No. 13, pp. 295–302, 2018.

304. Fang R., S. Zhao, P. Hou, M. Cheng, S. Wang, H.-M. Cheng, C. Liu, and F. Li, “3D Interconnected Electrode Materials With Ultrahigh Areal Sulfur Loading for Li–S Batteries”, *Advanced Materials*, Vol. 28, No. 17, pp. 3374–3382, 2016.

305. Michaelis C., N. Erisen, D. Eroglu, and G. M. Koenig, “Electrochemical Performance and Modeling of Lithium-Sulfur Batteries With Varying Carbon to Sulfur Ratios”, *International Journal of Energy Research*, Vol. 43, No. 2, pp. 874–883, 2019.

306. Chung S.-H. and A. Manthiram, “Designing Lithium-Sulfur Cells With Practically Necessary Parameters”, *Joule*, Vol. 2, No. 4, pp. 710–724, 2018.

307. Yuan S., J. L. Bao, L. Wang, Y. Xia, D. G. Truhlar, and Y. Wang, “Graphene-Supported Nitrogen and Boron Rich Carbon Layer for Improved Performance of Lithium–Sulfur Batteries Due to Enhanced Chemisorption of Lithium Polysulfides”, *Advanced Energy Materials*, Vol. 6, No. 5, p. 1501733, 2016.

308. Niu S., G. Zhou, W. Lv, H. Shi, C. Luo, Y. He, B. Li, Q.-H. Yang, and F. Kang, “Sulfur Confined in Nitrogen-Doped Microporous Carbon Used in a Carbonate-Based Electrolyte for Long-Life, Safe Lithium-Sulfur Batteries”, *Carbon*, Vol. 109, pp. 1–6, 2016.

309. Yang C.-P., Y.-X. Yin, H. Ye, K.-C. Jiang, J. Zhang, and Y.-G. Guo, “Insight Into the Effect of Boron Doping on Sulfur/Carbon Cathode in Lithium–Sulfur Batteries”, *ACS Applied Materials & Interfaces*, Vol. 6, No. 11, pp. 8789–8795, 2014.

310. Sun F., J. Wang, H. Chen, W. Li, W. Qiao, D. Long, and L. Ling, “High Efficiency Immobilization of Sulfur on Nitrogen-Enriched Mesoporous Carbons for Li–S Batteries”, *ACS Applied Materials & Interfaces*, Vol. 5, No. 12, pp. 5630–5638, 2013.

311. Liu S., J. Li, X. Yan, Q. Su, Y. Lu, J. Qiu, Z. Wang, X. Lin, J. Huang, R. Liu, B. Zheng, L. Chen, R. Fu, and D. Wu, "Superhierarchical Cobalt-Embedded Nitrogen-Doped Porous Carbon Nanosheets as Two-In-One Hosts for High-Performance Lithium–Sulfur Batteries", *Advanced Materials*, Vol. 30, No. 12, p. 1706895, 2018.

312. Chen L. and L. L. Shaw, "Recent Advances in Lithium–Sulfur Batteries", *Journal of Power Sources*, Vol. 267, pp. 770–783, 2014.

313. Li G., Z. Li, B. Zhang, and Z. Lin, "Developments of Electrolyte Systems for Lithium-Sulfur Batteries: A Review", *Frontiers in Energy Research*, Vol. 3, pp. 5.1-5.12, 2015.

314. Pope M. A. and I. A. Aksay, "Structural Design of Cathodes for Li-S Batteries", *Advanced Energy Materials*, Vol. 5, No. 16, p. 1500124, 2015.

315. Zhang S. S., "A New Finding on the Role of $LiNO_3$ in Lithium-Sulfur Battery", *Journal of Power Sources*, Vol. 322, pp. 99–105, 2016.

316. Jozwiuk A., H. Sommer, J. Janek, and T. Brezesinski, "Fair Performance Comparison of Different Carbon Blacks in Lithium–Sulfur Batteries With Practical Mass Loadings – Simple Design Competes With Complex Cathode Architecture", *Journal of Power Sources*, Vol. 296, pp. 454–461, 2015.

317. Adams B.D., E. V Carino, J.G. Connell, K.S. Han, R. Cao, J. Chen, J. Zheng, Q. Li, K.T. Mueller, W.A. Henderson, and J.-G. Zhang, "Long Term Stability of Li-S Batteries Using High Concentration Lithium Nitrate Electrolytes", *Nano Energy*, Vol. 40, pp. 607–617, 2017.

318. Choi J.-W., J.-K. Kim, G. Cheruvally, J.-H. Ahn, H.-J. Ahn, and K.-W. Kim, "Rechargeable Lithium/Sulfur Battery With Suitable Mixed Liquid Electrolytes", *Electrochimica Acta*, Vol. 52, No. 5, pp. 2075–2082, 2007.

319. Zhang S. S., “Improved Cyclability of Liquid Electrolyte Lithium/Sulfur Batteries by Optimizing Electrolyte/Sulfur Ratio”, *Energies*, Vol. 5, No. 12, pp. 5190–5197, 2012.

320. Zheng J., D. Lv, M. Gu, C. Wang, J.-G. Zhang, J. Liu, and J. Xiao, “How to Obtain Reproducible Results for Lithium Sulfur Batteries?”, *Journal of the Electrochemical Society*, Vol. 160, No. 11, pp. A2288–A2292, 2013.

321. Hagen M., P. Fanz, and J. Tübke, “Cell Energy Density and Electrolyte/Sulfur Ratio in Li–S Cells”, *Journal of Power Sources*, Vol. 264, pp. 30–34, 2014.

322. Kim J.-E., C.-S. Jin, K.-H. Shin, and S.-H. Yeon, “Optimized Cell Conditions for a High-Energy Density, Large-Scale Li–S Battery”, *International Journal of Energy Research*, Vol. 40, No. 5, pp. 670–676, 2016.

323. Yue J., M. Yan, Y.-X. Yin, and Y.-G. Guo, “Progress of the Interface Design in All-Solid-State Li–S Batteries”, *Advanced Functional Materials*, Vol. 28, No. 38, p. 1707533, 2018.

324. Chen S., F. Dai, M. L. Gordin, and D. Wang, “Exceptional Electrochemical Performance of Rechargeable Li–S Batteries With a Polysulfide-Containing Electrolyte”, *RSC Advances*, Vol. 3, No. 11, pp. 3540–3543, 2013.

325. Kazazi M., M. R. Vaezi, and A. Kazemzadeh, “Improving the Self-Discharge Behavior of Sulfur-Polypyrrole Cathode Material by $LiNO_3$ Electrolyte Additive”, *Ionics*, Vol. 20, No. 9, pp. 1291–1300, 2014.

326. Barghamadi M., A.S. Best, A.I. Bhatt, A.F. Hollenkamp, P.J. Mahon, M. Musameh, and T. Rüther, “Effect of Anion on Behaviour of Li-S Battery Electrolyte Solutions Based on N-Methyl-N-Butyl-Pyrrolidinium Ionic Liquids”, *Electrochimica Acta*, Vol. 180, pp. 636–644, 2015.

327. Wu F., Q. Zhu, R. Chen, N. Chen, Y. Chen, and L. Li, “A Safe Electrolyte With Counterbalance Between the Ionic Liquid and Tris(Ethylene Glycol)Dimethyl Ether

for High Performance Lithium-Sulfur Batteries", *Electrochimica Acta*, Vol. 184, pp. 356–363, 2015.

328. Meisner Q.J., T. Rojas, T. Glossmann, A. Hintennach, Q. Liu, J. Cao, P.C. Redfern, A.T. Ngo, L.A. Curtiss, and Z. Zhang, "Impact of Co-Solvent and LiTFSI Concentration on Ionic Liquid-Based Electrolytes for Li-S Battery", J*ournal of the Electrochemical Society*, Vol. 167, No. 7, p. 70528, 2020.

329. Barghamadi M., A.S. Best, A.I. Bhatt, A.F. Hollenkamp, M. Musameh, R.J. Rees, and T. Rüther, "Lithium–Sulfur Batteries—The Solution Is in the Electrolyte, But Is the Electrolyte a Solution?", *Energy & Environmental Science*, Vol. 7, No. 12, pp. 3902–3920, 2014.

330. Li G., W. Lei, D. Luo, Y. Deng, Z. Deng, D. Wang, A. Yu, and Z. Chen, "Stringed 'Tube On Cube' Nanohybrids as Compact Cathode Matrix for High-Loading and Lean-Electrolyte Lithium–Sulfur Batteries", *Energy & Environmental Science*, Vol. 11, No. 9, pp. 2372–2381, 2018.

331. Dörfler S., S. Walus, J. Locke, A. Fotouhi, D.J. Auger, N. Shateri, T. Abendroth, P. Härtel, H. Althues, and S. Kaskel, "Recent Progress and Emerging Application Areas for Lithium–Sulfur Battery Technology", *Energy Technology*, Vol. 9, No. 1, p. 2000694, 2021.

332. Bhargav A., J. He, A. Gupta, and A. Manthiram, "Lithium-Sulfur Batteries: Attaining the Critical Metrics", *Joule*, Vol. 4, No. 2, pp. 285–291, 2020.

333. Cheng L., L. A. Curtiss, K. R. Zavadil, A. A. Gewirth, Y. Shao, and K. G. Gallagher, "Sparingly Solvating Electrolytes for High Energy Density Lithium–Sulfur Batteries", *ACS Energy Letters*, Vol. 1, No. 3, pp. 503–509, 2016.

334. Sun K., A.K. Matarasso, R.M. Epler, X. Tong, D. Su, A.C. Marschilok, K.J. Takeuchi, E.S. Takeuchi, and H. Gan, "Effect of Electrolyte on High Sulfur Loading Li-S

Batteries", *Journal of the Electrochemical Society*, Vol. 165, No. 2., pp. A416-423, 2018.

335. Chung S.-H., L. Luo, and A. Manthiram, "TiS_2–Polysulfide Hybrid Cathode With High Sulfur Loading and Low Electrolyte Consumption for Lithium–Sulfur Batteries", *ACS Energy Letters*, Vol. 3, No. 3, pp. 568–573, 2018.

336. Mu T., J. Rarey, and J. Gmehling, "Performance of COSMO-RS With Sigma Profiles From Different Model Chemistries", *Industrial and Engineering Chemistry Research*, Vol. 46, No. 20, pp. 6612–6629, 2007.

337. Paduszyński K., "An Overview of the Performance of the COSMO-RS Approach in Predicting the Activity Coefficients of Molecular Solutes in Ionic Liquids and Derived Properties at Infinite Dilution", *Physical Chemistry Chemical Physics*, Vol. 19, No. 19, pp. 11835–11850, 2017.

338. Yanagi M., K. Ueno, A. Ando, S. Li, Y. Matsumae, J. Liu, K. Dokko, and M. Watanabe, "Effects of Polysulfide Solubility and Li-Ion Transport on Performance of Li–S Batteries Using Sparingly Solvating Electrolytes", *Journal of the Electrochemical Society*, Vol. 167, No. 7, p. 070531, 2020.

339. Dong K., S. Zhang, and J. Wang, "Understanding the Hydrogen Bonds in Ionic Liquids and Their Roles in Properties and Reactions", *Chemical Communications*, Vol. 52, No. 41, pp. 6744–6764, 2016.

340. Tan J., J. Matz, P. Dong, M. Ye, and J. Shen, "Appreciating the Role of Polysulfides in Lithium-Sulfur Batteries and Regulation Strategies by Electrolytes Engineering", *Energy Storage Materials*, Vol. 42, pp. 645–678, 2021.

341. Karelson M., V. S. Lobanov, and A. R. Katritzky, "Quantum-Chemical Descriptors in QSAR/QSPR Studies", *Chemical Reviews*, Vol. 96, No. 3, pp. 1027–1044, 1996.

342. Wang L., J. Ding, L. Pan, D. Cao, H. Jiang, and X. Ding, "Quantum Chemical Descriptors in Quantitative Structure–Activity Relationship Models and Their Applications", *Chemometrics and Intelligent Laboratory Systems*, Vol. 217, p. 104384, 2021.

343. Aghaie M. and S. Zendehboudi, "Estimation of CO_2 Solubility in Ionic Liquids Using Connectionist Tools Based On Thermodynamic and Structural Characteristics", *Fuel*, Vol. 279, p. 117984, 2020.

344. Dhakal P. and J. K. Shah, "Developing Machine Learning Models for Ionic Conductivity of Imidazolium-Based Ionic Liquids", *Fluid Phase Equilibria*, Vol. 549, p. 113208, 2021.

345. Koutsoukos S., F. Philippi, F. Malaret, and T. Welton, "A Review on Machine Learning Algorithms for the Ionic Liquid Chemical Space", *Chemical Science*, Vol. 12, No. 20, pp. 6820–6843, 2021.

346. Zheng W., A. Mohammed, L.G. Hines, D. Xiao, O.J. Martinez, R.A. Bartsch, S.L. Simon, O. Russina, A. Triolo, and E.L. Quitevis, "Effect of Cation Symmetry on the Morphology and Physicochemical Properties of Imidazolium Ionic Liquids", *Journal of Physical Chemistry B*, Vol. 115, No. 20, pp. 6572–6584, 2011.

347. Pereiro A.B., J.M.M. Araújo, S. Martinho, F. Alves, S. Nunes, A. Matias, C.M.M. Duarte, L.P.N. Rebelo, and I.M. Marrucho, "Fluorinated Ionic Liquids: Properties and Applications", *ACS Sustainable Chemical Engineering*, Vol. 1, No. 4, pp. 427–439, 2013.

348. Angulakshmi N., R. B. Dhanalakshmi, S. Sathya, J. Ahn, and A. M. Stephan, "Understanding the Electrolytes of Lithium−Sulfur Batteries", *Batteries & Supercaps*, Vol. 4, No. 7, pp. 1064–1095, 2021.

349. Nakamura N., S. Ahn, T. Momma, and T. Osaka, "Future Potential for Lithium-Sulfur Batteries", *Journal of Power Sources*, Vol. 558, p. 232566, 2023.

350. Azimi N., Z. Xue, L. Hu, C. Takoudis, S. Zhang, and Z. Zhang, “Additive Effect on the Electrochemical Performance of Lithium–Sulfur Battery”, *Electrochimica Acta*, Vol. 154, pp. 205–210, 2015.

351. Xiong S., X. Kai, X. Hong, and Y. Diao, “Effect of LiBOB as Additive on Electrochemical Properties of Lithium–Sulfur Batteries”, *Ionics*, Vol. 18, No. 3, pp. 249–254, 2012.

352. Xiang H., P. Shi, P. Bhattacharya, X. Chen, D. Mei, M.E. Bowden, J. Zheng, J.-G. Zhang, and W. Xu, “Enhanced Charging Capability of Lithium Metal Batteries Based on Lithium Bis(Trifluoromethanesulfonyl)Imide-Lithium Bis(Oxalato)Borate Dual-Salt Electrolytes”, *Journal of Power Sources*, Vol. 318, pp. 170–177, 2016.

353. Nasrabadi M., M. A. Ghasemzadeh, and M. R. Zand Monfared, “The Preparation and Characterization of UiO-66 Metal–Organic Frameworks for the Delivery of the Drug Ciprofloxacin and an Evaluation of Their Antibacterial Activities”, *New Journal of Chemistry*, Vol. 43, No. 40, pp. 16033–16040, 2019.

354. Cavka J.H., S. Jakobsen, U. Olsbye, N. Guillou, C. Lamberti, S. Bordiga, and K.P. Lillerud, “A New Zirconium Inorganic Building Brick Forming Metal Organic Frameworks With Exceptional Stability”, *Journal of American Chemical Society*, Vol. 130, No. 42, pp. 13850–13851, 2008.

355. Ciucci F., “Revisiting Parameter Identification in Electrochemical Impedance Spectroscopy: Weighted Least Squares and Optimal Experimental Design”, *Electrochimica Acta*, Vol. 87, pp. 532–545, 2013.

356. Sun K., H. Liu, and H. Gan, “Cathode Loading Effect on Sulfur Utilization in Lithium–Sulfur Battery”, *Journal of Electrochemical Energy Conversion and Storage*, Vol. 13, No. 2, p. 021002, 2016.

357. Middlemiss A., A. J. R. Rennie, R. Sayers, and A. R. West, “Characterisation of Batteries by Electrochemical Impedance Spectroscopy”, *Energy Reports*, Vol. 6, pp. 232–241, 2020.

358. Dörfler S., S. Walus, J. Locke, A. Fotouhi, D.J. Auger, N. Shateri, T. Abendroth, P. Härtel, H. Althues, and S. Kaskel, “Recent Progress and Emerging Application Areas for Lithium–Sulfur Battery Technology”, *Energy Technology*, Vol. 9, No. 1, p. 2000694, 2021.

359. Zhu K., C. Wang, Z. Chi, F. Ke, Y. Yang, A. Wang, W. Wang, and L. Miao, “How Far Away Are Lithium-Sulfur Batteries From Commercialization?”, *Frontiers in Energy Research*, Vol. 7, p. 123, 2019.

360. Song H., H. Deng, C. Li, N. Feng, P. He, and H. Zhou, “Advances in Lithium-Containing Anodes of Aprotic Li–O_2 Batteries: Challenges and Strategies for Improvements”, *Small Methods*, Vol. 1, No. 8, p. 1700135, 2017.

361. Guo H., G. Hou, D. Li, Q. Sun, Q. Ai, P. Si, G. Min, J. Lou, J. Feng, and L. Ci, “High Current Enabled Stable Lithium Anode for Ultralong Cycling Life of Lithium–Oxygen Batteries”, *ACS Applied Materials & Interfaces*, Vol. 11, No. 34, pp. 30793–30800, 2019.

362. Kim Y., D. Koo, S. Ha, S.C. Jung, T. Yim, H. Kim, S.K. Oh, D.-M. Kim, A. Choi, Y. Kang, K.H. Ryu, M. Jang, Y.-K. Han, S.M. Oh, and K.T. Lee, “Two-Dimensional Phosphorene-Derived Protective Layers on a Lithium Metal Anode for Lithium-Oxygen Batteries”, *ACS Nano*, Vol. 12, No. 5, pp. 4419–4430, 2018.

363. Liu Q.-C., J.-J. Xu, S. Yuan, Z.-W. Chang, D. Xu, Y.-B. Yin, L. Li, H.-X. Zhong, Y.-S. Jiang, J.-M. Yan, and X.-B. Zhang, “Artificial Protection Film on Lithium Metal Anode Toward Long-Cycle-Life Lithium-Oxygen Batteries”, *Advanced Materials*, Vol. 27, No. 40, p. 6089, 2015.

364. Wang H.-F. and Q. Xu, “Materials Design for Rechargeable Metal-Air Batteries”, *Matter*, Vol. 1, No. 3, pp. 565–595, 2019.

365. Shao Y., F. Ding, J. Xiao, J. Zhang, W. Xu, S. Park, J.-G. Zhang, Y. Wang, and J. Liu, “Making Li-Air Batteries Rechargeable: Material Challenges”, *Advanced Functional Materials*, Vol. 23, No. 8, pp. 987–1004, 2013.

366. Wen Z., C. Shen, and Y. Lu, “Air Electrode for the Lithium–Air Batteries: Materials and Structure Designs”, *ChemPlusChem*, Vol. 80, No. 2, pp. 270–287, 2015.

367. Mahmood N. and Y. Hou, “Electrode Nanostructures in Lithium-Based Batteries”, *Advanced Science*, Vol. 1, No. 1, p. 1400012, 2014.

368. Nasybulin E., W. Xu, M. H. Engelhard, Z. Nie, X. S. Li, and J.-G. Zhang, “Stability of Polymer Binders in Li–O_2 Batteries”, *Journal of Power Sources*, Vol. 243, pp. 899–907, 2013.

369. Black R., S. H. Oh, J.-H. Lee, T. Yim, B. Adams, and L. F. Nazar, “Screening for Superoxide Reactivity in Li-O_2 Batteries: Effect On Li_2O_2/LiOH Crystallization”, *Journal of the American Chemical Society*, Vol. 134, No. 6, pp. 2902–2905, 2012.

370. Freunberger A., Y. Chen, N. E. Drewett, L. J. Hardwick, F. Bardé, and P. G. Bruce, “The Lithium–Oxygen Battery With Ether-Based Electrolytes”, *Angewandte Chemie*, Vol. 50, No. 37, pp. 8609–8613, 2011.

371. Papp J.K., J.D. Forster, C.M. Burke, H.W. Kim, A.C. Luntz, R.M. Shelby, J.J. Urban, and B.D. McCloskey, “Poly(Vinylidene Fluoride) (PVDF) Binder Degradation in Li–O_2 Batteries: A Consideration for the Characterization of Lithium Superoxide”, *The Journal of Physical Chemistry Letters*, Vol. 8, No. 6, pp. 1169–1174, 2017.

372. Younesi R., S. Urbonaite, F. Björefors, and K. Edström, “Influence of the Cathode Porosity on the Discharge Performance of the Lithium–Oxygen Battery”, *Journal of Power Sources*, Vol. 196, No. 22, pp. 9835–9838, 2011.

373. Chatterjee A., S. W. Or, and Y. Cao, “Transition Metal Hollow Nanocages as Promising Cathodes for the Long-Term Cyclability of Li–O_2 Batteries”, *Nanomaterials*, Vol. 8, No. 5, p. 308, 2018.

374. Wang D., X. Mu, P. He, and H. Zhou, “Materials for Advanced Li-O_2 Batteries: Explorations, Challenges and Prospects”, *Materials Today*, Vol. 26, pp. 87–99, 2019.

375. Elia A., J.-B. Park, Y.-K. Sun, B. Scrosati, and J. Hassoun, “Role of the Lithium Salt in the Performance of Lithium–Oxygen Batteries: A Comparative Study”, *ChemElectroChem*, Vol. 1, No. 1, pp. 47–50, 2014.

376. Younesi R., G. M. Veith, P. Johansson, K. Edström, and T. Vegge, “Lithium Salts for Advanced Lithium Batteries: Li–Metal, Li–O_2, and Li–S”, *Energy & Environmental Science*, Vol. 8, No. 7, pp. 1905–1922, 2015.

377. Kwak W.-J., D. Hirshberg, D. Sharon, M. Afri, A.A. Frimer, H.-G. Jung, D. Aurbach, and Y.-K. Sun, “Li–O_2 Cells With LiBr As An Electrolyte and a Redox Mediator”, *Energy & Environmental Science*, Vol. 9, No. 7, pp. 2334–2345, 2016.

378. Chen Y., S. A. Freunberger, Z. Peng, O. Fontaine, and P. G. Bruce, “Charging a Li-O_2 Battery Using a Redox Mediator.”, *Nature Chemistry*, Vol. 5, No. 6, pp. 489–494, 2013.

379. Park S.H., Y.J. Cheon, Y.J. Lee, K.H. Shin, Y.Y. Hwang, Y.S. Jeong, and Y.J. Lee, “Maximal Utilization of a High-Loading Cathode in Li–O_2 Batteries: A Double Oxygen Supply System”, *ACS Applied Materials & Interfaces*, Vol. 11, No. 34, pp. 30872–30879, 2019.

380. Cheng F. and J. Chen, “Metal–Air Batteries: From Oxygen Reduction Electrochemistry to Cathode Catalysts”, *Chemical Society Reviews*, Vol. 41, No. 6, p. 2172, 2012.

381. Hall L. H., Brian. Mohney, and L. B. Kier, “The Electrotopological State: Structure Information at the Atomic Level for Molecular Graphs”, *Journal of Chemical Information and Computer Science*, Vol. 31, No. 1, pp. 76–82, 1991.

382. Labute P., “A Widely Applicable Set of Descriptors”, *Journal of Molecular Graphics and Modelling*, Vol. 18, No. 4–5, pp. 464–477, 2000.

383. Rogers D. and M. Hahn, “Extended-Connectivity Fingerprints”, *Journal of Chemical Information and Modeling*, Vol. 50, No. 5, pp. 742–754, 2010.

384. Balaban A. T., “Highly Discriminating Distance-Based Topological Index”, *Chemical Physics Letters*, Vol. 89, No. 5, pp. 399–404, 1982.

385. Bertz H., “The First General Index of Molecular Complexity”, *Journal of the American Chemical Society*, Vol. 103, No. 12, pp. 3599–3601, 1981.

386. Bonchev D. and N. Trinajstić, “Information Theory, Distance Matrix, and Molecular Branching”, *The Journal of Chemical Physics*, Vol. 67, No. 10, pp. 4517–4533, 1977.

387. Han S. and H. Kim, “Optimal Feature Set Size in Random Forest Regression”, *Applied Sciences*, Vol. 11, No. 8, p. 3428, 2021.

388. Corvo M.C., J. Sardinha, T. Casimiro, G. Marin, M. Seferin, S. Einloft, S.C. Menezes, J. Dupont, and E.J. Cabrita, “A Rational Approach To CO_2 Capture by Imidazolium Ionic Liquids: Tuning CO_2 Solubility by Cation Alkyl Branching”, *ChemSusChem*, Vol. 8, No. 11, pp. 1935–1946, 2015.

389. Ding Y., M. Chen, C. Guo, P. Zhang, and J. Wang, “Molecular Fingerprint-Based Machine Learning Assisted QSAR Model Development for Prediction of Ionic Liquid Properties”, *Journal of Molecular Liquids*, Vol. 326, p. 115212, 2021.

390. Jian Y., Y. Wang, and A. Barati Farimani, "Predicting CO_2 Absorption in Ionic Liquids With Molecular Descriptors and Explainable Graph Neural Networks", *ACS Sustainable Chemical Engineering*, Vol. 10, No. 50, pp. 16681–16691, 2022.

391. Lei Z., C. Dai, and B. Chen, "Gas Solubility in Ionic Liquids", *Chemical Reviews*, Vol. 114, No. 2, pp. 1289–1326, 2014.

392. Zhang X., Z. Liu, and W. Wang, "Screening of Ionic Liquids to Capture CO_2 by COSMO-RS and Experiments", *AIChE Journal*, Vol. 54, No. 10, pp. 2717–2728, 2008.

393. Ramalingam A. and T. Banerjee, "Prediction and Validation of Carbon Dioxide Gas Solubility in Ionic Liquids at T=298k and Atmospheric Pressure Using Quantum Chemical Approach", *Chemical Product and Process Modeling*, Vol. 6, No. 1, pp. 1-27, 2011.

394. Stanton T., "Evaluation and Use of BCUT Descriptors in QSAR and QSPR Studies", *Journal of Chemical Information and Computer Science*, Vol. 39, No. 1, pp. 11–20, 1999.

395. Ertl P., B. Rohde, and P. Selzer, "Fast Calculation of Molecular Polar Surface Area as a Sum of Fragment-Based Contributions and Its Application to the Prediction of Drug Transport Properties", *Journal of Medicinal Chemistry*, Vol. 43, No. 20, pp. 3714–3717, 2000.

396. Wildman S. A. and G. M. Crippen, "Prediction of Physicochemical Parameters by Atomic Contributions", *Journal of Chemical Information and Computer Science*, Vol. 39, No. 5, pp. 868–873, 1999.

397. Bickerton G. R., G. V. Paolini, J. Besnard, S. Muresan, and A. L. Hopkins, "Quantifying the Chemical Beauty of Drugs", *Nature Chemistry*, Vol. 4, No. 2, pp. 90–98, 2012.

APPENDIX A: SUPPORTING INFORMATION ON SECTION 4.1.1

The additional information on Section 4.1.1 is given in this section. First, the details of the database is given in Table A.1 and than the details of the alternative materials are listed.

Table A.1. The details of the database.

Dataset	Number of Data	Number of Publications
Cells using liquid electrolyte	1463	303
Cells using catholyte	142	33
Cells using liquid + solid electrolyte	33	10
Cells using solid electrolyte	22	7
Total	1660	353

Details of the alternative materials are as follows:

- Hollow Structured Carbon1&2*:* Hollow Carbon Foam
- *Hollow Structured Carbon3:* Acetylene Black Nano Hollow Carbon, Double Shelled HCS, HCS, Hollow Carbon Foam, Hollow Carbon Nanospheres, Hollow Carbon Spheres, Hollow Porous Carbon, Hollow Porous Carbon Bowl, Hollow Porous Carbon Sphere, Mesoporous Carbon Hollow Spheres, Mesoporous HCS, Multi-Shelled Hollow Carbon Nanosphere, Porous Hollow Carbon Nanocapsule Monoliths
- Hollow Structured Carbon4*:* Hollow Carbon Nanospheres, Multi-Shelled Hollow Carbon Nanosphere
- *Modified Li anode:* Hard Carbon+Carbon Black+PVDF+Polymer Separator+Li Metal, Li Metal+ Al_2NO_3 Layer, Li Metal+Glass Fiber Layer, Li Metal+Hydroquinol+rGO, Li&In Alloys, Lithiated Si/SiO_x Nanosphere, Nanostructured Li Contained in Fibrous Li_7B_6 Matrix, Prelithiated Ge, Stabilized Li Powder, Stabilized Li Powder+Hard Carbon+PVDF, Graphite Powder+Super P+PVDF+Polymer Separator+Li, Prelithiated Graphite
- Others1: Graphite Coated Al Foil, Cu Foil+CNT Sheets, Graphene Layer, Graphene, Cu Foil, Gas Diffusion Layer, Stainless Steel, Copper, Carbon Coated Ti Foil, Au-Coated Stainless-Steel

- Others2: Graphene Oxide, HKUST-1, LATP Glass-Ceramic, Vermiculite
- Others3: TiS_2, CoS_2, LiTFSI, FeS_2
- Others4: TiS_2, CoS_2, $CoMoS_{3.13}$
- Others5: CNT+IP, TiN, PTFE, Silica Etched Carbon, MWCNT+Polypyrrole, Silica, Ammonium Bicarbonate, HKUST-1, Nano MgO, Teflonized Carbon Black, ZIF-8, MnO_2, Carbon Polysulfide Polymer, Carbon Polysulfide Polymer+Graphene
- Others6: Conductive Agent
- Others7: MoC+MoO_x, Phosphorene Nanosheets, Silicon Carbide Whisker Foam, Vanadium Nitride, Vanadium Oxide, HKUST-1, TiO_2
- Others8: Amylopectin, Diatomite
- Others9: GO, $CaCl_2$, $InCl_3$, $MgCl_2$, WS_2
- Others10: 1,3-diisopropenylbenzen copolymer, Ni, Polyethylenimine, Zeolitic ZIF-8, ZIF-8, HKUST-1, MOF-5˚
- Others11: 2-ethylimidazole MOF, Amylopectin, Anthraquinone, Imidazole MOF, Metal Organic Framework
- Others12: TiO_2, Nano MnS, Hollow MoO_2 Sphere, MnO_2, PDDA, SiO_2, $Ti_3C_2T_x$, ZrO_2, ZrO_2, VO_2 nanobelts
- Others13: Polydopamine
- Others14: Trithiocyanuric Acid, PVP
- Others15: Nano Co, Nano CoS_2, Si/SiO_2
- Others16: 3-D Diamond-Cage Porous Polymer Frameworks, Co_3S_4 Nanotubes, Core–Shell Structured Spoly(Sodium P-Styrenesulfonate) , Covalent Organic Frameworks, Crosslinked Polystyrene, Hollow $NiCo_2O_4$ Micrutubes, $LiFePO_4$, LiV_3O_8, Metal Cotton, MnO_2, PEG+ MnO_2, Poly(Divinyl Benzene), Polyacrylonitrile, Polydopamine, Porous Aromatic Framework, Porous Organic Polymer, Porous Triazine-Based Frameworks, Porous Trithiocyanuric Acid Crystals , Prussian Blue, Sepiolite, Silica, SiO_2, SnO_2 Nanocomposites, $Ti_3C_2T_x$, Ti_4O_7 Nanoparticles, Ti_4O_7 Nanorods, TiO_2, TiO_2 Spheres With Mesopores, ZIF-8, α-Mno2 Nanowires
- Others17: PEDOT+Poly(styrene sulfonate), + SiO_2
- Others18: Boron, Sulfur, Cobalt
- Others19: TiO_2, Iodine, Diatomite, CeO_2, Cobalt Oxyhydroxide, Mo_4O_{11}, Boron, NbS_2, Si/SiO_2, Boron+Oxygen, Fluorine, Dodecyl Benzene Sulfonic Acid, MnO_2

- Others20: PVP, Sodium Alginate, PDADMA-T, PEG, Polypyrrole+Polyurethane nanocomposite, Beta-Cyclodextrin, LA133+ SBR, Alginic Acid Sodium Salt, Polyvinyl alcohol, Poly(acrylonitrile-methyl methacrylate), Kynar, Gum Arabic, Thiokol, Fluoropolymer, Na Alginate, Gelatin, PVC, Cation Aqueous Polyurethane Resin, Poly(vinylidene difluoride-co-chlorotrifluoroethylene), Poly(vinylidene difluoride-tri- fluoroethylene), Poly(acrylic acid)
- Others21: Hexa-fluoropropene, Polyethylenimine(PEI)
- Others22: PVP, Kynar
- Others23: DMDS, CS_2, $PYR_{14}TFSI$
- Others24: DMC, DMC:DEC, EMC, EMC:DEC
- Others25: $Li(G3)_1TFSA$, ACN:TTE, Carbonate:DMC, DEGDME, Diglyme, DMA, DME, DOL:$CHF_2CF_2CH_2OCF_2CF_2H$, DOL:DMC, DOL:EGDME, DOL:PEGDME, EC:DMC(anode) &Tetrahydrofuran(cathode), Methyl Isopropyl Sulfone, N-methyl-N-propylpyrrolidine+bisTFSI, PEGDME, 1-methyl-3-propyl imidazolium+ TFSI, Sulfolane, Sulfonate, TEGDME(anode side)+DMA(cathode side), TMS:TTE, Tri(ethylene glycol)-substituted trimethylsilane, TTE:DOL
- Others26: LiFSI, LiFSI+LiTFSI, LiPF6(anode), LiTDI, LiTFSI+LiTDI
- Other Carbons1: Amorphous Carbon Shell
- Other Carbons2: Carbon Felt, Carbon Hybrid Spheres, Carbon Microspheres, Carbon Nanoflakes, Carbon Nanoparticles, Carbon Nanospheres, Carbon Polyhedrons, Carbon Slice, Layered Carbon, Meso Carbon Micro Beads, Mesocarbon Microbeads(Graphite), Microcrystalline Graphite Minerals, Nanostructured Carbon, Non-Layered Carbons, Solid Carbon Spheres, Yolk–Shell Carbon Nanospheres Microporous Shell, Mesoporous Core
- Other Carbons3: Carbon Polyhedrons, Carbon Hydrid Spheres
- Porous Carbons1: Porous Carbon
- Porous Carbons2: CMK-3
- Porous Carbons3: CMK-3, Porous Carbons, Porous Carbons Nanospheres
- Porous Carbons4: Porous Carbon Nanospheres
- Porous Carbons5: Mesoporous Carbon, Porous Carbon
- Porous Carbons6: Double Wrapped Porous Carbon, Porous Carbon, Hierarchically Porous Carbon, Mesoporous Carbon

- Porous Carbons7: Double Wrapped Porous Carbon
- Porous carbons8: CMK-3, Hierarchical Porous Carbon , Hierarchically Pore Structured Carbon, Meso Carbon Micro Beads, Mesophase Micro Bead Carbon, Mesoporous Carbon, Micro-Macro Porous Carbon, Microporous Carbon Polyhedrons, Microspherical Mesoporous Carbon, Nanoporous Carbon , Nanoporous Carbon Beads, Ordered Porous Carbon, Peapodlike Mesoporous Carbon, Porous Carbon, Porous Carbon Nanosheets, Porous Rattle-Type Carbon Sphere, Spherical Ordered Mesoporous Carbon, Ultramicroporous Carbon
- Porous Carbons9: CMK-3, Spherical Ordered Mesoporous Carbon, Mesoporous Carbon, Peapodlike Mesoporous Carbon
- Structured Carbon1: CNF, rGO, Nitrogen-Doped Porous Hollow Carbon Sphere, Graphitized Carbon Nanofibers, Graphite, Graphene, CNT
- Structured Carbon2: Vapor Given Carbon Fiber, rGO, Carbon Cloth, Carbon Nanofiber, Carbon Sponge, CNF, Cotton-Carbon, Graphene, GO, Graphene+Cotton-Carbon, Graphite, Graphitized Carbon Black, OMC
- Structured Carbon3: Carbon Fiber Foam, CNF, Graphene, CNT
- Structured Carbons4: Activated Carbon Aerogels, Activated CNT, Activated Nanoporous Carbon Beads, Monolithic Carbon, Microporous Activated Carbon Fibers

Sulfur weight percent estimation was also done. The regression model is performed by analyzing 241 data points in which sulfur is melt diffused into conductive medium at a specific temperature and duration. Other encapsulation methods are not used in the analysis since they induce significantly different conditions. According to the analysis, the achieved S wt.%'s can be calculated with

$$S\ wt.\%\ Achieved = 34.3202 - 0.1568\ x\ Temperature - 0.2211x\ Time + 0.856\ x\ S\ wt.\%\ Targeted, \quad (A.1)$$

Equation (A.1). In this analysis 10 fold cross validation is performed. The data was randomly divided into 10 groups; nine groups were used for model building while the remaining group of data was used for testing the model. This procedure was repeated 10 times with different testing groups to make sure that the model is valid in entire data interval. The training and testing RMSE values were found to be 5.38 and 6.34 respectively; they are quite small

considering that we categorized S wt.% within 25 % intervals. The training and testing plots for measured versus predicted S wt.% (achieved) are given in the Figure A.1.

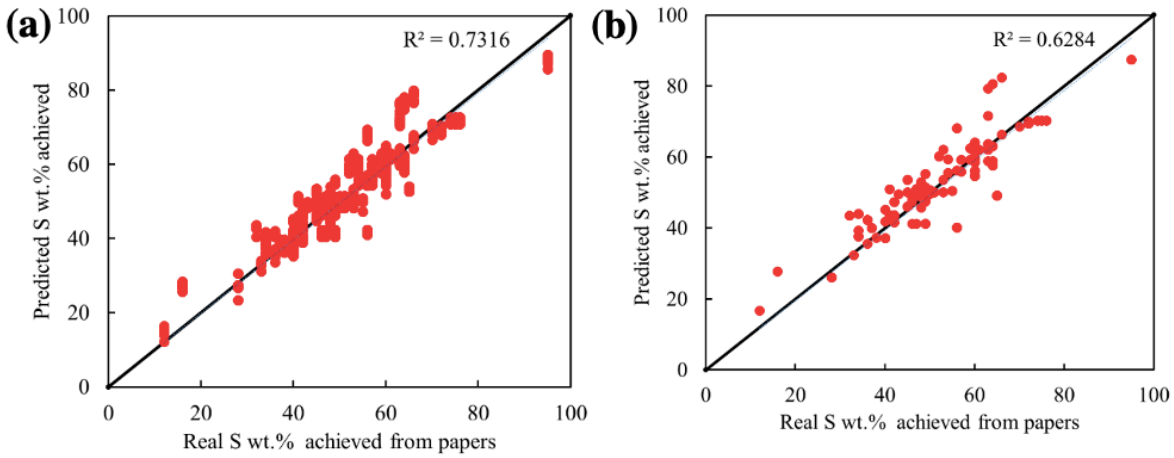

Figure A.1. The training (a) and the testing (b) plots of regression model for achieved S wt.% calculation.

APPENDIX B: SUPPORTING INFORMATION ON SECTION 4.1.2

Here, the additional figures and tables are given in this section.

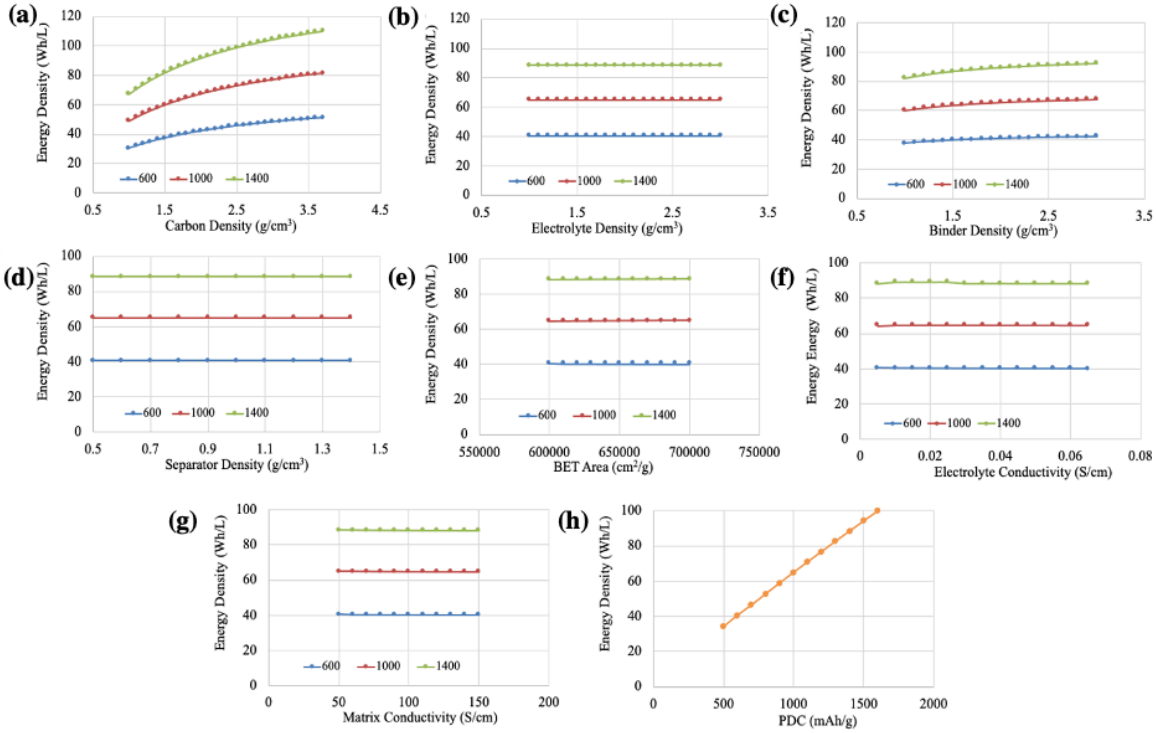

Figure B.1. The sensitivity analysis for the calculated energy density (Wh/L) determined at cathode discharge capacities of 600mAh/g S, 1000 mAh/g and 1400 mAh/g using the modified BatPac model.

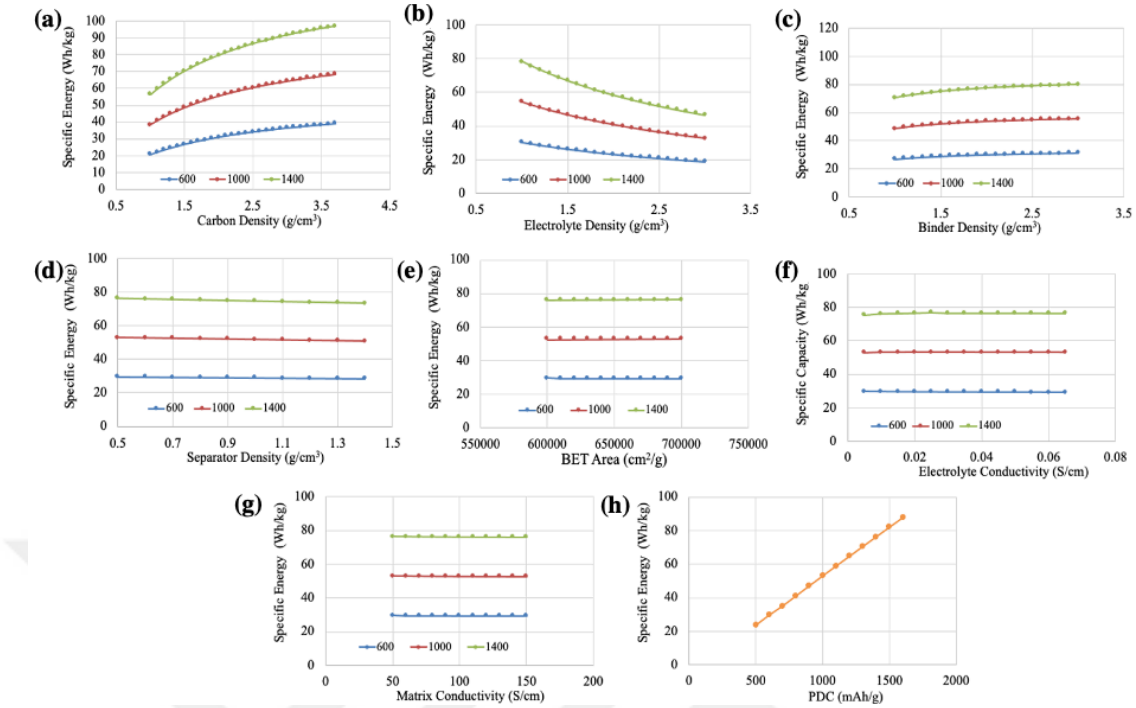

Figure B.2. The sensitivity analysis for the calculated specific energy (Wh/kg) determined at cathode discharge capacities of 600mAh/g S, 1000 mAh/g and 1400 mAh/g using the modified BatPac model.

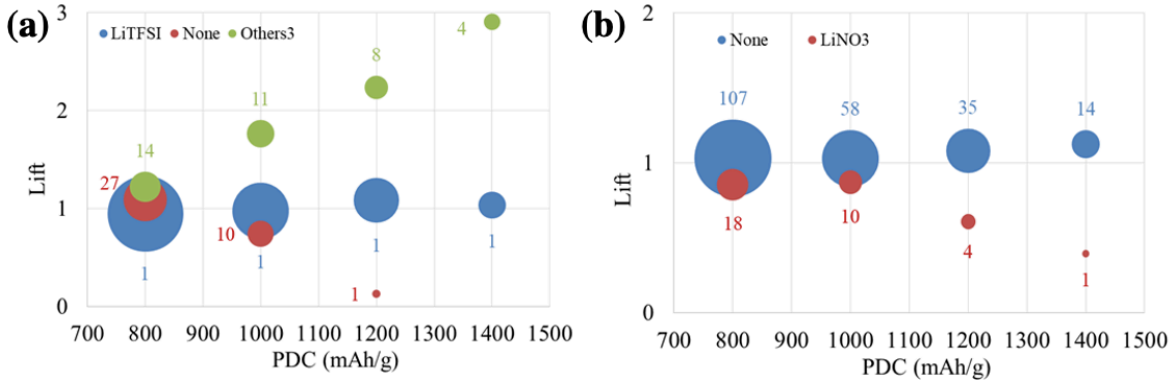

Figure B.3. Lift vs. peak discharge capacity of electrolyte salt (a) and additive (b) of molecular solvent.

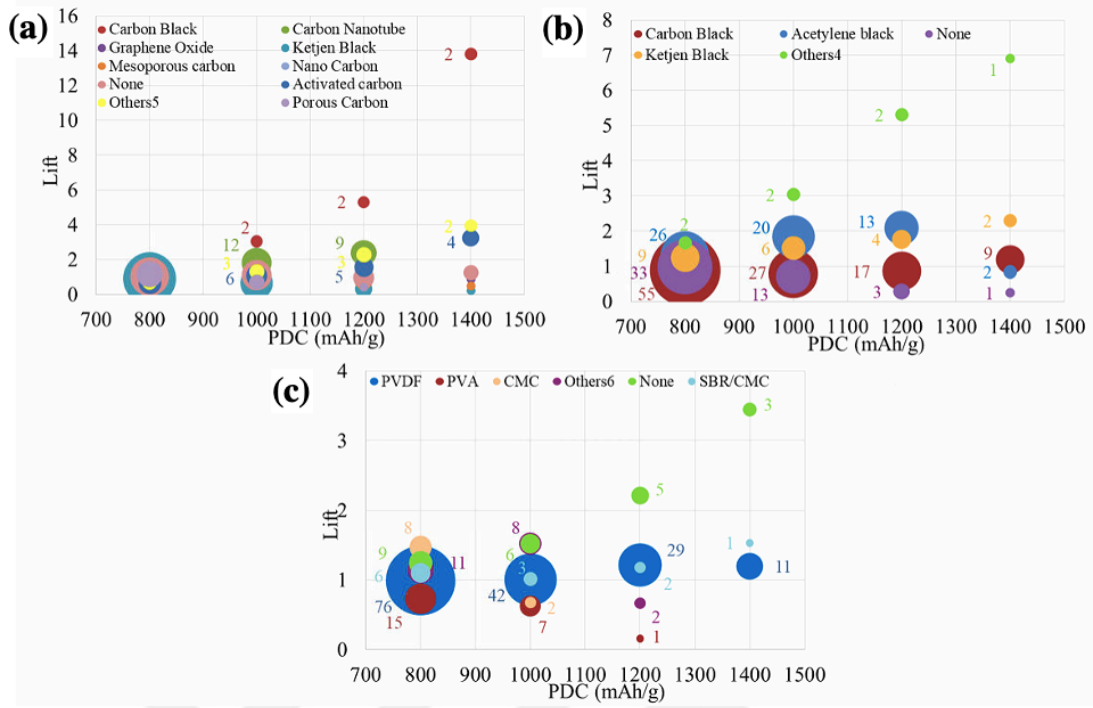

Figure B.4. Lift vs. peak discharge capacity of encapsulation material (a), conductive additive (b) and binder (c) in the sulfur cathode.

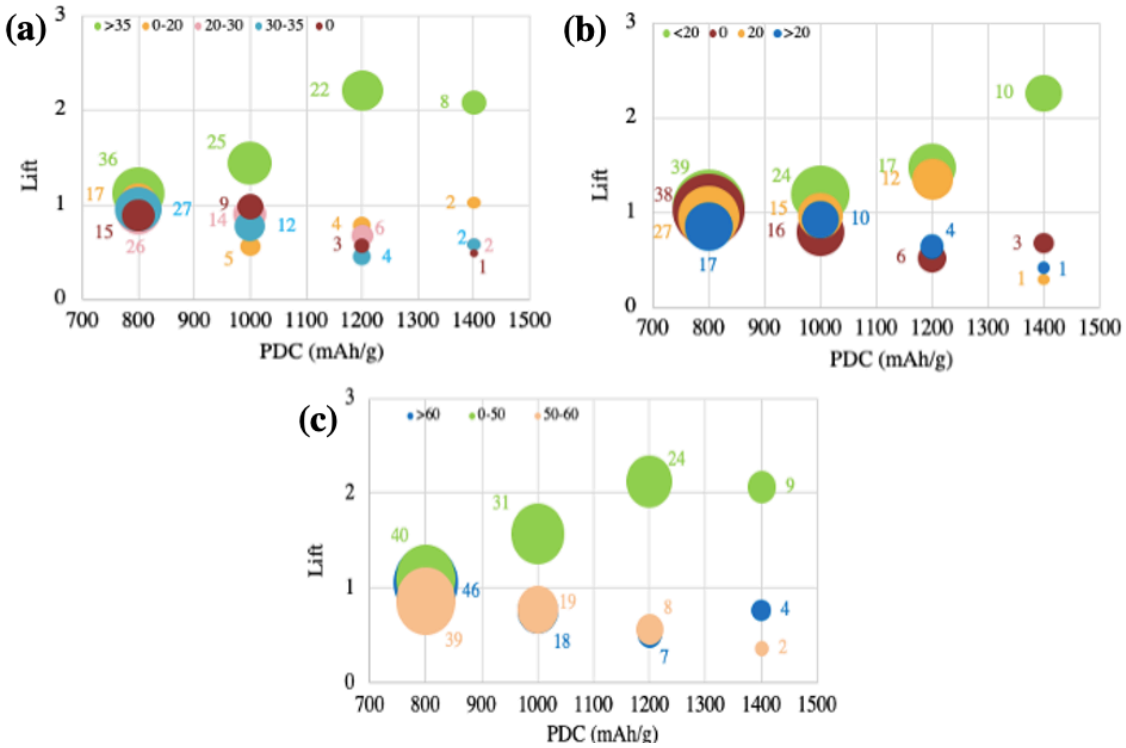

Figure B.5. Lift vs. peak discharge capacity of encapsulation material wt.% (a), conductive additive wt.%(b) and sulfur wt.% (c) in the sulfur cathode.

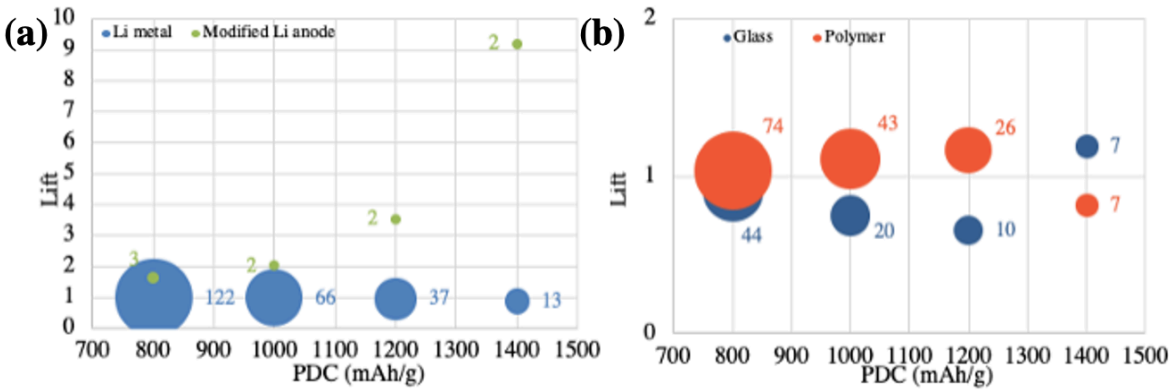

Figure B.6. Lift vs. peak discharge capacity of anode material (a) and separator (b).

Table B. 1. ARM results for energy densities ≥ 60 Wh/L.

Factors	Levels	Support	Confidence	Lift	Count
Conductive_Material_Categorized	Others4	0.010	0.050	5.10	1
Binder_Categorized	CMC	0.069	0.350	3.97	7
E/S_Ratio_Categorized	0-15.0	0.186	0.950	3.59	19
S_Loading_Cat	>4.0	0.088	0.450	3.06	9
Conductive_Material_Categorized	None	0.069	0.350	2.98	7
Encapsulation_wt%_Categorized	30-35	0.069	0.350	2.98	7
Molecular_Solvent_Categorized	TEGDME	0.049	0.250	2.83	5
Encapsulation_Material_Categorized	Carbon Nanotube	0.049	0.250	2.55	5
IL_Abbreviation	P1,2O1_TFSI	0.049	0.250	2.55	5
S_wt%_Categorized	0-50	0.049	0.250	2.32	5
Conductive_wt%_Categorized	0	0.069	0.350	2.10	7
IL_Abbreviation	Li(G4)_TFSI	0.069	0.350	1.88	7
Conductive_wt%_Categorized	20	0.088	0.450	1.84	9
S_wt%_Categorized	>60	0.098	0.500	1.82	10
Encapsulation_Material_Categorized	Ketjen Black	0.069	0.350	1.70	7
Encapsulation_Material_Categorized	Graphene Oxide	0.049	0.250	1.59	5
Encapsulation_wt%_Categorized	>35	0.049	0.250	1.59	5
Electrolyte_Salt_Categorized	None	0.069	0.350	1.49	7
IL/Solvent_vol.%_Categorized	100	0.069	0.350	1.49	7
Molecular_Solvent_Categorized	No	0.069	0.350	1.49	7
Separator_Categorized	Polymer	0.167	0.850	1.45	17
Encapsulation_Material_Categorized	Mesoporous carbon	0.029	0.150	1.28	3
Conductive_Material_Categorized	Acetylene black	0.049	0.250	1.21	5
Molecular_Solvent_Categorized	DOL:DME	0.078	0.400	1.20	8

APPENDIX C: SUPPORTING INFORMATION ON SECTION 4.1.3

The additional information about the dataset obtained from COSMO-RS calculations are given in this section. In addition, prediction results of IL properties are also presented.

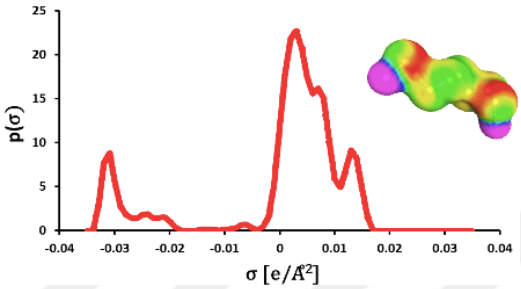

Figure C.1. The sigma (σ) profile and corresponding sigma surface of Li_2S_8 molecule obtained from TMOLEX.

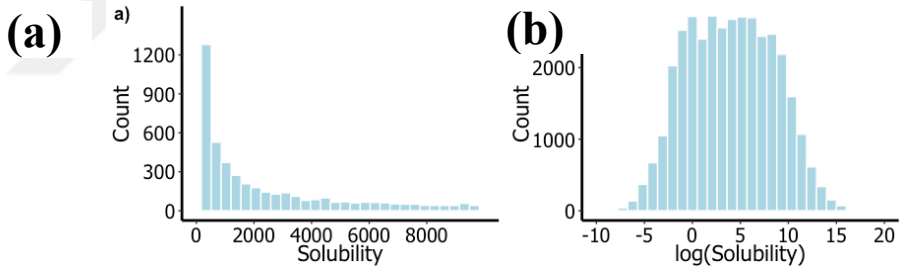

Figure C.2. The COSMO-RS solubility (mol/mol) of ILs (a) and its log transformation for the entire dataset (b).

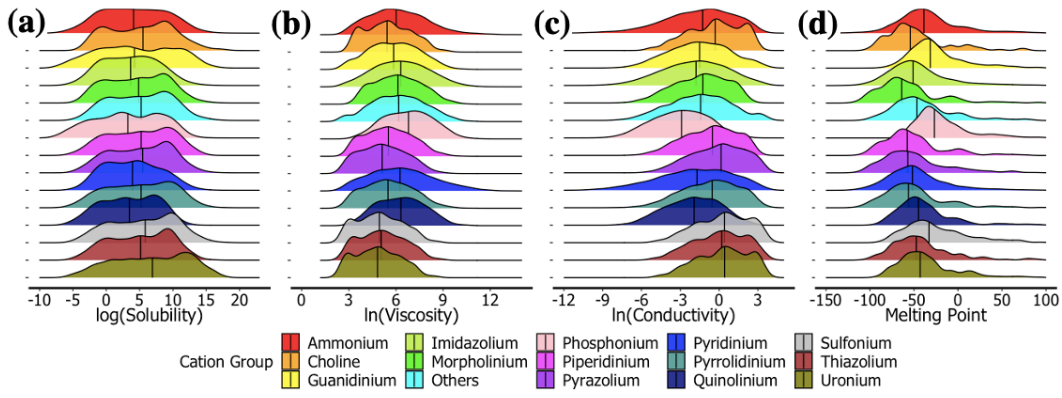

Figure C.3. The COSMO-RS calculated log(solubility (mol/mol)) (a), ln(viscosity (mPa.s)) (b), ln(conductivity (S/cm)) (c), melting point (°C) (d), of ILs based on cation group.

Table C.1. COSMO-RS and experimental solubilities of Li_2S_8.

Abbreviation	Cosmo-RS Li2S8(mol/mol)	log(CosmoRS Li2S8)	Park et al.	log(Park et al. Li2S8)
P13_TFSI	0.43	-0.36	10.68	1.03
P13_BETA	0.11	-0.97	2.45	0.39
P13_FSA	0.04	-1.44	1.58	0.20
P14_TFSI	0.25	-0.60	8.86	0.95
PP13_TFSI	0.34	-0.47	5.98	0.78
C4DMIM_TFSI	0.36	-0.44	5.43	0.73
DEME_TFSI	0.38	-0.42	7.69	0.89
P2225_TFSI	0.09	-1.05	4.16	0.62
P14_OTF	1357.63	3.13	957.50	2.98

BETA: bis(pentafluoroethylsulfonyl)amide, C4dmim: 1-butyl-2,3-dimethyli-imidazolium, DEME:N,N-diethyl-N-methyl-N-(2-methoxyethyl)-ammonium, FSI: bis(fluorosulfonyl)imide, OTF: trifluoromethane-sulfonate, P13:1-methyl-1-propyl-pyrrolidinium, P14: 1-butyl-1-methyl-pyrrolidinium, P2225: triethyl-pentyl-phosphonium, PP13:1-methyl-1-propyl-piperidinium, TFSI: bis(trifluoromethane)sulfonimide

Table C.2. The cationic and the anionic properties of the selected ionic liquids used in Li-S cells.

	Abb.	**Mol. Wt (amu)**	**E.HOMO (eV)**	**E.LUMO (eV)**	**Dipole (debye)**	**CPK Area (Å)**	**CPK Ovality**	**Polarizability**	**HBD Count**	**HBA Count**	**ZPE (kJ. mol)**
Cation	PP14	156.3	-14.9	-4.2	3.8	219.3	1.3	55.2	0.0	1.0	799.2
	DEME	90.1	-10.6	2.5	0.0	136.3	1.3	47.0	0.0	2.0	359.7
	TBMA	200.4	-14.7	-4.2	2.4	295.4	1.5	60.6	0.0	1.0	1073.6
	BMIM	125.2	-14.6	-5.0	7.9	202.8	1.4	53.2	0.0	2.0	572.3
Anion	TFSI	280.1	-7.2	2.1	0.0	208.4	1.5	52.2	0.0	7.0	132.5
	PF_6	145.0	-9.1	5.4	0.0	100.4	1.2	43.9	0.0	0.0	37.2
	CF_3SO_3	149.1	-6.4	4.8	2.4	117.9	1.2	45.8	0.0	4.0	64.6
	$MeSO_4$	111.1	-6.1	6.3	7.7	109.8	1.2	45.0	0.0	5.0	131.4

BMIM: 1-butyl-3-methyl-imidazolium, CF3SO3: trifluoromethane-sulfonate, DEME: N,N-diethyl-N-methyl-N-(2-methoxyethyl)ammonium, MeSO4: methylsulfate, PF6: hexafluorophosphate, PP14: 1-butyl-1-methylpiperidinium, TBMA: tributylmethylammonium, TFSI: bis(trifluoromethane)sulfonimide

Table C.3. The hyperparameters used in Xgboost analysis.

Models	Max_depth	Nrounds	Eta
Solubility	3	225	0.1
ln(viscosity)	4	150	0.1
ln(conductivity)	3	250	0.1
Melting point	4	300	0.1

The other factors were ser as gamma=1, subsample = 1, min_child_weight = 1, colsample_bytree = 0.8

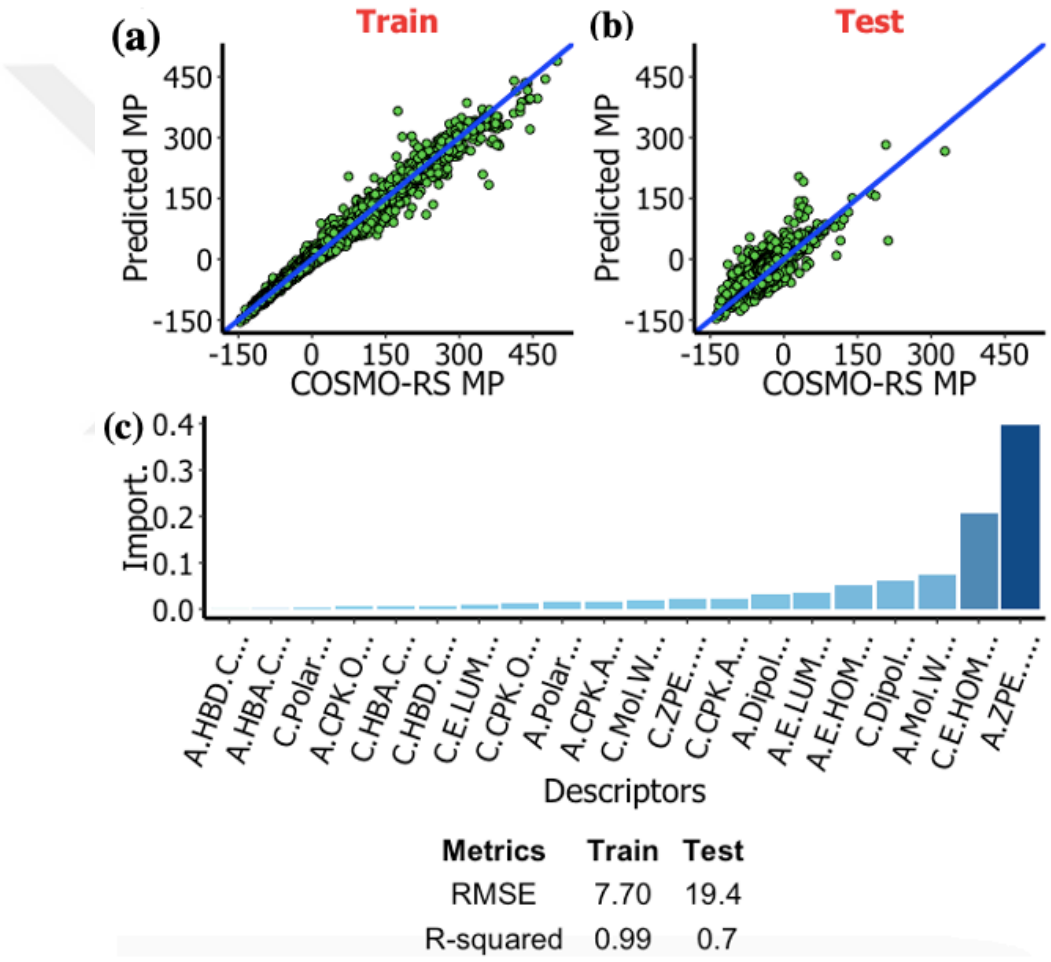

Figure C.4. Prediction results of melting point for train (a), test (b) sets and model importance (c).

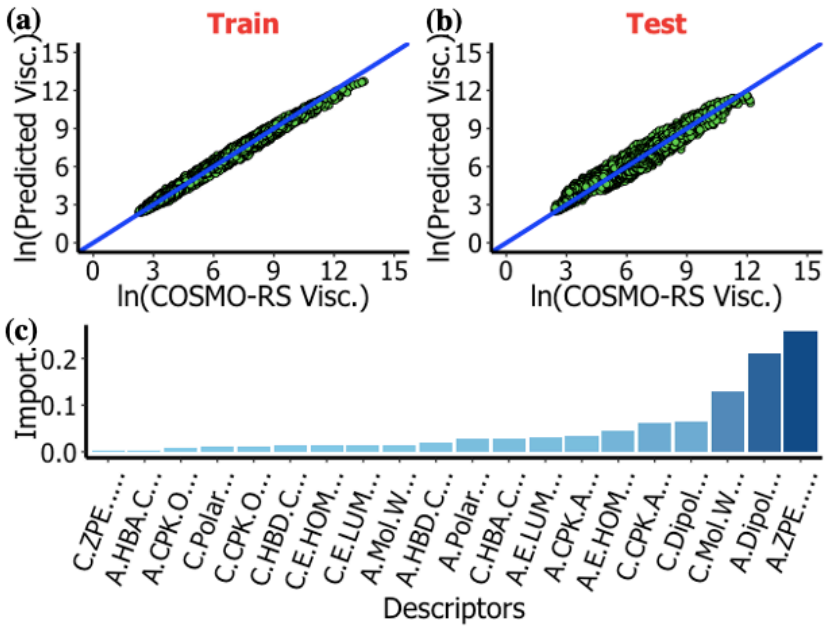

Metrics	Train	Test
RMSE	0.18	0.48
R-squared	0.99	0.92

Figure C.5. Prediction results of ln(viscosity) for train (a), test(b) sets and model importance (c).

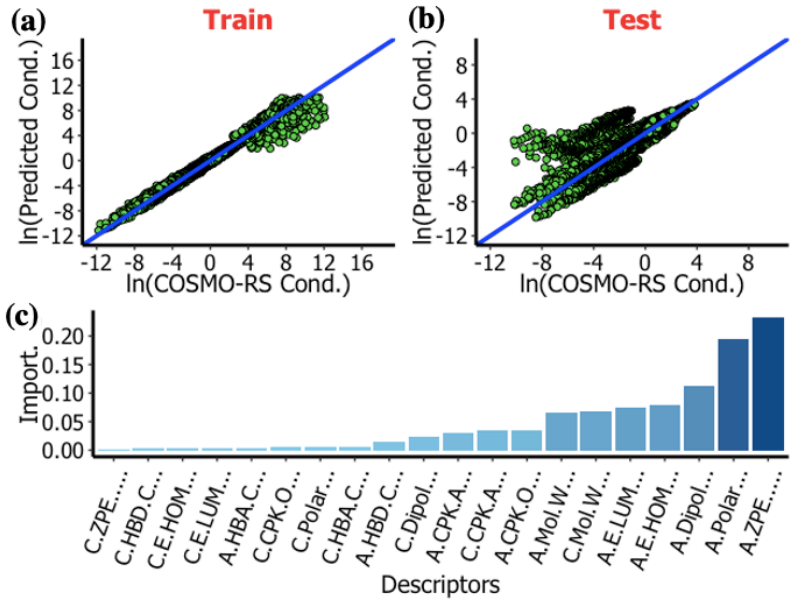

Metrics	Train	Test
RMSE	0.40	1.80
R-squared	0.99	0.58

Figure C.6. Prediction results of ln(conductivity) for train (a), test(b) sets and model importance (c).

Table C.4. ARM results for classification of Li_2S_8 solubility (top results for anionic and cationic descriptors)*

RHS**	Support	Confidence	Lift	Count
Anion_group=Bis_imide	0.005	0.298	7.31	194
Anion_group=Borate	0.009	0.502	4.10	326
Anion_group=Others	0.002	0.103	1.68	67
Cation_group=Piperidinium	0.001	0.038	1.58	25
Cation_group=Pyrrolidinium	0.001	0.080	1.56	52
Cation_group=Morpholinium	0.001	0.034	1.39	22
Anion_group=Halo_elemental_complexes	0.002	0.092	1.29	60
Cation_group=Quinolinium	0.001	0.051	1.25	33
Cation_group=Pyridinium	0.004	0.209	1.16	136
Cation_group=Ammonium	0.003	0.140	1.06	91
Cation_group=Imidazolium	0.006	0.358	0.99	233
Cation_group=Guanidinium	0.001	0.032	0.60	21

*The rules satisfying the ~3% confidence and ~0.1% support thresholds are shown.
**RHS:Right hand side of the condition {Solubility=A, Viscosity=A, Melting point=A, Conductivity=A}

APPENDIX D: SUPPORTING INFORMATION ON SECTION 4.1.4

The material characterization results for elemental analysis, TGA results, SEM images, XRD and FTIR patterns are given in Figure D.1-Figure D.2, respectively.

Table D.1. Elemental analysis results.

Sample	%N	%C	%H	%S
UG-5	0.31	24.54	0.56	57.33
UG-3	0.29	29.32	0.34	61.15
UG-1	0.44	9.24	0.22	68.79

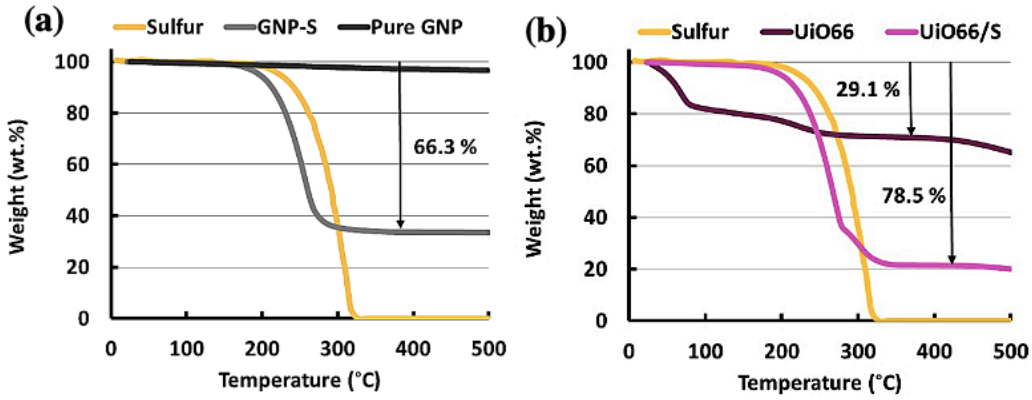

Figure D.1. TGA analysis results for GNP (a) and UiO-66 (b).

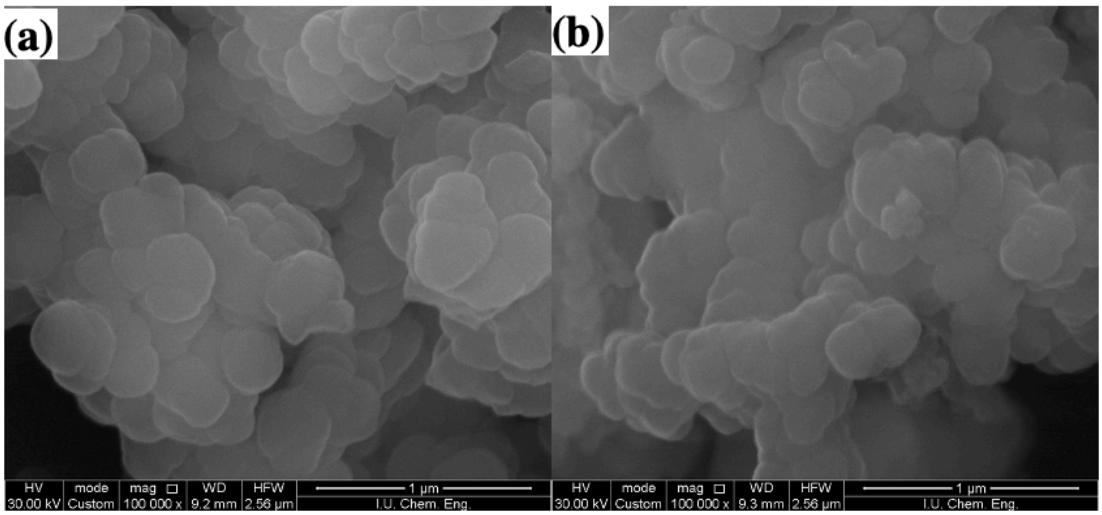

Figure D.2. SEM results for UiO-66 (a) and UG-1 composite (b).

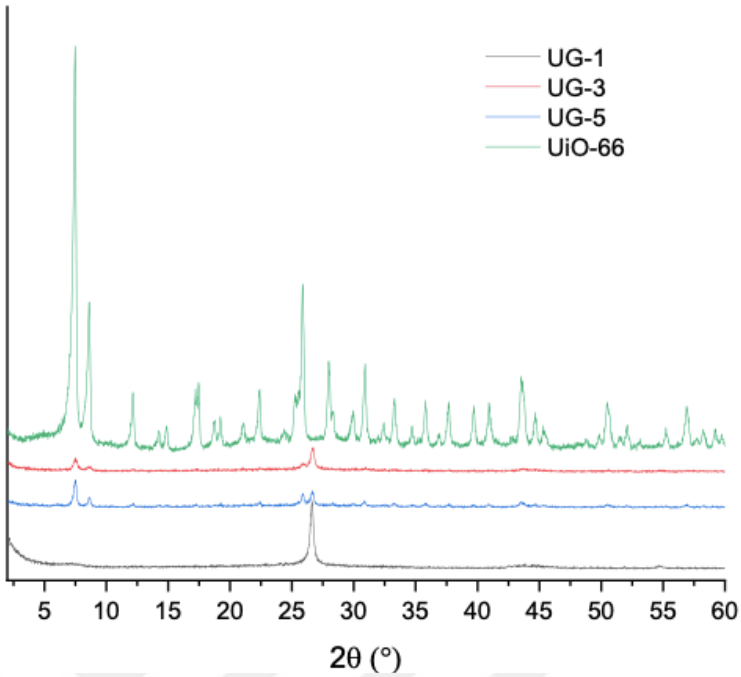

Figure D.3. XRD Patterns of UiO-66, UG-1, UG-3, and UG-5 nanoparticles.

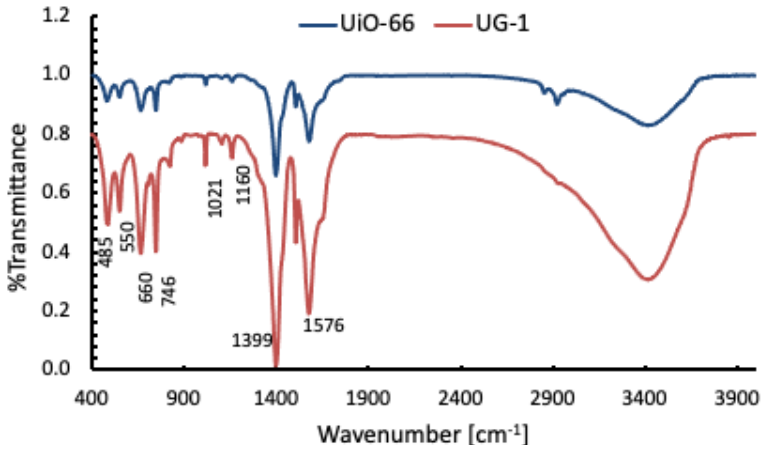

Figure D.4. FTIR plots of UiO-66 and GNP/UiO-66 nanoparticles. UG-1 is chosen as the representative composite.

APPENDIX E: SUPPORTING INFORMATION ON SECTION 4.1.5

The experimentally tested material contents and the cell design parameters are given in Table E.1. Afterwards, the system-level performances are given in Figure E.1, for the conditions listed in the table. The cycling performances and the details are given in Figure E.2 and Table E.2, respectively.

Table E.1. The details of the materials investigated in the Section 4.1.5.

Sample	Details	Co	V	S wt.%	S Load	E/S
CKBS Co*	Co:KB precursor ratio (1:1 wt.%)	+	-	70	1.24	20
CKBS Co**	Co:KB precursor ratio (1:1.5 wt.%)	+	-	70	1.24	20
CKBS Co***	Co:KB precursor ratio (1:2 wt.%)	+	-	70	1.24	20
KBS (Group 1)	-	-	-	70	1.24	20
VCKBS (Group 1)	Co:KB precursor ratio (1:1.5 wt.%), $1.23x10^{-4}$ mol V	+	+	70	1.24	20
VCKBS a	Co:KB precursor ratio (1:1.5 wt.%), $8.24x10^{-5}$ mol V	+	+	70	1.24	20
VCKBS b	Co:KB precursor ratio (1:1.5 wt.%), $1.6x10^{-4}$ mol V	+	+	70	1.24	20
VKBS	Co:KB precursor ratio (1:1.5 wt.%), $1.23x10^{-4}$ mol V	-	+	70	1.24	20
VCKBS 50	Co:KB precursor ratio (1:1.5 wt.%), $1.23x10^{-4}$ mol V	+	+	50	1.24	20
VCKBS 60	Co:KB precursor ratio (1:1.5 wt.%), $1.23x10^{-4}$ mol V	+	+	60	1.24	20
VCKBS 80	Co:KB precursor ratio (1:1.5 wt.%), $1.23x10^{-4}$ mol V	+	+	80	1.24	20
VCKBS- Group 2	Co:KB precursor ratio (1:1.5 wt.%), $1.23x10^{-4}$ mol V	+	+	70	2.4	2.4
KBS-Group 2	-	-	-	70	2.4	2.4

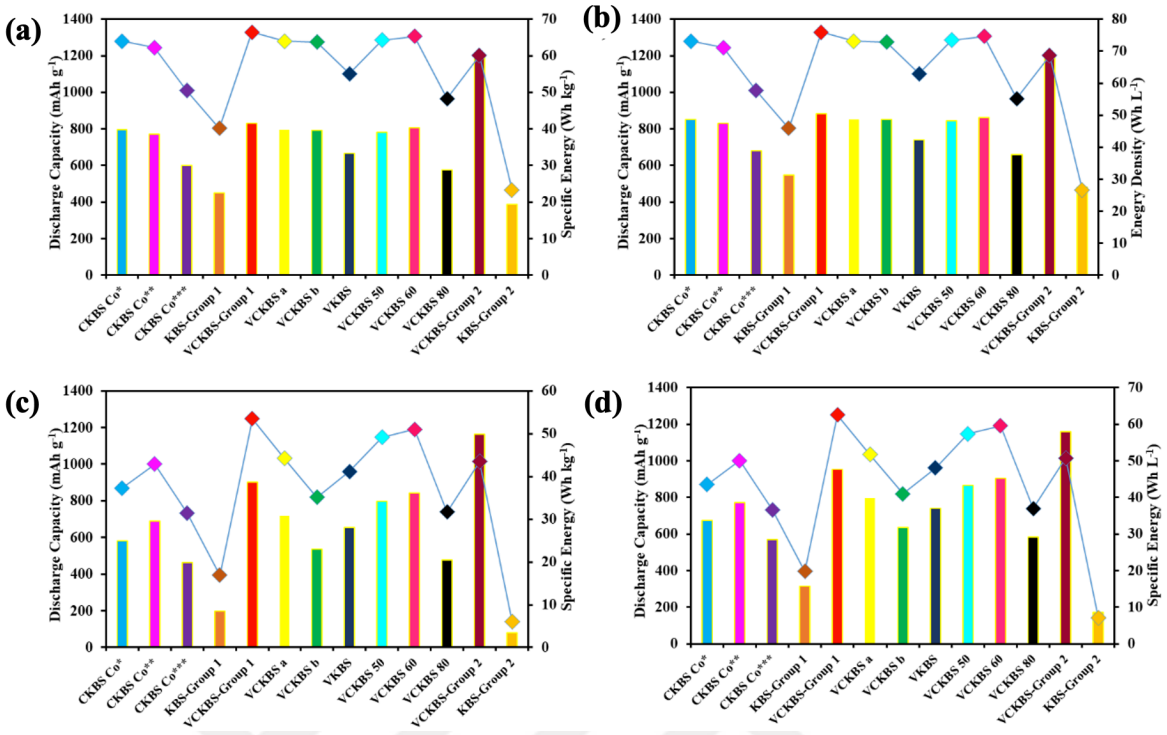

Figure E.1. Discharge capacities, system-level specific energies, and energy densities of all the cathodes for the 1st discharge (a)-(b) and 100th discharge (c)-(d).

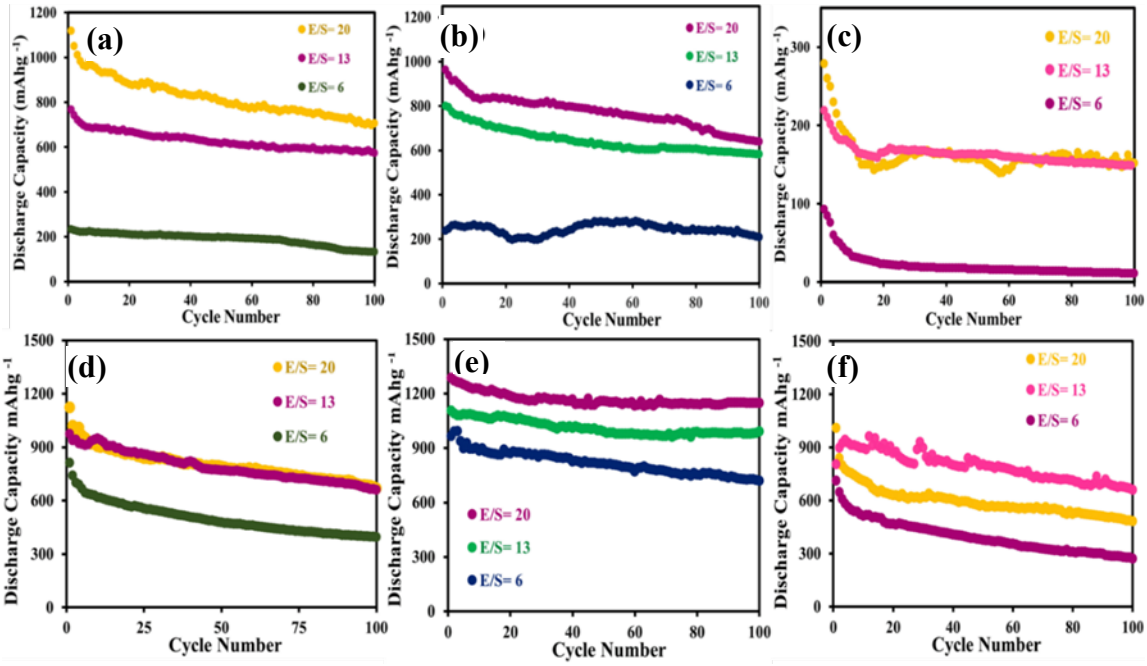

Figure E.2. Cycling performances: KBS cathodes with S loadings of 0.8 mg/cm^2 (a), 1.2 mg/cm^2 (b), and 3 mg/cm^2 (c), and VCKBS cathodes with S loadings of 0.8 mg/cm^2 (d), 1.2 mg/cm^2 (e), and 3 mg/cm^2 (f) at 0.1 C.

Table E.2. Li-S cell performance for KBS and VCKBS cathodes.

E/S ratio [mL/g]	**S loading [mg/cm^2]**	**Initial discharge capacity**	
		KBS	**VCKBS**
20	0.8	1117	1123
13	0.8	768	973
6	0.8	241	811
20	1.2	962	1285
13	1.2	799	1106
6	1.2	237	965
20	3	279	1009
13	3	219	804
6	3	93	711
Cathode contains 10 wt% PVDF binder and 45 wt% sulfur. Electrolyte is 1 M LiTFSI and 0.1 M $LiNO_3$ in DOL: DME (1: 1 vol%).			

APPENDIX F: SUPPORTING INFORMATION ON SECTION 4.2.1

Contents of common labels used for rarely used materials are as follows:

- Modified Li anode: $LiFePO_4$ + PTFE +Super P, Li metal+polymer buffer layer, Li metal+LTAP layer, Li metal+(Al_2O_3+PVDF-HFP) layer, Li metal+(Li_2CO_3+Carbon) layer and pretreated Li metals with chemicals
- Other carbons1: 3-D ordered mesoporous/macroporous carbon sphere arrays, Vapor grown carbon fiber, Carbon spheres, Ordered mesoporous carbon nanofiber arrays
- Other carbons2: Hollow spherical carbon, Pd-modified hollow spherical carbon, Carbon cloth, Carbon nanocube, Graphitized carbon foam, High surface area carbon, Inverse opal carbon, ^{13}C enriched amorphous carbon, Diamond like carbon (DLC), Carbon nanoballs, Glassy carbon, Graphitized carbon black
- Others1: NiO, MoS_2 Nanoflakes, Pt Nanoparticles, C_3N_4, S doped graphene nanosheets, B_4C nanoparticles, Sb-Doped Tin Oxide, Sb-Doped Tin Oxide Supported Ru Nanoparticles, O and N doped Carbon NanoWeb, Mo_2C, β Silicon carbide, GO+CNT
- Others2:Polydopamine
- Others3:PbRO, CuFe, C_3N_4, Core-shelled Fe/Fe_3O_4, Nanocrystalline Pyrochlore Catalyst, Mesoporous Lead Ruthenate, Mp pyrochlore, Polyimide, Fe-N-C Catalyst Nanoparticles, Pt_3Co, PEDOT+PSS (poly(3,4-ethylenedioxythiophene) polystyrene sulfonate)
- Others4: Ni, Teflon PTFE, Teflonized acetylene black, Teflon polytetrafluoroethylene 30B fluoropolymer resin, Teflon, Dry teflon, PTFE coated teflonized acetylene black, An ionomer, LITHion binder, Lithiated carbon
- Others5: 1,3-dioxolane, 2-methyltetrahydrofuran (2-Me-THF), Dimethylformamide, Diglyme
- Monoglyme, Ethylene carbonate:Propylene carbonate:1,2-dimethoxyethane, Triethyl phosphate (TEPa), Di(ethyleneglycol) di-n-butyl ether (i.e. butyl diglyme, BDG), Ethylene carbonate: dimethyl carbonate:ethylmethyl carbonate (EC:DMC:EMC) ,

Diethyl ether:Triglyme, Tetraethylene glycol dimethyl ether (TEGDME):Propylene carbonate (PC), 2,3-Dimethyl-2,3-dimethoxybutan

- Others6: Tris(2,2,2-trifluoroethyl) phosphate (TFP), 1,2-dimethoxyethane(DM), 1,2-dimethoxyethane (DME), Tris(2,2,2-trifluoroethyl) phosphite (TTFP), 2,2,2-trifluoroethyl)phosphite(TTFP), DME:Ethyl nonafluoro butylether(MFE), 1,2-dimethoxyethane (DME):TTFP, Diethyl carbonate (DEC), EC:DM, Tetrahydrofuran THF
- Others7: LiClO4 (only in anode), Li[NTf2], $LiNO_3$, $LiBF_4$, Lithium trifluoromethanesulfonyl (LiTFS), Lithium bis(trifluoromethansulfonyl)amide (LiTFSA), Lithium trifluoromethanesulfonate (LiTf)

The assumptions used in decision tree analysis are listed below:

- The data containing solid electrolyte was not included to the analysis.
- The bulk cathode materials of Ti composite, N-doped carbons and CNF were collected in one group as “Others” while “Carbon black+ CNT” and “Carbon black+ Graphene” labeled as “Carbon Black+Other Carbons”. Finally, “rGO” was included in “Graphene” group. The data containing gold was not included in the analysis.
- The cathode ingredients Pt_3Co, Ru and Co_4N were included in “Pt”, “RuO_2” and “Co oxide” classes, respectively. “CoMn oxide”, “Perovskite”, “$NiCo_2O_4$” and “LaFe oxide” were included in “Others”. The data containing “Pt+Au”, “Au+Pd”, Au, Pd and PdO were not used.
- EC:PC and “Ionic Liquids” were labeled as “Others” in electrolyte solvent variable.
- PVDF-HFP and “Others” classes for the binder were not used in the analysis.

Table F.1. Confusion Matrix of Decision Tree for Train Data.

	A	**B**	**C**	**Recall**
A	64	14	8	0.74
B	9	53	11	0.73
C	0	7	58	0.89
Precision	0.88	0.72	0.75	

Table F.2. Confusion Matrix of Decision Tree for Test Data.

	A	B	C	Recall
A	20	4	0	0.83
B	6	17	3	0.65
C	0	5	19	0.79
Precision	0.77	0.65	0.86	

Table F.3. ARM results for capacity testing group for capacities higher than or equal to 3000 mAh/g.

Descriptors	Support	Confidence	Lift	Count
{Bulk_Cathode_Categorized=N-doped carbons}	0.0078	0.0223	2.87	6
{Ingredient_Categorized=Co4N}	0.0013	0.0037	2.87	1
{Ingredient_Categorized=CoMn oxide}	0.0052	0.0149	2.87	4
{Ingredient_Categorized=Mo compound}	0.0013	0.0037	2.87	1
{Ingredient_Categorized=NiO+NiCo2O4 microspheres }	0.0091	0.0260	2.87	7*
{Ingredient_Categorized=Other oxides}	0.0052	0.0149	2.87	4
{Ingredient_Categorized=Pt3Co}	0.0013	0.0037	2.87	1
{Bulk_Cathode_Categorized=Ionic liquid CNT}	0.0052	0.0149	2.30	4
{Ingredient_Categorized=Co oxide+Others}	0.0052	0.0149	2.30	4
{Ingredient_Categorized=LaFe oxide}	0.0103	0.0297	2.30	8*
{Ingredient_Categorized=Ru}	0.0052	0.0149	2.30	4
{Gas_Diffusion_Layer_Categorized=Others}	0.0039	0.0112	2.16	3
{Salt_E_Categorized=Others}	0.0259	0.0743	1.98	20
{Bulk_Cathode_Categorized=Graphene}	0.0556	0.1599	1.96	43
{Ingredient_Categorized=Perovskite}	0.0246	0.0706	1.88	19
{E_Solvent_Categorized=Triglyme}	0.0466	0.1338	1.88	36
{Bulk_Cathode_Categorized=Graphene oxide}	0.0091	0.0260	1.83	7
{Separator_Categorized=Solid Electrolyte}	0.0065	0.0186	1.80	5
{E_Solvent_Categorized=DMSO}	0.0530	0.1524	1.79	41
{Bulk_Cathode_Categorized=Porous carbon}	0.0233	0.0669	1.78	18
{Reactant_Categorized=Others}	0.0103	0.0297	1.77	8
{E_Solvent_Categorized=Solid Electrolyte}	0.0039	0.0112	1.72	3
{Gas_Diffusion_Layer_Categorized=Carbon paper}	0.1164	0.3346	1.71	90
{Bulk_Cathode_Categorized=Carbon black+other carbons}	0.0129	0.0372	1.69	10
{Ingredient_Categorized=Others}	0.0103	0.0297	1.64	8
{Salt_E_Categorized=NO}	0.0103	0.0297	1.53	8
{Active_Material_Loading_Categorized=[0.8-1.2)}	0.0802	0.2305	1.50	62
{Bulk_Cathode_Categorized=Carbon black+CNT}	0.0065	0.0186	1.44	5*

Table F.3. ARM results for capacity testing group for capacities higher than or equal to 3000 mAh/g. (cont.)

Descriptors	Support	Confidence	Lift	Count
{Bulk_Cathode_Categorized=CNF}	0.0052	0.0149	1.44	4
{Bulk_Cathode_Categorized=N-doped CNT}	0.0078	0.0223	1.44	6*
{Gas_Diffusion_Layer_Categorized=Carbon cloth}	0.0039	0.0112	1.44	3
{E_Solvent_Categorized=Tetraglyme}	0.1889	0.5428	1.41	146
{Active_Material_Loading_Categorized=(0-0.8)}	0.1100	0.3160	1.30	85
{Bulk_Cathode_Categorized=rGO}	0.0116	0.0335	1.29	9
{Binder_Categorized=PVDF}	0.1617	0.4647	1.28	125

Table F.4. ARM results for voltage testing group for capacities in between 750 mAh/g and 1000 mAh/g.

Descriptors	Support	Confidence	Lift	Count
{Active_Material_Percentage_Categorized=20--60}	0.008	0.033	4.33	1
{Bulk_Cathode_Categorized=Graphene oxide}	0.008	0.033	4.33	1
{Bulk_Cathode_Categorized=Other carbons}	0.015	0.067	4.33	2*
{Ingredient_Categorized=Mo compound}	0.023	0.100	4.33	3
{Reactant_Categorized=Others}	0.008	0.033	4.33	1
{Ingredient_Categorized=Ru oxide+Mn oxide}	0.054	0.233	3.37	7*
{Bulk_Cathode_Categorized=N-doped carbons}	0.038	0.167	3.10	5
{Ingredient_Categorized=Co4N}	0.015	0.067	2.89	2*
{Bulk_Cathode_Categorized=CNF}	0.023	0.100	2.60	3*
{Ingredient_Categorized=Ru}	0.023	0.100	2.60	3
{E_Solvent_Categorized=Ionic Liquid}	0.038	0.167	2.17	5*
{E_Solvent_Categorized=PC}	0.008	0.033	2.17	1
{E_Solvent_Categorized=Solid E+Liquid E}	0.008	0.033	2.17	1
{E_Solvent_Categorized=DMSO}	0.038	0.167	1.97	5
{Binder_Categorized=PTFE}	0.085	0.367	1.83	11
{E_Solvent_Categorized=DME}	0.015	0.067	1.44	2
{Reactant_Categorized=Dry Air}	0.008	0.033	1.44	1
{Active_Material_Percentage_Categorized=100}	0.100	0.433	1.41	13
{Binder_Categorized=NO}	0.100	0.433	1.41	13
{Anode_Categorized=Modified Li anode}	0.046	0.200	1.37	6
{Separator_Categorized=Glass+polymeric}	0.023	0.100	1.30	3*

Table F.4. ARM results for voltage testing group for capacities in between 750 mAh/g and 1000 mAh/g. (cont.)

Descriptors	Support	Confidence	Lift	Count
{Bulk_Cathode_Categorized=Graphene}	0.031	0.133	1.24	4
{Active_Material_Loading_Categorized=(0-0.8)}	0.108	0.467	1.24	14

Table F.5. ARM results for voltage testing group for capacities in between 500 mAh/g and 750 mAh/g.

Descriptors	Support	Confidence	Lift	Count
{Binder_Categorized=Others}	0.018	0.091	5.09	2*
{Bulk_Cathode_Categorized=N-doped carbons}	0.018	0.091	5.09	2
{E_Solvent_Categorized=EC:DMC}	0.009	0.045	5.09	1
{E_Solvent_Categorized=PC}	0.009	0.045	5.09	1
{E_Solvent_Categorized=Solid E+Liquid E}	0.018	0.091	5.09	2*
{Salt_E_Categorized=Others}	0.018	0.091	5.09	2*
{Separator_Categorized=Solid E}	0.018	0.091	5.09	2*
{Ingredient_Categorized=Mo compound}	0.027	0.136	3.82	3*
{Reactant_Categorized=Air}	0.027	0.136	3.82	3
{Bulk_Cathode_Categorized=Graphene}	0.054	0.273	3.05	6
{Bulk_Cathode_Categorized=Others}	0.036	0.182	2.91	4
{E_Solvent_Categorized=Ionic Liquid}	0.018	0.091	2.55	2
{Ingredient_Categorized=Perovskite}	0.009	0.045	2.55	1
{Ingredient_Categorized=Ru}	0.009	0.045	2.55	1
{E_Solvent_Categorized=DMSO}	0.027	0.136	2.18	3*
{Bulk_Cathode_Categorized=CNT}	0.045	0.227	1.96	5
{Salt_E_Categorized=LiClO4}	0.036	0.182	1.85	4
{Binder_Categorized=NO}	0.045	0.227	1.82	5
{Active_Material_Percentage_Categorized=100}	0.045	0.227	1.70	5
{Salt_E_Categorized=LiCF3SO3}	0.063	0.318	1.55	7
{Ingredient_Categorized=Mn oxide}	0.036	0.182	1.36	4
{Binder_Categorized=PTFE}	0.080	0.409	1.35	9
{Active_Material_Percentage_Categorized=80--90}	0.107	0.545	1.27	12
{Reactant_Categorized=Dry Air}	0.009	0.045	1.27	1

Table F.5. ARM results for voltage testing group for capacities in between 500 mAh/g and 750 mAh/g. (cont.)

Descriptors	**Support**	**Confidence**	**Lift**	**Count**
{Salt_E_Categorized=LiPF6}	0.009	0.045	1.27	1
{Separator_Categorized=Glass+polymeric}	0.009	0.045	1.27	1
{Separator_Categorized=Polymeric}	0.018	0.091	1.27	2
{Ingredient_Categorized=NO}	0.107	0.545	1.25	12
{Active_Material_Loading_Categorized=(0-0.8)}	0.063	0.318	1.23	7

APPENDIX G: SUPPORTING INFORMATION ON SECTION 4.2.2

The details for IL screening study of the Li-O_2 batteries are given in this section.

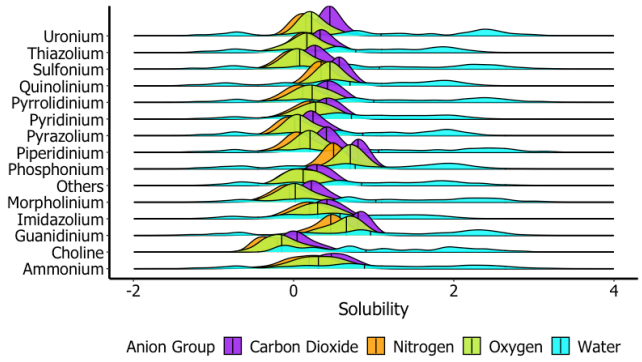

Figure G.1. The gas solubilities based on cation groups.

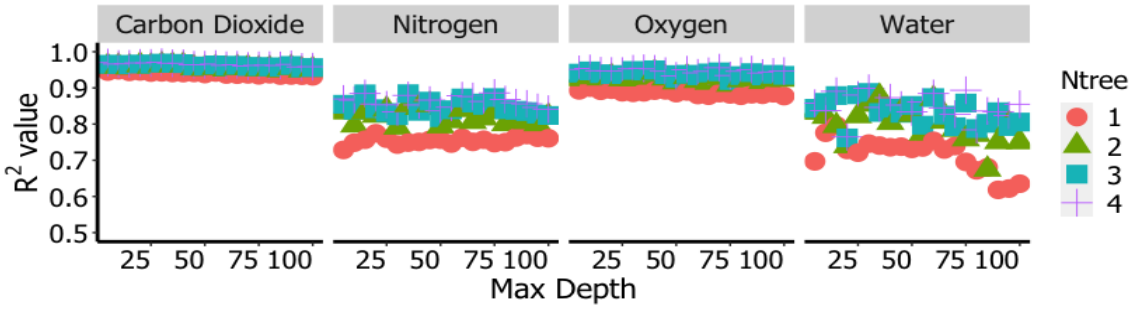

Figure G.2. The average of the 5-fold cross-validation R^2 value for the gas predictions for the whole dataset, shapes represent Ntree.

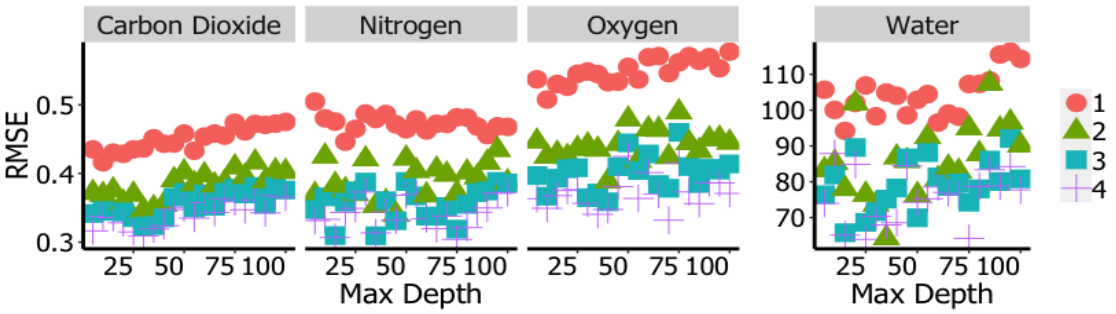

Figure G.3. The average of the 5-fold cross-validation RMSE value for the gas predictions for the whole dataset, shapes represent Ntree.

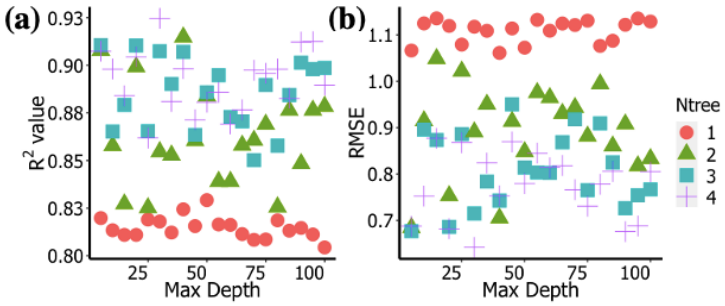

Figure G.4. The average of the 5-fold cross-validation R^2 and RMSE value for the ln(water solubility) predictions for the whole dataset.

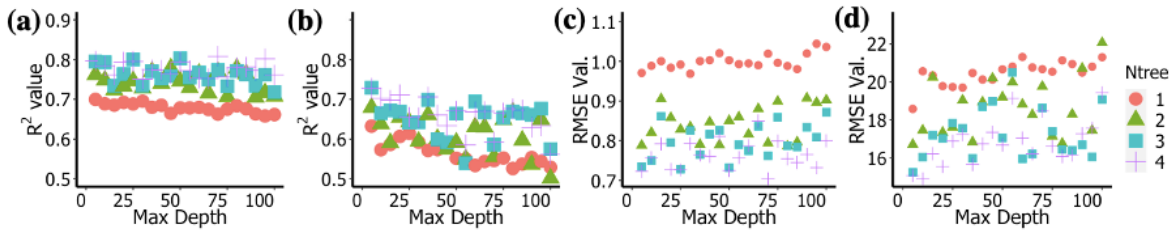

Figure G.5. The average of the 5-fold cross-validation R^2 value for ln(viscosity) (a), melting point(b) and RMSE value for ln(viscosity) (c), melting point(d) for the whole dataset.

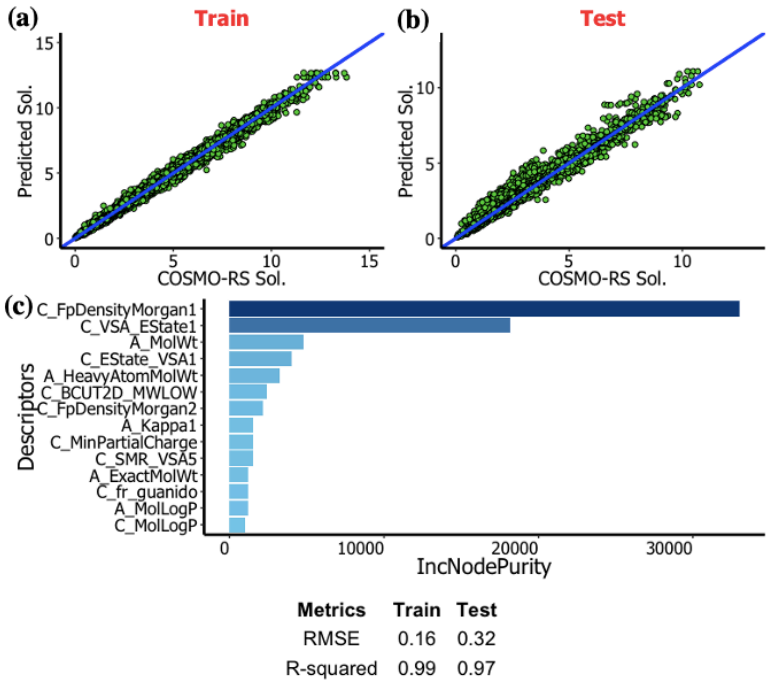

Metrics	Train	Test
RMSE	0.16	0.32
R-squared	0.99	0.97

Figure G.6. ML results on the carbon dioxide solubilities for the train (a), test (b) sets with importance (c) values, the performance metrics are provided at the bottom.

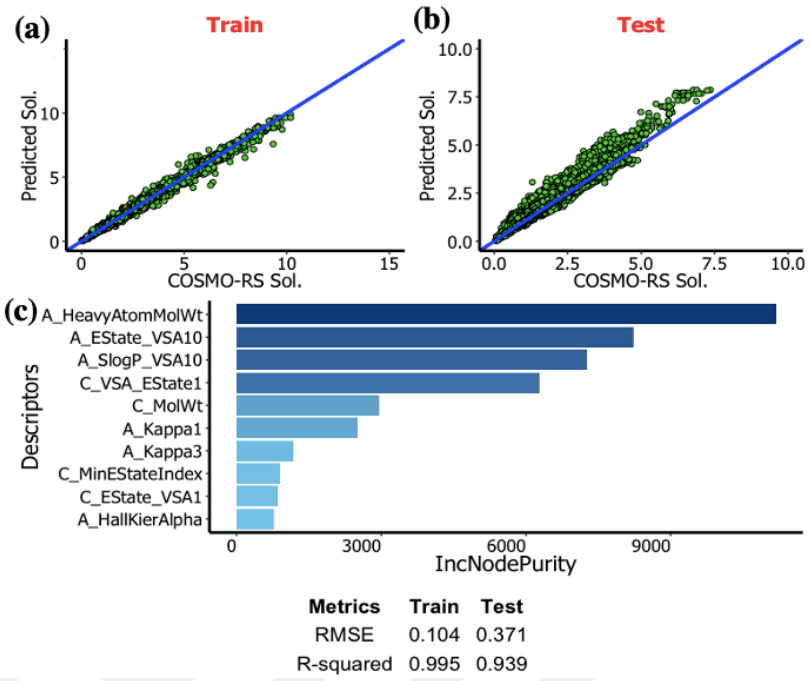

Figure G.7. ML results on the nitrogen solubilities for the train (a), test (b) sets with importance (c) values, the performance metrics are provided at the bottom.

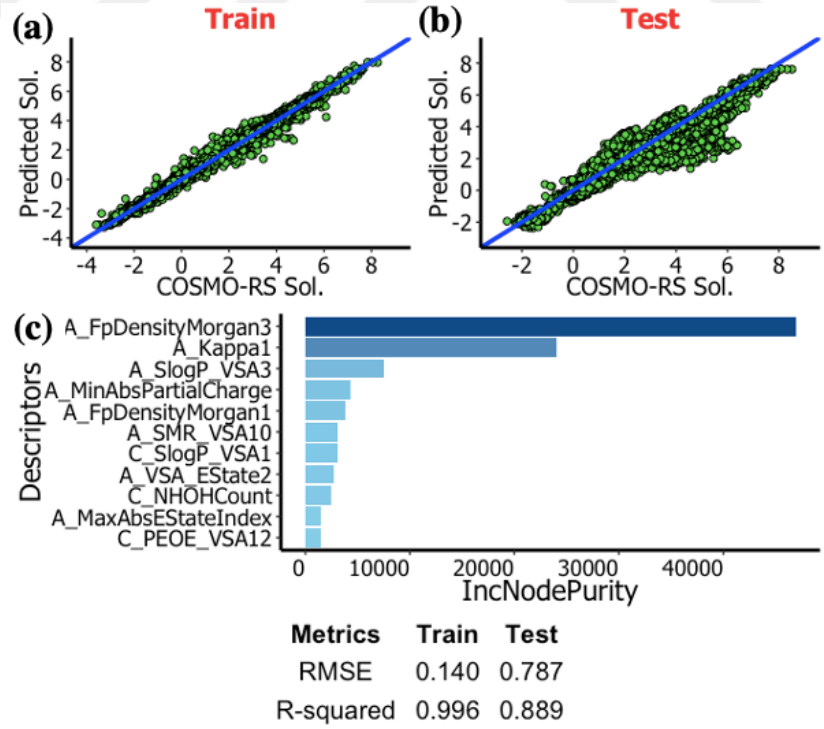

Figure G.8. ML results on the water solubilities in natural logarithm scale for train (a), test (b) sets with importance (c) values, the performance metrics are provided at the bottom.

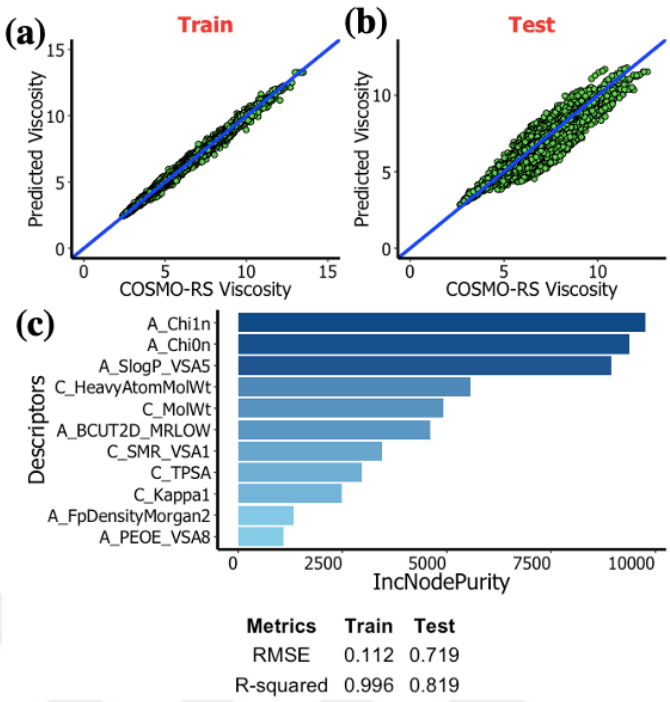

Figure G.9. ML results on the viscosities at 298 K in mPa.s in natural logarithm scale for the train (a), test (b) sets with importance (c) values, the performance metrics are provided at the bottom.

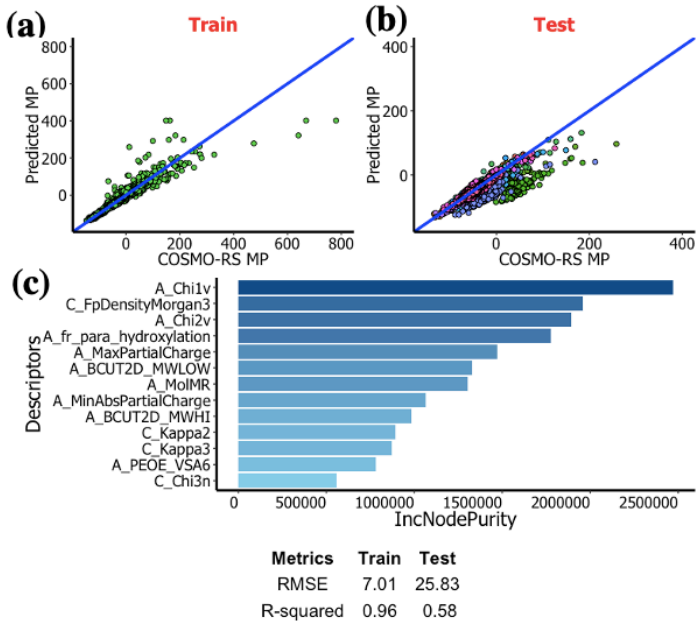

Figure G.10. ML results on the melting points in ºC in natural logarithm scale for the train (a), test (b) sets with importance (c) values, the performance metrics are provided at the bottom.

Table G.1. The original 208 descriptors calculated from RDKit library [215].

Feature Names	**Feature Descriptions**	**No**	**Ref.**
MolWt	MolWt (average molecular weights), HeavyAtomMolWt (excluding Hydrogens), ExactMolWt (exact molecular weights)	3	-
Compositional	FractionCSP3(fraction of C atoms that are SP3 hybridized), NHOHCount (# of NHs and OHs), HeavyAtomCount, NOCount, NumAliphaticCarbocycles, NumAliphaticHeterocycles, NumAliphaticRings, NumAromaticCarbocycles, NumAromaticHeterocycles, NumAromaticRings, NumHAcceptors, NumHDonors, NumHeteroatoms, NumRotatableBonds, NumSaturatedCarbocycles, NumSaturatedHeterocycles, NumSaturatedRings, RingCount, NumValenceElectrons, NumRadicalElectrons	20	-
fr_fagments	the number of specific fractions, for example: phenol group	85	-
HallKierAlpha	Hall&Kier alpha value, the atom identification in the molecular shape: the sum of relative atomic radii of atoms concerning C(sp3) atoms	1	[381]
Kappa1 - Kappa3	First, Second and Third order shape attributes for one, two and three bond fragments where 1=cyclicity, 2=starcity-linearity likeliness, 3=centrality of branching	3	
Chi0-Chi1,	The sum of connectivity terms calculated by the number of skeletal neighbors; 0 for vertex, 1 for edges, >2 for larger subgraphs	2	
Chi0n - Chi4n	The sum of connectivity terms calculated by the number of valence and core electrons; 0 for vertex(atoms), 1 for edges(bonds), >2 for larger subgraphs	5	
Chi0v - Chi4v	The sum of connectivity terms calculated by the number of valence electrons excluding the number of hydrogens; 0 for vertex(atoms), 1 for edges(bonds), >2 for larger subgraphs	5	
LabuteASA	Labute's Approximate Surface Area	1	[382]
PEOE_VSA1 - PEOE_VSA14	Gasteiger 22 (PEOE) method of calculating partial charges, which is based on the iterative equalization of atomic orbital electronegativities and surface area contributions	14	
SMR_VSA1 - SMR_VSA10	Molar refractivitycontributions and surface area contributions	10	
SlogP_VSA1 - SlogP_VSA12	LogP(octanol/water; lipophilicity index) contributions and surface area	12	
EState_VSA1 - EState_VSA11	Electronic state contributions and surface area contributions, with specified intervals	11	
VSA_EState1 - VSA_EState10	Electronic state contributions and surface area contributions, with different specified intervals	10	
BCUT2D_PHI-BCUT2D_PLOW	P is the parameters specifically Molecular weight (MW), Gasteiger charge (CHG), Crippen logP and molar refractivity (MR)	8	[394]
TPSA	Topological polar surface area, difference between the reference is only N and O atom contributions are included	1	[395]
BalabanJ	Topological index showing the complexity	1	[384]
BertzCT	Topological index meant to quantify "complexity" of molecules	1	[385]
Ipc	Topological index effective in branching	1	[386]
FpDensityMorgan-FpDensityMorgan3	Topological index about the structure-radius 1,2 and 3	3	[383]

Table G.1. The original 208 descriptors calculated from RDKit library [215]. (cont.)

MolLogP, MolMR	LogP(octanol/water; lipophilicity index), MolMR:molecular refractivity, molecular sum of each atom taking atomic type into account	2	[396]
qed	Drug-likeliness by taking molecular weight, logP, topological polar surface area and some others into account	1	[397]
EstateIndex & Partial_charge	Max, Min, MaxAbs, MinAbs versions, Estate:Electrotopological State: Include both topological and electronic factors such as polarity and charge	8	[381]

Table G.2. The hyperparameters tuned for each gas by 5-fold cross-validation of RF modeling.

Gas	**Maximum Depth**	**Ntree**
Carbon Dioxide	3	30
Nitrogen	3	20
Oxygen	3	10
Water	3	20
ln(viscosity)	3	10
Melting Point	3	10